NASA Conference Publication 3279

High-Speed Research: 1994 Sonic Boom Workshop

Atmospheric Propagation and Acceptability Studies

Edited by
David A. McCurdy

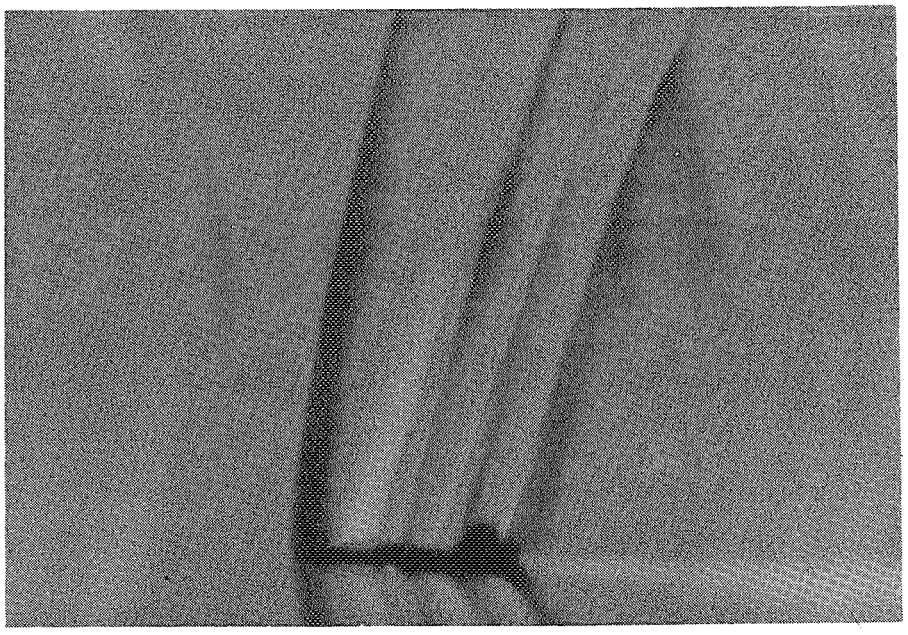

Proceedings of a workshop sponsored by the National Aeronautics and Space Administration, Washington, D.C., and held in Hampton, Virginia
June 1–3, 1994

October 1994

NASA Conference Publication 3279

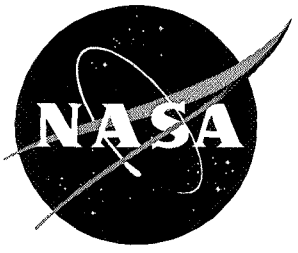

High-Speed Research: 1994 Sonic Boom Workshop

Atmospheric Propagation and Acceptability Studies

Edited by
David A. McCurdy
Langley Research Center • Hampton, Virginia

Proceedings of a workshop sponsored by the
National Aeronautics and Space Administration,
Washington, D.C., and held in
Hampton, Virginia
June 1–3, 1994

National Aeronautics and Space Administration
Langley Research Center • Hampton, Virginia 23681-0001

October 1994

This publication is available from the following sources:

NASA Center for AeroSpace Information
800 Elkridge Landing Road
Linthicum Heights, MD 21090-2934
(301) 621-0390

National Technical Information Service (NTIS)
5285 Port Royal Road
Springfield, VA 22161-2171
(703) 487-4650

Preface

The third High-Speed Research Sonic Boom Workshop was held at NASA Langley Research Center on June 1–3, 1994. The purpose of this workshop was to provide a forum for government, industry, and university participants to present and discuss progress in their research. The workshop was organized into sessions dealing with atmospheric propagation; acceptability studies; and configuration design, analysis, and testing. Attendance at the workshop was by invitation only.

The workshop proceedings include papers on atmospheric propagation and acceptability studies. Papers discussing atmospheric effects on the sonic boom waveform addressed several issues. It has long been assumed that the effects of molecular relaxation are adequately accounted for by assuming that a steady-state balance between absorption and nonlinear wave steepening exists. It was shown that the unsteadiness induced by the nonuniform atmosphere precludes attaining this steady state. Further, it was shown that the random atmosphere acts as a filter, effectively filtering out high frequency components of the distorted waveform. Several different propagation models were compared, and an analysis of the sonic boom at the edge of the primary carpet established that the levels there are bounded. Finally, a discussion of the levels of the sonic boom below the sea surface was presented. Papers on acceptability examined the reaction of people to long-term sonic boom exposure.

The use of trade names of manufacturers in this report does not constitute an official endorsement of such products or manufacturers, either expressed or implied, by the National Aeronautics and Space Administration.

David A. McCurdy
Langley Research Center

CONTENTS

Preface iii

An Optical Technique for Examining Aircraft Shock Wave Structures in Flight 1
Leonard M. Weinstein

Effect of Stratification and Geometrical Spreading on Sonic Boom Rise Time 19
Robin O. Cleveland, Mark F. Hamilton, and David T. Blackstock

An Evaluation of Rise Time Characterization and Prediction Methods 39
Leick D. Robinson

Finestructure of Transient Waves in a Random Medium: The Correlation and Spectral Density Functions 47
Alan R. Wenzel

Numerical Model for the Weakly Nonlinear Propagation of Sound Through Turbulence 61
Bart Lipkens and Philippe Blanc-Benon

Sonic Boom Interaction with Turbulence 81
Zvi Rusak and Thomas E. Giddings

Atmospheric Propagation at Larger Lateral Distances From the Flight Track 99
Allan D. Pierce

Atmospheric Effects on the Risetime and Waveshape of Sonic Booms 123
Richard Raspet, Henry E. Bass, and Patrice Boulanger

The Effect of Aircraft Speed on the Penetration of Sonic Boom Noise Into a Flat Ocean 137
Victor W. Sparrow

Simple Atmospheric Perturbation Models for Sonic-Boom-Signature Distortion Studies 157
L. J. Ehernberger, Morton G. Wurtele, and Robert D. Sharman

USAF Single-Event Sonic Boom Prediction Model: PCBoom3 171
Kenneth J. Plotkin, Micah Downing, and Juliet A. Page

Deriving a Dosage-Response Relationship for Community Response to High-Energy Impulsive Noise 185
Sanford Fidell and Karl S. Pearsons

An In-Home Study of Subjective Response to Simulated Sonic Booms 193
David A. McCurdy, Sherilyn A. Brown, and R. David Hilliard

Residents' Reactions to Long-Term Sonic Boom Exposure: Preliminary Results 209
James M. Fields, Carey Moulton, Robert M. Baumgartner, and Jeff Thomas

Participants 219

AN OPTICAL TECHNIQUE FOR EXAMINING AIRCRAFT SHOCK WAVE STRUCTURES IN FLIGHT

Leonard M. Weinstein
NASA Langley Research Center
Hampton, VA

INTRODUCTION

The detailed properties of sonic booms have to be better understood before commercial, next generation, supersonic and hypersonic aircraft can be properly developed. Experimental tests and measurements are needed to help sort the physical details of the flows at realistic test conditions. Some of these tests can be made in wind tunnels, but the need for full flight conditions simulation, the problem of tunnel wall interference, and the short distance the shocks can be examined from the aircraft, limit the usefulness of wind tunnel tests.

Previous measurement techniques for examining the flow field of aircraft in flight have included pressure measurements on the aircraft, ground based pressure measurements, and flow field measurements made with chase aircraft. Obtaining data with chase planes is a slow and difficult process, and is limited in how close it can be obtained to the test aircraft. A need clearly existed for a better technique to examine the shock structure from the plane to large distances from the plane.

A new technique has been recently developed to obtain schlieren photographs of aircraft in flight (SAF). Preliminary results have been obtained, and the technique holds promise as a tool to study the shape and approximate strength of the shock wave structure around the test aircraft, and examine shock wave details all the way from the aircraft to near the ground. The current paper describes this approach, and gives some preliminary test results.

WIND TUNNEL SCHLIEREN PHOTOGRAPH

The photograph in figure 1 was obtained with a focusing schlieren system in the 0.3 m Transonic Cryogenic Tunnel. It illustrates a failed attempt to obtain a Mach 1.2 flow field over a large shuttle model. The interaction between the body shock and the tunnel wall resulted in a partially started flow, with both supersonic and subsonic regions. This picture demonstrates the difficulty of testing reasonably large models in supersonic wind tunnels. The large amount of flow detail visible also shows the value of direct flow visualization.

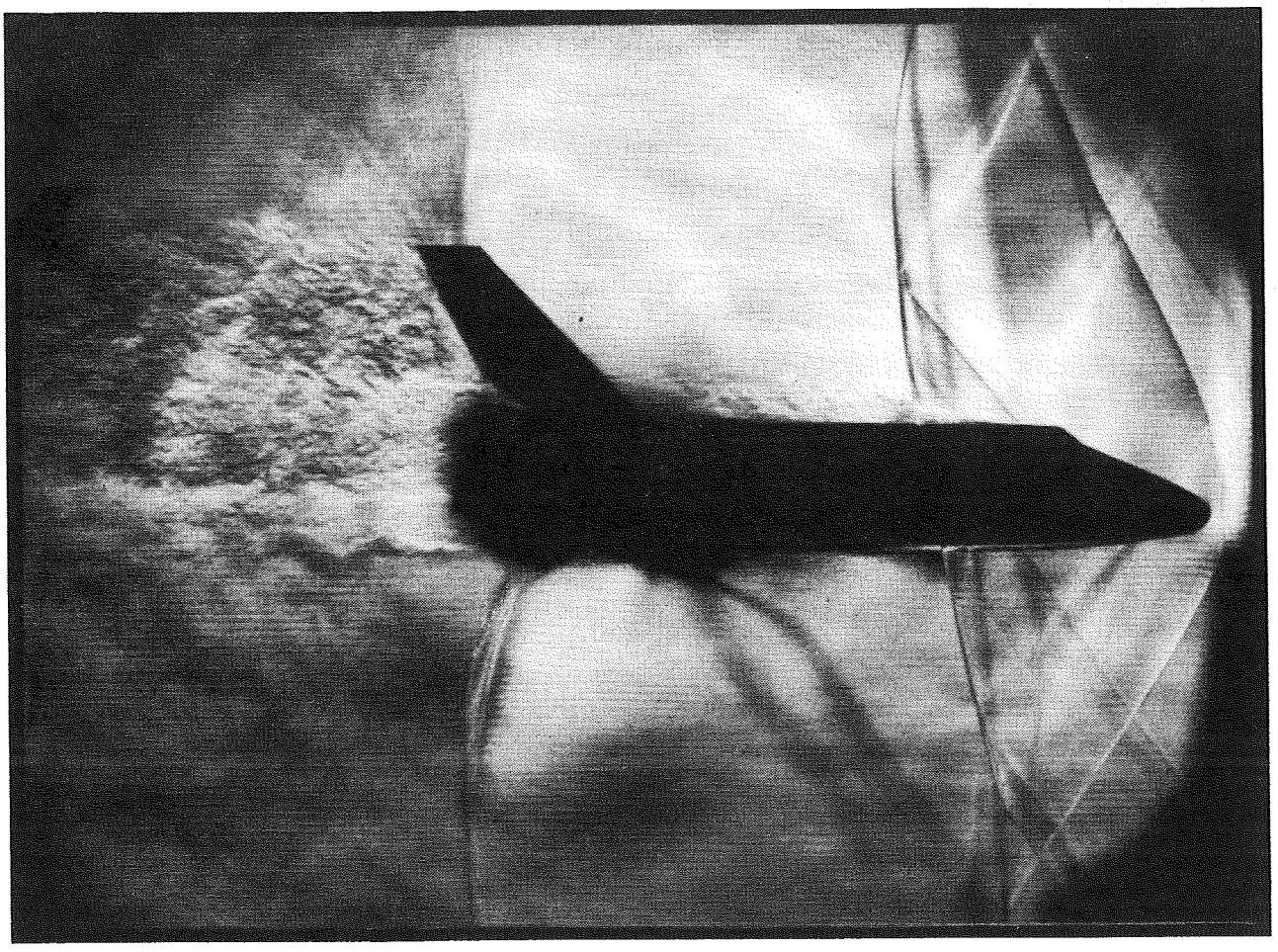

Figure 1. Focusing schlieren of shuttle model in 0.3 m TCT.

REFRACTION IMAGE OF F-111 FLOW FIELD

Figure 2 shows an F-111 flying just over Mach 1, with a non uniform background sky. The strong shock waves distort the image of the background sky by refraction, enough to displace features and make the shocks visible. The low sensitivity of this technique, and the need for the non uniform background greatly limits this direct imaging technique.

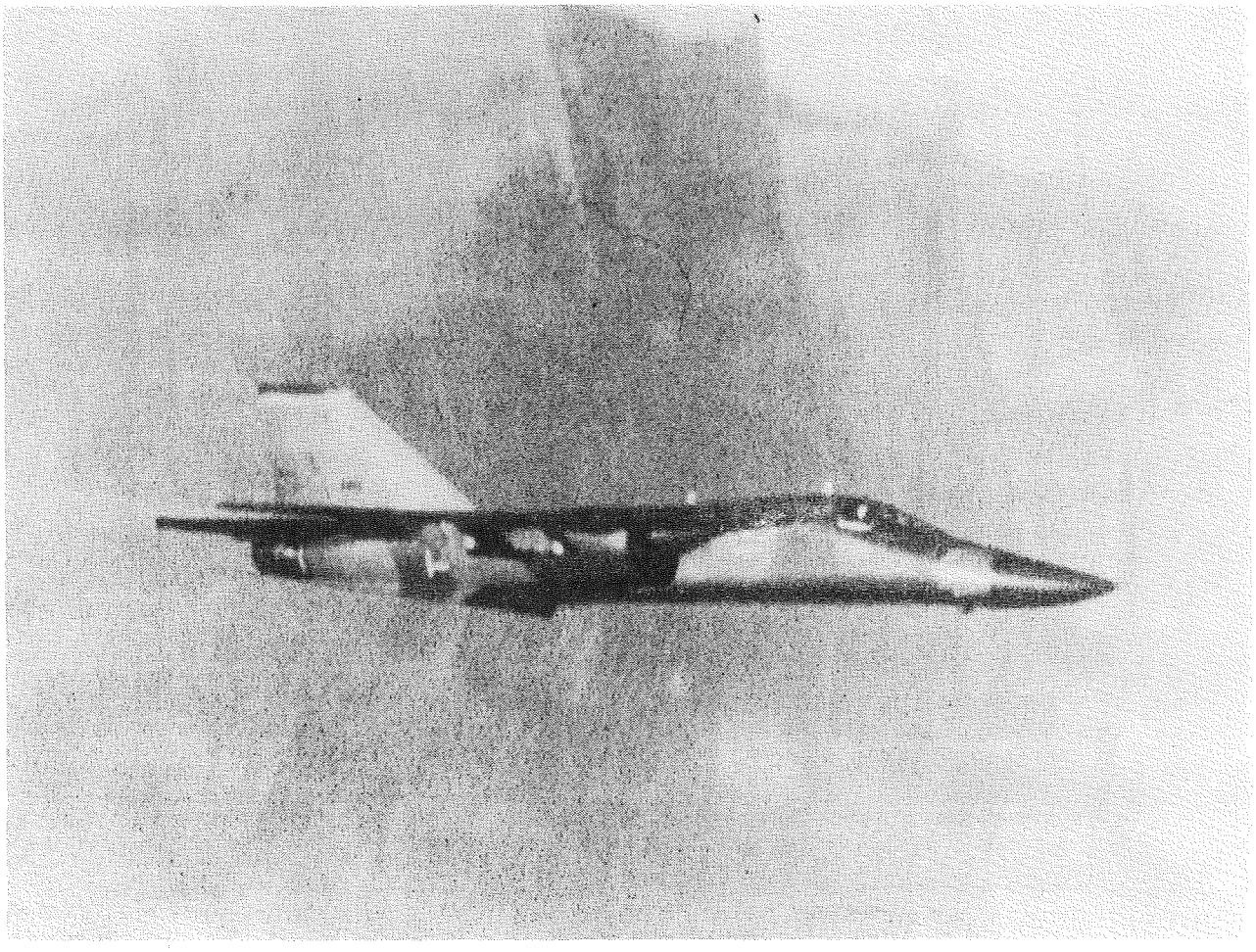

Figure 2. Refraction image of F-111 flow field

FOCUSING SCHLIEREN

The new flow visualization technique, which will be described later, uses some of the features of focusing schlieren systems. A brief description of focusing schlieren is given to help understand the new concept.

The features of a focusing schlieren system are shown in figure 3. An array of points or lines from a source grid are imaged by a camera lens. A photographic negative image of the source grid is then obtained to use as a cutoff grid. Each point on the source grid now has a corresponding "knife edge" spatial filter, and each source and cutoff point pair make an uncollimated conventional schlieren system with a very small field of view. However, the multiple sources from the source grid are selected to be close enough together so that each point on the final test section image is obtained from several source points. The net result is that a large field of view is obtained, with different parts of the source grid being used to obtain different parts of the image. The field of view is now determined by the total size of the source grid (rather than lens diameter).

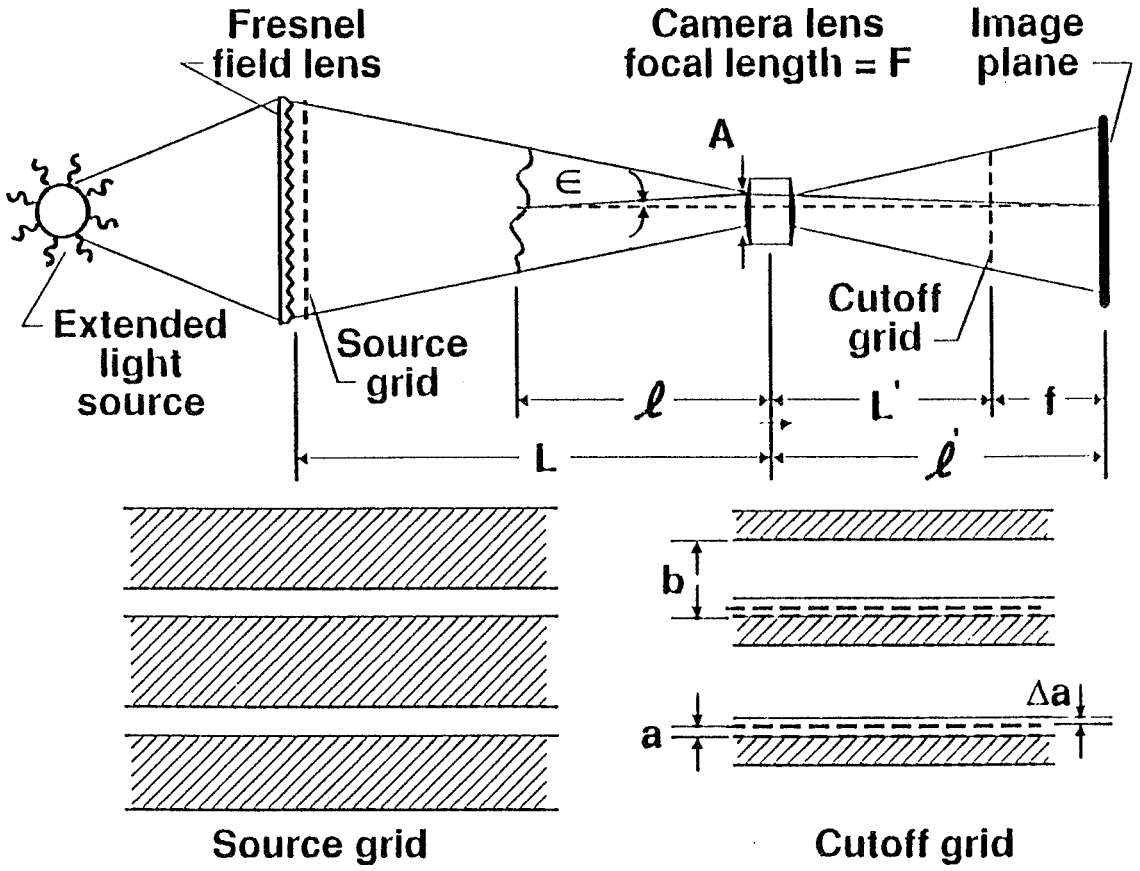

Figure 3. Details of Focusing schlieren system.

SCHLIEREN FOR AIRCRAFT IN FLIGHT SETUP

The schlieren for aircraft in flight (SAF) was developed by combining some of the features of astronomical photography with focusing schlieren and streak photography. The setup used is shown in figure 4. A telescope is used to track the sun (or moon) so that the image is stationary at the focus. A neutral filter is used to lower intensity to a safe level. An opaque mask with a narrow curved slit is positioned to block all but a thin portion of the edge of the sun and a small region of sky next to the edge. A thin region at the edge of the sun is thus the light source, and the mask is the cutoff, for a single curved grid line as in a focusing schlieren system. An aircraft is flow through a field of view crossing this sliver of light, and the aircraft image is sharply focused on to a film plane. The film is moved to follow the aircraft image movement. A narrow slice of a schlieren image of the aircraft flow field is formed at each instant of time, and over the full exposure this slice is scanned along the image. This produces a composite streak camera schlieren image of the flow field examined.

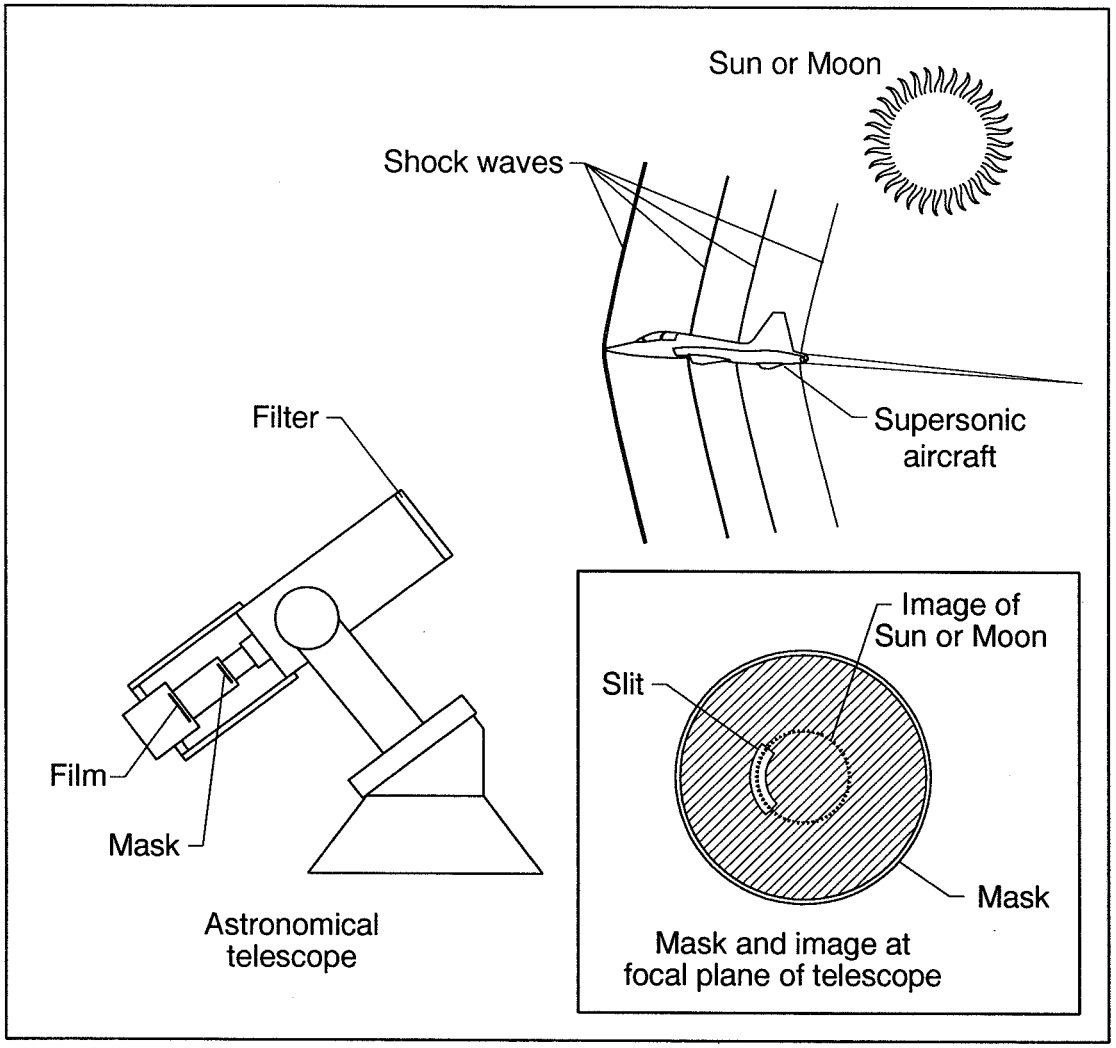

Figure 4. Setup of schlieren for aircraft in flight.

RESOLUTION AND FIELD OF VIEW FOR SAF

The maximum possible resolution of detail in images is affected by several factors. The maximum resolution (diffraction limit) of a telescope is determined by the telescope aperture. In addition, the atmospheric turbulence, accuracy of focus, tracking accuracy during exposure, and film limitations may result in less than diffraction limited resolution. Unless the telescope is on a high mountain, or in a chase plane, the daytime atmospheric limited resolution is seldom better than 1 arcsec, and more often closer to 2 arcsec. To prevent significant additional limitation due to the telescope, a telescope of at least 5 inch aperture is desired (which can approach 1 arcsec resolution with near diffraction limited performance). For the following table, a net image resolution of 2 arcsec was assumed for all causes combined.

The field of view photographed is the physical height at the aircraft distance corresponding to the angle of the portion of the sun used for a grid line. The sun covers slightly over 1/2 degree, and about 1/3 degree is used for the grid line in SAF. This angle was used to compute the field of view in the table.

Table I. Resolution and Field of View as a Function of Slant Range

SLANT RANGE (ft.)	(for 2 arcsec) RESOLUTION (inches)	(for 1/3 deg) FIELD OF VIEW (ft.)
8,000	0.9	46
16,000	1.9	92
32,000	3.7	184
64,000	7.4	368
128,000	14.9	736

PHOTOGRAPH OF SETUP AT WALLOPS FLIGHT FACILITY

The prototype system used to demonstrate the SAF concept used an 8 inch aperture, f/10 telescope, which was large enough to carry a reasonable amount of equipment, and was still small enough to carry around and set up easily.

The SAF system was carried to Wallops Flight Facility and set on the end of a runway. Figure 5 shows the system set up for the initial effort. Several tests flights were made with a T-38 at M=0.9 (but with supersonic flow over the wings) at a slant range of 16,000 ft., to try and photograph the flow field at high resolution. The flights were required to be subsonic for these tests since they were made over land. The field of view was only 46 ft. at that range. A combination of clouds, equipment problems, and the difficulty of passing through this small area prevented success in the early flights.

Figure 5. SAF set up on runway at Wallops.

SAF OF T-38 AT 32,000 FT. AND M=1.1

The aircraft range was increased to 32,000 ft. and the plane was flown fully supersonic for additional tests. This resulted in a 92 ft. field of view, and a large extent of supersonic flow. Assateague island (close to Wallops) was selected as the site to set up the SAF equipment. This location was used because the supersonic flights had to be made over water, 5 miles away from land, to prevent sonic booms from bothering people.

At 10:30 a.m.on Dec. 13, 1993, the T-38 was flown at M=1.1 at an altitude of 13,700 ft. This resulted in a 32,000 ft. slant range from the camera. The Wallops ILS system was used to guide the plane through the test area. The photo shown in figure 6 was the first SAF photo of the T-38 flow field.

The image is very grainy because of the film used for the preliminary test. In addition, the relay lens used to reimage the aircraft onto the film was not well corrected except near the center of the image. Since the plane was near the edge of the field of view, the image was noticeably less sharp around the plane. In addition, some banding (curved streaks due to uneven film motion) resulted in uneven exposure of the image. Even with these limitations, the image clearly showed the shock wave details. About one plane length above the aircraft, 6 shocks are seen to merge into 4.

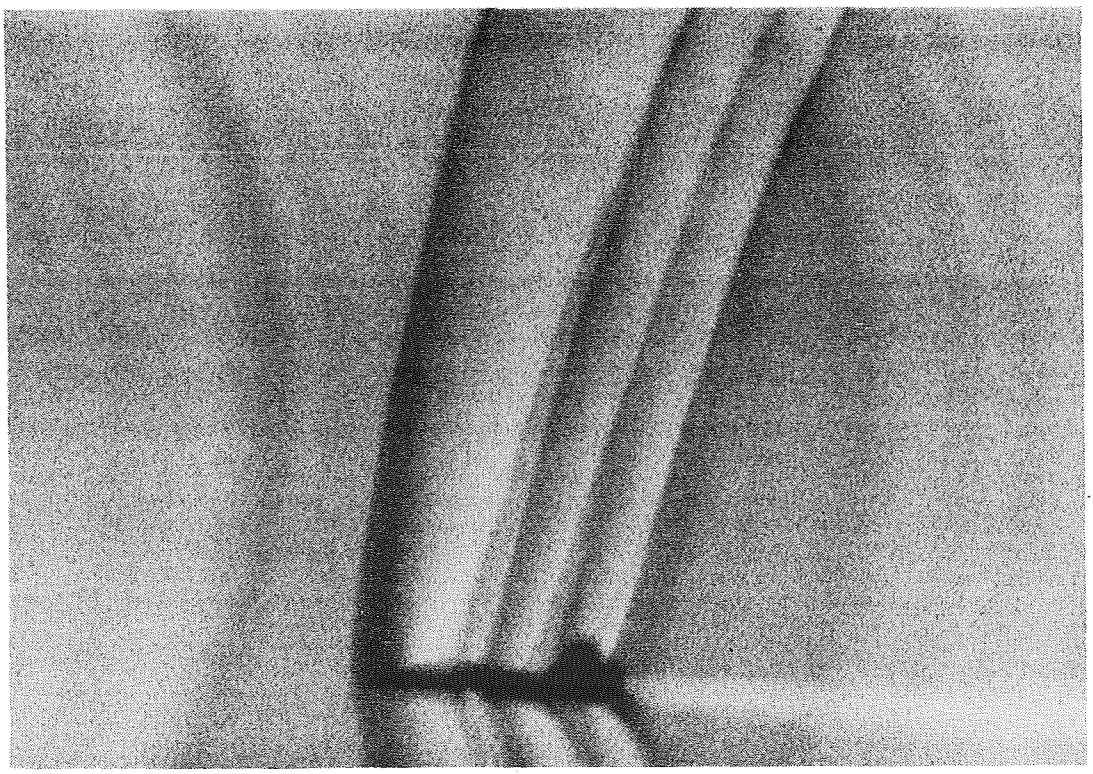

Figure 6. SAF of T-38 at 32,000 ft. slant range and M=1.1.

USE OF SAF TO STUDY SONIC BOOMS

The demonstration of SAF as a tool to examine the flow field of aircraft in flight led to the possibility of using it as part of a sonic boom study. A joint cooperative effort was initiated at Langley to evaluate the possible use of SAF to examine both near and far field shock structure for aircraft used in these studies.

A shock wave system weakens as it moves away from a supersonic aircraft, and the shock system also distorts as it moves through local variations in the atmosphere. In addition, the aircraft used in sonic boom studies are generally flown at significantly higher altitudes than the T-38 flight was. This means that lower atmospheric densities are encountered, and the resolution is reduced for more distant subjects. The SAF system was taken out to Dryden Flight Facility to evaluate these effects, and see if limitation would be encountered.

Modifications were made to overcome some of the problems encountered in the Wallops test. A finer grain film was selected to cut graininess. The relay optical system was modified to obtain better sharpness on the outer part of the image. The film used was also selected to have higher contrast, to increase sensitivity. This last feature also made the "banding" much worse, but it was thought this would not prevent evaluation of the performance, even though it would make bad looking pictures.

The need to fly at fairly large altitudes combined with the desire to keep slant range reasonably small, and the need for the atmosphere to be as undisturbed as possible, constrained the flights to mid morning.

CONVENTIONAL PHOTOGRAPH OF F-18 IN FLIGHT

F-18's were selected to do the SAF evaluation flight tests at Dryden. This aircraft was easily capable of reaching the desired mach number and altitude desired, and was available for the test. Figure 7 shows a conventional photograph of an F-18 in flight to show details of the aircraft.

Figure 7. Conventional photograph of F-18 in flight.

GALILEO HILL

The SAF system was set up on the peak of Galileo Hill in California City. This is close to Dryden, and was in a good location to obtain SAF pictures. Figure 8 shows the hill, which is about 700 ft taller than the surrounding area.

Figure 8. Photograph of Galileo hill.

SAF OF F-18 AT 60,000 FT RANGE AND M=1.4

On April 13,1994, the first SAF test was made at Dryden. Two F-18's were flown at M=1.4, one mile apart, with the trailing plane 300 ft. below the leading plane. This was done to increase the chance of photographing at least one of the planes. The leading plane was about 35,000 ft. above sea level, and the SAF system was about 3,200 ft. above sea level. This resulted in a slant range of about 60,000 ft. from the planes to the camera at closest approach. The viewing angle of the sun results in an oblique view rather than a side view of the aircraft. The photograph shown in figure 9 was taken just after 9 a.m., and shows the flow field around the lead plane.

SAF is sensitive to density gradients normal to the local grid line. Since the grid line curves, and since the shocks swept back, the best orientation of grid is to curve back toward the shock direction. The photo in the figure had the grid reversed, and this resulted in lower sensitivity, especially near the edges of the photo.

The camera was also slightly out of focus, so the resolution was lower than expected. The image banding was very bad, as was expected, but did not prevent the flow field from being seen. The aircraft shape shows up well, and shocks are clearly visible, even though the plane was about 12 miles away.

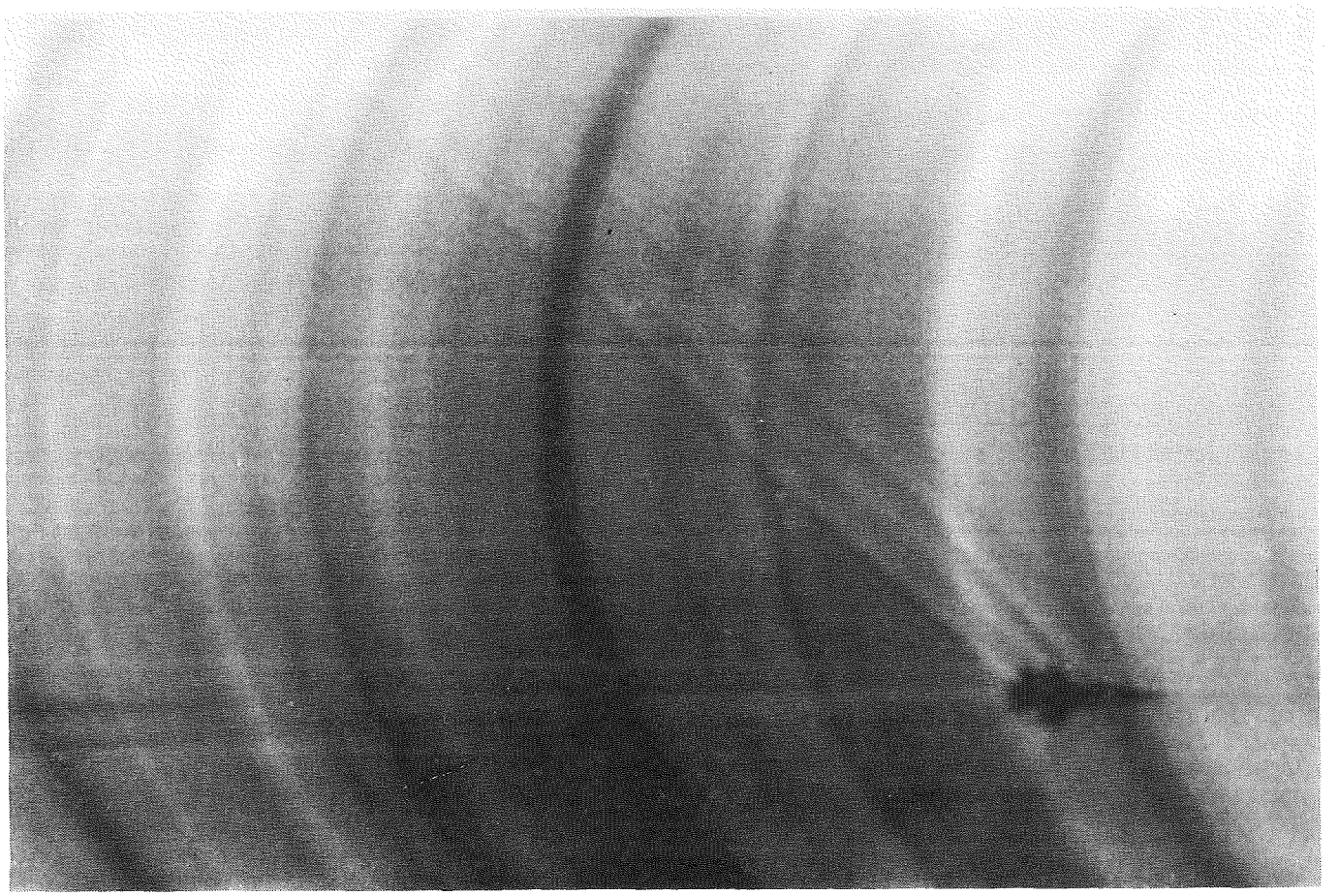

Figure 9. SAF of F-18 at 60,000 ft. slant range and M=1.4

SAF OF SHOCK 1,060 FT. BELOW F-18

On April 15, several additional flights were made by the two F-18's to try to get shock detail at different distances below the aircraft. The grid was reversed from the previous photo to obtain the best sensitivity possible. The photo shown in figure 10 was obtained just before 9 a.m., for the trailing plane. The photo shows the shock at 1,060 ft. below the plane. The complex multiple shock pattern has already merged to just two visible shocks.

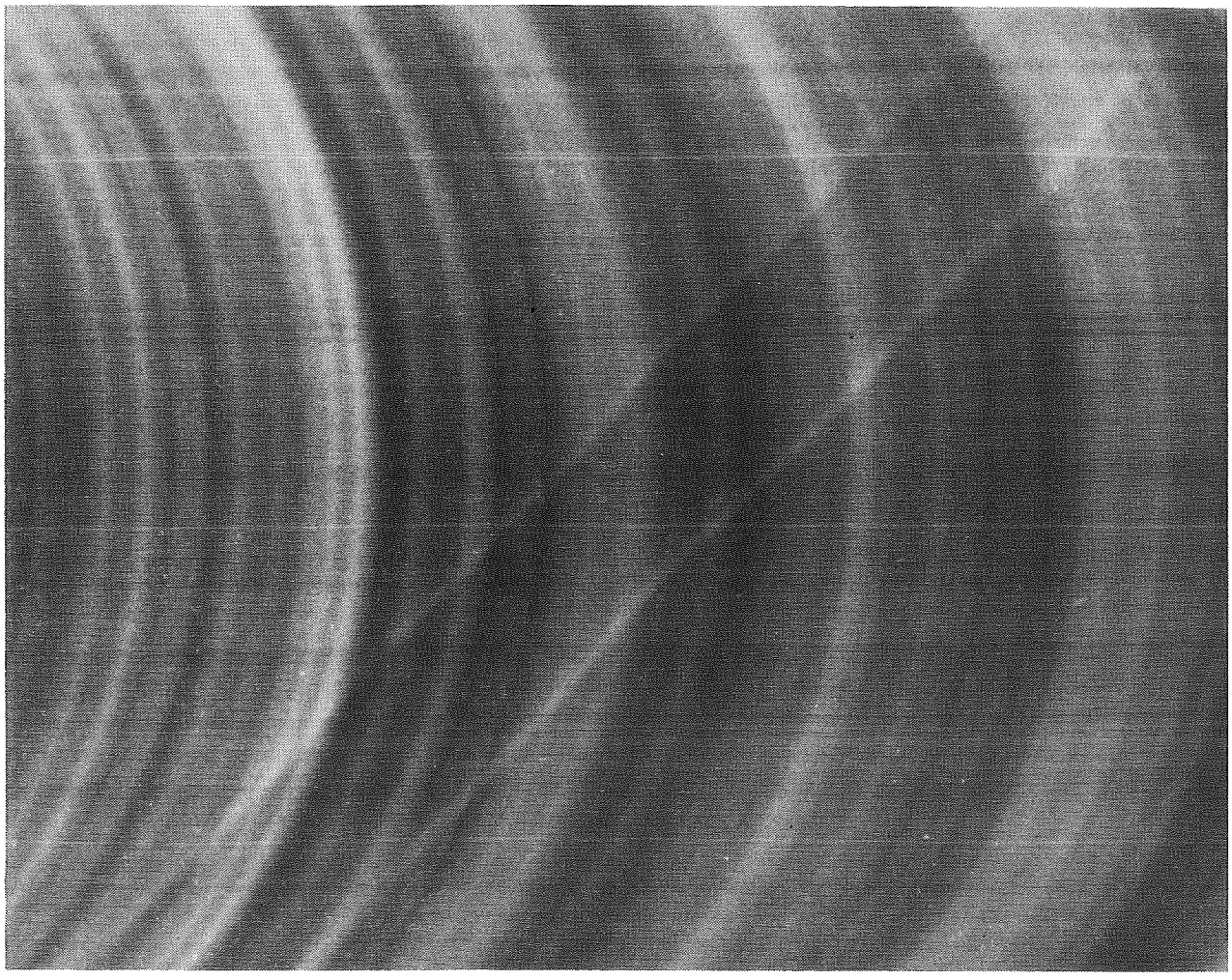

Figure 10. SAF of shock 1,060 ft.below F-18.

VARIATION OF LONGITUDINAL SHOCK SEPARATION WITH DISTANCE

Three passes by the flights made on April 15 resulted in 6 shock photos being obtained. These ranged from 510 ft. below the plane (diagonal distance) to 3,830 ft. below. The photographs for the shocks at the largest distance were not correctly exposed, so were not as good as the others. However, all shock photos were usable. The maximum distance the shocks can be photographed has not been determined, but clearly is very far from the aircraft. Figure 11 shows the change in length of the separation of front to back shock, normalized by the plane length, plotted against the diagonal distance below the aircraft.

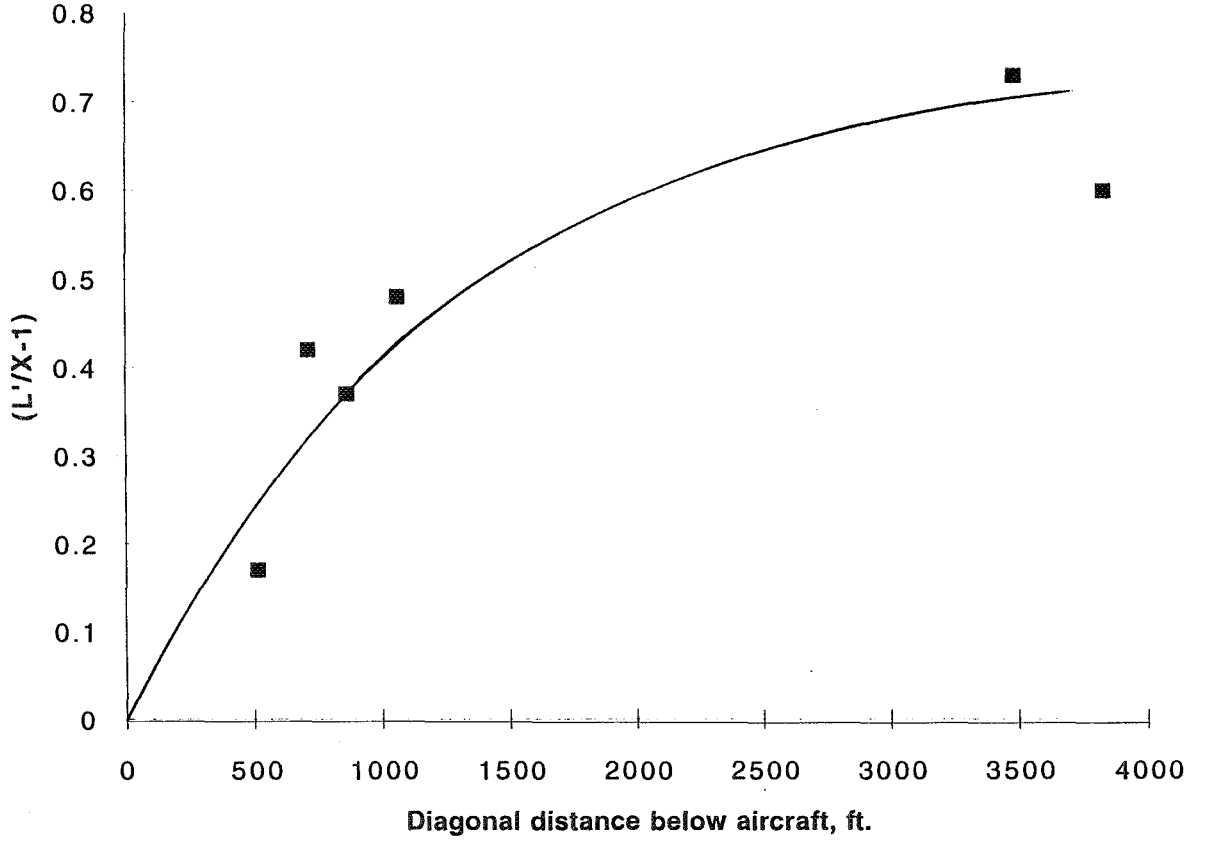

Figure 11. Variation of longitudinal shock seperation with distance below F-18.

PROBLEMS FROM PROTOTYPE SAF, AND SUGGESTED SOLUTIONS

There were several problems encountered in the prototype SAF system. A list of these, and possible ways to overcome them (including some that have been already implemented), are given in table 2.

Table II. Problems From Prototype SAF System, and Suggested Solutions

PROBLEMS	SOLUTIONS
Poor focus with low power eyepiece	Use higher power eyepiece, or auto focus
Grainy and low resolution film	Fine grain, high resolution film, or high resolution electronic imagery
Film banding	Smooth film transport, or TDI electronic imaging
Sun tracking errors	Auto sun tracker
Camera rotation with equatorial tracker	Use altazimuth rather than equitorial tracker
Fly plane through correct location	Use precision navigation, or multiple SAF cameras with overlapping fields of view

ALTERNATE VERSIONS OF SAF

The prototype SAF camera was used as a development system, and was far from optimized. Different versions can be made to better accomplish specific tasks. Table 3 shows some alternate versions and what special capabilities can be accomplished with them.

Table III. Variations of SAF Systems

VARIATION	SPECIAL CAPABILITY
Chase plane version	High resolution, possibility of near side view
Small compact system	Easy portability, flight use
TDI camera instead of film	No banding, instant replay
SAF multiple camera array (one station)	Large field of view
SAF multiple station array	Flight Dynamics
Point SAF camera with photo detector	Time history of flow field at single point
Near ground source/detector system	Near ground time history of signal

SUMMARY

The basic capability of schlieren for aircraft in flight imaging technology has been demonstrated at NASA's Wallops Flight Facility, and Dryden Flight Facility. Photos of T-38 and F-18 aircraft along with their flow fields, have been obtained at 6 and 12 miles range respectively, and shock wave pictures have been obtained as far as 3,830 ft. diagonally below the F-18.

Problems in the limitation of the initial design, operational procedures, and recording medium have been either solved, or possible solutions suggested.

An improved SAF system is currently being designed, and will be tested when ready. Use of arrays of SAF cameras, and special versions of systems should further increase the possible capabilities of this approach.

The limits of the technology have not yet been reached, but even the demonstrated capability should be useful for sonic boom studies.

EFFECT OF STRATIFICATION AND GEOMETRICAL SPREADING ON SONIC BOOM RISE TIME [1]

Robin O. Cleveland, Mark F. Hamilton and David T. Blackstock
Applied Research Laboratories,
The University of Texas at Austin, Austin, TX 78713-8029,
and
Mechanical Engineering Department,
The University of Texas at Austin, Austin, TX 78712-1063

SUMMARY

Sonic boom propagation is not steady, even in a nonturbulent atmosphere. The shock overpressure Δp is affected by geometrical spreading, stratification of the atmosphere, and even the N shape of the waveform. Nevertheless, for purposes of predicting shock profile and rise time, it has commonly been assumed that the shock is in steady state. For example, molecular relaxation, which is a major factor controlling sonic boom rise time, is strongly dependent on relative humidity. Because humidity varies with altitude, rise time varies as the sonic boom propagates downward. The question is whether rise time depends only on local conditions or is also affected by the history of humidity variation along the propagation path. Kang [1, Chap. 7.2] argues that shocks respond to change in humidity quickly enough that they are in effect always in steady state. In other words only local conditions are important. Robinson [2, Chap 5.2] however disagrees with this hypothesis. Raspet *et. al.* [3] found that perturbed 100 Pa shocks (step waveform) require propagation distances of order 1 km for the rise time to return to within 10% of its steady shock value.

The purpose of our investigation is to determine the effect of unsteadiness (not associated with turbulence) on rise time. The unsteadiness considered here is due to (1) geometrical spreading, (2) stratification, which includes variation in density, temperature, and relative humidity, and (3) N

[1] Work supported by NASA

shaped waveform. A very general Burgers equation, which includes all these effects, is the propagation model for our study. The equation is solved by a new computational algorithm in which all the calculations are done in the time domain.

The present paper is a progress report in which some of the factors contributing to unsteadiness are studied, namely geometrical spreading and variation in relative humidity. The work of Pierce and Kang [4], which motivated our study, is first reviewed. We proceed with a discussion of the Burgers equation model and the algorithm for solving the equation. Some comparison tests to establish the validity of the algorithm are presented. The algorithm is then used to determine the distance required for a steady-state shock, on encountering an abrupt change in relative humidity, to reach a new steady state based on the new humidity. It is found that the transition distance for plane shocks of amplitude 70 Pa is about 4 km when the change in relative humidity is 10%. Shocks of amplitude 140 Pa require less distance. The effect of spherical and cylindrical spreading is also considered. We demonstrate that a spreading shock wave never reaches steady state and that its rise time will be less than the equivalent steady state shock. Finally we show that an N wave has a slightly short rise time than a step shock of the same amplitude.

OUTLINE

- Introduction
- Review of Pierce-Kang result
- Burgers equation model
- Time-domain algorithm
- Validation tests of algorithm
- Rise time as a function of
    1. Change in relative humidity
    2. Geometrical spreading
    3. Waveform

REVIEW OF THE PIERCE-KANG PREDICTION OF SONIC BOOM RISE TIME

Pierce and Kang [4] calculated sonic boom rise time by solving a model propagation equation called Burgers' equation [5]. An important contribution was to augment the classical Burgers equation with terms that describe molecular relaxation due to both nitrogen and oxygen. By assuming that the sonic boom shock near the ground is in steady state, Pierce and Kang simplified their Burgers equation and solved it numerically. Rise time predictions obtained from their solution were then compared with rise time data from a large number of sonic boom measurements taken at Edwards Air Force Base in 1987 [6]. In their initial comparison almost all the measured rise times lay well above the predicted curve [7], as shown in the left-hand plot of Fig. 1. The discrepancy was attributed to atmospheric turbulence. Later, however, when they made a correction for pressure doubling at the ground, they found their prediction to fall in the middle of the data [8]; see the right-hand plot in Fig. 1. Although the data would seem to corroborate their prediction, the role of turbulence casts doubt on this conclusion. Model experiments done at our laboratory [9, 10] indicate that turbulence almost always increases rise time, rarely decreases it. If turbulence does have this effect, then molecular relaxation should be expected to provide a lower bound for the data, not approximate a mean for the data. Why then does the Pierce-Kang prediction not serve as a lower bound?

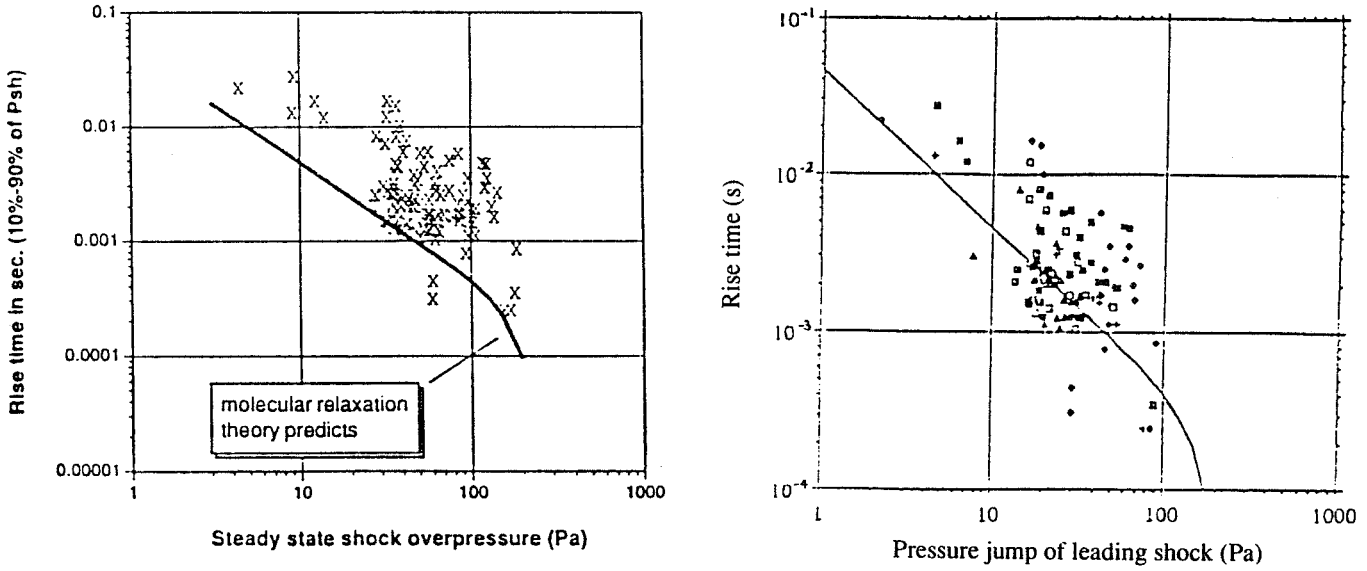

Figure 1: The left-hand plot shows Kang and Pierce's initial prediction [7]. The right-hand plot shows the corrected prediction [8].

Our hypothesis to answer this question is based on results found in Refs. [2, 3]. We suspect that the shock wave at the head of a sonic boom does not respond quickly enough to variation in atmospheric conditions (and to other changes that affect the profile, such as geometrical spreading and even wave shape), to justify the steady-state assumption. If our hypothesis is correct, then to improve on the Pierce-Kang prediction requires that more than local conditions be taken into account. Past history along the propagation path must be significant. Figure 2 shows profiles of temperature and relative humidity measured during a sonic boom experiment [1, pp 157–161]. It is seen that conditions can change rapidly, particularly during the lower part of the propagation path. To determine whether the sonic boom profile can respond quickly to changes of this order, we have calculated the effect on rise time of an abrupt change in atmospheric conditions. Thus far we have concentrated on changes in relative humidity. For purposes of this paper, temperature and pressure are fixed at their ground level values.

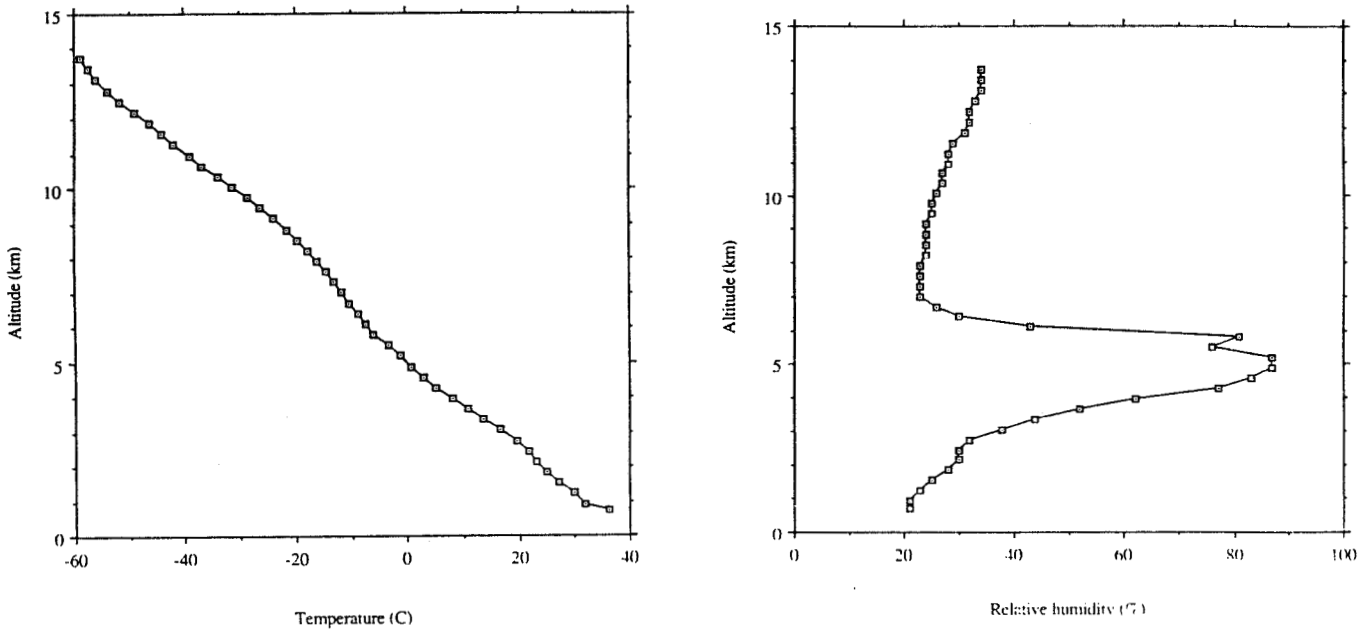

Figure 2: Atmospheric conditions measured during the sonic boom experiment.

THE BURGERS EQUATION

The "classical" Burgers equation is the standard model equation for plane finite-amplitude waves in a thermoviscous medium:

$$\frac{\partial p}{\partial x} - \frac{\beta}{2\rho_0 c_0^3}\frac{\partial p^2}{\partial t'} = \delta_{\mathrm{TV}}\frac{\partial^2 p}{\partial t'^2} \,. \tag{1}$$

Here p is acoustic pressure, t time, $t' = t - x/c_0$ retarded time, x distance, c_0 small-signal sound speed, ρ_0 ambient density, β coefficient of nonlinearity, and δ_{TV} the thermoviscous loss coefficient. Pierce [11] added terms to account for relaxation processes. Each relaxation process ν is characterized by a relaxation time τ_ν and a change in small-signal sound speed $(\Delta c)_\nu$ due to the relaxation. In operator notation Pierce's "augmented Burgers equation" may be written

$$\frac{\partial p}{\partial x} - \frac{\beta}{2\rho_0 c_0^3}\frac{\partial p^2}{\partial t'} = \delta_{\mathrm{TV}}\frac{\partial^2 p}{\partial t'^2} + \sum_\nu \frac{(\Delta c)_\nu \tau_\nu}{c_0^2}\frac{\frac{\partial^2}{\partial t'^2}}{1+\tau_\nu\frac{\partial}{\partial t'}}\, p \,. \tag{2}$$

Equation 2 is still for plane waves. If geometrical spreading is included, the equation becomes

$$\frac{\partial p}{\partial x} + \frac{a}{x}p - \frac{\beta}{2\rho_0 c_0^3}\frac{\partial p^2}{\partial t'} = \delta_{\mathrm{TV}}\frac{\partial^2 p}{\partial t'^2} + \sum_\nu \frac{(\Delta c)_\nu \tau_\nu}{c_0^2}\frac{\frac{\partial^2}{\partial t'^2}}{1+\tau_\nu\frac{\partial}{\partial t'}}\, p \,, \tag{3}$$

where the spreading factor a is 0 for plane waves, $\frac{1}{2}$ for cylindrical waves, and 1 for spherical waves. This is the equation we have solved numerically to obtain the results reported in this paper.

Burgers' equation may be further generalized to include effects of (1) stratification and (2) diffraction. Stratification may be included by scaling the dependent variable p and stretching the independent range variable x [12]. The Burgers equation for this case is not considered in this report but will be taken up in the future. To include diffraction effects, one must use the KZK equation, which is a multi-dimensional form of Burgers' equation; see, for example, Refs. [13, 14]. As a spinoff from the present work, relaxation effects have been included in a computer code that solves the KZK equation, but no formal report of the results has yet been given.

NUMERICAL PROPAGATION

Solutions of the generalized Burgers equation that are not in steady state involve solving a partial differential equation. Except for a few rare cases the solution can only be obtained numerically and it is common to use some sort of marching scheme. A time waveform is digitized with M samples and then small steps are taken in the propagation direction. At each step absorption and nonlinearity are solved in series. It is popular to do the absorption effects in the frequency domain as this requires M complex multiplications. However in the frequency domain the nonlinear term involves a convolution — which requires of the order of M^2 operations. To speed up the code the nonlinear distortion can be applied in the time domain as it requires only order M operations. To go between the time and frequency domain one can use the fast fourier transform which requires order $M \log M$ operations. Algorithms like the Pestorius [15] code flip-flop between the time and frequency domains at each step to take advantage of computing absorption in the frequency domain and nonlinear distortion in the time domain, the price being the use of the FFT.

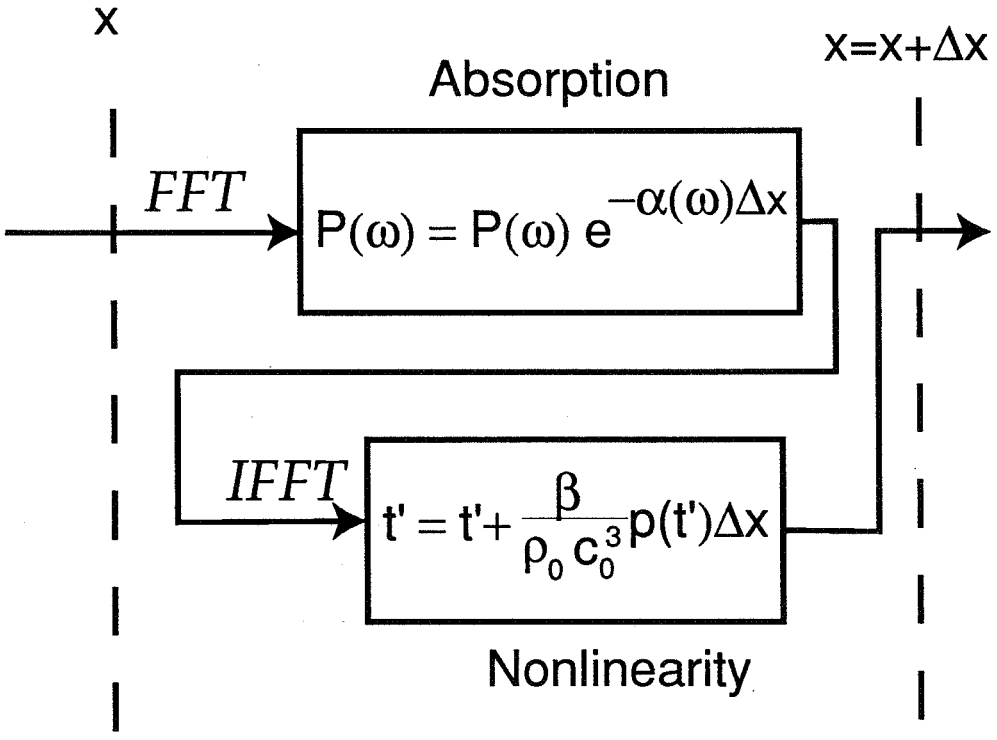

Figure 3: Pestorius type approach to solving the Burgers equation.

TIME DOMAIN ALGORITHM

It would be nice to stay in one domain but without having to pay the price of M^2 operations for a convolution. Lee and Hamilton [13, 14] have developed a method of computing the absorption in the time domain. They approximate the absorption with a finite difference equation. This yields a tridiagonal matrix system which can be solved in order M operations. The code they developed was used to solve the KZK equation, which is a generalization of the Burgers equation to include diffraction effects. We have extended the code to account for molecular relaxation and spreading effects. The work presented here does not, however, include diffraction effects.

Apart from its numerical advantage the fully time domain algorithm has the nice property that it can propagate pulses. Because the FFT isn't used, the endpoints of the waveform need not match to make a periodic waveform. Therefore step shocks and N waves are easily dealt with. The algorithm is particularly suited to finding a steady state solution. Raspet *et. al* [3] had to use a square pulse to find the steady state behavior of a shock. Square pulses have a limited propagation range before they turn into sawtooth waves. In the time domain code a pure shock can be propagated with out difficulty.

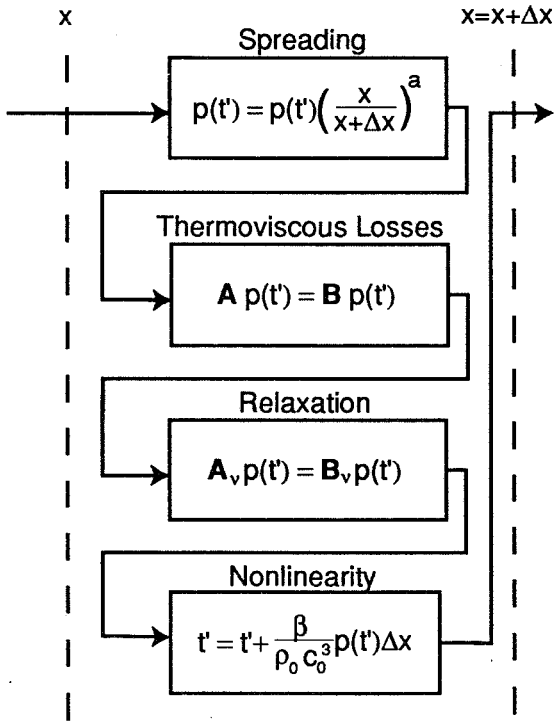

Figure 4: Time domain approach to solving the Burgers equation.

STEADY STATE: NONLINEARITY AND THERMOVISCOUS LOSSES

A number of cases were run to test the validity of the code. The first was to obtain the steady-state solution of the classical Burgers equation for a thermoviscous fluid. The known analytical solution for the steady shock is the hyperbolic tangent function. Figure 5 shows how a shock front is propagated with the time domain code; σ is the distance variable. The first figure shows the initial profile, chosen because it looked interesting. The other figures show how the profile develops. The final figure, $\sigma = 2$, shows that the numerical result agrees very well with the analytical solution.

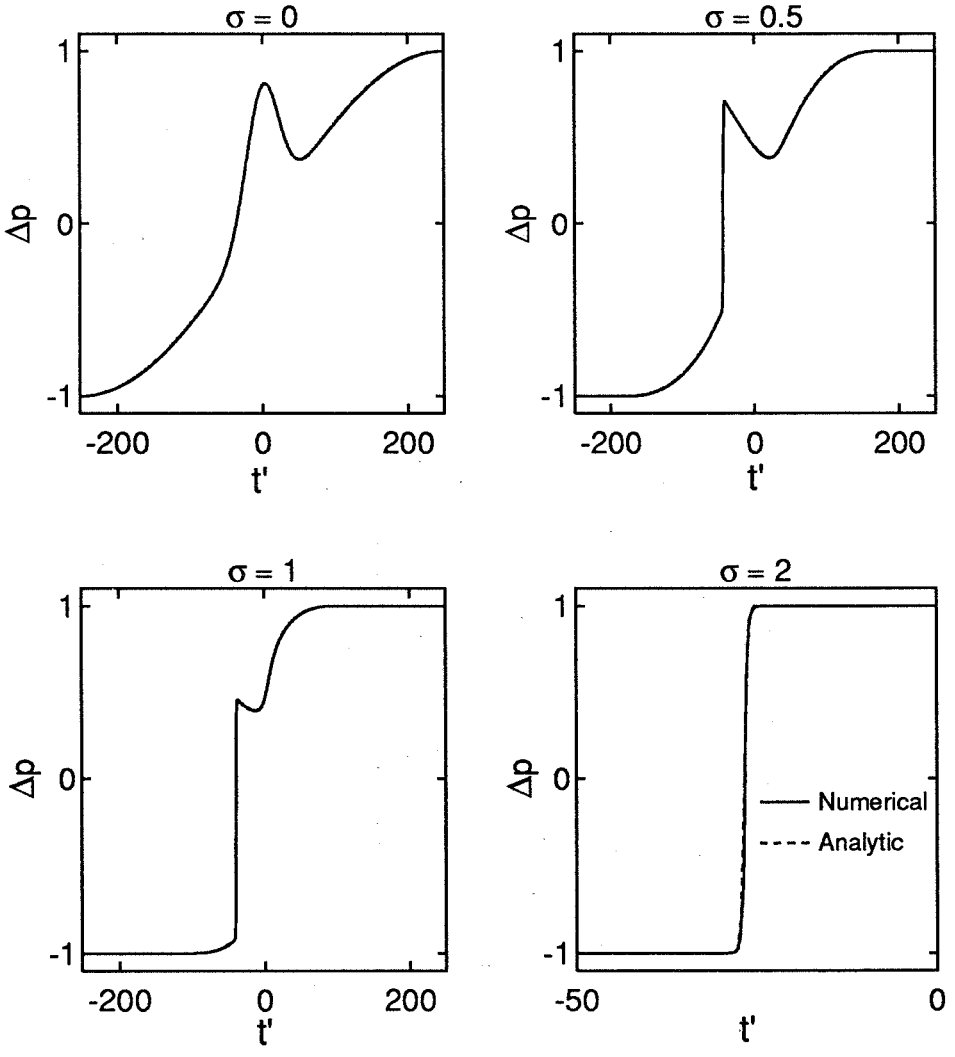

Figure 5: Propagation of a shock in a thermoviscous medium.

STEADY STATE: NONLINEARITY AND ONE RELAXATION PROCESS

We now determine whether the relaxation part of the code behaves correctly. Polykova *et. al.* [16] obtained the steady-state solution for a finite amplitude wave in a medium with one relaxation process but no thermoviscous losses. Their result (denoted PSK in Fig 6) is

$$\frac{t - t_0}{\tau_\nu} = \ln \frac{(1 + p/p_0)^{D-1}}{(1 + p/p_0)^{D+1}} ,$$

where

$$D = \frac{(\Delta c)_\nu \rho_0 c_0}{p_0 \beta} .$$

Figure 6 shows the result from the propagation program in a monorelaxing fluid. For the values chosen relaxation was not enough to stop the waveform from becoming multivalued. In the analytical result weak shock theory was used to ensure a single valued function. Multivaluedness was prevented in the numerical algorithm by including a small amount of thermoviscous losses.

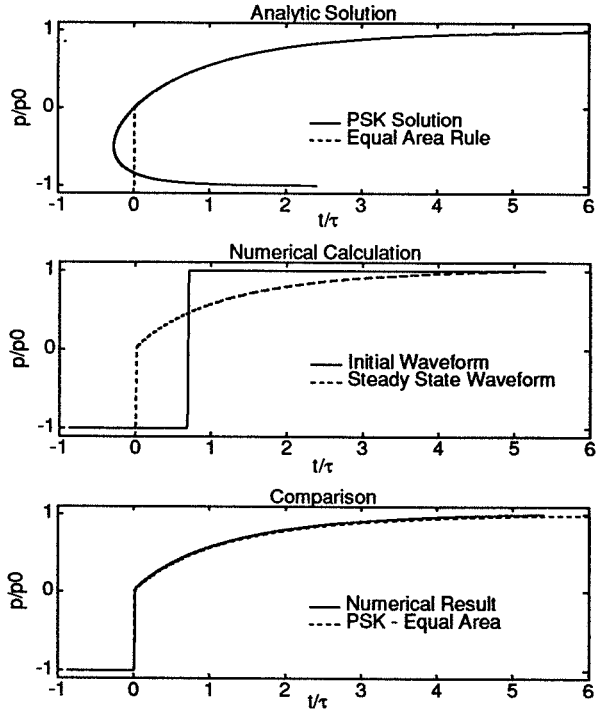

Figure 6: The top figure shows the analytical result for the steady-state solution in relaxing medium with no thermoviscous effects; $D = 0.5$. The middle figure shows the initial and steady-state profiles obtained by the time domain code. The bottom figure compares the analytical and numerical steady-state profiles.

STEADY STATE IN AIR

The last verification test was against Kang's result. A plane shock front is sent into a standard atmosphere with a relative humidity of 10%. This allows us to compare results with a steady-state result in Kang's thesis. In our calculation the shock started out with a hyperbolic tangent profile and was then propagated until the profile no longer changed. Figure 7 compares the two results.

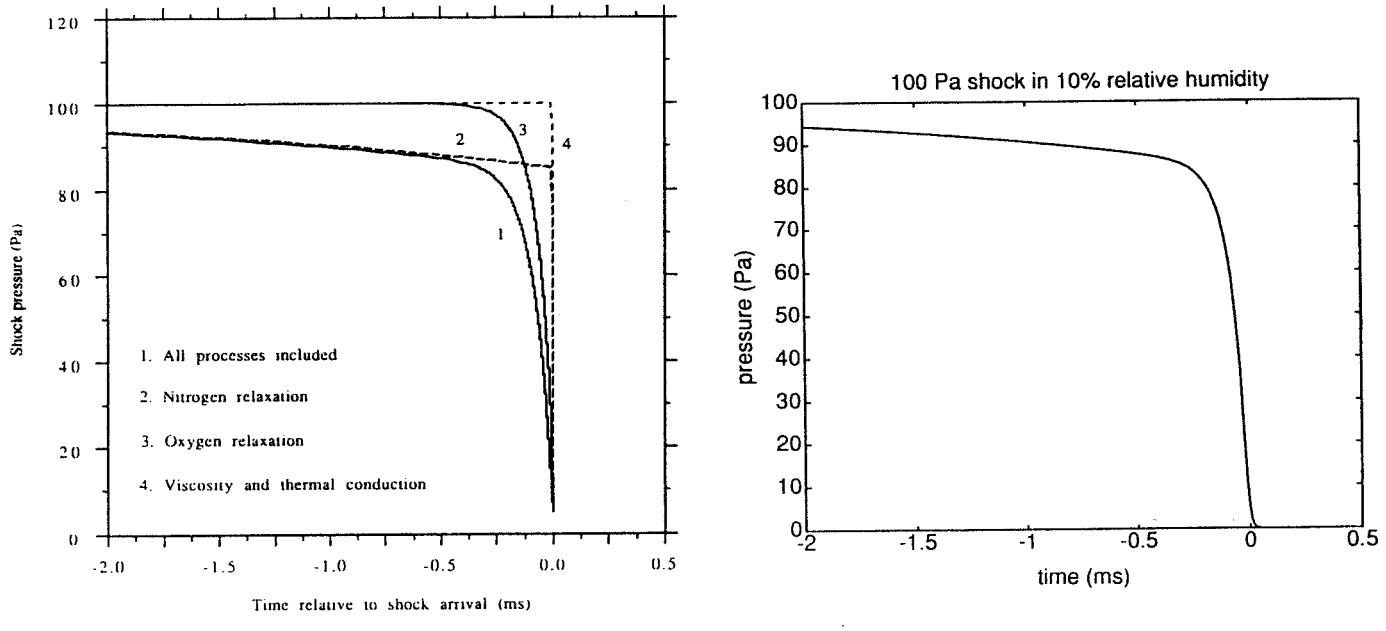

Figure 7: Steady-state solution in air; $T = 20\,^{\circ}\mathrm{C}$, $P_0 = 1$ atm, and a relative humidity of 10%. On the left is Kang's profile [1, Fig. 5.8]. On the right is the profile from the time domain code.

EFFECTS ON RISE TIME

We will now use the time domain code to investigate the behavior of the rise time of shocks in the air. In all calculations the temperature is 20 °C, and the pressure is 1 atm.

First we examine how long it takes waveform to recover from a small but abrupt change in relative humidity. A plane wave shock is propagated in air of given relative humidity until it reaches steady state. This steady-state waveform is then used as the input waveform for an atmosphere with another relative humidity.

Second we investigate the effect of spreading on the rise time of a shock front. Shocks that are in steady state are propagated as spreading waves; because the amplitude of the shock decreases the rise time is expected to increase. We present results for the combined effects of spreading and a change in relative humidity. Finally we investigate the difference between the rise time of an N wave and a step shock.

TRANSITION DISTANCE FOR 70 Pa SHOCKS

We use the term transition distance to describe how far a shock needs to travel to go from one steady-state profile to another. A somewhat similar term "healing distance" is commonly used in literature related to turbulence for the distance a perturbed shock needs to return to its original state [3]. In this case we shall look at transition distances due to a change in relative humidity.

Figure 8 shows rise time as a function of propagation distance for a plane step shock of amplitude 70 Pa which starts in a medium of 20% relative humidity. The relative humidity of the second atmosphere is 10%, 20% or 30%. The results show the transition distance to be at least 5 km. The plot in Fig. 9 shows the rise time for a shock initially in an atmosphere of 50% relative humidity. Transition distances are greater than 2 km.

The initial fluctuations in the rise time are due to rather gross changes in the profile. The changes are such that the 10% to 90% definition is not a very suitable measure of rise time. Similar fluctuations were observed by Raspet *et. al.* [3].

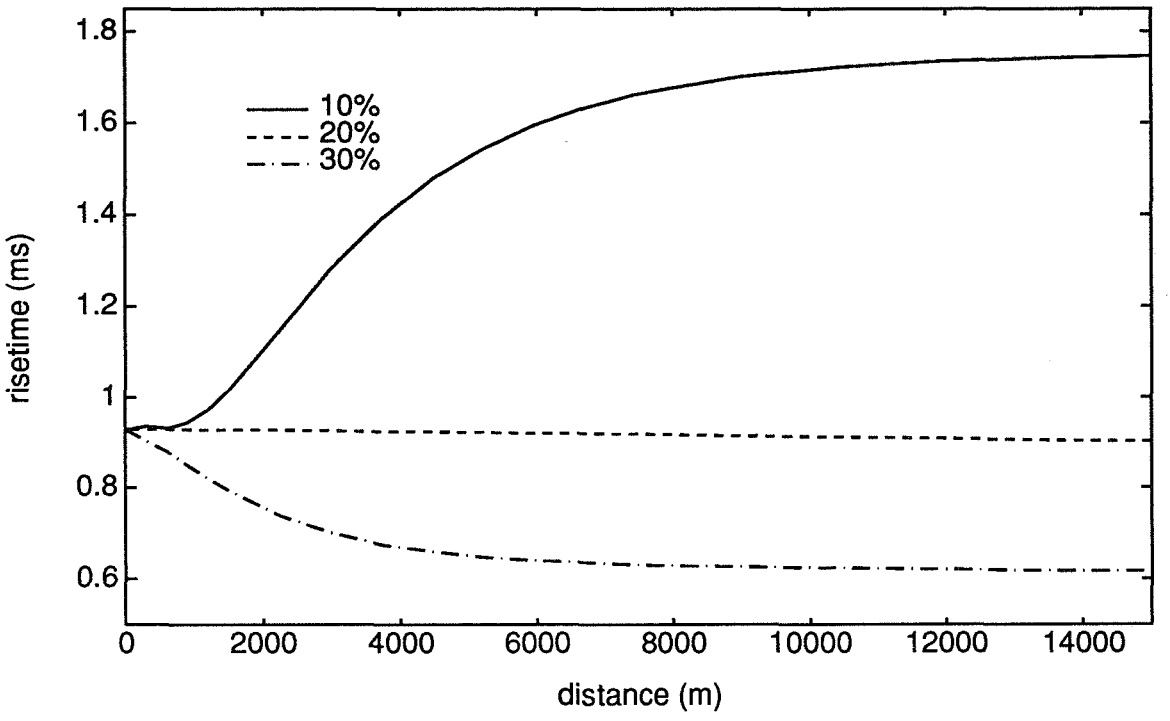

Figure 8: Change in rise time for a waveform leaving a medium of 20% relative humidity.

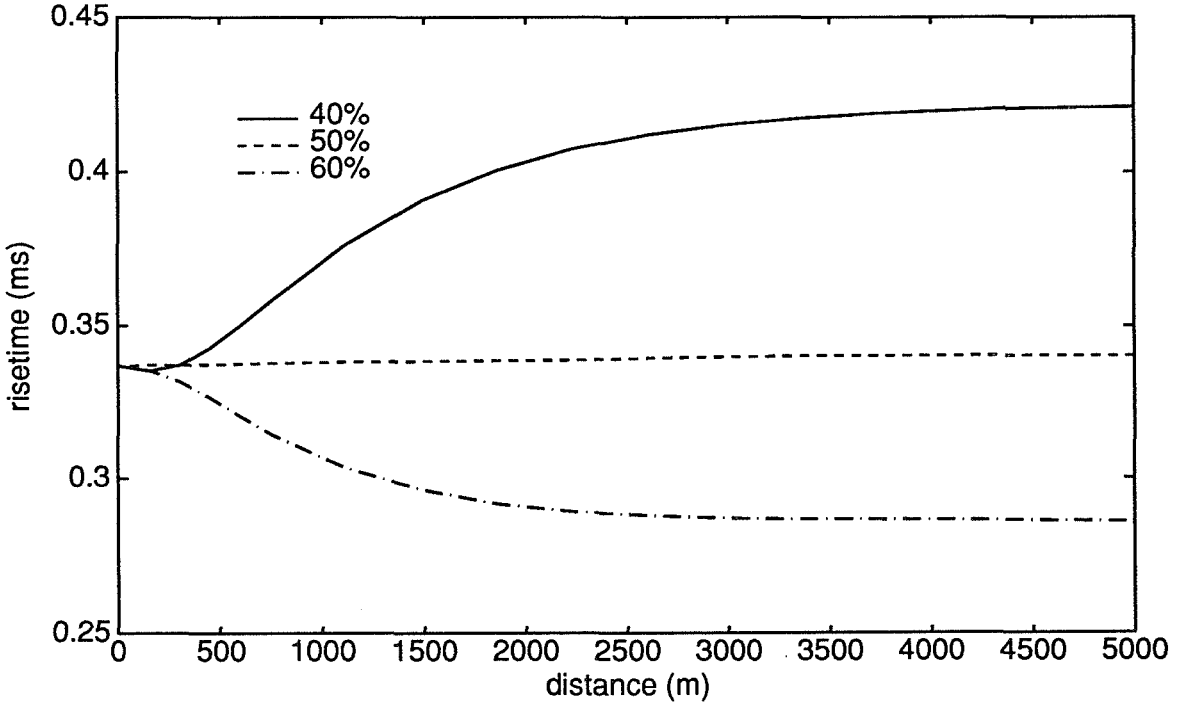

Figure 9: Change in rise time for a waveform leaving a medium of 50% relative humidity.

TRANSITION DISTANCE FOR 140 Pa SHOCKS

Figure 10 shows the behavior of a shock wave of amplitude 140 Pa which starts off in air of 20% relative humidity. The transition distance needed when the new relative humidity is 30% is about 2 km. However the transition distance is at least 6 km when the new relative humidity is 10%.

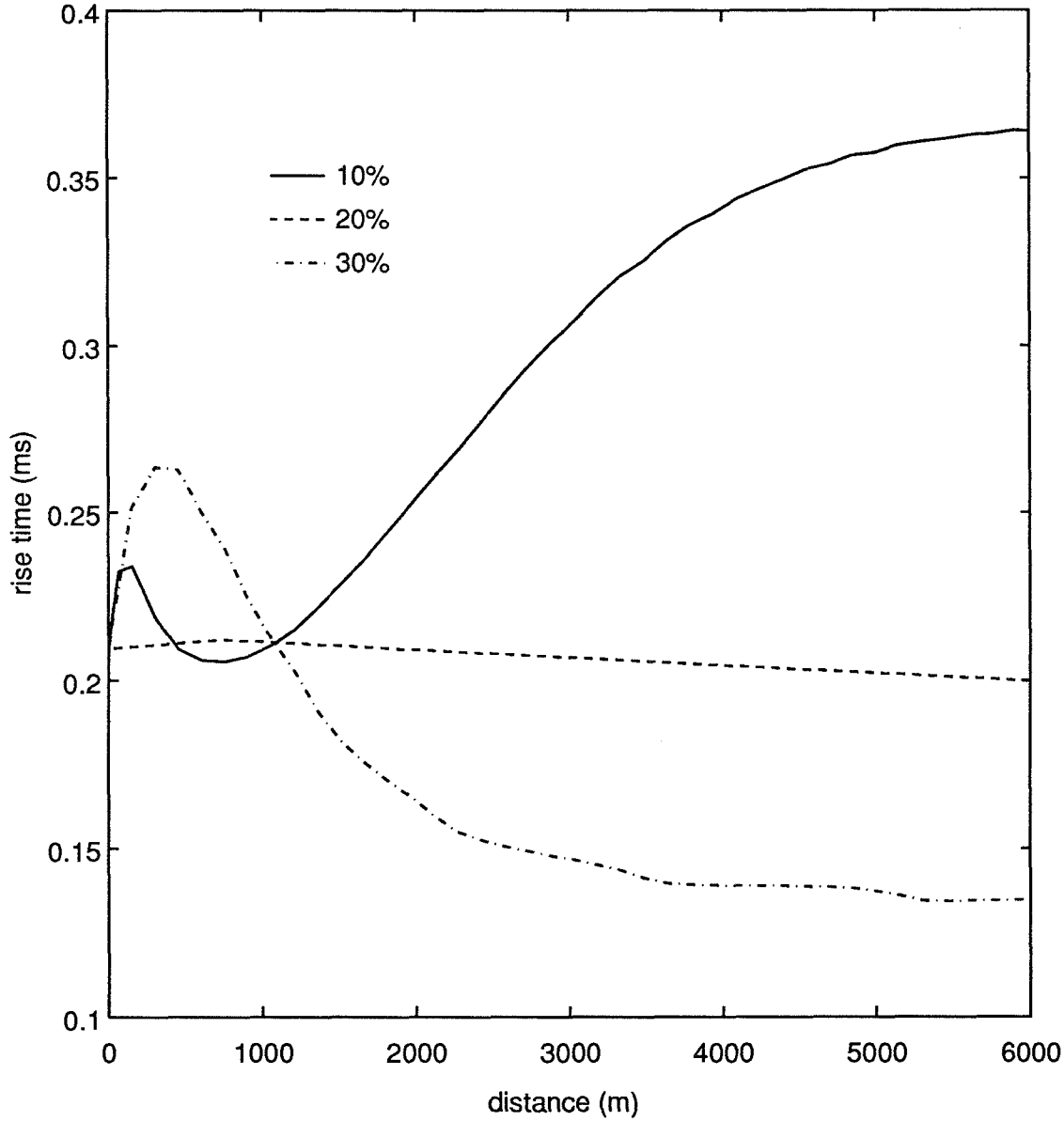

Figure 10: Change in rise time for a 140 Pa shock leaving a medium of 20% relative humidity.

SPREADING

The amplitude of a spherically spreading shock should decrease as

$$\Delta p = \frac{x_0}{x}\Delta p_0 \ , \tag{4}$$

and for cylindrical spreading,

$$\Delta p = \sqrt{\frac{x_0}{x}}\Delta p_0 \ .$$

The steady state rise time found from the analytical solution of the classical Burgers equation is

$$\Delta\tau = \ln(9)\frac{4\delta_{\mathrm{TV}}\rho_0 c_0^3}{\beta\Delta p} \tag{5}$$

As the amplitude of the waveform decreases the rise time increases because the nonlinear steepening effects are weaker. However it is not clear that a spreading waveform will be in steady state. This would require the absorption mechanism to respond immediately to the spreading. Naugol'nykh [18] argued that a spreading shock in a thermoviscous medium should have a rise time that is shorter than the steady-state value because the absorption mechanism can't work fast enough.

If a spreading shock remains in steady state then, from Eq. (5) the rise time should vary inversely as the pressure jump. Since for spherically spreading waves the pressure varies inversely with distance, Eq. (4), we have

$$\Delta\tau \propto x \ .$$

To investigate the validity of this relation we started with the hyperbolic tangent profile appropriate for a plane step shock. The shock was then propagated as a spreading wave. Figure 11 shows the initial waveform and how the shock diffuses as it loses amplitude. Figure 12 compares the steady state prediction of the rise time to the numerically calculated rise time. Note that the steady state prediction always overestimates the rise time. Absorption cannot act quickly enough to diffuse the profile before more amplitude decrease, due to spreading, occurs.

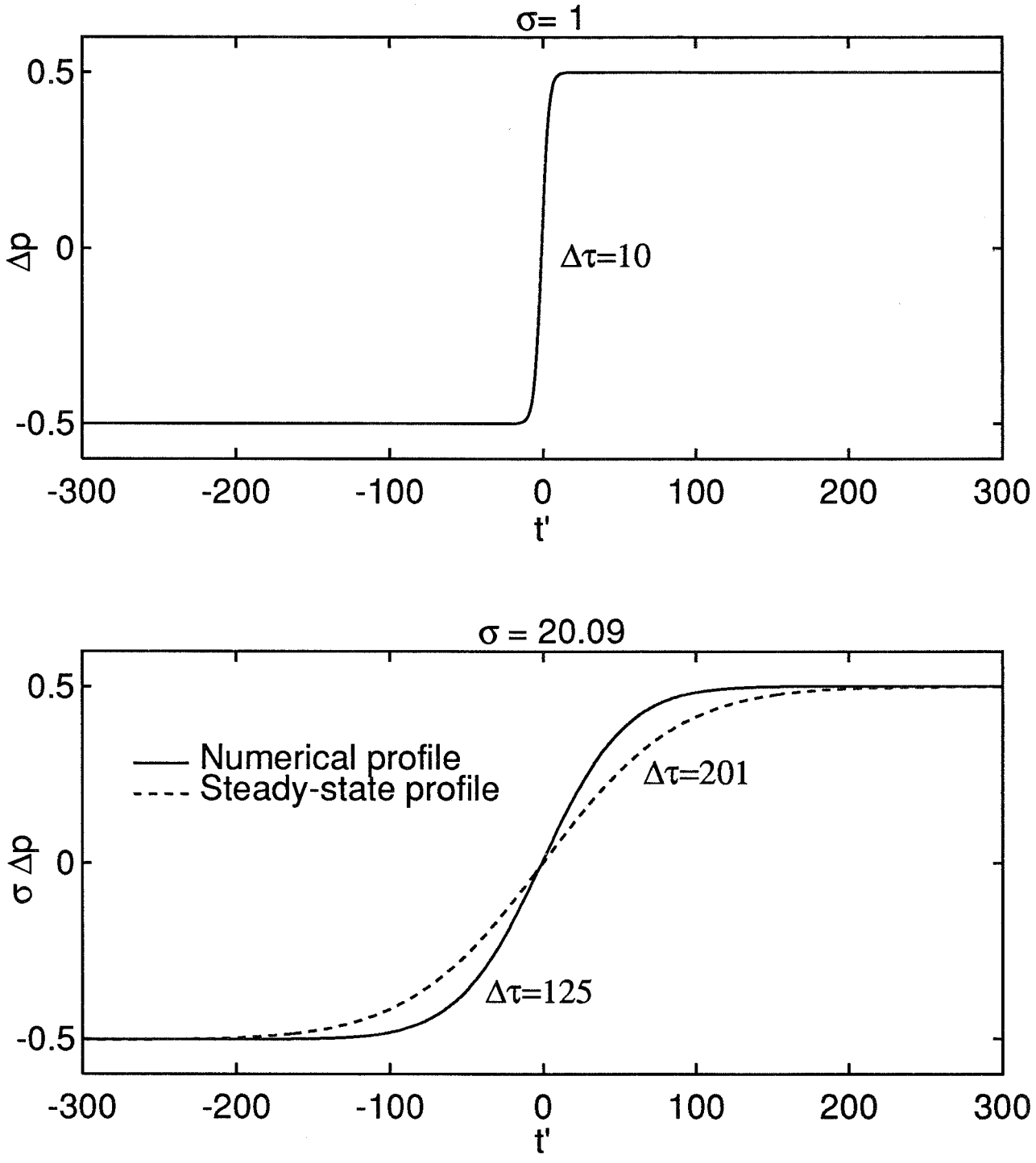

Figure 11: A shock front that starts off in steady-state in a thermoviscous medium is propagated as a spherical wave. The upper plot shows the initial waveform. The lower plot shows the waveform at 20 times the source radius; the steady-state waveform is also shown.

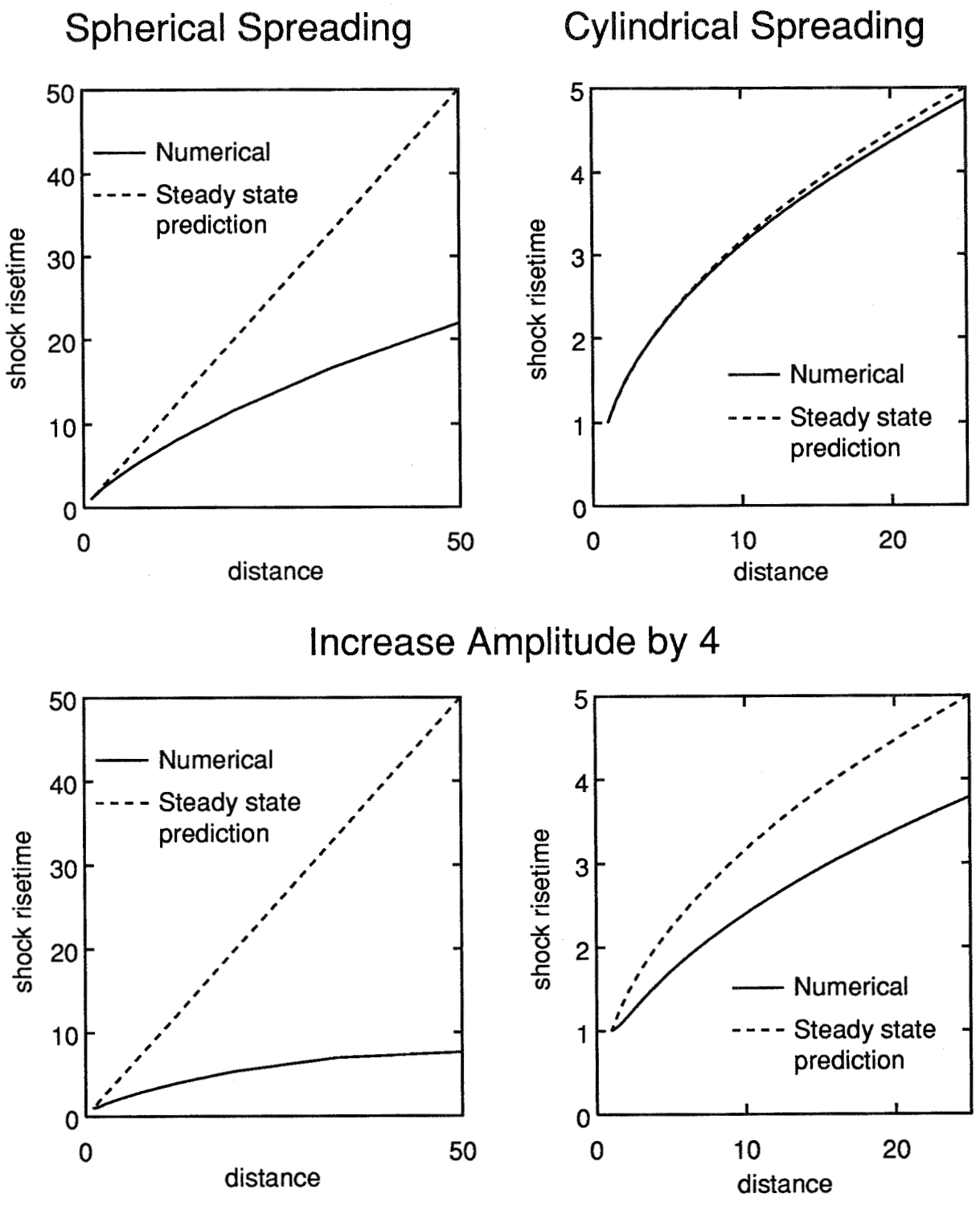

Figure 12: The rise time of a step shock in a thermoviscous medium. The waveform starts off in steady-state and is propagated as either a spherically or cylindrically spreading wave. Two different initial amplitudes are used. Rise time is normalized to the initial rise time and distance is normalized to the source radius.

EFFECT OF SPREADING ON TRANSITION DISTANCE

We now investigate the combined effects of spreading and a change in relative humidity. A source is assumed to be 15 km away and the shock front is propagated at an angle corresponding to a sonic cone from an aircraft flying at Mach 2. Cylindrical spreading is used. Figure 13 shows the rise time curves and compares them to the plane wave curves taken from Fig. 8. In Fig. 14 we compare the rise time curves to those of spreading waves in a homogeneous atmosphere, which are the effective asymptotes. We see that the waveform is never in steady state but that the asymptotes are reached in 6–8 km.

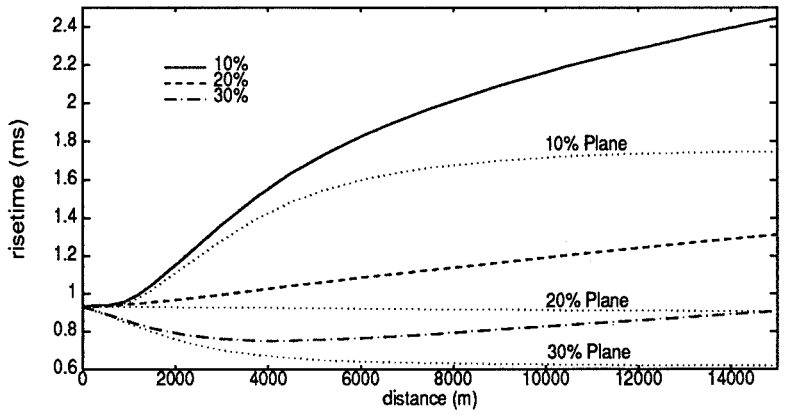

Figure 13: The rise time of a shock that is cylindrically spreading; the shock starts from a steady-state profile for an atmosphere with 20% relative humidity. The dotted lines show the results for plane waves as shown in Fig. 8. Note that the steady-state rise time is not achieved.

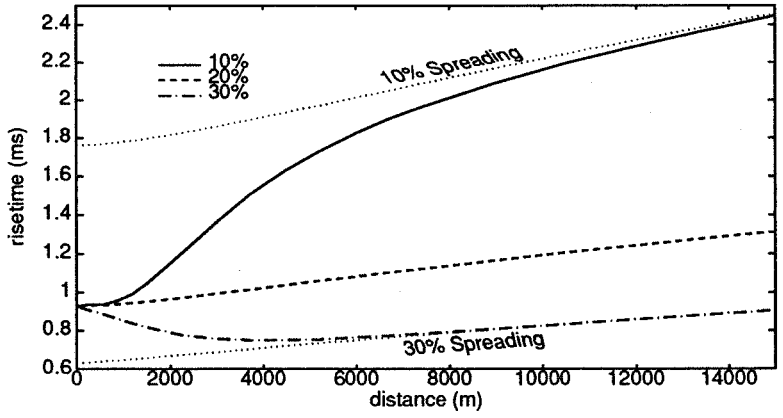

Figure 14: The same curves as in Fig. 13, except that the dotted lines show the results for cylindrically spreading waves in a homogeneous atmosphere; these are the asymptotic results.

EFFECT OF PROFILE ON THE RISE TIME

Finally we compare rise time for an N wave with that for a steady-state step shock. Figure 15 shows the curves for a plane N wave that has propagated a long distance in a medium with a relative humidity of 50%. The amplitude of the N wave is 48 Pa. We see that a steady-state shock of the same amplitude has a longer rise time. However a steady-state shock of amplitude 50.4 Pa has the same rise time. It appears that the profile corresponds to that of a higher amplitude shock because the amplitude of the N wave decreases with propagation distance. Just as was seen with spreading waves, the absorption cannot keep up with the loss in shock amplitude.

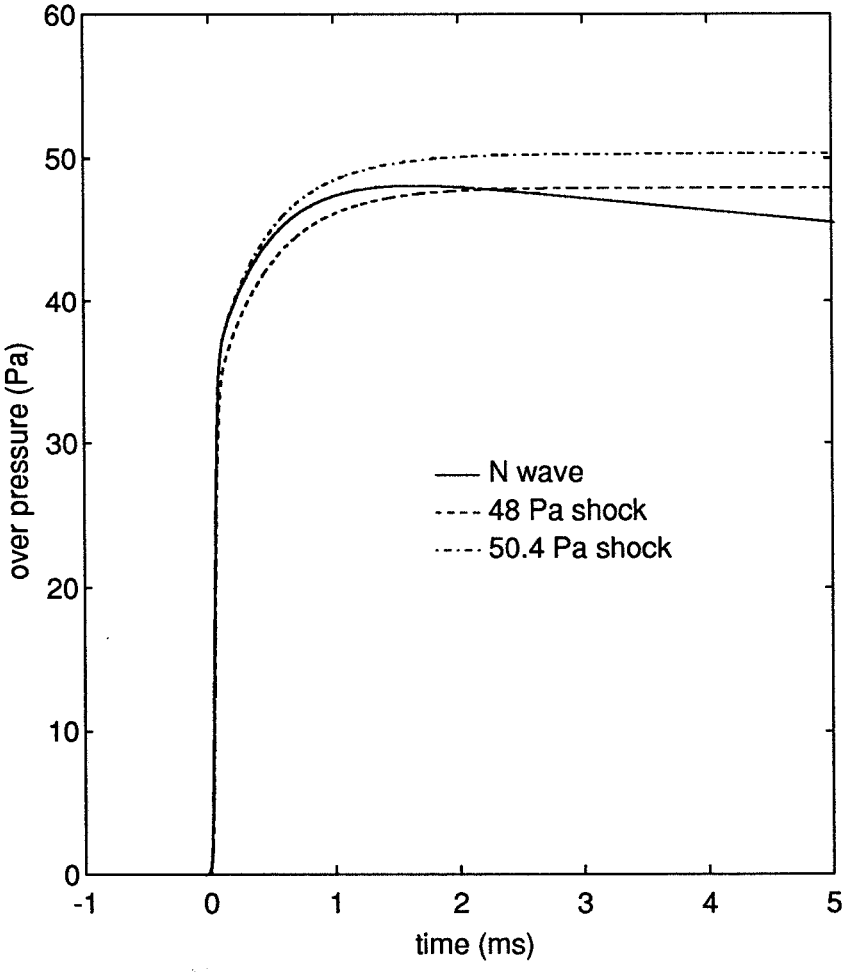

Figure 15: The solid line is an N wave with duration of 125 ms. It has propagated for 30 km. The dashed line is a step-shock of the same amplitude. The dot-dash line is a shock of the same rise time as the N wave. This shock has an amplitude of 50.4 Pa.

CONCLUSION

Our study indicates that assuming a steady-state profile for the head shock of a sonic boom tends to cause an overestimate of the rise time. First, we have found that substantial propagation distance is required for a shock to respond to abrupt but small changes in relative humidity. When the absorption increases, the actual rise time is always less than the steady-shock value. Second, neglect of geometrical spreading results in an overestimate of rise time. Third, modeling the N wave as a step shock also raises the rise time, although the effect is small. All of these results are consistent with the conclusion that for a decaying shock dissipation is always "struggling to catch up with nonlinearity."

References

[1] J. Kang, "Nonlinear acoustic propagation of shock waves through the atmosphere with molecular relaxation," Ph. D. Thesis, Department of Mechanical Engineering, Pennsylvania State University (1991).

[2] L. D. Robinson "Sonic boom propagation through an inhomogeneous windy atmosphere" Ph. D. dissertation, Department of Physics, University of Texas at Austin, (1991).

[3] R. Raspet, H. Bass, L. Yao and W. Wu, "Steady state risetimes of shock waves in the atmosphere," in NASA CP 3172: High-Speed Research Workshop on Sonic Boom, NASA Langley Research Center, Hampton, Virginia, C. M. Darden, ed., Vol. I, pp. 109-116 (1992).

[4] A. D. Pierce and J. Kang, "Molecular relaxation effects on sonic boom waveforms," in *Frontiers of nonlinear acoustics: Proceedings of the 12th ISNA*, M. F. Hamilton and D. T. Blackstock, eds. (Elsevier Applied Science, London, 1990), pp. 165-170.

[5] D. T. Blackstock, "Thermoviscous attenuation of plane, periodic, finite-amplitude sound waves," *J. Acoust. Soc. Am.* **36**, 534-542 (1964).

[6] R. A. Lee and J. M. Downing, "Sonic boom produced by United States Air Force and United States Navy aircraft: measured data," AL-TR-1991-0099, Biodynamic Environment Branch, Biodynamics and Bioengineering Division, Armstrong Laboratory, Wright-Patterson Air Force Base, Ohio (1991).

[7] A. D. Pierce and V. W. Sparrow "Relaxation and turbulence effects on sonic boom signatures," First Annual High-Speed Research Workshop, Williamsburg, Virginia (1991).

[8] Allan D. Pierce "Relaxation and turbulence effects on sonic boom signatures," in NASA CP 101321: Second Annual High-Speed Research Workshop on Sonic Boom, Moffett Field, California, pp. 1-18 (1993).

[9] B. Lipkens, "Experimental and theoretical study of the propagation of N waves through a turbulent medium," Ph. D. dissertation, Department of Mechanical Engineering, University of Texas at Austin (1993).

[10] B. Lipkens and D. T. Blackstock, "Model experiment to study the effect of turbulence on rise time and waveform of N waves," in NASA CP 3172: High-Speed Research Workshop on Sonic Boom, NASA Langley Research Center, Hampton, Virginia, C. M. Darden, ed., Vol. I, pp. 97-108 (1992).

[11] A. D. Pierce, *Acoustics: An introduction to its physical principles and applications* (McGraw-Hill, New York, 1981).

[12] R. O. Cleveland and D. T. Blackstock, "Waveform freezing of sonic booms in the atmosphere," *J. Acoust. Soc. Am.* **92** (4), 2331 (A) (1992).

[13] Y-S. Lee and M. F. Hamilton, "Nonlinear effects in pulsed sound beams," in *Ultrasonics International 91 Conference Proceedings*, D. E. Gray, ed. (Butterworth-Heinemann, Oxford, 1991), pp 177-180.

[14] Y-S. Lee and M. F. Hamilton, "Time-domain modeling of pulsed finite-amplitude sound beams," submitted to *J. Acoust. Soc. Am.* in March 1994.

[15] F. M. Pestorius, "Propagation of plane acoustics noise of finite amplitude," Technical Report ARL-TR-73-23, Applied Research Laboratories, The University of Texas at Austin (August 1973), AD 778 868.

[16] A. L. Polyakova, S. I. Soluyan, and R. V. Khokhlov, "Propagation of finite amplitude disturbances in a relaxing medium," *Sov. Phys. Acoust.* **8**, 78–82 (1962).

[17] M. F. Hamilton and E. A. Zabolotskaya, draft of "Dispersion," Chap. 5 in *Nonlinear Acoustics* to be published by Academic Press, New York.

[18] K. A. Naugol'nykh, "Transition of a shock wave into a sound wave," *Sov. Phys. Acoust.* **18**(4), 475–477 (1973).

AN EVALUATION OF RISE TIME CHARACTERIZATION AND PREDICTION METHODS

Leick D. Robinson
Science Applications International Corporation
Austin, TX

INTRODUCTION

One common method of extrapolating sonic boom waveforms from aircraft to ground is to calculate the nonlinear distortion, and then add a rise time to each shock by a simple empirical rule. One common rule is the "3 over P" rule which calculates the rise time in milliseconds as three divided by the shock amplitude in psf[1].

This rule was compared with the results of ZEPHYRUS, a comprehensive algorithm which calculates sonic boom propagation and extrapolation with the combined effects of nonlinearity, attenuation, dispersion, geometric spreading, and refraction in a stratified atmosphere[2]. It is shown here that the simple empirical rule considerably overestimates the rise time estimate. In addition, the empirical rule does not account for variations in the rise time due to humidity variation or propagation history.

It is also demonstrated that the rise time is only an approximate indicator of perceived loudness. Three waveforms with identical characteristics (shock placement, amplitude, and rise time), but with different shock shapes are shown to give different calculated loudness.

This paper is based in part on work performed at the Applied Research Laboratories, the University of Texas at Austin, and supported by NASA Langley.

RISE TIME VS. PRESSURE AMPLITUDE

A number of waveform propagation calculations were performed, using the ZEPHYRUS algorithm, for the case of an aircraft moving at Mach 1.5 at an altitude of 55,000 feet (16,764 m). For simplicity, the initial sonic boom waveform was modeled as an N-wave 200 msec in duration. The calculations were performed for a number of initial wave amplitudes and ground-level humidities. In each case, the initial waveform was extrapolated to the ground, and the ground-level amplitude and rise time of the initial shock was calculated (here, the rise time is calculated as 10% to 90% of peak amplitude). These results are plotted in Fig. 1. This is compared with the "3 over P" prediction.

Three features are immediately evident. First, the "3 over P" method has no humidity dependence, which is clearly evident in the ZEPHYRUS results. Second, the "3 over P" method considerably overestimates the ZEPHYRUS calculation for every case, with the best agreement for very dry air. Finally, the "3 over P" method comes closer to agreement with the ZEPHYRUS results for high amplitude waves, with increasing overestimation as the amplitude decreases.

RISE TIME AND PROPAGATION HISTORY

The consistent overestimation is probably due, in part, to the fact that the "3 over P" curve is based upon the rise time corresponding to a steady-state step shock, or a well-developed shock in which the mechanisms affecting rise time have reached a state of equilibrium for the environment at ground level. However, it has been demonstrated by Raspet, Bass, Yao, and Wu[3], as well as by this author[4], that the typical healing distance of the shocks at ground level is on the order of hundreds of meters to kilometers, a longer distance than that for which the ground-level conditions have been in effect along the propagation history, and thus the shocks at ground level are not in steady-state. If the propagation history is accounted for, as in the ZEPHYRUS result, shorter rise times are predicted.

The angle of incidence of the sonic boom with the ground depends upon the aircraft Mach number. Longer rise times, closer to steady-state, would be expected for Mach numbers close to one, in which the incident wave is closer to a grazing angle with the ground, and thus the wave is at near ground conditions for a longer period in its propagation history. Of course, significant refraction effects would be expected in this regime.

RISE TIME AND SHOCK SHAPE

It has also been demonstrated previously by this author that, for the same ground-level pressure amplitude, the rise time varies considerably as a function of the slope of the waveform behind the lead shock[4]. Thus, the shape of the waveform near the shock is also important in determining rise time.

The shape of the shock itself is also of intrinsic importance. Although the shock rise time is useful as a rough indicator of the expected loudness, too much reliance on the rise time can be misleading. The shape of the shock has a strong effect on the high-frequency content of the sonic boom and thus on the loudness. In Fig. 2, three waveforms are shown with identical shock characteristics (shock placement, rise time, and amplitude), but with different shock shapes: (1) linear step shock, (2) shock interpolated with a hyperbolic tangent, and (3) the ZEPHYRUS prediction. The loudness of each waveform was computed using the SIG7CZ code (written by Brenda Sullivan at NASA Langley), and the results are displayed in Table 1.

Table 1. Loudness Results

	dB (PL)	dBC	dBA
Step shock	93.32	98.27	78.91
Tanh	92.29	98.29	78.70
ZEPHYRUS	95.59	98.29	82.27

For the PL and A weightings, the ZEPHYRUS prediction is several dB louder than the other predictions. The reason can be seen in Figs. 3 and 4, which display the leading and tailing shocks. In the ZEPHYRUS prediction, the dispersion due to the molecular relaxation effects is shown to

produce a highly asymmetric shock with a very steep initial phase. In turn, the high frequency content corresponding to this steep initial phase produces the increase in loudness.

CONCLUSIONS

It has been shown here that simple methods of sonic boom extrapolation may be too crude to give accurate predictions, as they ignore the effects of humidity, propagation history, and waveform shape. In addition, the commonly used "3 over P" rule considerably overestimates the rise time.

The rise time is a useful indicator of loudness, but may be relied upon too much. It has been shown here that the shock shape can affect the loudness of the overall waveform. Simple shock interpolations may produce a loudness estimate that is too low by several dB. In the case of the "3 over P" rule, this underestimation of loudness would be further exacerbated by the rise time overestimation.

REFERENCES

1. Durston, Donald: A Preliminary Evaluation of Sonic Boom Extrapolation and Loudness Calculation Methods. Proceedings of the NASA High Speed Research Program Sonic Boom Workshop, Vol. II, Ames Research Center, Moffett Field, CA, May 12-14 1993.

2. Robinson, Leick: Sonic Boom Propagation through an Inhomogeneous, Windy Atmosphere. Ph.D. dissertation, The University of Texas at Austin, Dec. 1991.

3. Raspet, Richard; Bass, Henry; Yao, Lixin; and Wu, Wenliang: Steady State Rise Times of Shock Waves in the Atmosphere. Proceedings of the NASA High Speed Research Program Sonic Boom Workshop, Langley Research Center, Hampton, VA, Feb. 25-27, 1992. NASA CP-3172, Vol. 1, pp. 109-115.

4. Robinson, Leick: A Numerical Model for the Propagation of Sonic Booms through an Inhomogeneous, Windy Atmosphere. Presented at the 123rd Meeting of the Acoustical Society of America, Salt Lake City, Utah, May 11-15 1992.

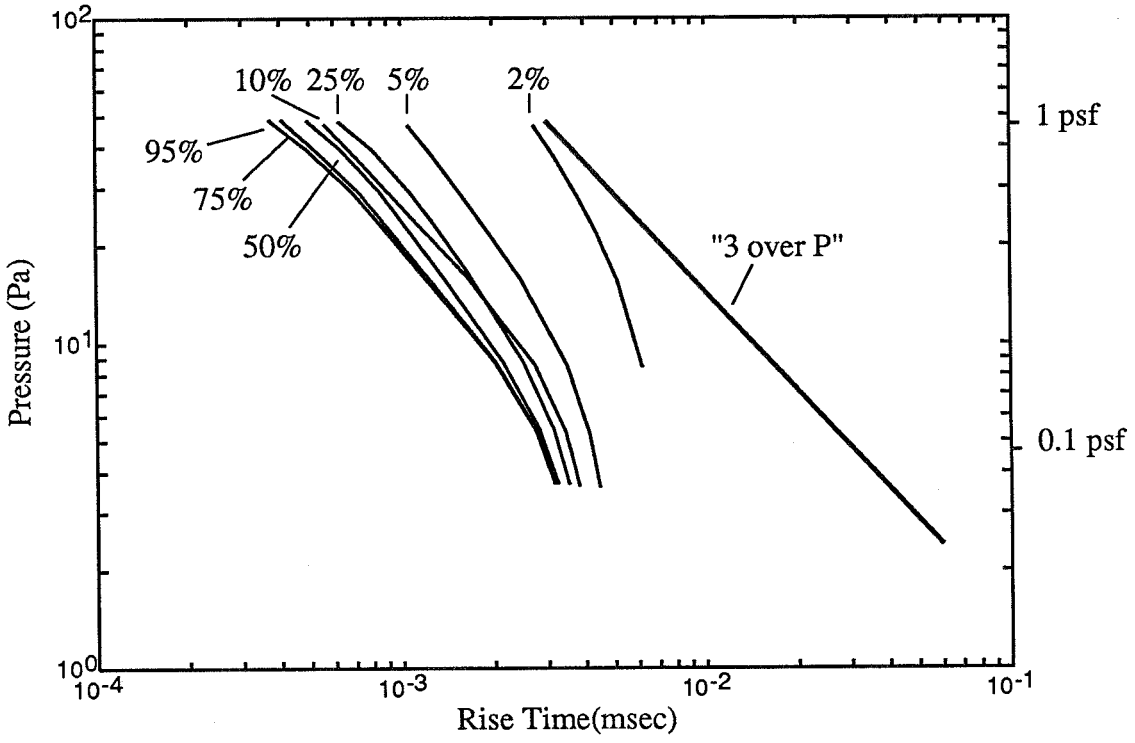

Figure 1. Rise time vs. shock amplitude for 2%, 5%, 10%, 25%, 75%, and 95% relative humidity at ground level and the "3 over P" curve

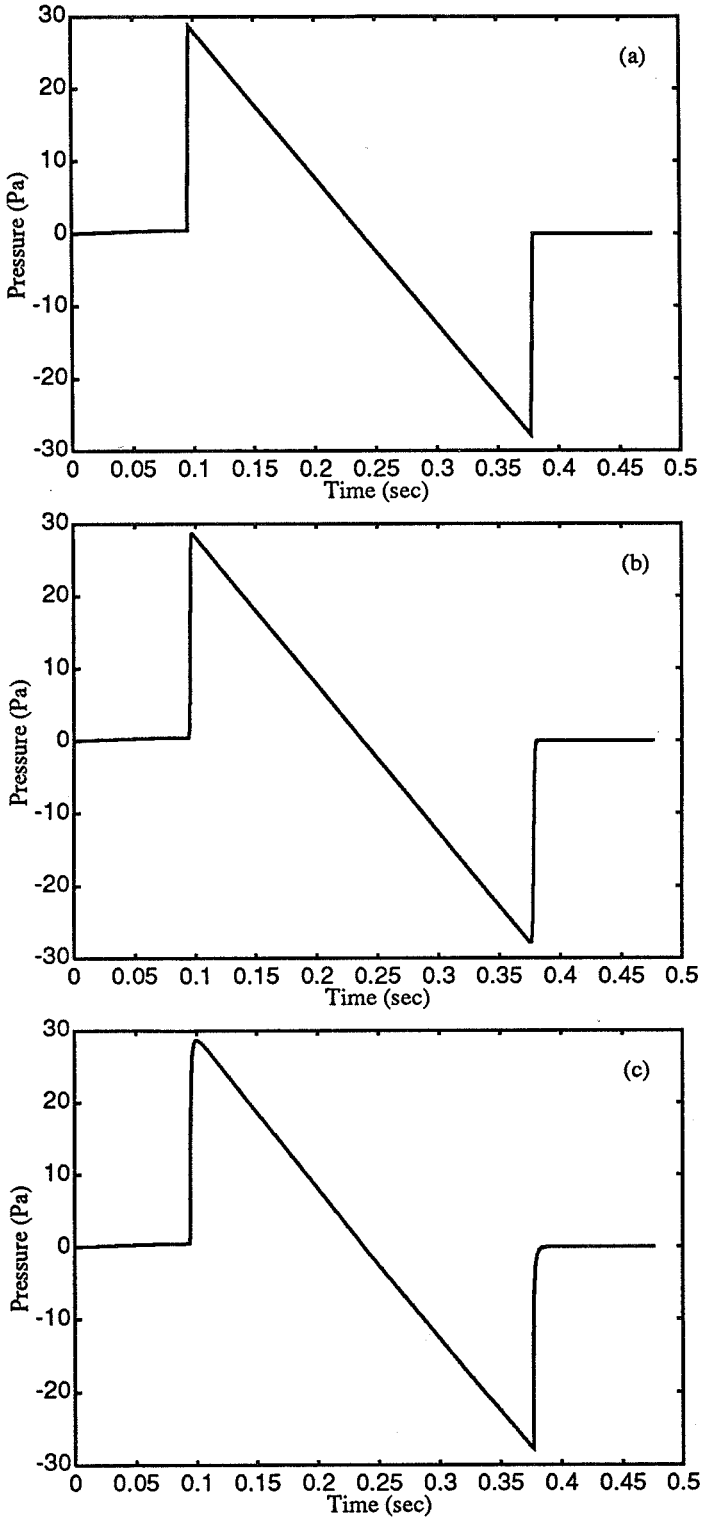

Figure 2. Calculated waveforms: (a) linear step shock, (b) hyperbolic tangent, and (c) the ZEPHYRUS prediction

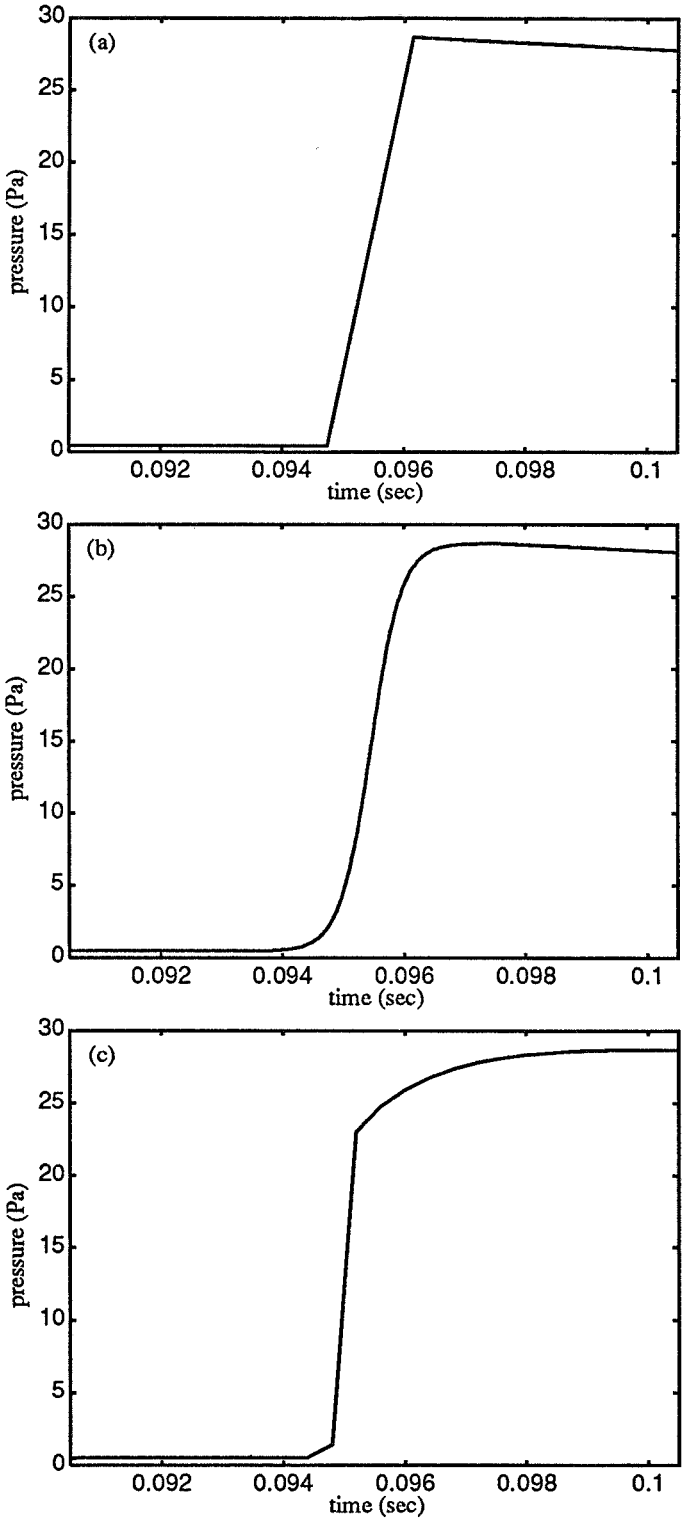

Figure 3. Leading shock: (a) linear step shock, (b) hyperbolic tangent, and (c) the ZEPHYRUS prediction

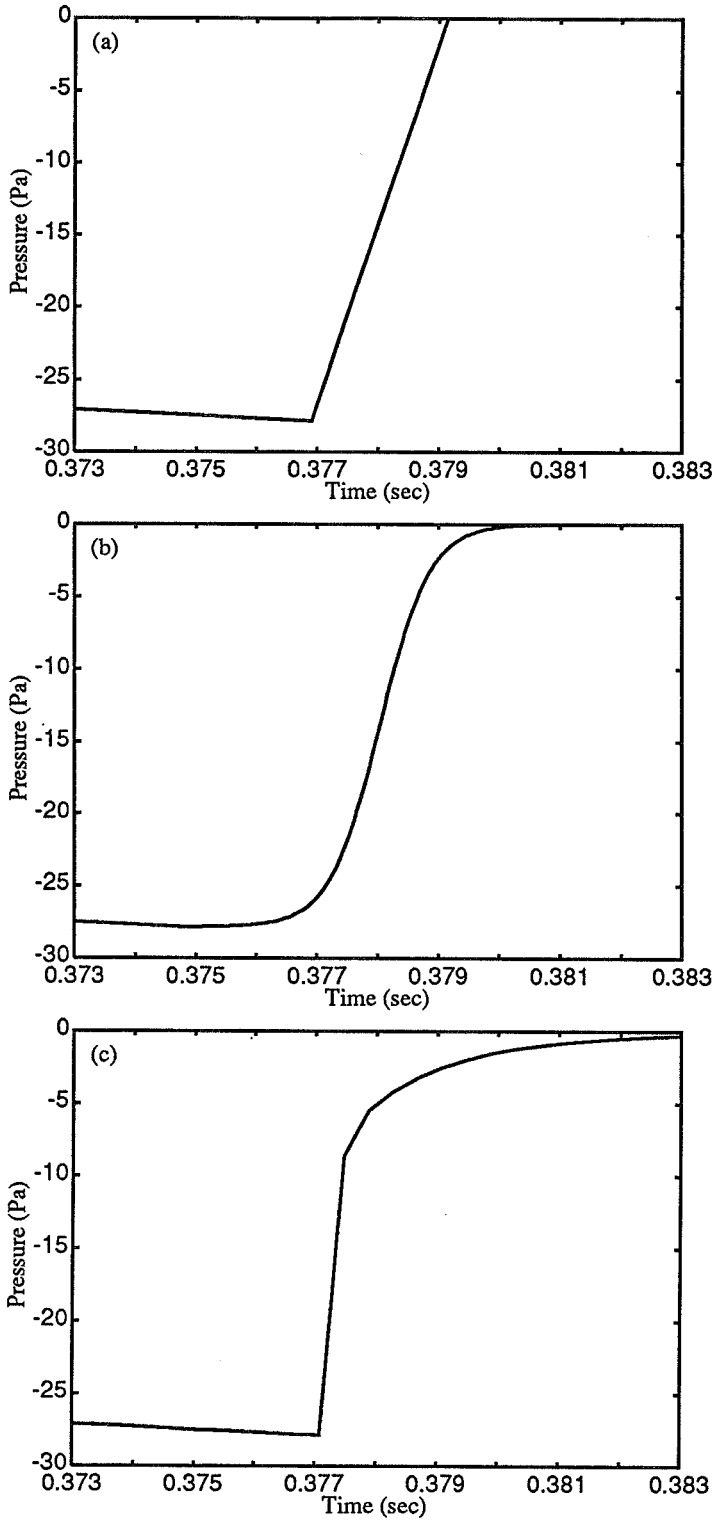

Figure 4. Trailing shock: (a) linear step shock, (b) hyperbolic tangent, and (c) the ZEPHYRUS prediction

FINESTRUCTURE OF TRANSIENT WAVES IN A RANDOM MEDIUM: THE CORRELATION AND SPECTRAL DENSITY FUNCTIONS

Alan R. Wenzel
Virginia Tech

INTRODUCTION

This is essentially a progress report on a theoretical investigation of the propagation of transient waves in a random medium. The emphasis in this study is on applications to sonic-boom propagation, particularly as regards the effect of atmospheric turbulence on the sonic-boom waveform. The analysis is general, however, and is applicable to other types of waves besides sonic-boom waves.

The phenomenon of primary concern in this investigation is the finestructure of the wave. The first figure shows what is meant by the finestructure.

NOTE: Research supported by NASA Langley Research Center

1. PRELIMINARIES

The uppermost sketch shows a typical transient waveform as it might look if observed under ideal conditions; i.e., in the absence of scattering, refraction, or any other mechanisms which might act to distort the waveform. This is what I call the incident wave.

When a wave propagates in a real medium, such as the atmosphere, a random high-frequency structure, called the finestructure, generally apears on the waveform, giving it the appearance shown in the bottom sketch. The finestructure is defined formally, at least insofar as the present investigation is concerned, as the difference between the observed wave and its ensemble average, and generally has an appearance much like that shown in the middle sketch.

The finestructure is believed to arise as a result of scattering and redistribution of wave energy by the random inhomogeneities of the medium. The finestructure is particularly important in connection with sonic-boom propagation, since the strong high-frequency component that often appears near the front of the N-wave may contribute appreciably to the perceived noisiness of the sonic boom.

The finestructure is most conveniently characterized by its statistical properties, such as the variance, the standard deviation, the correlation function, and the spectral density function. The spectral density function is the quantity that is most relevant to the question of annoyance, particularly as regards sonic-boom waves, since it contains information on the frequency content of the finestructure. The spectral density function is the quantity of primary interest in this study.

Incident Wave

Finestructure

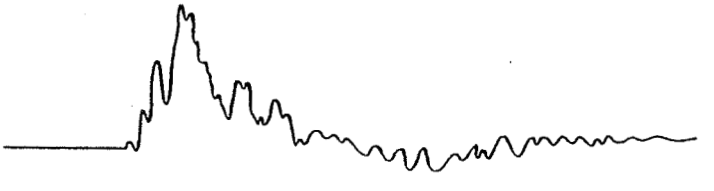

Observed Wave

2. FORMULATION

The investigation is based on a relatively simple mathematical model. In this model the medium is assumed to be one-dimensional, with properties that vary only with the spatial coordinate; i.e., the medium is assumed to be independent of time. The medium is also assumed to be quiescent, which means that only thermal scattering is being considered. (Mechanical turbulence, which gives rise to inertial scattering, is ignored.) In addition, the medium is assumed to be non-dissipative. Non-linear effects are disregarded.

The starting point of the analysis is the time-dependent scalar wave equation in one spatial dimension x. (Note that derivatives are denoted by superscripts rather than by subscripts.) Here w is the wave function; f is the source term.

The sound speed c_*, which is assumed to be a random function of x, is written as shown, where c is a constant reference speed and μ is a stationary random function of x having zero mean and unit variance. (The angle brackets denote an ensemble average.) The paramter ϵ is the standard deviation of the index of refraction of the medium, and is assumed to be small.

It should be pointed out that, in the atmosphere, the standard deviation of the acoustic index of refraction is typically about one part in one thousand, so that the assumption that ϵ is small, which is to say, the assumption that the medium is only weakly inhomogeneous, is appropriate for the study of sonic-boom propagation.

The initial conditions reflect the assumption that the medium is at rest prior to the initial disturbance.

$$c_*^{-2} w^{tt} - w^{xx} = f;\ t > 0,\ -\infty < x < +\infty$$

$$c_*(x) = \frac{c}{1 - \epsilon\mu(x)},\ <\mu>= 0,\ <\mu^2>= 1$$

$$w(x,0) = w^t(x,0) = 0$$

3. PERTURBATION METHOD

The assumption of a weakly inhomogeneous medium allows the problem to be solved by a perturbation method. To begin, assume that the wave function w has an expansion (which may be asymptotic) in powers of ϵ. By substituting this expansion back into the wave equation, equations for the coefficients w_0, w_1, etc. are derived in the usual way. The first two such equations, for w_0 and w_1, are shown. It turns out to be sufficient to carry out this procedure only as far as the first-order term (the w_1 term). The wave function w is then approximated by the first two terms of the expansion, as indicated on the last line.

Instead of specifying the source term f, it turns out to be more convenient to specify the zeroth-order wave function; i.e., the w_0 term, which corresponds to the incident wave. It is written as shown, where h, which is an arbitrary function, defines the waveform of the incident wave.

Writing the incident wave in this form is equivalent to specifying a source term that is concentrated at the origin, having a time dependence determined by the function h.

With w_0 specified in terms of the function h, the right-hand side of the equation for w_1 is determined, provided that μ is regarded as a known function. That equation can be solved by the method of characteristics. That method is well known, and so will not be described here. Instead, let's look next at how an expression for the correlation function of the finestructure is derived, once an expression for w_1 has been obtained.

$$w(x,t;\epsilon) = w_0(x,t) + \epsilon w_1(x,t) + \epsilon^2 w_2(x,t) + \ldots$$

$$c^{-2} w_0^{tt} - w_0^{xx} = f$$

$$c^{-2} w_1^{tt} - w_1^{xx} = 2c^{-2} \mu w_0^{tt}$$

$$\vdots$$

$$w_0(x,t) = h(t - |x|/c)$$

$$w = w_0 + \epsilon w_1 + \mathcal{O}(\epsilon^2)$$

4. CORRELATION FUNCTION

To get a general expression for the correlation function of the finestructure, start with the expression for w and average it, noting that the average of w_1 is zero. (The average of w_1 is zero because it is linear in the random function μ, which has average zero.) Note that the average field differs from the incident field by terms of order ϵ^2.

Next, subtract to get an expression for $\tilde{w}$, the fluctuating field, defined as the difference of w and its average. The quantity $\tilde{w}$ corresponds to the finestructure. An expression for the temporal correlation function of the finestructure at any point x is then obtained by forming, at x, the product of $\tilde{w}$ with itself at the two time values t_1 and t_2.

The averaging procedure used here is not the usual ensemble averaging. Instead, it's a travel-time-corrected averaging procedure that I call asynchronous ensemble averaging. The essential idea of the method is that, instead of measuring time with respect to some universal reference time, such as the time that the wave is emitted by the source, it is measured, for each wave in the ensemble, relative to the time that that wave arrives at the observer. The advantage of using a travel-time-corrected averaging procedure of this type is that it avoids certain spurious effects that arise as a consequence of averaging over an ensemble of waves that have become dispersed due to variations in travel time among the different members of the ensemble.

A travel-time corrected averaging procedure similar to the one used here was used by Allan Pierce in one of his papers on sonic-boom propagation.

I should mention also that asynchronous averaging has the effect of renormalizing the perturbation series for the wave function, which results in the elimination of some secular terms from the expression for the first-order field.

In order to apply asynchronous averaging in deriving an expression for the correlation function of the finestructure, one replaces t_1 by $\tau + r$, where τ is the travel time from the source (the origin) to the observation point x, and r is the time relative to the arrival time at which the observation is being made. The variable t_2 is replaced by $\tau + r + s$, where s denotes the separation time between the two observation times. The result is an expression for the correlation function of the finestructure, which is denoted by K. Note that terms of order ϵ^3 have been dropped from the expression for K.

The spectral density function is then obtained by taking the cosine transform of K with respect to s.

(See next page.)

CORRELATION FUNCTION

$$w = w_0 + \epsilon w_1 + \mathcal{O}(\epsilon^2)$$

$$< w > = w_0 + \mathcal{O}(\epsilon^2)$$

$$w - < w > \equiv \widetilde{w} = \epsilon w_1 + \mathcal{O}(\epsilon^2)$$

$$< \widetilde{w}(x,t_1)\widetilde{w}(x,t_2) > = \epsilon^2 < w_1(x,t_1)w_1(x,t_2) > + \mathcal{O}(\epsilon^3)$$

$$t_1 = \tau + r; \quad t_2 = \tau + r + s; \quad r \geq 0, s \geq 0$$

$$K(x,r,s) = < \widetilde{w}(x,\tau + r)\widetilde{w}(x,\tau + r + s) >$$

$$= \epsilon^2 < w_1(x,\tau + r)w_1(x,\tau + r + s) >$$

5. GENERAL RESULTS

The result of the analysis sketched above is the general expression shown for the correlation function of the finestructure. The function γ that appears in this formula is a temporal correlation function that's related to the spatial correlation function of the medium by the change of variable indicated. The function h determines the waveform of the incident wave, as discussed previously; the primes denote derivatives. The lower limit of the second inner integral; i.e., $\bar{\xi}$, is defined as shown.

This formula is valid provided that the propagation path length x is much greater than the integral scale, or outer scale, L, of the medium. (This condition is satisfied in virtually all cases of practical interest.) Note also that this expression is valid only for r positive. When r is negative, i.e., before the wave has arrived, the correlation function is zero.

This formula, which expresses the correlation function of the finestructure in terms of the incident waveform and the correlation function of the medium (the last two quantities both being arbitrary), is the main result of this investigation.

The spectral density function of the finestructure is obtained by taking the cosine transform of K with respect to s (the separation variable).

One point about this expression that's worth noting is that it is independent of the propagation range x. The reason for this is that, according to the theory, by the time the incident wave has propagated a distance of the order of an outer scale length into the medium the finestructure has become, in a statistical sense, fully developed. Beyond this range, i.e., for $x >> L$, there is, for all practical purposes, no further evolution of the statistical properties of the finestructure.

The correlation function K is, however, strongly dependent on the magnitude of the randomness of the medium, as is shown by the presence of the term ϵ^2 on the right-hand side of this expression.

Note also that the correlation function K depends on r (the elapsed time since onset), as well as on s, the separation time. The spectral density function of the finestructure will therefore also depend on r. The correlation and spectral density functions of the finestructure are thus time-dependent functions. This is a consequence of the fact that the finestructure of a transient signal is generally a non-stationary random process.

The formula shown expresses the function K as the sum of two iterated integrals. Of these, the two inner integrals involve only the function h. If that function has a sufficiently simple form, then the inner integrals can be evaluated analytically, after which only a pair of single integrals is left to deal with.

One case in which this type of simplification is feasible is

when the incident wave has the form of a simple ramp function, since then the function h is piecewise constant. The relevant calculations have been carried out, and the results are shown on the next figure. (This type of simplification is also feasible when the incident wave has the form of an N-wave, but the calculations for that case have not been done.)

GENERAL RESULTS

$$K(r,s) = \frac{1}{2}\epsilon^2\left[\int_0^r \gamma(\xi)\int_\xi^r h'(\eta-\xi)h'(\eta+s)d\eta d\xi + \int_{-s}^r \gamma(\xi+s)\int_{\bar{\xi}}^r h'(\eta-\xi)h'(\eta)d\eta d\xi\right]$$

$$\gamma(\xi) = <\phi(s)\phi(s+\xi)>,\ \phi(s) = \mu\left(\frac{1}{2}cs\right)$$

$$\bar{\xi} = \max(0,\xi),\ x >> L,\ r \geq 0,\ s \geq 0$$

6. RAMP FUNCTION

The sketch shows the function h(t) for the case of a ramp-function incident wave. The amplitude P and the rise time δ are shown on the sketch, as are the two time values r and r+s at which the finestructure is evaluated in order to form the two-point correlation function. The results described here are for the case in which the points r and r+s are both behind the rise phase of the incident wave, as indicated. This is the case of most practical importance.

As has been mentioned, the two inner integrals in the expression for K shown on the previous vu-graph can, in this case, be evaluated exactly. The result of that calculation is the first equation shown. Note that, although K is written generally as a function of both r and s, the right-hand side of this expression is in fact independent of r, showing that the finestructure is a stationary stochastic process in this case.

An expression for the spectral density function of the finestructure, denoted by D, is obtained by taking the cosine transform of K with respect to s. The result is given by the second equation. The function β is the transform of γ.

Of these two quantities, the spectral density function; i.e., D, is, as has already been emphasized, the quantity of primary interest in this study. The expression for this quantity will be examined more closely in a moment. First, however, let's take a quick look at what happens to these two formulas in the limit as δ goes to zero, i.e., as the ramp function becomes a step function.

The limiting forms of K and D, denoted by $K_0(s)$ and $D_0(\omega)$, respectively, are easy to calculate, and are given by the last two equations. The function $K_0(s)$ is then the correlation function, while $D_0(\omega)$ is the spectral density function, of the finestructure for the case in which the incident wave is a step function.

It should be pointed out that no analytical problems arise in calculating these limits. There is thus no problem with singular behavior of the finestructure in the limit as the ramp-function incident wave becomes a step function.

These last two formulas show that, when the incident wave is a step function, the correlation function of the finestructure is proportional to the correlation function of the medium, and, similarly, the spectral density function of the finestructure is proportional to the spectral density function of the medium.

When the incident wave has the form of a ramp function, however, with a non-zero rise time, these simple relations no longer obtain. This situation, particularly as regards the spectral density function, will be examined in more detail in the next section.

RAMP FUNCTION

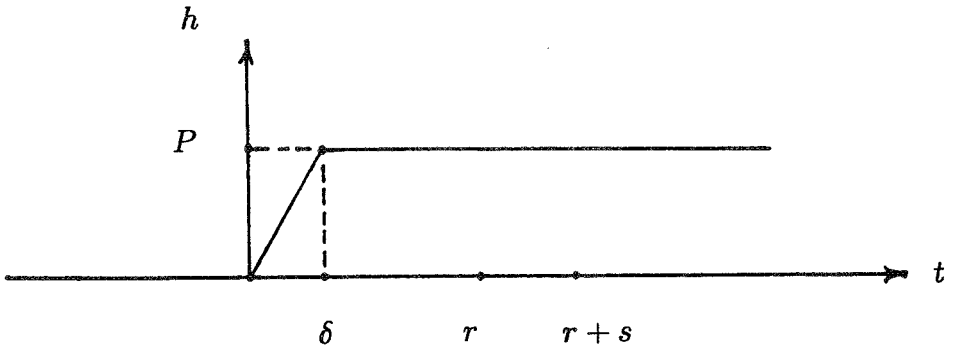

$$K(r,s) = \frac{\epsilon^2 P^2}{2\delta^2} \int_0^\delta (\delta - \xi)\,[\gamma(s-\xi) + \gamma(s+\xi)]\,d\xi$$

$$D(r,\omega) = \epsilon^2\, P^2\ \frac{1-\cos(\delta\omega)}{(\delta\omega)^2}\,\beta(\omega)$$

$\delta \to 0$:

$$K(r,s) \to \frac{1}{2}\,\epsilon^2 P^2\,\delta(s) \equiv K_0(s)$$

$$D(r,\omega) \to \frac{1}{2}\,\epsilon^2 P^2\,\beta(\omega) \equiv D_0(\omega)$$

7. RAMP FUNCTION (cont'd)

In order to examine some of the implications of the result obtained above for the ramp-function finestructure spectrum D, it's convenient to write the expression for that quantity in the form shown on the first line. In this formula the function D_0 is the finestructure spectrum for the case of zero rise time, i.e., for the step-function incident wave, as described above. The function A determines how the finestructure spectrum differs from D_0 when the rise time δ is non-zero.

The function A is sketched in the figure. Note that it is effectively zero when its argument is greater than about 2π. What this means is that (referring to the formula for D) the finestructure spectrum is effectively zero at all frequencies for which $\delta\omega$ is greater than about 2π, or, what is equivalent, when f, the frequency in Hz, is greater than about $1/\delta$.

This result shows that, the greater the rise time of the incident wave, the less high-frequency energy there is in the finestructure. A couple of examples of this effect, involving parameter values typical of sonic-boom propagation, are shown: When the rise time is one millisecond, there is effectively no energy in the finestructure spectrum at frequencies above about 1 kHz. If the rise time is increased to two milliseconds, then the lower limit of the frequency range for which the finestructure spectrum is devoid of energy drops to 500 Hz.

Note, however, that, since the function A is equal to unity when its argument is equal to zero, the low-frequency portion of the finestructure spectrum is relatively unaffected by changes in the rise time.

Since it's generally the high-frequency portion of the acoustic spectrum that's most annoying to the human ear, what these results imply is that, at least for a ramp-function wave in one dimension, increasing the rise time of the incident wave will tend to reduce the annoyance associated with the finestructure. Whether this result holds in three dimensions as well remains to be seen, but if it does it has obvious implications as regards the idea of shaping the sonic boom in order to reduce its annoyance.

The results just described could, of course, be expressed just as well in terms of time scales, rather than in terms of frequency. Expressed in those terms, the results imply that a ramp-function wave propagating in a random medium will contain very little structure having time scales smaller than the rise time. This prediction agrees with observations of sonic-boom and other types of transient waves, which rarely show any appreciable structure having time scales smaller than the rise time.

RAMP FUNCTION (cont'd)

$$D(r,\omega) = A(\delta\omega)\, D_0(\omega)$$

$$A(\theta) = 2\ \frac{1-\cos\theta}{\theta^2}$$

The function $A(\delta\omega)$, and therefore the finestructure spectrum, is effectively zero for $\delta\omega \gtrsim 2\pi$, or $f \gtrsim 1/\delta$.

Sonic boom: $\delta = .001$ sec; $f \gtrsim 1000$ Hz

$\delta = .002$ sec; $f \gtrsim 500$ Hz

$\Rightarrow D(r,\omega) \simeq 0$

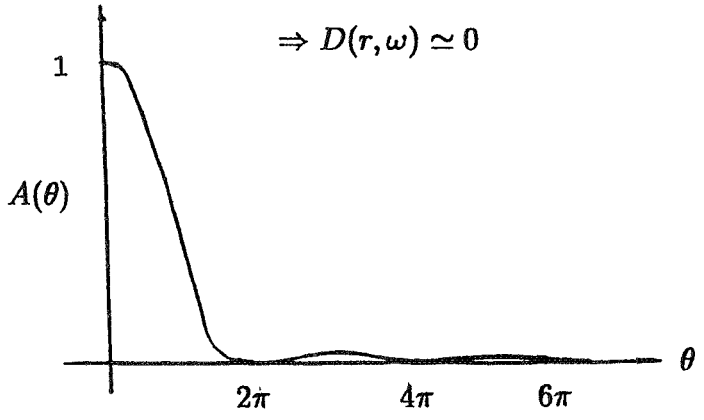

8. SUMMARY

The main results of this investigation can be summarized as follows. First, the approach described here has been found to yield fairly concise, general expressions for the correlation and spectral density functions of the finestructure. Second, the results for the case of a ramp-function incident wave agree with the observation that the important time scales associated with the finestructure of sonic-boom and other types of transient waves are generally comparable to, or greater than, the rise time. Finally, the results (again for the ramp-function incident wave) indicate that an increase in the rise time of the incident wave is associated with a reduction in the high-frequency content of the finestructure.

This last result, assuming that it holds in the three-dimensional case as well, has implications as regards the idea of shaping the sonic boom in order to reduce its annoyance. It suggests that increasing the rise time of the sonic boom will make it quieter, even in the presence of turbulence.

NUMERICAL MODEL FOR THE WEAKLY NONLINEAR PROPAGATION OF SOUND THROUGH TURBULENCE

Bart Lipkens and Philippe Blanc–Benon
Laboratoire de Mécanique des Fluides et Acoustique
URA–CNRS 263
Ecole Centrale de Lyon
Ecully, France

INTRODUCTION

When finite amplitude (or intense) sound, such as a sonic boom, propagates through a turbulent atmosphere, the propagation is strongly affected by the turbulence. The interaction between sound and turbulence has mostly been studied as a linear phenomenon, i.e., the nonlinear behavior of the intense sound has been neglected. It has been shown that turbulence has an effect on the perceived loudness of sonic booms, mainly by changing its peak pressure and rise time. Peak pressure and rise time are important factors that determine the loudness of the sonic boom when heard outdoors [1, 2]. However, the interaction between turbulence and nonlinear effects has mostly not been included in propagation studies of sonic booms. It is therefore important to investigate the influence of acoustical nonlinearity on the interaction of intense sound with turbulence.

As stated in the introduction, the motivation for the research presented here is an investigation of the effect of turbulence on the nonlinear propagation of sonic booms and spark-produced N waves. In a previous study [2] Lipkens showed that model experiments are successful in simulating the sonic boom propagation through a turbulent atmosphere. A nonlinear propagation model for the propagation of sound through turbulence is presented here. Results from a numerical experiment that simulates the propagation of spark-produced N waves through turbulence are shown. Finally, some conclusions of the effect of turbulence on the nonlinear propagation of N waves are given.

Overview

- Motivation: study the effect of turbulence on the nonlinear propagation of sonic booms (N waves)
- Model experiment is successful in simulating the sonic boom propagation through atmospheric turbulence
- Nonlinear propagation model
- Results
- Conclusion

Figure 1: Overview of presentation.

In Fig. 2 the setup of the model experiment is shown. The discharge of a capacitor across the gap between the two electrodes creates a spark. The spark–produced N wave propagates across the turbulent field of a plane jet. A wide–band condensor microphone picks up the signal. A centrifugal fan blows the air into the settling chamber. The air exits through the narrow slit and forms a plane jet. A detailed description is presented in Ref. [2].

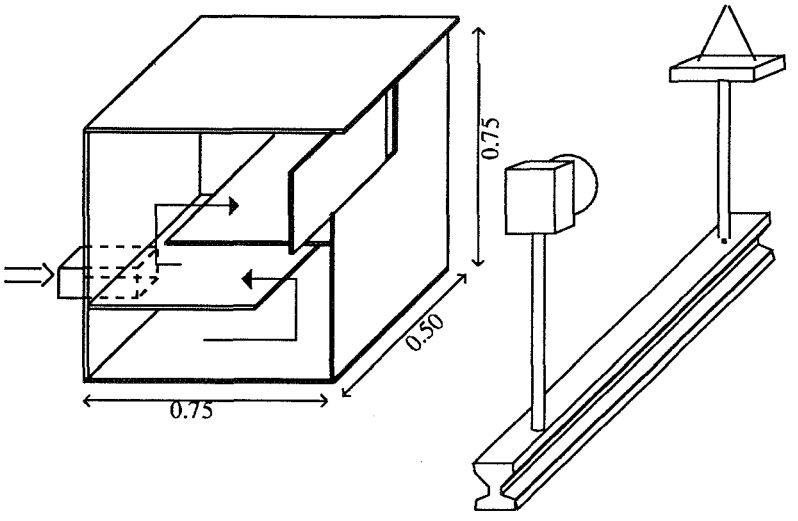

Figure 2: Model experiment setup.

In Fig. 3 several waveforms of the model experiment are shown. The upper left graph presents the waveform in absence of turbulence. All other waves have propagated through the turbulence. The distortion observed in the waveforms is very similar to that in sonic boom signatures, see e.g., [4]. Rounded and peaked waveforms are shown, as well as double and triple peaked waveforms.

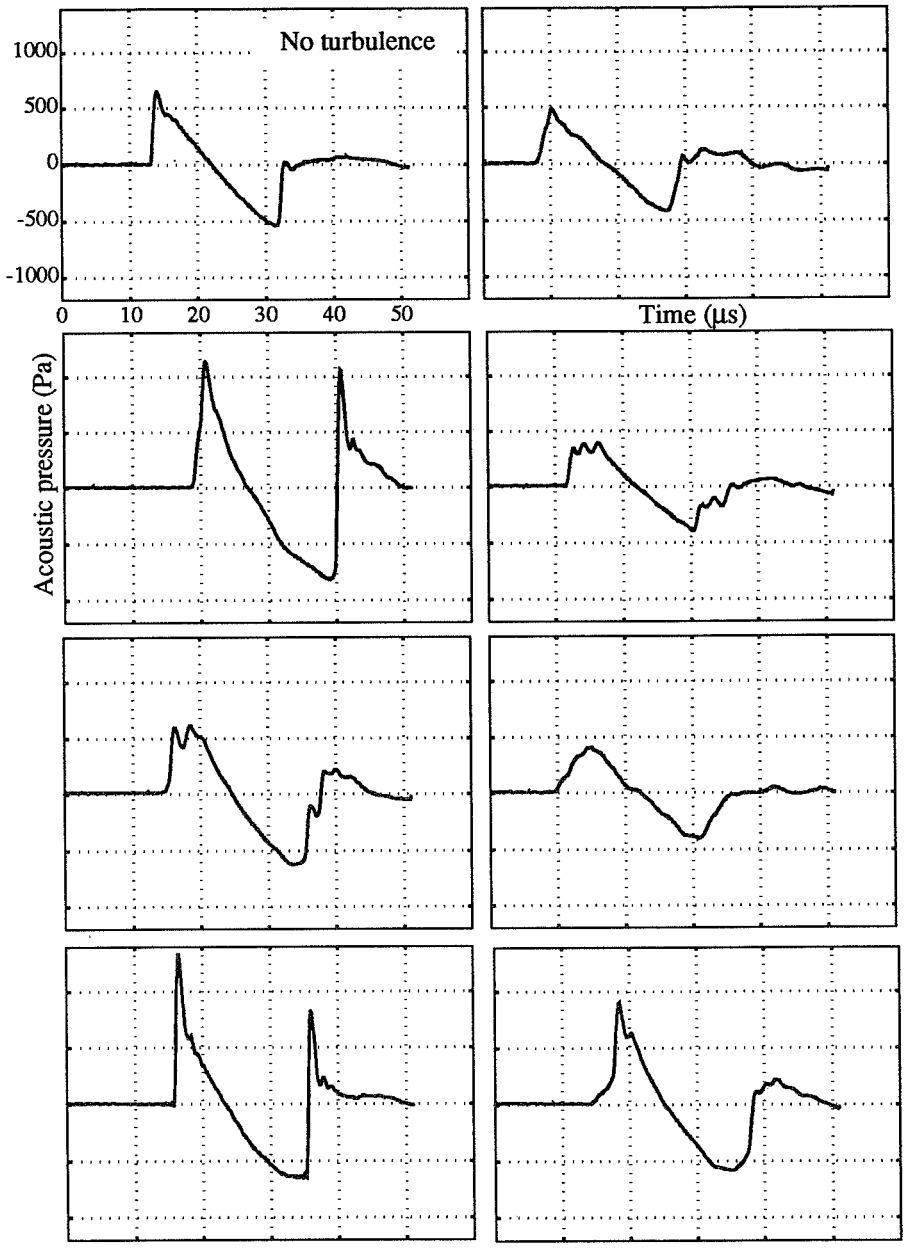

Figure 3: Waveform examples of the model experiment.

We developed a model that simulates the weakly nonlinear acoustic propagation through turbulence. The main assumptions are: (1) linear geometric acoustics is sufficient to propagate the waves through the turbulent fields and (2) a nonlinear transport equation governs the propagation along the rays. We assume that the turbulence is frozen during passage of the wave. Thus, we model the turbulent medium as a set of independent realizations of a random field. The turbulent field of each realization is constructed as a sum of a finite number of Fourier modes. The model is flexible. Two–dimensional (2D) or three–dimensional (3D), scalar (e.g., temperature) or vectorial (e.g., velocity) fields can be constructed. The acoustic propagation model then consists of two parts. First, linear geometric acoustics is used to trace rays through each individual realization of the turbulent field. Then, a Pestorius' type algorithm [4] is used to solve numerically the nonlinear propagation equation along the rays.

Nonlinear Propagation Model

- assumptions: - linear geometric acoustics is used to trace rays
  - nonlinear transport equation along the rays
- turbulence model: - 2D or 3D, temperature or velocity turbulence
  - realizations constructed as a sum of discrete Fourier modes
- ray tracing through each realization of the turbulence
- nonlinear transport equation: - transformation into Burgers equation
  - solved by a Pestorius type algorithm

Figure 4: Nonlinear propagation model.

The turbulent field is homogeneous and isotropic with a zero mean value. In Eq. 1 the construction of a turbulent velocity field as a sum of N modes is shown [6]. The direction of the turbulent wave vector $\vec{K}^i$ of each mode is random and determined by the random angle θ_i (in 2D) (Fig. 5). The homogeneity of the turbulent field is assured by the random phase shift ϕ_i. The amplitude of each mode is determined by a predefined energy spectrum. For the results reported here a Gaussian longitudinal correlation function was assumed. The associated energy spectrum is shown in Fig. 6.

Turbulence model

$$\vec{v}'(\vec{x}) = \sum_{1}^{N} \vec{u}_i\left(\vec{K}^i\right) \cos\left(\vec{K}^i \cdot \vec{x} + \phi^i\right) \tag{1}$$

$$\vec{u}_i\left(\vec{K}^i\right) \cdot \vec{K}^i = 0$$

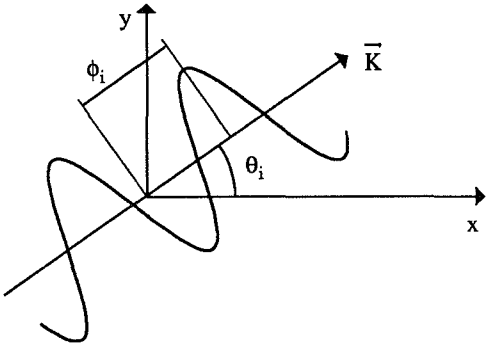

Figure 5: Wave vector geometry of a single Fourier velocity mode in 2D.

Two–dimensional kinetic energy spectrum

Gaussian longitudinal correlation function $f(r) = \exp\left(-r^2/L^2\right)$

Two–dimensional energy spectrum $E(K) = \frac{v'^2}{8} K^3 L^4 \exp\left(-K^2 L^2/4\right)$

Amplitude of each Fourier mode $\mid \vec{u}_i \mid = \sqrt{E(K)\,\Delta K}$

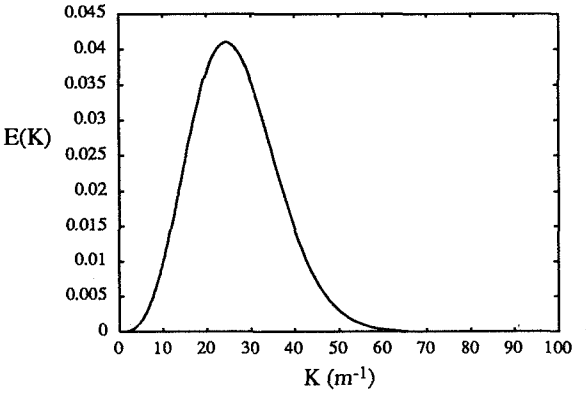

Figure 6: 2D energy spectrum for a Gaussian correlation function.

Equations 2–5 present the well–known formulation of acoustic propagation in the geometric acoustics limit [7]. The position vector $\vec{x}$ (Eq. 2) and the nondimensional wave vector $\vec{p}$ (Eq. 3) at a current point on the ray trajectory are completely determined by the value of s and the initial position along the incident wavefront. The local geodesic elements (Eqs. 4–5) govern the evolution of the wavefront along each ray and permit the calculation of the cross–sectional area of an infinitesimal ray tube. The parameters θ_0 and α_0 characterize the initial wavefront. The effect of the random field is represented by the index $N = c_0/c$ of the medium and the Mach number $\vec{M} = \vec{v}/c$ of the turbulent flow. Once initial conditions are known, a Runge–Kutta fourth–order scheme is used to solve the differential system. The step size ds is a function of the maximum wave number value of the turbulent energy spectrum, and equals $ds = 1/2k_{\max}$. It is important to note that the description of the turbulent field in terms of Fourier modes allows us to obtain analytically all the spatial derivatives in the system. Numerical errors are thus reduced.

Geometrical acoustics: Ray path equations

$$\frac{d\vec{x}}{ds} = \frac{1}{N}\left(\vec{\nu} + \vec{M}\right) \tag{2}$$

$$\frac{d\vec{p}}{ds} = \frac{1}{N}\left(\nabla N - \left(\nabla \vec{M}\right)\cdot \vec{p}\right) \tag{3}$$

$$\frac{d\vec{R}}{ds} = \frac{1}{pN}\left(\vec{Q} - \vec{\nu}\cdot\vec{Q}\vec{\nu}\right) \tag{4}$$

$$\frac{d\vec{Q}}{ds} = \frac{1}{N}\left(\vec{R}\cdot\nabla\nabla N - \vec{R}\cdot\left(\nabla\nabla\vec{M}\right)\cdot\vec{p} - \left(\nabla\vec{M}\right)\cdot\vec{Q}\right) - \frac{1}{N^2}\left(\vec{R}\cdot\nabla N\right)\left(\nabla N - \left(\nabla\vec{M}\right)\cdot\vec{p}\right) \tag{5}$$

where:

N is the index of the medium, i. e. $N = c_0/c$

$\vec{M} = \vec{v}/c$ is the Mach number vector, and $\vec{v}$ is the fluid velocity vector

$\vec{x}$ is the vector describing the ray path

$\vec{\nu}$ is the unit vector tangent to the ray path, i. e. $\vec{\nu} = \vec{p}/p$ and $\vec{p} = \vec{k}/k_0$

$\vec{k}$ is the wavenumber vector and $k_0 = \omega/c_0$

$\vec{R}$ is the vector describing the local geodesic elements of the wavefront, i. e. $\vec{R}^{\theta} = (\partial\vec{x}/\partial\theta_0)_{\alpha_0}$ and $\vec{R}^{\alpha} = (\partial\vec{x}/\partial\alpha_0)_{\theta_0}$

$\vec{Q}$ are the conjugate elements of $\vec{R}$

In Fig. 7 two typical examples of ray–tracing through a random field are shown. The upper graph presents an example of a random temperature field with a scale of $L = 0.1$ m. During the first correlation lengths the rays are only slightly distorted and the initial plane wave structure is still apparent. At greater propagation distances the deflection of the rays is more pronounced, neighboring rays begin to cross, strong concentrations occur at different lateral positions, and caustics appear. The lower graph shows the propagation through a random velocity field. The length scale is the same, and the index fluctuations for the scalar and vectorial fields are identical, i.e., $\epsilon = -T'/2T_0 = -v_x'/c_0$, where T' is the rms temperature fluctuation and v_x' is the velocity fluctuation component in the propagation direction. The ray distortion for the velocity field is stronger than for the scalar field. The distance of caustics formation is shorter than for the scalar field.

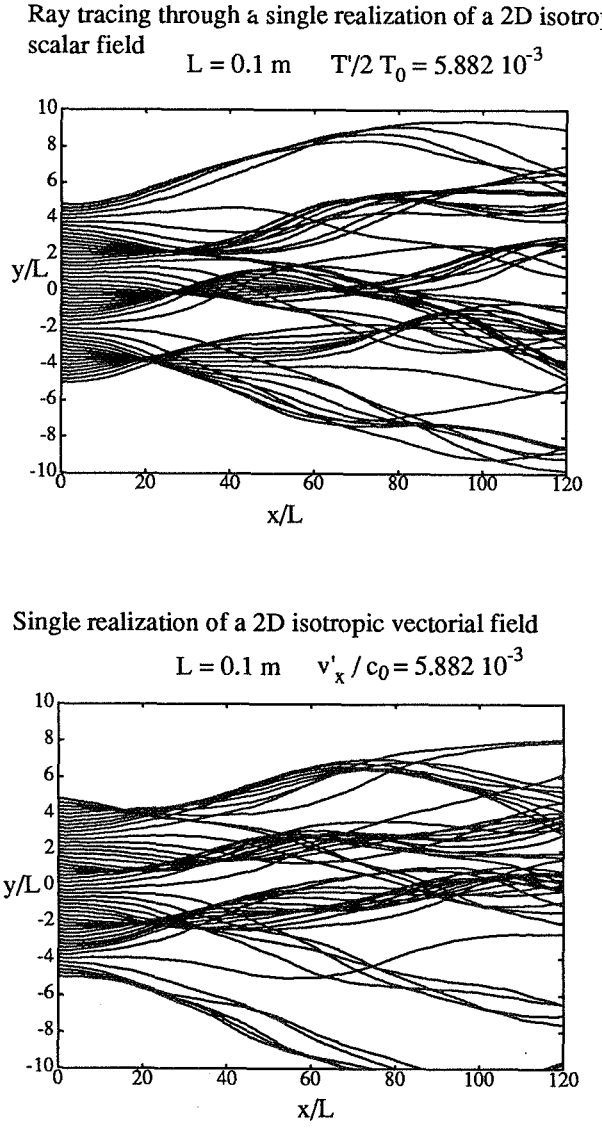

Figure 7: Examples of ray–tracing through a random temperature and velocity field.

The main assumptions in the derivation of the nonlinear transport equation are: (1) only quasi–linear terms are retained in the derivation, (2) lossless propagation is assumed, and (3) the geometric acoustics approximation is applied. Using the assumptions, we derive a transport equation (Eq. 6), where s represents the arclength along the ray, β is the coefficient of nonlinearity, t' is the retarded time coordinate, and A is the cross–section of the ray tube. Through a transformation of the dependent and independent variable the transport equation takes the form of the Burgers equation (Eq. 9) for plane wave propagation in a homogeneous medium. The distortion distance variable Z describes the equivalent plane wave distortion for a wave propagating in a random medium. Equation 8 is integrated numerically along the rays and yields the equivalent distortion value. The Burgers equation (Eq. 9) is solved numerically by a Pestorius' type algorithm [5]. The nonlinear distortion is applied in the time domain and an ad–hoc absorption is applied in the frequency domain.

Nonlinear transport equation:

Main assumptions: - quasi-linear
- lossless
- geometric acoustics approximation

$$\frac{\partial}{\partial s}\left[\frac{p^2|A|}{c\rho_0}\left(1+\vec{\nu}\cdot\vec{M}\right)\mid\vec{\nu}+\vec{M}\mid\right]-\frac{2\beta|A|}{\rho_0^2c_0^4}p^2p_{t'}=0 \tag{6}$$

Transformation of the dependent and independent variable
Let $\Pi = Kp$, where

$$K=\sqrt{\frac{|A|}{|A_0|}\frac{\rho_0c_0}{\rho c}\left(1+\vec{\nu}\cdot\vec{M}\right)\mid\vec{\nu}+\vec{M}\mid} \tag{7}$$

and

$$\frac{dZ}{ds}=\sqrt{\frac{|A_0|}{|A|}\frac{\beta^2}{\beta_0^2}\frac{\rho_0c_0^5}{\rho c^5}\left(1+\vec{\nu}\cdot\vec{M}\right)^{-3}\mid\vec{\nu}+\vec{M}\mid^{-3}} \tag{8}$$

The transport equation is transformed into the homogeneous plane wave Burgers equation

$$\frac{\partial\Pi}{\partial Z}-\frac{\beta_0}{\rho_0c_0^3}\Pi\,\Pi_{t'}=0 \tag{9}$$

COMPUTATION STRATEGY

The computation strategy involves the following steps. First, individual realizations of the turbulent field are contructed. Second, eigenrays that connect source and receiver are computed, and the properties K and Z are calculated along the eigenrays. Third, a Pestorius' type algorithm is used to propagate a given waveform nonlinearly along the eigenrays. Finally, the waveforms associated with all eigenrays are combined to obtain the signal at the receiver. If a waveform passes through a caustic, the propagation proceeds up to the caustic, then a $-90°$ phase shift is applied in the frequency domain, and propagation proceeds again.

Strategy

- create realizations of turbulent field
- compute eigenrays and properties (K,Z) along the eigenrays
- use Pestorius algorithm to propagate a waveform nonlinearly along the eigenrays
- combine eigenrays to obtain signal at the receiver
- if waveform passes through a caustic, propagation proceeds up to the caustic, then a $-90°$ phase shift is applied in the frequency domain, and propagation continues

EXAMPLE OF EIGENRAY CALCULATION FOR ONE REALIZATION

The upper graph in Fig. 8 represents the 7 eigenrays that connect the initial plane wavefront with the receiver located at 8 m on the x-axis. The second graph shows the values of K along the rays. When the eigenray passes through a caustic, the value of K drops to zero, i.e., an infinite pressure, a consequence of the linear geometric acoustics assumption. As is observed, one eigenray passed through two caustics, three rays passed through one caustic, and three rays did not yet pass through a caustic. The third graph presents the equivalent plane wave distortion distance Z. For the ray that passed through two caustics, the equivalent distortion distance is nearly 14 m when the actual propagation distance to the receiver is about 8 m. Thus, the nonlinear distortion along this ray is equivalent to that of a plane wave that propagated about 14 m in a homogeneous medium. For one ray that did not propagate through a caustic, the equivalent distortion distance is just slightly more than 2 m, and hence the nonlinear distortion will be very weak compared to the homogeneous case.

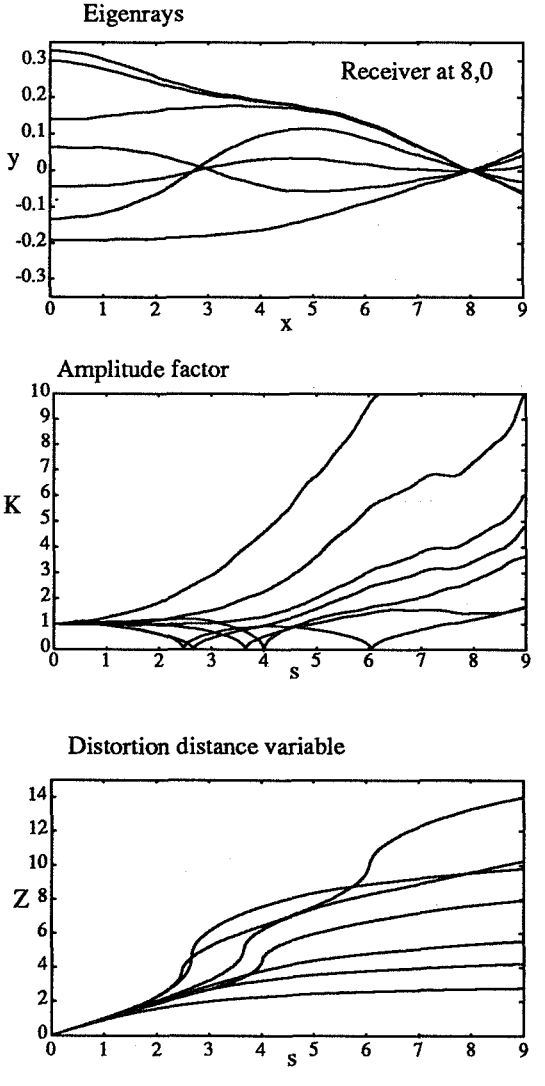

Figure 8: Examples of eigenray and associated K and Z calculation.

PARAMETERS FOR THE NUMERICAL STUDY

The parameters for the numerical experiment are shown in Fig. 9. Both temperature and velocity turbulent fields are constructed. Both fields have a length scale of $L = 2.5$ cm. The index of fluctuations ϵ is identical for both fields. The rms velocity fluctuation is 2.5 m/s and the rms temperature fluctuation is 4.27 K. Each realization is constructed as a sum of 60 Fourier modes equally divided between a lower wave number value of 0.1 L and an upper value of 10 L. Statistics are calculated for an ensemble of 100 realizations. The incident acoustic wave is a plane N wave of peak pressure 500 Pa, duration 15 μs, and rise time 1 μs. The propagation medium is air, and classical thermo-viscous absorption is included in the Pestorius' algorithm as well as O_2 and N_2 relaxation.

Parameters for numerical study

- Turbulence: 60 modes between 0.1 L and 10 L

  L = 2.5 cm

  v' = 2.5 m/s and T' = 4.27 K

  100 realizations

- plane N wave: 500 Pa peak pressure

  15 μs duration

  1 μs rise time

- medium: classical absorption

  0_2 and N_2 relaxation

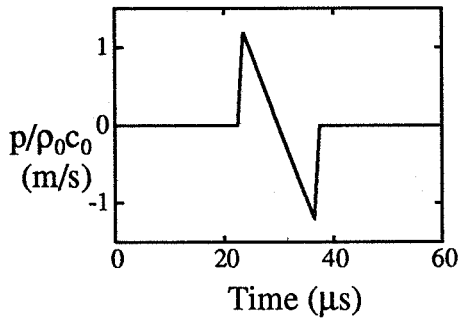

Figure 9: Parameters for the numerical study.

AVERAGED RESULTS FOR THE PARAMETERS Z AND K

In the upper graph of Fig. 10 the value of Z averaged over 100 realizations is shown. Three curves are presented, i.e., for the no turbulence, temperature turbulence, and velocity turbulence case. It is seen that the presence of turbulence always results in a lower value for the equivalent distortion distance. The effect is more pronounced when propagation distance increases, and stronger for the velocity turbulence. At a propagation distance of 2 m the equivalent distortion distance for the velocity turbulence is slightly more than 50% that of the no turbulence case. The lower graph presents the values of the amplitude factor K. The factor increases rapidly with propagation distance, and the effect is more pronounced for the velocity turbulence.

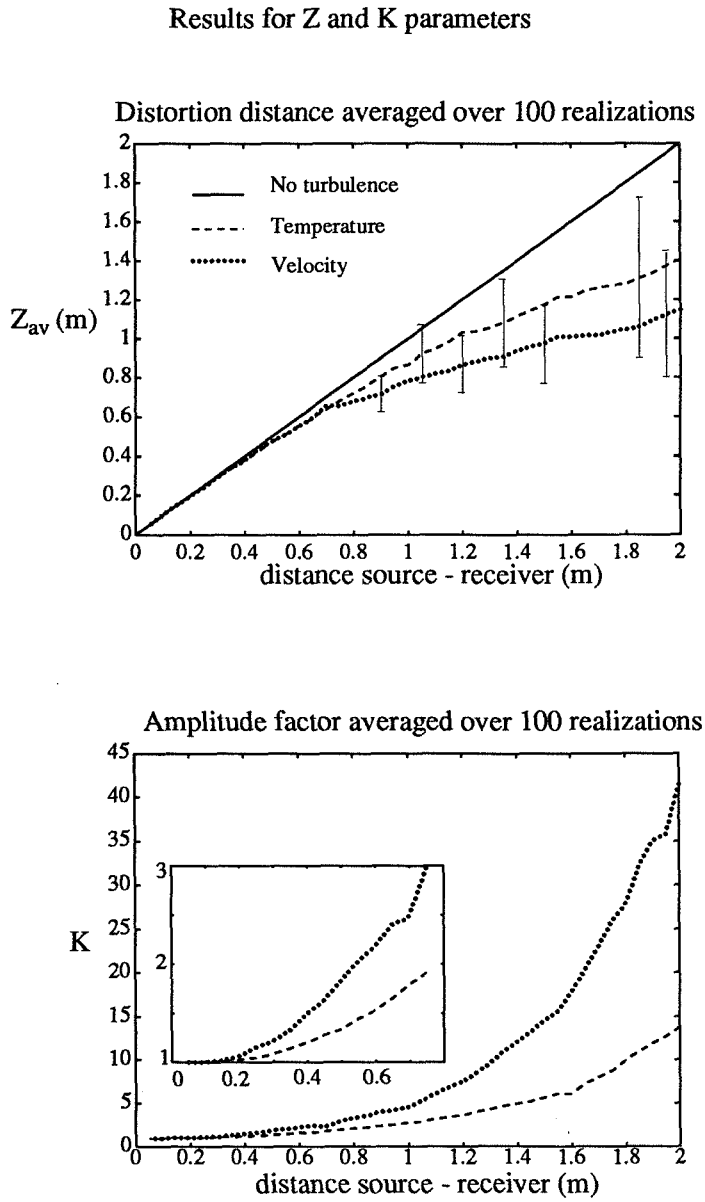

Figure 10: Averaged results for parameters Z and K.

EXAMPLE OF WAVEFORM CALCULATION

An example of a waveform calculation is shown in Fig. 11. The total waveform at the receiver is shown in the upper graph. For this particular example 5 eigenrays exist. The lower graph presents the contribution of the waveform of each eigenray to the total signal. Two waves have passed through a caustic, and the other three have not passed through a caustic. The latter three arrive at the receiver at nearly the same time and are hard to distinguish.

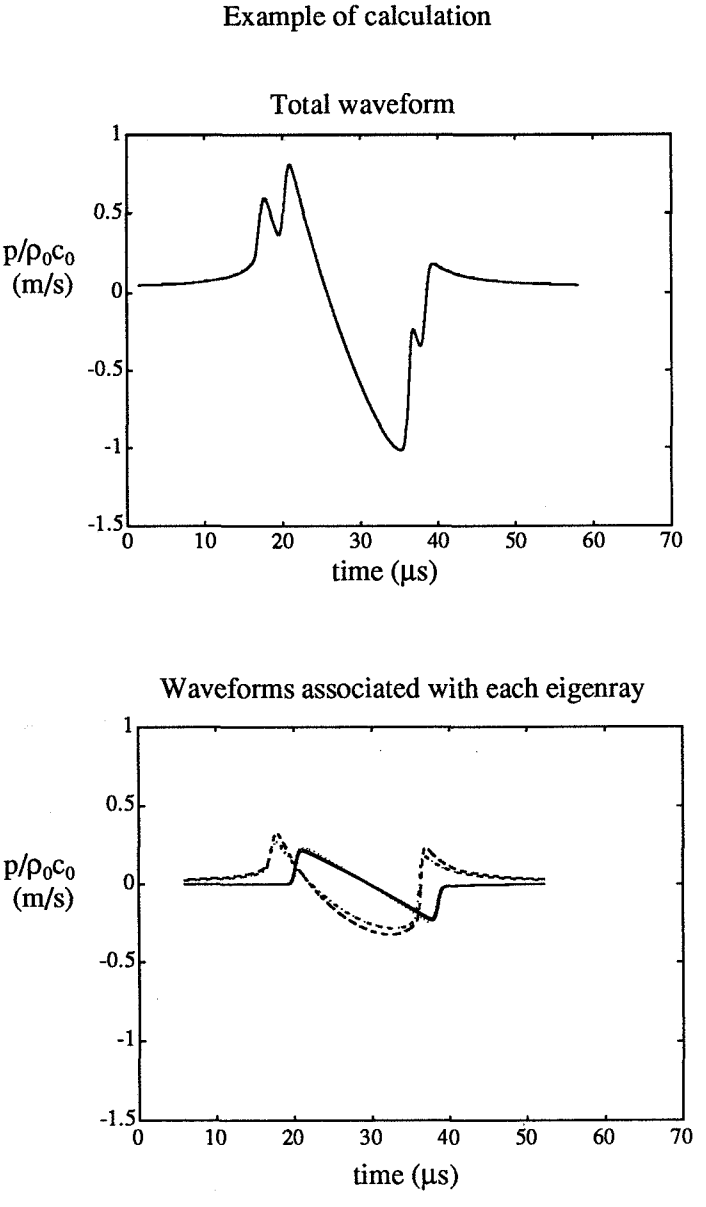

Figure 11: Example of waveform calculation.

WAVEFORM EXAMPLES

In Fig. 12 several examples of waveforms calculated at the receiver at a distance of 18 or $20L$ are shown. The upper left graph presents the waveform at a distance of $18L$ in absence of turbulence. All other waves have propagated through a turbulent field. In general the distortion of the waveform is similar to that measured in spark–produced N waves (Fig. 3).

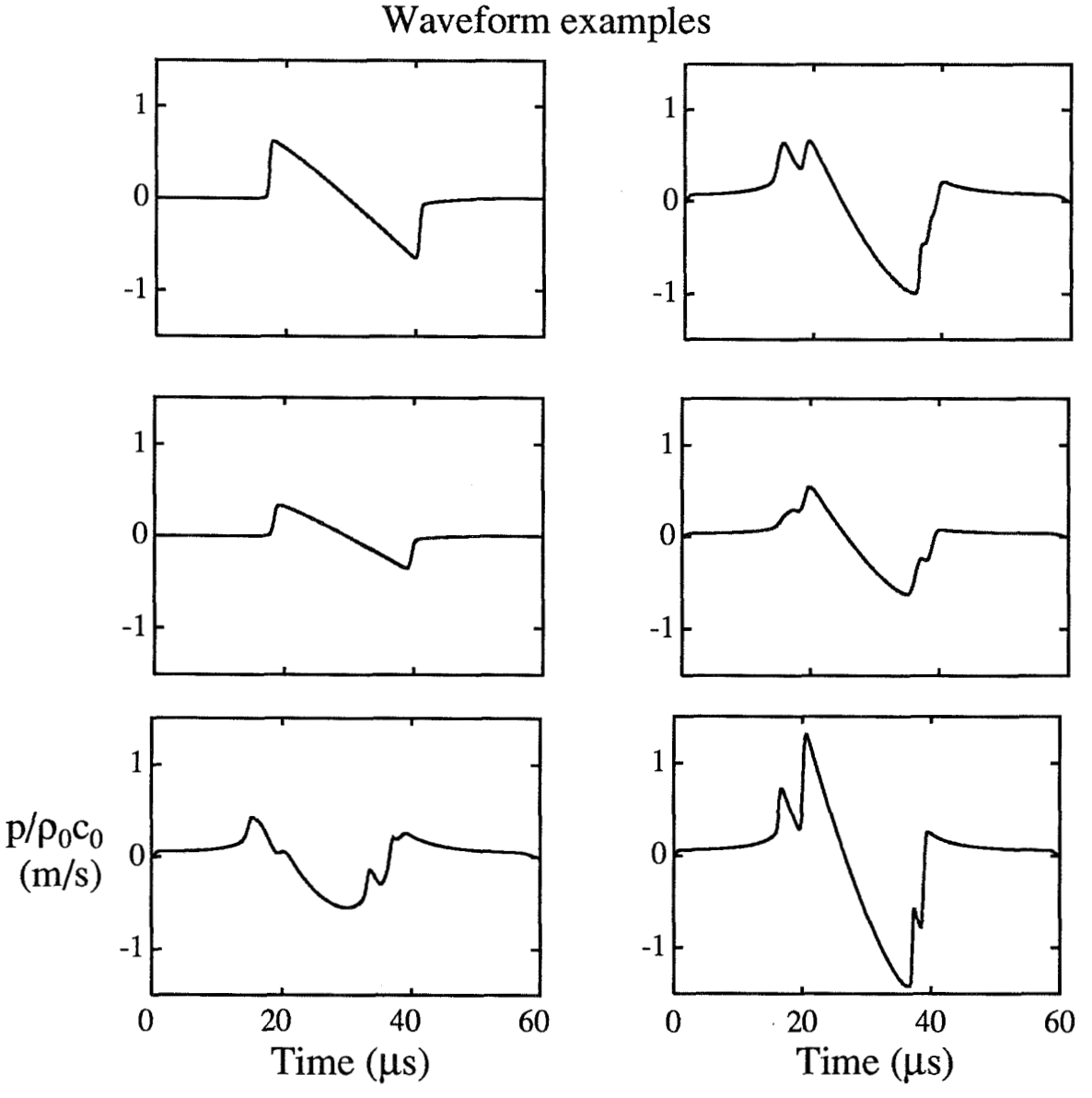

Figure 12: Waveform examples.

RESULTS FOR THE TOTAL WAVEFORM AT THE RECEIVER

The average values of peak pressure and rise time of the total waveform calculated at different receiver distances are shown in Fig. 13. The rise time is calculated as the time portion between 10% and 90% of the peak pressure of the total waveform. According to this definition, we notice that the rise time is essentially determined by the differences in arrival time of the eigenrays when more than one eigenray is present (see, e.g., Fig. 11). The average is taken over 100 realizations. In the presence of turbulence, peak pressure is always decreased. There is no notable difference between the temperature and velocity turbulence. At a distance of 1 m a decrease of about 25% is observed. This result confirms the model experiment results [3] that peak pressure on average is always decreased by turbulence. The lower graph presents the average value of rise time. On average, rise time is always increased by turbulence. At a propagation distance of 1 m, a tenfold increase is observed. Again, this result confirms that of the model experiment. The effect is more pronounced for the velocity fields. The curves start to deviate from the no turbulence case when the rays pass through the first caustic. The shorter distance to the first caustic for the velocity fields explains the quicker departure from the no turbulence values.

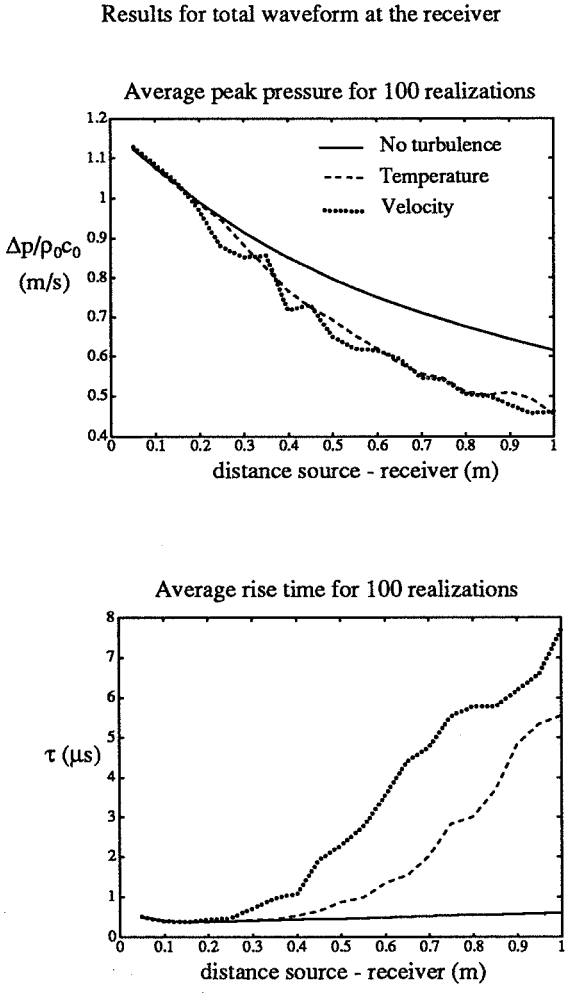

Figure 13: Average values of peak pressure and rise time of the total waveform for 100 realizations.

HISTOGRAMS OF PEAK PRESSURE AND RISE TIME

The histograms of peak pressure and rise time at different distances of propagation are shown in Fig. 14. The thick black vertical line in each graph represents the value for the plane wave case in absence of turbulence. The distribution for the peak pressure is asymmetric. Peak pressures smaller than the no turbulence value occur more often, but some large values of peak pressure are always present. The rise time histograms show that turbulence almost always causes the rise time to increase. When propagation distance increases, larger values for the rise time occur once the rays have passed through the first caustic (e.g., at a distance of 20 L). When rays pass through several caustics, rise times more than 20 times that of the no turbulence value are observed (e.g., at 40 L).

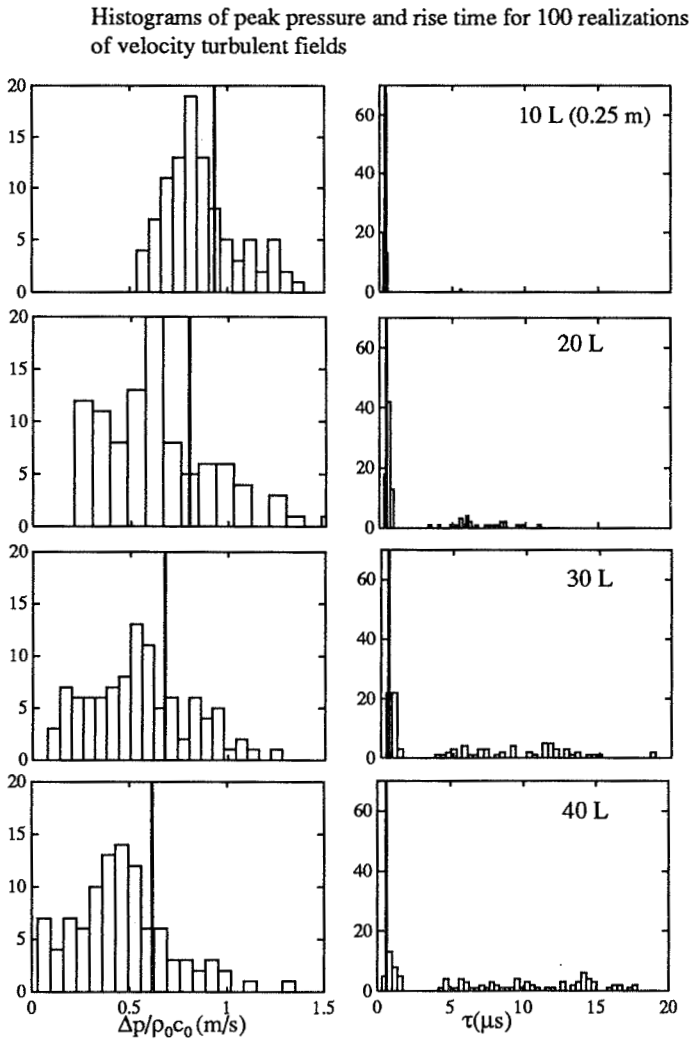

Figure 14: Histograms of peak pressure and rise time for 100 realizations.

RESULTS FOR THE INDIVIDUAL WAVEFORMS ASSOCIATED WITH EACH EIGENRAY

A second statistical calculation is performed. In order to filter out the effect of the difference in arrival time for all the eigenrays, we calculated the peak pressure and rise time of the individual waveforms associated with each eigenray. The waveform shown in Fig. 11 consists of 5 eigenrays. Instead of calculating the peak pressure and rise time of the global waveform, we calculate the peak pressure and rise time of the three waveforms that have not yet passed through a caustic. We do not take into account the rays that have passed through a caustic because the 10% to 90% criterion results in very large values. A better criterion for these waveforms would be a rise time value based on a maximum slope value. The result of the calculation is shown in Fig. 15. The average peak pressure is again always decreased by turbulence. Average peak pressure for velocity turbulence is lower than that for the temperature turbulence. The average rise time values are always increased by the turbulence. The difference is less marked when compared with the previous calculation. For the velocity turbulence a doubling of the rise time is observed at a propagation distance of 1 m. Again the effect is more pronounced for the velocity fields. The slope of the rise time versus distance curve is linear. The larger slope for the velocity fields is caused by the vectorial character of the fields.

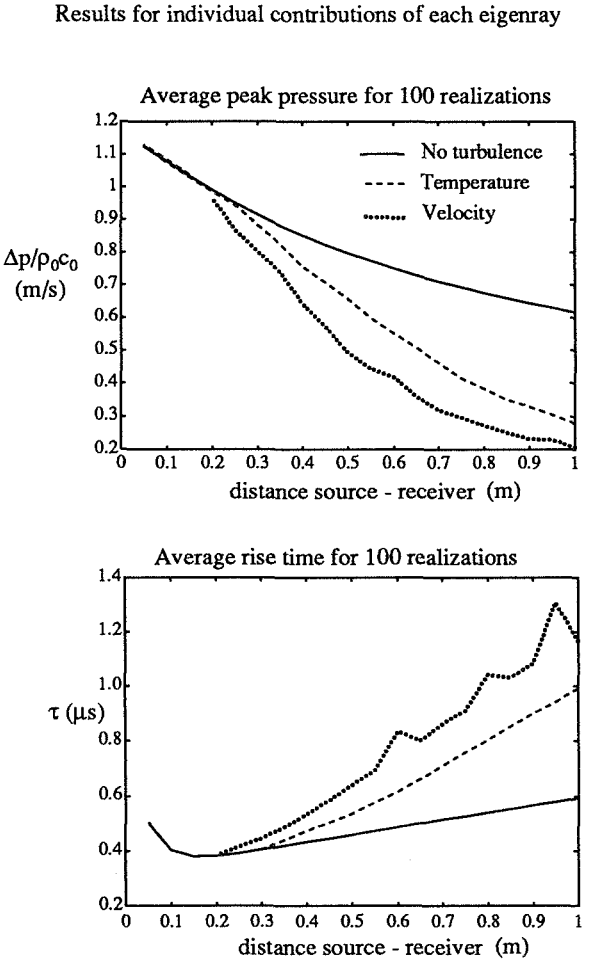

Figure 15: Average values of peak pressure and rise time of the waveforms associated with the eigenrays.

CONCLUSIONS

We presented a model for the nonlinear propagation of sonic booms and spark-produced N waves through turbulence. A numerical experiment that simulates the propagation of spark-produced N waves through 2D temperature and velocity turbulent fields was performed. The results from the numerical experiment confirm the experimental observations of the model experiment in which spark–produced N waves propagated through a plane jet turbulence. An important conclusion is that the presence of turbulence on average reduces the nonlinear distortion. It is however possible that for a particular realization the nonlinear distortion is stronger. On average, peak pressure is always decreased by turbulence. Turbulence almost always causes the rise time to increase. The computed waveforms show similar distortion as that obtained in the model experiment. The effect of turbulent velocity fields is more pronounced than that of temperature fields and is caused by the difference in character, i.e., vectorial for the velocity fields versus scalar for the temperature fields. Future work includes a calculation with a more realistic turbulent energy spectrum and the incorporation of boundaries.

Conclusions

- Model presented for the nonlinear acoustic propagation through turbulence.
- On average, turbulence reduces the nonlinear distortion.
- On average, peak pressure decreases after propagation through turbulence.
- Rise time is almost always increased by turbulence.
- Effect of velocity turbulence is more pronounced than that of thermal turbulence.

Figure 16: Conclusions.

References

[1] A. Niedzwiecki and H. S. Ribner, "Subjective loudness of N-wave sonic booms," *J. Acoust. Soc. Am.* **64**, 1622–1626 (1978).

[2] J. D. Leatherwood and B. M. Sullivan, "Subjective loudness response to simulated sonic booms," Proceedings, High-Speed Research Workshop on Sonic Boom, NASA Langley Research Center, Hampton, Virginia, C. M. Darden, ed., Vol. I, pp. 151-170 (1992).

[3] B. Lipkens, "Experimental and theoretical study of the propagation of N waves through a turbulent medium," Ph. D. dissertation, Department of Mechanical Engineering, University of Texas at Austin (1993).

[4] R. A. Lee and J. M. Downing, "Sonic boom produced by United States Air Force and United States Navy aircraft: measured data," AL-TR-1991-0099, Armstrong Laboratory, Wright-Patterson Air Force Base, Ohio (1991).

[5] F. M. Pestorius, "Propagation of plane acoustic noise of finite amplitude," ARL Technical Report No. 73–23, Applied Research Laboratories, The University of Texas at Austin (AD 778868) (1973).

[6] Ph. Blanc–Benon, *et al.*, "Occurrence of caustics for high-frequency acoustic waves propagating through turbulent fields," *Theoret. Comput. Fluid Dynamics* (1991) 2:271–278.

[7] S. M. Candel, "Numerical solution of conservation equations arising in linear wave theory: application to aeroacoustics," *J. Fluid Mech.* **83**, 465–493 (1977).

SONIC BOOM INTERACTION WITH TURBULENCE

Zvi Rusak and Thomas E. Giddings
Department of Mechanical Engineering, Aeronautical Engineering and Mechanics
Rensselaer Polytechnic Institute, Troy, New York 12180-3590

A recently develped transonic small-disturbance model is used to analyze the interactions of random disturbances with a weak shock. The model equation has an extended form of the classic small-disturbance equation for unsteady transonic aerodynamics. It shows that diffraction effects, nonlinear steepening effects, focusing and caustic effects and random induced vorticity fluctuations interact simultaneously to determine the development of the shock wave in space and time and the pressure field behind it. A finite-difference algorithm to solve the mixed-type elliptic hyperbolic flows around the shock wave is presented. Numerical calculations of shock wave interactions with various deterministic vorticity and temperature disturbances result in complicate shock wave structures and describe peaked as well as rounded pressure signatures behind the shock front, as were recorded in experiments of sonic booms running through atmospheric turbulence.

INTRODUCTION

The review of various experimental and theoretical investigations of the interaction of shock waves and specifically sonic booms with free stream vortical or turbulent flows shows (Rusak and Cole[1]) that this complex nonlinear interaction is still an open problem. Specifically, the improved simulation of sonic boom propagation through the real atmosphere requires a better understanding of the interaction of weak shocks with vortical perturbations and turbulence.

Analysis of experimental data and theoretical approaches shows that in the case of the sonic boom, the shock waves near the ground are very weak, but still stronger than any acoustic wave. Also, flow fluctuations due to the atmospheric turbulence or vortical shear flows can become comparable to the shock weak strength such that locally the shock strength can be either strongly reduced or magnified and the shock wave front can be distorted significantly. Therefore, linearized acoustics and its second-order scattering

problem, or first-order linear theories of shock-vorticity interaction do not represent correctly the development of the weak shock and the pressure field behind it. However, in a coordinate system moving with the basic weak shock, the problem may fit the transonic framework.

In a recent paper, Rusak and Cole[1] have presented a new extended transonic small-disturbance model to describe the interactions of random fluctuations with a weak shock wave. The model equation also has an extended form of the classic nonlinear acoustics equation that describes the propagation of sound beams with narrow angular spectrum (KKZ equation)[2-3] and is similar to the model equation of Pierce[4]. The model shows that diffraction effects, nonlinear steepening effects, focusing and caustic effects and random induced vorticity fluctuations interact simultaneously to determine the development of the shock wave in space and time and the pressure field behind it.

This paper summarizes the theory of Rusak and Cole[1]. A finite-difference algorithm to solve the mixed-type elliptic hyperbolic flows around the shock wave is also presented. Numerical calculations of weak shock wave interactions with deterministic vorticity and temperature disturbances describe both peaked or rounded pressure signatures as were recorded in experiments of sonic booms running through atmospheric turbulence[5-10].

A TRANSONIC SMALL DISTURBANCE MODEL

The analysis of the linearized problem of the interaction of a weak shock with small disturbances shows[1] that it is an invalid approach when the flow perturbations are of the order of the shock strength. Therefore, a different approach has been developed to study the interaction of weak shocks with comparable random fluctuations in the flow (Rusak and Cole)[1]. In a coordinate system moving with a basic given weak shock, the problem may fit the framework of transonic theory. A transonic small-disturbance model has been developed to analyze the flow across a basic weak shock running in the (−x) direction. A coordinate system attached to the basic shock is considered. The velocity vector ($\underset{\sim}{V}$), pressure (P), density ($\bar{\rho}$) and vorticity ($\underset{\sim}{\omega}$) are described every where in the flow by:

$$\underset{\sim}{V} = U_\infty \left\{ \underset{\sim}{i}(1 + \epsilon^{2/3} u + \epsilon u_1 + \epsilon^{4/3} u_2 + \cdots) \right.$$

$$\left. + \underset{\sim}{j}\,(\epsilon v_1 + \epsilon^{4/3} v_2 + \cdots) + \underset{\sim}{k}\,(\epsilon w_1 + \epsilon^{4/3} w_2 + \cdots) \right\}$$

$$P = p_\infty (1 + \epsilon^{2/3} p + \epsilon p_1 + \epsilon^{4/3} p_2 + \cdots) \tag{1}$$

$$\bar{\rho} = \rho_\infty (1 + \epsilon^{2/3} \rho + \epsilon \rho_1 + \epsilon^{4/3} \rho_2 + \cdots)$$

$$\underset{\sim}{\omega} = \epsilon^{2/3}(\underset{\sim}{j}\omega_y + \underset{\sim}{k}\omega_z) + \epsilon\,(\underset{\sim}{i}\omega_{x1} + \underset{\sim}{j}\omega_{y1} + \underset{\sim}{k}\omega_{z1}) + \cdots$$

where $U_\infty = a_\infty(1 + K/2\ \epsilon^{2/3})$ is the speed of the basic shock ($K > 0$) and a_∞, p_∞, ρ_∞ are the speed of sound, pressure and density of the unperturbed flow ahead of the shock. ($\epsilon^{2/3}$) represents the scale of strength of the basic weak shock where $\epsilon << 1$. A rescaling of the x-coordinate and time (t) has also been considered: $x^* = x/\epsilon^{1/3}$ and $t^* = ta_\infty \epsilon^{1/3}$, such that each of the terms in (1) is a function of (x^*, y, z, t^*). The rescaling in x means a stretching of the picture of the flow around the basic shock in order to capture the basic nonlinear effects that occur in the flow across the shock. The rescaling in time accounts for low-frequency unsteady perturbations in the flow. The constant K reflects that the speed of the basic shock wave is slightly higher than the speed of sound ahead of the shock. The substitution of Eqs. (1) into the continuity, momentum and energy equations results in (Rusak and Cole[1]):

$$u + \rho = f(y,z,t^*) \tag{2a}$$

$$\gamma u + p = g(y,z,t^*) \tag{2b}$$

$$-2\frac{\partial u}{\partial t^*} + \left(-K - f + g - (\gamma+1)u\right)\frac{\partial u}{\partial x^*} + \frac{\partial v_1}{\partial y} + \frac{\partial w_1}{\partial z} = -\frac{1}{\gamma}\frac{\partial g}{\partial t^*} \tag{2c}$$

$$\omega_y = \frac{\partial u}{\partial z} - \frac{\partial w_1}{\partial x^*} = \frac{1}{\gamma}\frac{\partial g}{\partial z} \tag{2d}$$

$$-\omega_z = \frac{\partial u}{\partial y} - \frac{\partial v_1}{\partial x^*} = \frac{1}{\gamma}\frac{\partial g}{\partial y} \tag{2e}$$

where f and g are random induced fluctuations due to the free turbulence. The function g is related to the vorticity fluctuations in the flow and the function f is due to temperature or speed of sound fluctuations. Equations (2) show that the axial perturbation (u), pressure perturbation (p) and density perturbation (ρ), that are of the order of the shock strength ($\epsilon^{2/3}$), interact with the transverse velocity perturbations v_1 and w_1, that are of a smaller scale (ϵ).

The substitution of $u = g/\gamma + \bar{u}$ in (2c), (2d) and (2e) results in a problem for solving a velocity potential function $\phi(x^*, y, z, t^*)$ where:

$$\bar{u} = \frac{\partial \phi}{\partial x^*}, \quad v_1 = \frac{\partial \phi}{\partial y}, \quad w_1 = \frac{\partial \phi}{\partial z}, \quad p = -\gamma \frac{\partial \phi}{\partial x^*} \tag{3a}$$

$$2\phi_{x^*t^*} + \left[K + \frac{g}{\gamma} + f + (\gamma + 1)\phi_{x^*}\right]\phi_{x^*x^*} - (\phi_{yy} + \phi_{zz}) = -\frac{1}{\gamma}\frac{\partial g}{\partial t^*}. \tag{3b}$$

In a conservative form Eq. (3b) is given by:

$$\left[2\,\phi_{x^*} + \frac{1}{\gamma} g\right]_{t^*} + \left[(K + g/\gamma + f)\,\phi_{x^*} + (\gamma + 1)\,\phi_{x^*}^2/2\right]_{x^*} - (\phi_y)_y - (\phi_z)_z = 0. \tag{3c}$$

The exact shock jump conditions (Ref. 11) must be satisfied along any shock surface $x^* - h(y, z, t^*) = 0$ that may appear in the solution. To the leading orders, they result in:

$$[f] = 0, \qquad [g] = 0, \tag{4a}$$

$$-2\left[\phi_{x^*}\right]\frac{\partial h}{\partial t^*} + (K + \frac{g}{\gamma} + f)\left[\phi_{x^*}\right] + (\gamma + 1)\left[\frac{\phi_{x^*}^2}{2}\right] + \left[\phi_y\right]\frac{\partial h}{\partial y} + \left[\phi_z\right]\frac{\partial h}{\partial z} = 0, \tag{4b}$$

$$\left[\phi_y\right] + \left[\phi_{x^*}\right]\frac{\partial h}{\partial y} = 0, \qquad \left[\phi_z\right] + \left[\phi_{x^*}\right]\frac{\partial h}{\partial z} = 0. \tag{4c}$$

where [a] represents the jump across the shock property a, $[a] = 7_B - a_A$. Equations (4a) show that to the leading order there is no jump in entropy across the shock, [S] = 0. Equations (1) and (2) also show that the local Mach number M_ℓ at any point in the flow is given by:

$$M_\ell^2 - 1 = \epsilon^{2/3}\, u^*, \qquad u^* = \left\{(\gamma+1)\,\phi_{x^*} + K + f + \frac{g}{\gamma}\right\}. \tag{5}$$

The flow is locally supersonic when $(\gamma+1)\,\phi_{x^*} + K + f + g/\gamma > 0$, sonic when $(\gamma+1)\,\phi_{x^*} + K + f + g/\gamma = 0$, and subsonic when $(\gamma+1)\,\phi_{x^*} + K + f + g/\gamma < 0$. Equations (3) and (4) are an extended version of the classic small-disturbance equation for unsteady transonic aerodynamics (Cole and Cook[12]). The changes are due to the random terms g and f. Starting from given functions for f and g and initial conditions that describe a given basic shock, Eqs. (3) and (4) can be integrated in space and time to describe the development of the shock wave and pressure field behind it.

An alternative approach has also been found by taking an x*-derivative of (2c) and using Eq. (2a). The pressure perturbation (p) satisfies the equation:

$$\frac{\partial}{\partial x^*}\left[\frac{\partial p}{\partial t^*} + \frac{K + f + g/\gamma}{2} - \frac{\gamma+1}{2\gamma}\, p\, \frac{\partial p}{\partial x^*}\right] = \frac{1}{2}\left[\frac{\partial^2 p}{\partial y^2} + \frac{\partial^2 p}{\partial z^2}\right]. \tag{6}$$

Equation (6) is an extended version of the classic KKZ equation that describes the propagation of nonlinear sound beams with narrow angular spectrum in an inviscid fluid (Zabolotskaya et al.[2], Kuznetsov[3]). Equation (6) also has a similar form to the model equation that has been recently developed by Pierce[4] using logical considerations only.

Equations (3) and (6) show that diffraction effects, nonlinear steepening, focusing and caustic effects, and random induced fluctuations due to turbulence interact simultaneously to determine the development of the shock wave in space and time and the pressure field behind it. Turbulence tends to change the local speed of sound in the flow across the shock and through this effect to reduce or to magnify the strength of the jump along the basic shock (see Eq. (5)) or to distort the shock front. These changes may result in unsteady motion of the shock front or in caustic vertices or in reflected shocks behind the incident wave that can produce the variety of pressure signatures of sonic booms that are measured in experiments[5-10].

FINITE DIFFERENCE SCHEME

A finite difference algorithm to solve the unsteady mixed-type elliptic-hyperbolic flow around the shock wave has been developed. Murman and Cole[13] and Cole and Cook[12] techniques are used. A fully conservative scheme that is based on the conservative form of Eq. (3c) is derived. In this way the difference equations also contain the shock relations (Eqs. (4)).

Consider a uniform finite difference mesh (Δx^*, Δy, Δz, Δt^*) in space and time, with points (x^*, y, z, t^*) labeled by (i, j, k, n). The results can be easily generalized to a variable mesh. Equation (3c) can be expressed in a conservative flux form for a box centered on a mesh point (i, j, k). Therefore,

$$\frac{1}{\Delta t^*}\left\{\left(2\phi_{x^*}+\frac{1}{\gamma}g\right)_{(i,j,k,n)}-\left(2\phi_{x^*}+\frac{1}{\gamma}g\right)_{(i,j,k,n-1)}\right\}$$

$$+\frac{1}{\Delta x^*}\left\{\left(\left(K+\frac{1}{\gamma}g+f\right)\phi_{x^*}+(\gamma+1)\,\phi_{x^*}^2/2\right)_{(i+1/2,j,k,n)}\right.$$

$$\left.-\left(\left(K+\frac{1}{\gamma}g+f\right)\phi_{x^*}+(\gamma+1)\,\phi_{x^*}^2/2\right)_{(i-1/2,j,k,n)}\right.$$

$$-\frac{1}{\Delta y}\left\{(\Phi_y)_{(i,j+1/2,k,n)}-(\phi_y)_{(i,j-1/2,k,n)}\right\}$$

$$-\frac{1}{\Delta z}\left\{(\Phi_z)_{(i,j,k+1/2,n)}-(\phi_z)_{(i,j,k-1/2,n)}\right\}=0. \qquad (7)$$

In Eq. (7), (ϕ_y) and (ϕ_z) are always calculated from a centered expression. However, the approximation of (ϕ_{x^*}) strongly depends on whether locally, at a point, the flow is subsonic, supersonic, sonic or if it is a shock point. Extending References 12 and 13 methodologies to our case and using Eq. (5), a centered approximation and a backward expression are given for u^*:

$$u^{*c}_{(i,j,k,n)} = K + f(j,k,n) + \frac{1}{\gamma} g(j,k,n)$$

$$+ \frac{\gamma+1}{2\Delta x^*} \left(\phi(i+1,j,k,n) - \phi(i-1,j,k,n) \right)$$

$$u^{*b}_{(i,j,k,n)} = K + f(j,k,n) + \frac{1}{\gamma} g(j,k,n)$$

$$+ \frac{\gamma+1}{2\Delta x^*} \left(\phi(i,j,k,n) - \phi(i-2,j,k,n) \right). \qquad (8)$$

The local type of the flow is determined by the following table:[12,13]

condition	u^{*c}	u^{*b}	local flow is
1	< 0	< 0	subsonic
2	> 0	> 0	supersonic
3	> 0	< 0	a sonic point
4	< 0	> 0	a shock point

Table 1. Algorithm for local type of flow

Equation (7) has been developed in a specific form according to the local type of the flow. The variety of difference forms for locally subsonic, supersonic, sonic or shock points are described in Rusak and Cole.[1]

Starting from initial conditions that describe a given shock wave in the space for $t = 0$ (or $n = 0$), and given temperature fluctuations $f(y,z,t)$ and vorticity perturbations $g(y,z,t)$, the various difference forms can be applied for $n = 1$ at any mesh point according to Table 1. They can be solved by an iterative point or line – or plane – relaxation algorithm until at any point max $|G(i,j,k,1)| < \delta$ where δ is a given small tolerance of convergence. Then $\phi_{x^*}(i,j,k,1)$ can be calculated at any mesh point and the process is restarted for the next time step. In this way the shock motion and pressure field behind it can be integrated in space and time and the effect of various deterministic and random fluctuations f and g can be studied.

NUMERICAL RESULTS

The finite difference algorithm to solve Eq. (3b) has been applied to a variety of two-dimensional and steady shock wave interactions with vorticity and temperature disturbances. Several problems have been studied where a nominal shock wave with $K = 1.2$ centered in the middle of the computational domain has been considered. The following boundary conditions were used: $\phi_{x^*} = 0$ along inlet surface, $\phi_{x^*} = -1.0$ along outlet surface (which satisfy the basic shock jump relations) and $\phi_{y^*} = 0$ along upper and lower surfaces.

The first case considered vorticity fluctuations only where $f = 0$ and

$$g(y) = \begin{cases} 0 & 0 \leq y \leq 1/4 \\ 0.5 \sin 4\pi(y - 1/4) & 1/4 \leq y \leq 3/4 \\ 0 & 3/4 \leq y \leq 1 \, . \end{cases} \tag{9}$$

Calculated pressure fields and profiles along various cross sections are shown in Figures 1 and 2. The bending of the shocks is in phase with the velocity perturbations (i.e., a positive velocity perturbation produces a downstream deflection and visa versa) as was also described by Ribner[14]. Relative to nominal shock conditions (Figure 2a), the pressure jump decreases noticeably (approximately 40%) where the shock is bent upstream (Figure 2b), and increases significantly (approximately 40%) where the shock is distorted downstream (Figure 2d). The rippled wavefront leads to focusing and defocusing effects behind the shock, where diffraction effects also become dominant.

In the second case only temperature disturbances have been considered where $g = 0$ and

$$f(y) = \begin{cases} 0 & 0 \leq y \leq 1/4 \\ 0.5 \sin 16\pi(y - 1/4) & 1/4 \leq y \leq 3/4 \\ 0 & 3/4 \leq y \leq 1 \, . \end{cases} \tag{10}$$

Pressure fields and profiles along cross sections are presented in Figures 3 and 4. Again, shock wave distortion results in significant local pressure jump reductions and increases

(see Figures 4b and c). Basic effects involved are similar to those described in the first case. Temperature or speed of sound disturbances strongly affect the basic shock as much as vorticity disturbances.

The third case combined shock wave interaction with both vorticity and temperature disturbances as are given by Eqs. (9) and (10), respectively. Calculated results are shown in Figures 5 and 6. The shock front distortion is more pronounced and composed of the basic two harmonics of the imposed disturbances. It is found that shock pressure jump at certain locations is nearly eliminated due to the combined effects, resulting in a rounded pressure profile (Figure 6b). At other locations along the shock front, the pressure jump is significantly increased relative to the nominal shock jump with approximately 70% (see Figure 6c).

CONCLUSIONS

A new transonic small-disturbance model has been developed where a rescaling of the axial coordinate and time has been considered to capture the basic nonlinear effects that occur in the flow across the shock. This model results in two alternative approaches: (1) an equation for solving a velocity potential function that is described by an extended version of the classic small-disturbance equation for unsteady transonic aerodynamics[12], and (2) a nonlinear stochastic equation to describe the pressure field that is similar to the model equation recently presented by Pierce[4] using logical considerations only. This equation also has an extended form of the classic equation that describes the propagation of nonlinear sound beams with narrow angular spectrum[2,3].

Both approaches show that diffraction effects, nonlinear steepening, focusing and caustic effects and random induced turbulence fluctuations interact simultaneously to determine the development of a shock wave in space and time and the pressure field behind it. Turbulence fluctuations tend to change the local speed of sound in the flow across the shock and through this effect to reduce or magnify the strength of the basic shock.

A finite difference scheme that uses Murman and Cole[13] finite-difference techniques for solving mixed-typed elliptic hyperbolic flows with shock waves has also been presented. Numerical simulations of two-dimensional and steady shock wave interactions with various deterministic vorticity and temperature disturbances have been shown. Results describe

complicate shock wave structures and peaks as well as rounded local pressure signatures behind the distorted shock fronts. Similar signatures were recorded in the experiments of sonic booms running through atmospheric turbulence[5-10].

ACKNOWLEDGEMENT

This work was carried out with the support of the NASA Langley Research Center under Award NAG-1-1362 and NASA Training Grant NGT-S1113. The authors would like to acknowledge Dr. G.L. McAninch for funding and monitoring this research.

REFERENCES

1. Rusak, Z. and Cole, J.D., "Interaction of the Sonic Boom with Atmospheric Turbulence," NASA CP 10132, May 1993, pp. 65-91. (Also: AIAA Paper 93-1943).

2. Zabolotskaya, E.A. and Khorkhlov, R.V., *Akust. Zhurnal* 15, 1, 1969, pp. 40.

3. Kuznetsov, V.O., *Akust. Zhurnal* 6, 4, 1970, pp. 548.

4. Pierce, A.D., "Wave Equations and Computational Models for Sonic Boom Propagation Through a Turbulent Atmosphere," NASA CP-3172, February 1992, pp. 31-48.

5. Hubbard, H.H., Maglieri, D.J., Huckel, V. and Hilton, D.A., "Ground Measurements of Sonic Boom Pressures for the Altitude Range of 10,000 to 75,000 Feet," NASA TR R-198, July 1964.

6. Maglieri, D.J., "Sonic Boom Flight Research – Some Effects of Airplane Operations and the Atmosphere on Sonic Boom Signatures," in *Sonic Boom Research,* Edited by Seebass, A.R., NASA SP-147, April 1967.

7. Garrick, I.E. and Maglieri, D.J., "A Summary of Results on Sonic Boom Pressure-Signature Variations Associated with Atmospheric Conditions," NASA TN D-4588, May 1968.

8. Downing, M.J., "Lateral Spread of Sonic Boom Measurements from U.S. Air Force Boomfile Flight Tests," NASA CP-3172, February 1992, pp 117-135.

9. Willshire, Jr., W.L. and Devilbiss, D.W., "Preliminary Results from the White Sands Missile Range Sonic Boom Propagation Experiments," NASA CP-3172, February 1992, pp. 137-149.

10. Lipkens, B. and Blackstock, T.T., "Model Experiment to Study the Effect of Turbulence on Risetime and Waveform of N Waves," NASA CP-3172, February 1992, pp. 97-107.

11. Courant, R. and Friedrichs, K.O., *Supersonic Flow and Shock Waves,* Interscience Publishers, Inc., New York, pp. 297-302, 1948.

12. Cole, J.D. and Cook, L.P., *Transonic Aerodynamics,* North-Holland, 1986.

13. Murman, E.M. and Cole, J.D., "Calculation of Plane Steady Transonic Flows," *AIAA Journal,* Vol. 9, pp. 114-121.

14. Ribner, H.S., "Cylindrical Sound Wave Generated by Shock-Vortex Interaction," *AIAA Journal,* Vol. 23, No. 11, 1985, pp. 1708-1715.

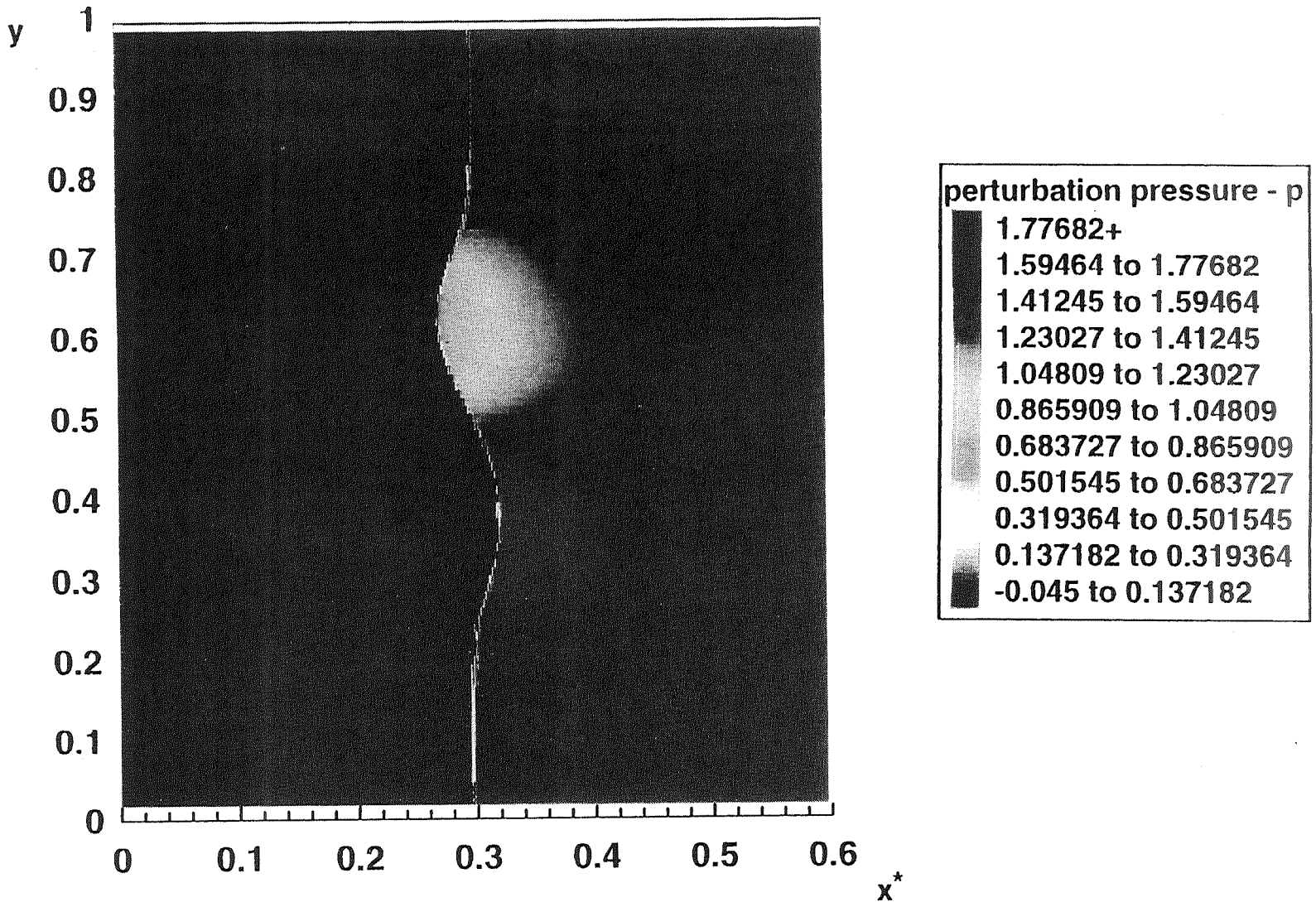

Figure 1. Pressure field for vorticity fluctuations (9).

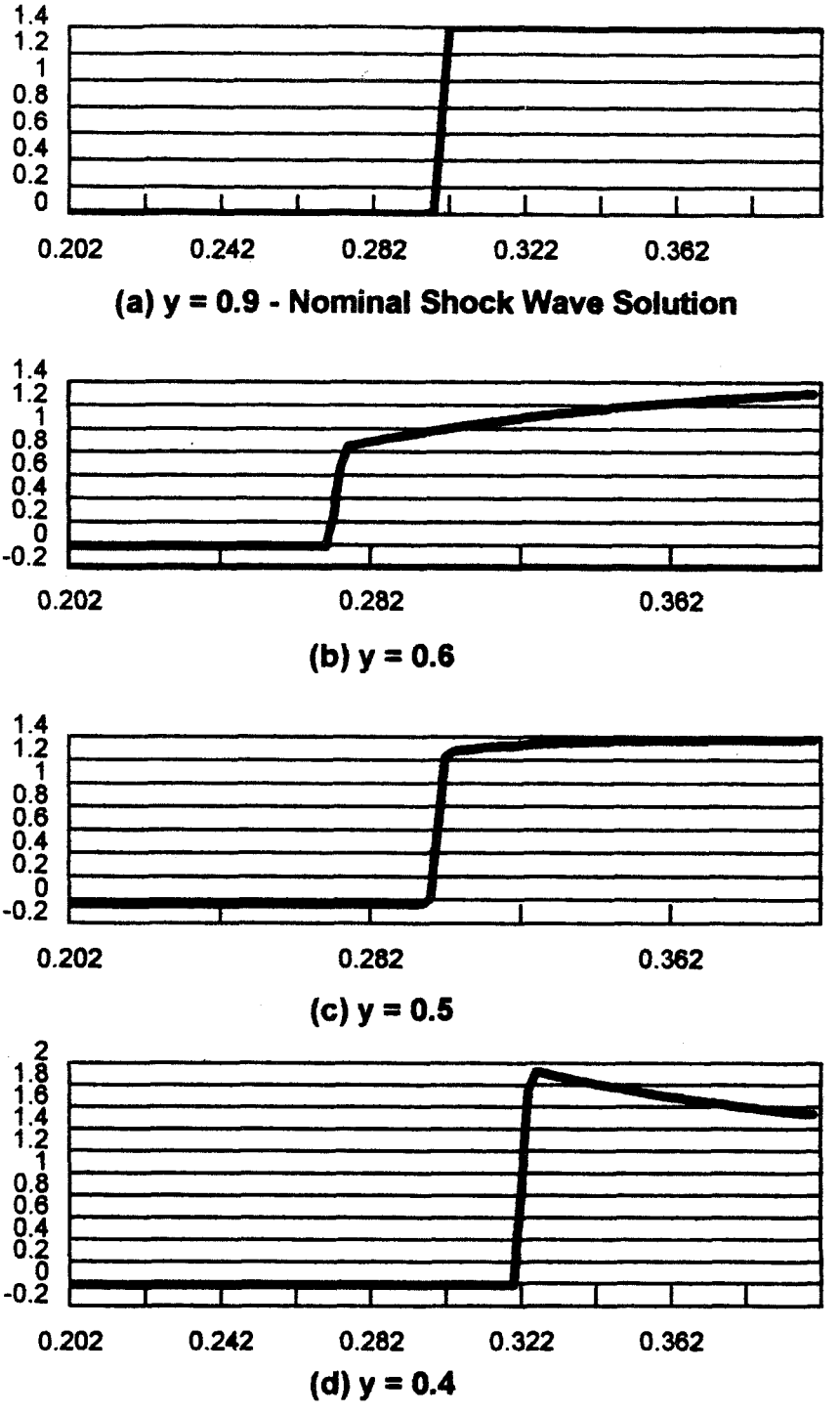

Figure 2. Pressure profiles along various cross sections for vorticity fluctuations (9).

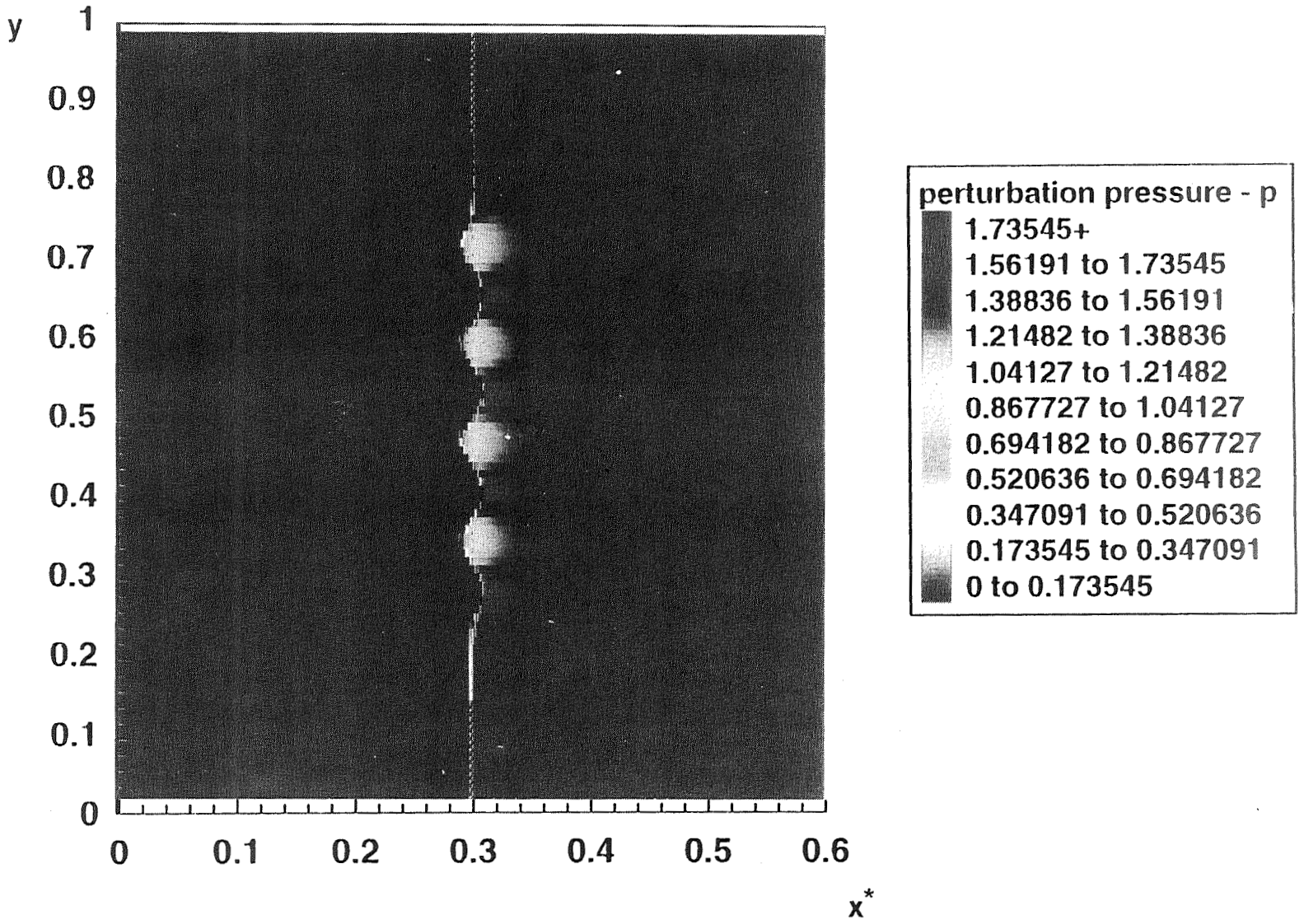

Figure 3. Pressure field for temperature disturbances (10).

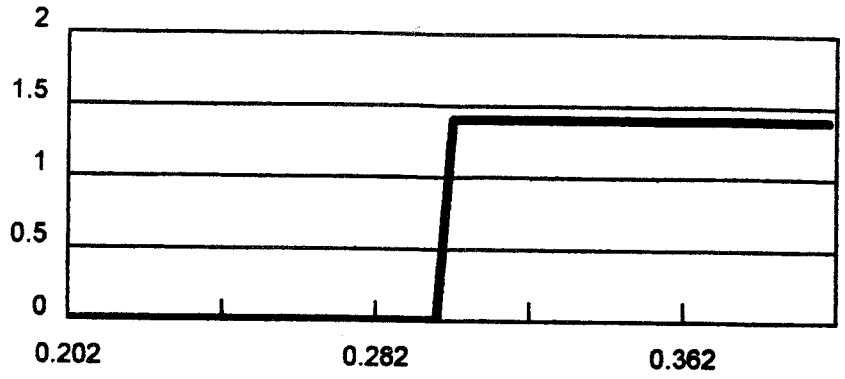

(a) y = 0.9 - Nominal Shock Wave Solution

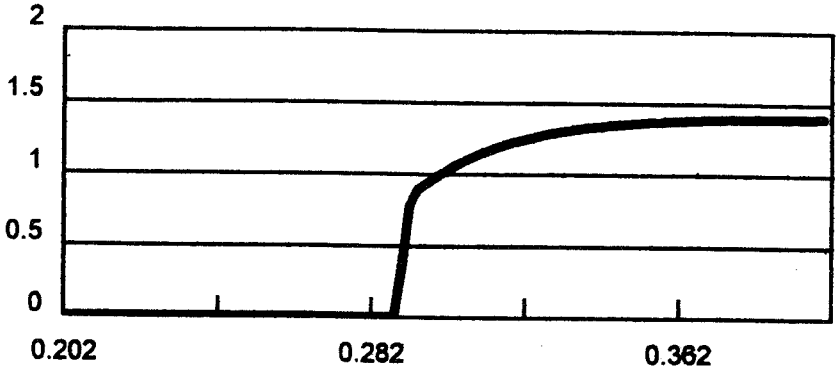

(b) y = 0.6

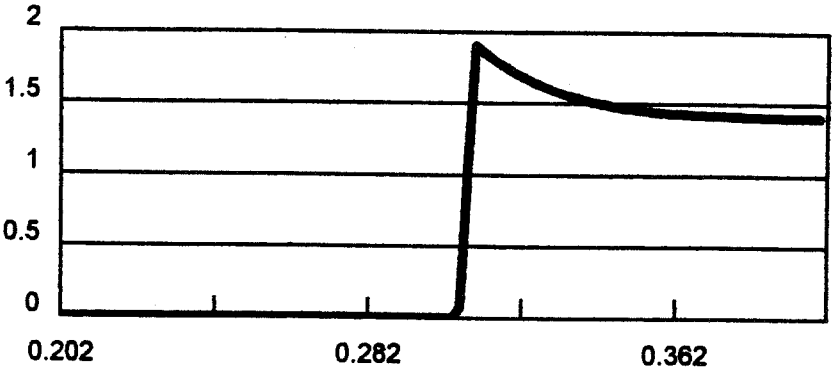

(c) y = 0.41

Figure 4. Pressure profiles along various cross sections for temperature disturbances (10).

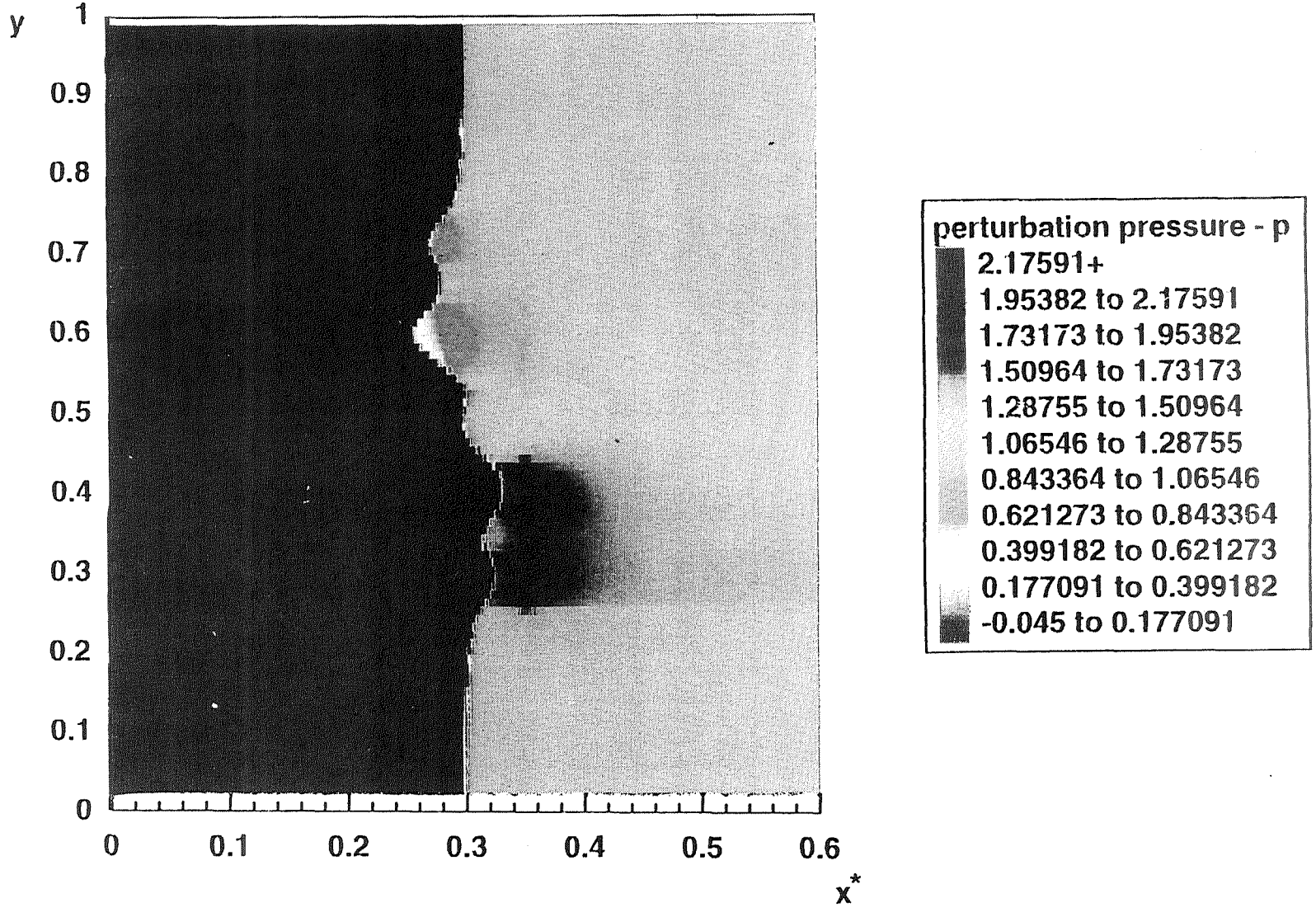

Figure 5. Pressure field for combined vorticity and temperature disturbances.

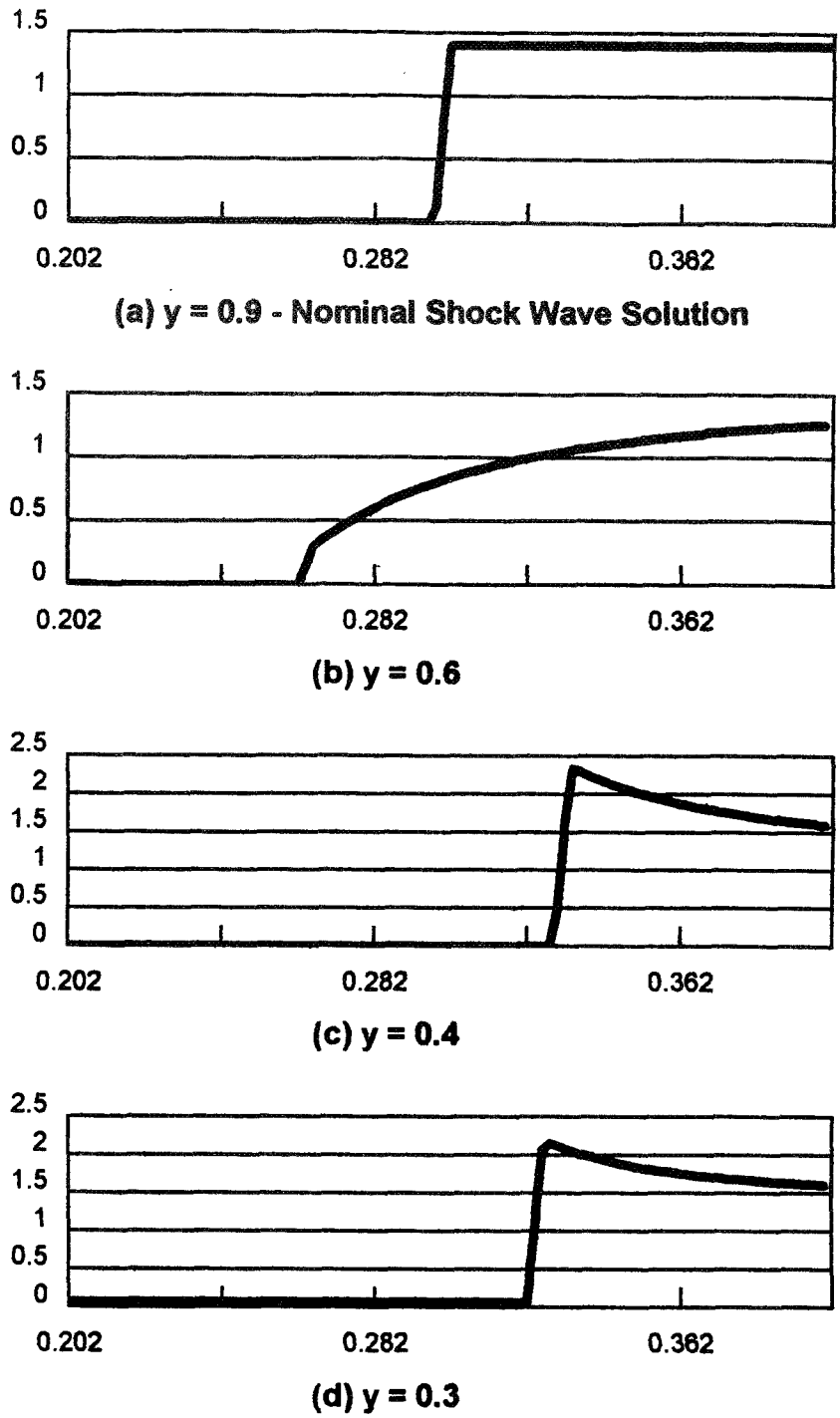

Figure 6. Pressure profiles along various cross sections for combined disturbances.

ATMOSPHERIC PROPAGATION AT LARGER LATERAL DISTANCES FROM THE FLIGHT TRACK

Allan D. Pierce
Department of Aerospace and Mechanical Engineering
Boston University
110 Cummington Street
Boston, MA 02215

INTRODUCTION

Sonic booms received on the ground tend to be restricted to a region of finite lateral extent below the flight track. This occurs because of refraction and because the effective speed of sound, even with winds taken into account, decreases with altitude in the lower atmosphere. Not all rays proceeding initially downwards from the flight track within an allowable range of initial directions will reach the ground. The restricted region which can be reached by rays impacting the ground is known as the primary carpet. However, weak rumbles are heard in the nominal shadow zone beyond the edge of this carpet. A full wave theory is necessary for explaining waveforms in that region, and the present paper gives a matched asymptotic expansion technique for a suitable approximate full wave theory that involves a relatively small number of parameters. The outer solution is derived from the structure of the system of rays that impact near the corridor edge; the inner solution involves a solution of the parabolic equation and results in the special functions encountered in the diffraction of sound over the tops of hills. (Work supported by Armstrong Aerospace Medical Research Laboratory, Human Systems Division (AFSC), United States Air Force, Wright-Patterson AFB, Ohio 45433-6573.)

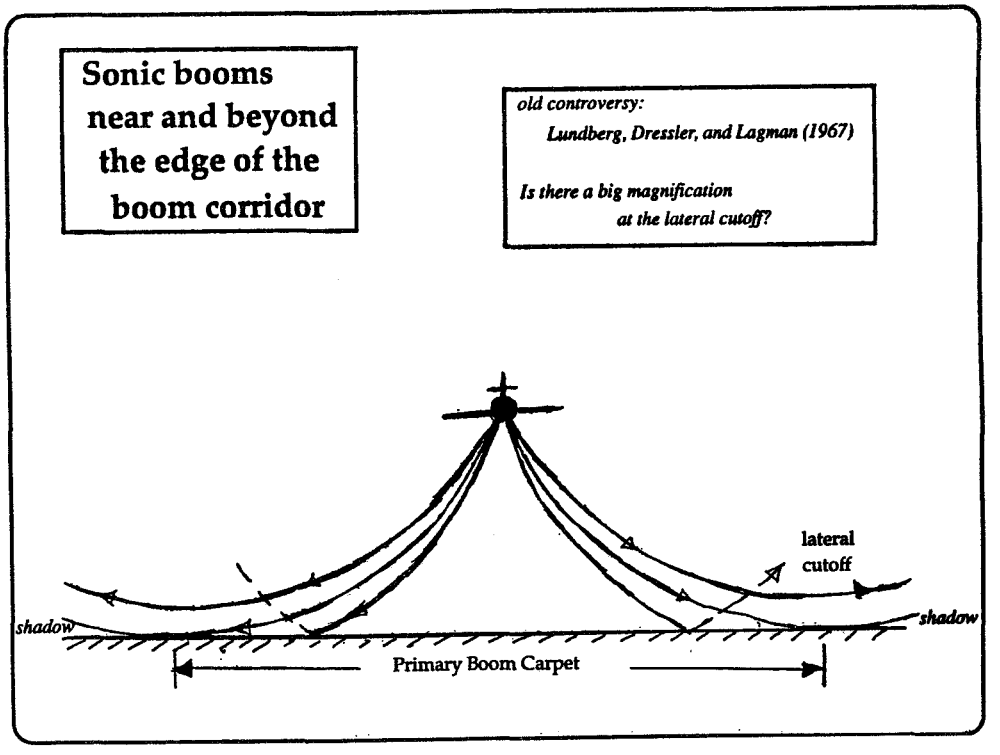

RAYS UNDER INFLUENCE OF LINEAR SOUND SPEED GRADIENT

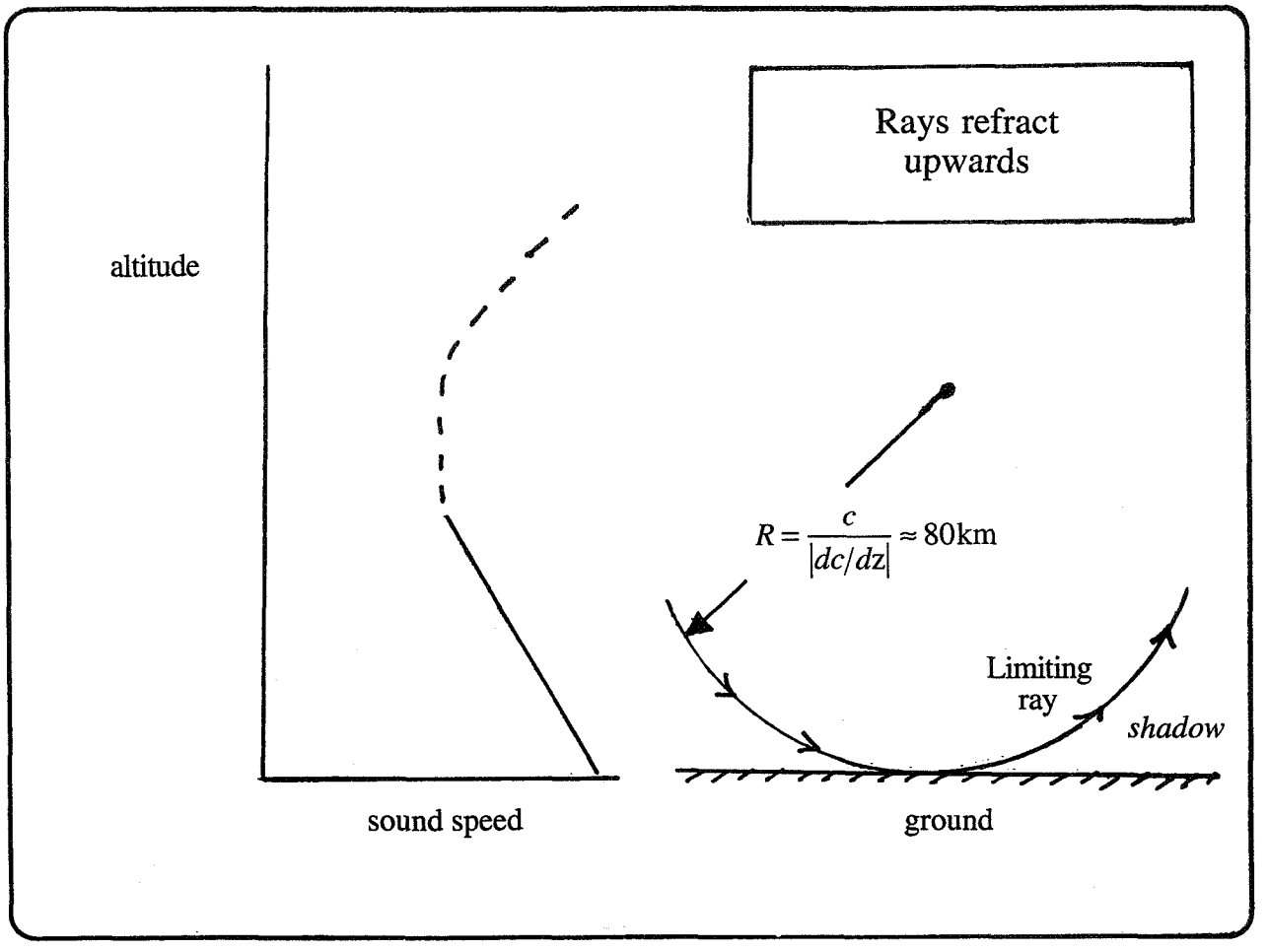

LIMITING RAYS FROM ABOVE

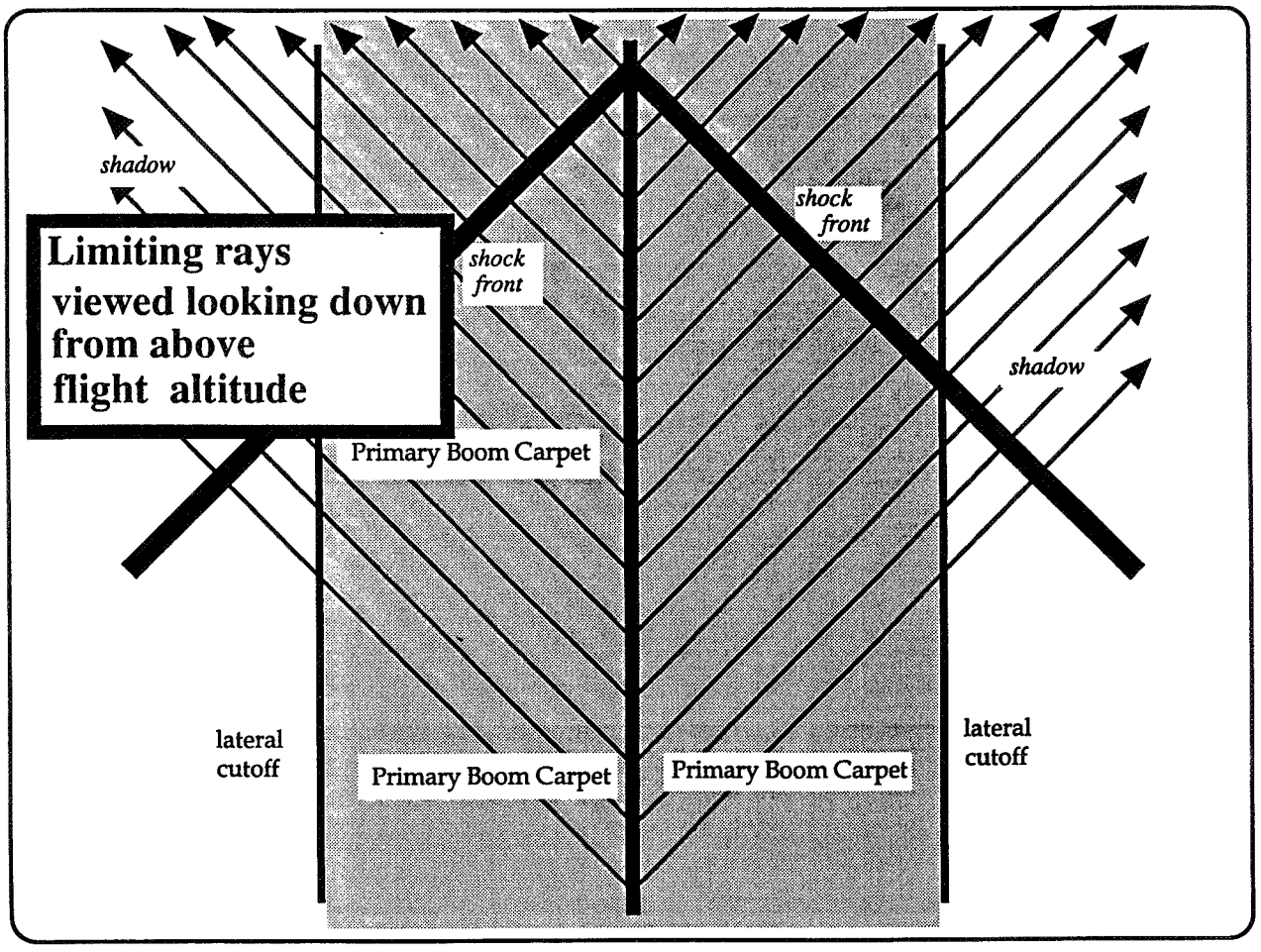

DETERMINATION OF ANGLE WITH CARPET EDGE

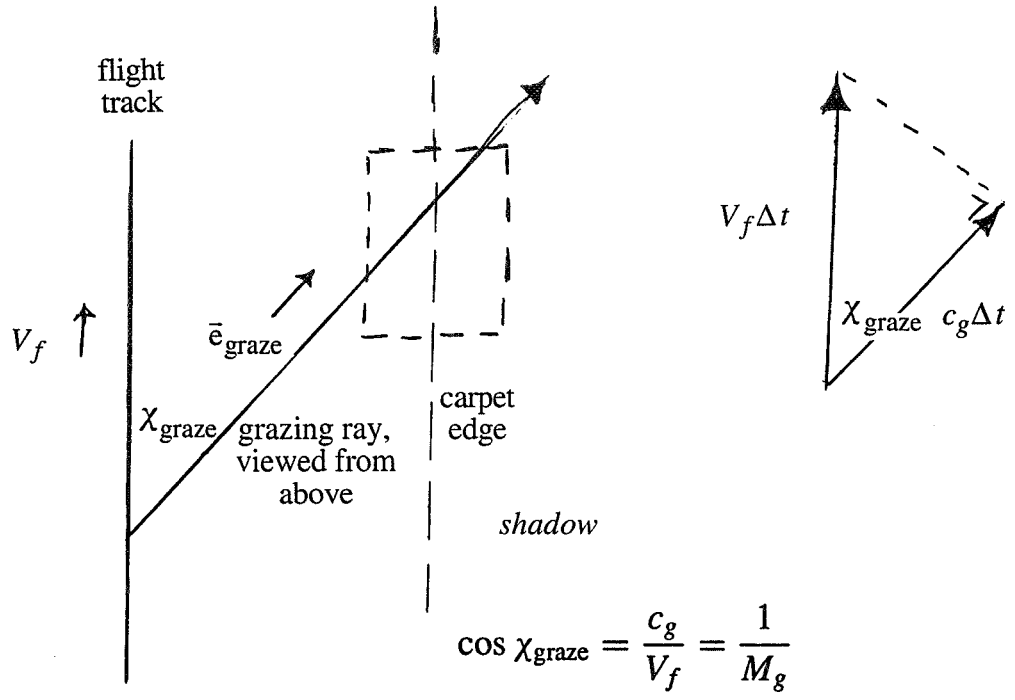

$$\cos \chi_{graze} = \frac{c_g}{V_f} = \frac{1}{M_g}$$

M_g = flight Mach number relative to sound speed at ground

DETERMINATION OF EFFECTIVE SOUND SPEED

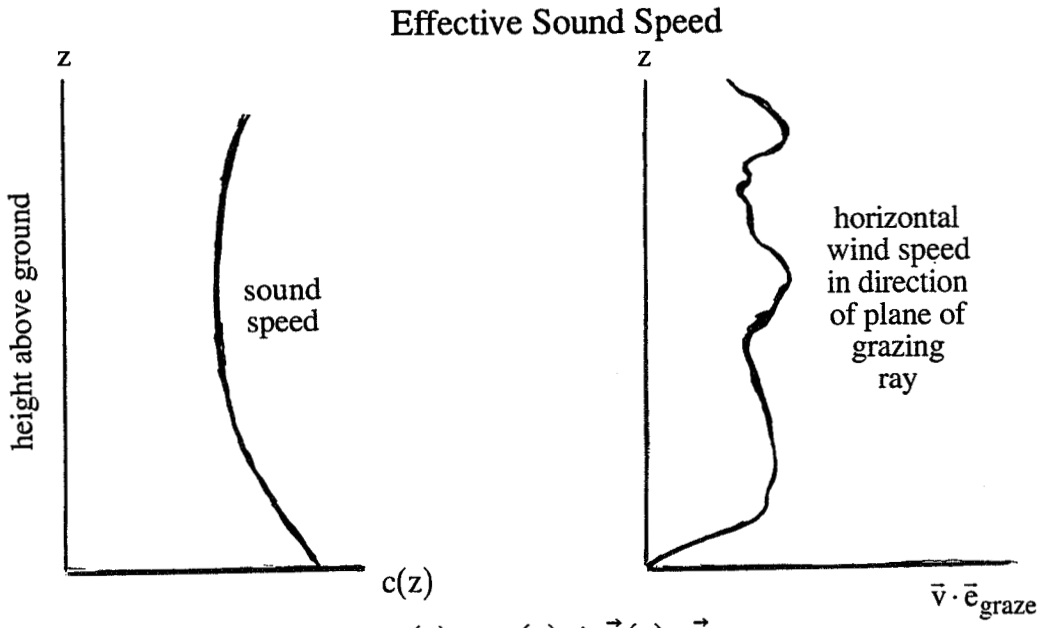

$$c_{eff}(z) = c(z) + \vec{v}(z) \cdot \vec{e}_{graze}$$

$\vec{v}(z) \cdot \vec{e}_{graze}$ = horizontal wind component in direction of grazing ray

APPARENT TOP OF ATMOSPHERE

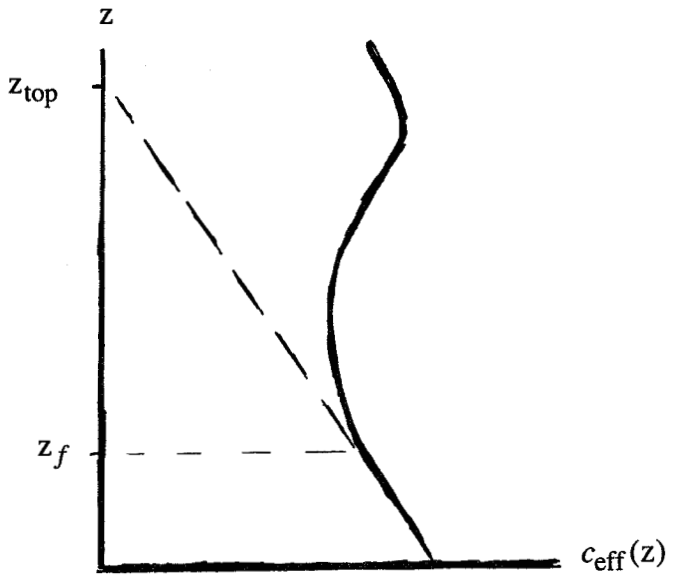

z_{top} = height of apparent top of atmosphere,
based on linear extrapolation of sound speed
beyond flight altitude

For US Standard Atmosphere without winds:

$$z_{top} = 88.4\,\text{km}$$

Radius of curvature of the grazing ray

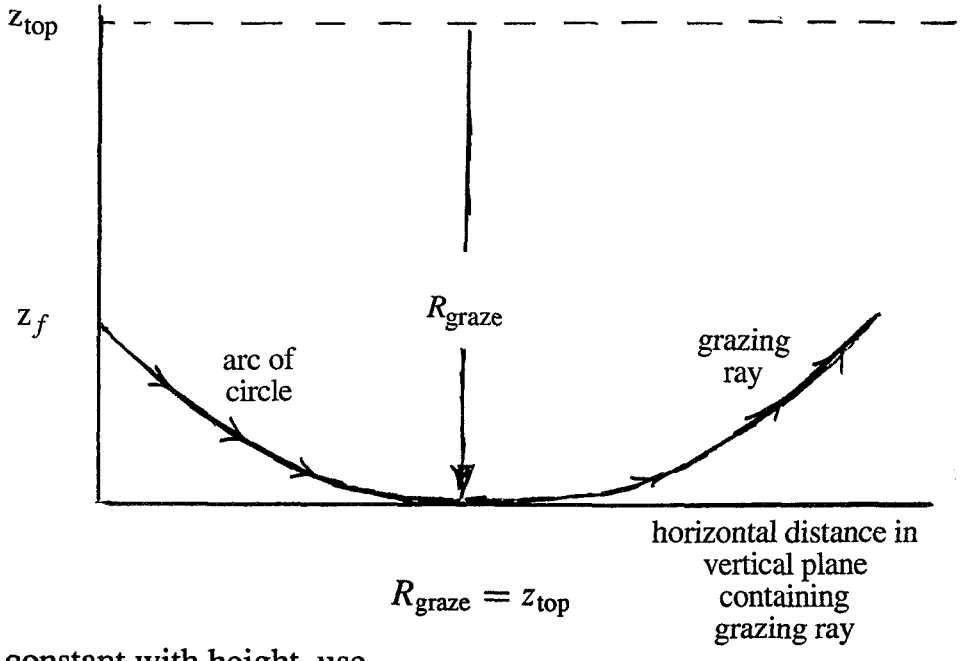

$$R_{graze} = z_{top}$$

If dc/dz not constant with height, use

$$R_{graze} = \frac{4c_g}{z_f}\left[\int_0^{z_f} \frac{dz}{(c_g - c)^{1/2}}\right]^2$$

DETERMINATION OF CARPET HALF-WIDTH

Half-width of primary carpet:

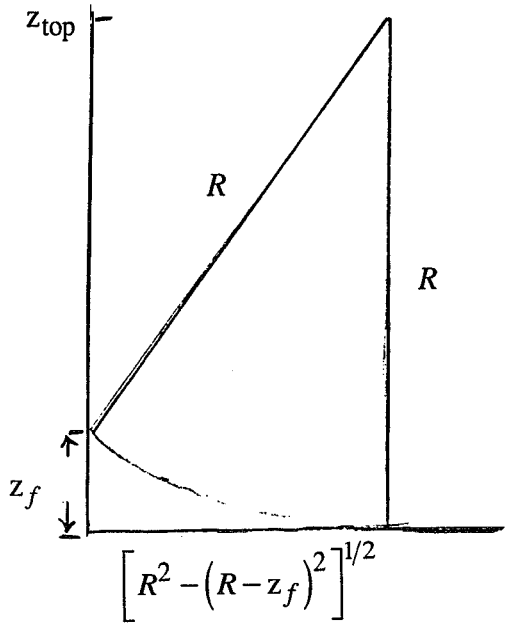

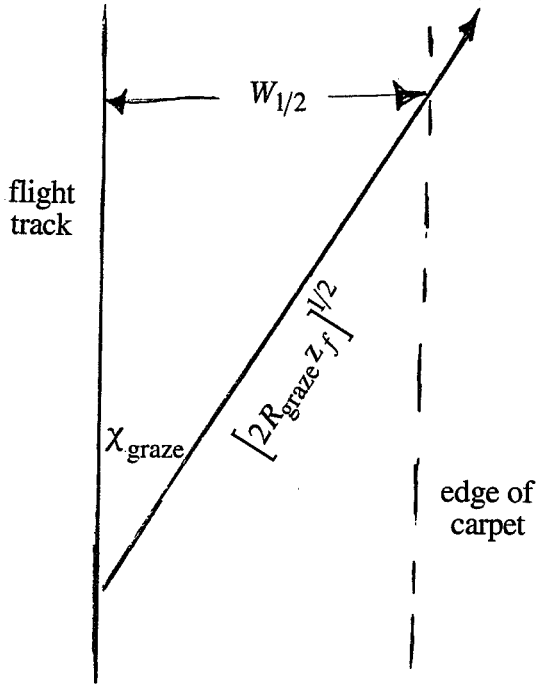

$$\text{half-width} = [2R_{graze}z_f]^{1/2} \sin \chi_{graze}$$

$$\sin \chi_{graze} = \left[1 - (1/M_g)^2\right]^{1/2}$$

THEORETICAL PREDICTION OF RAY TUBE AREA

Ray-tube area at ground:

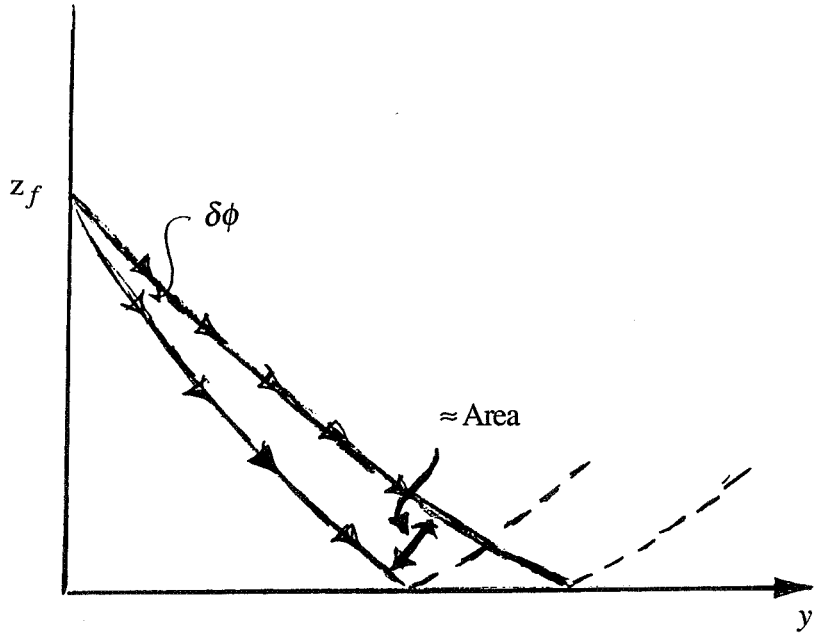

$$\text{Area} = (\text{constant})[y^2 + z_f^2]^{1/2}\delta\phi$$

just as if rays were spreading cylindrically

Result is for limiting case of high Mach number; no significant difference is expected at moderate Mach number.

Concept of a transition region:

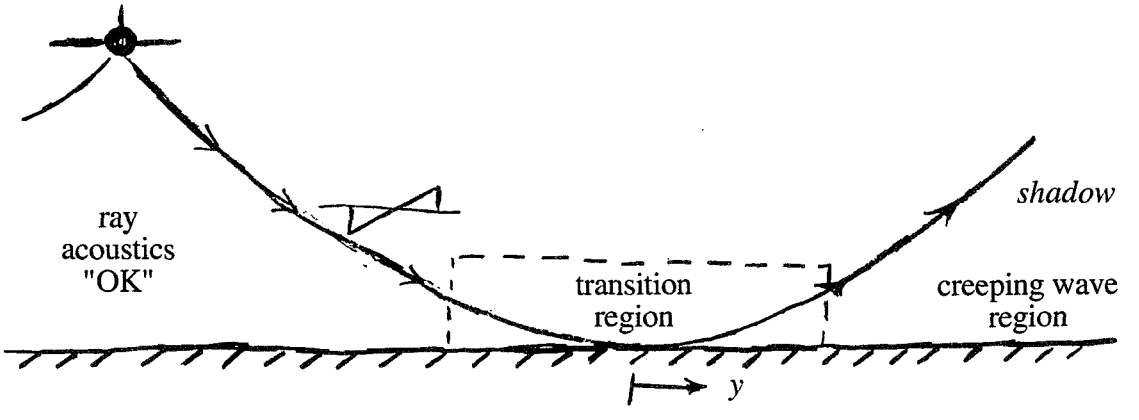

Region near the ground and centered at edge of primary carpet, within which ray acoustics is not valid

Converse of Earth-flattening approximation:

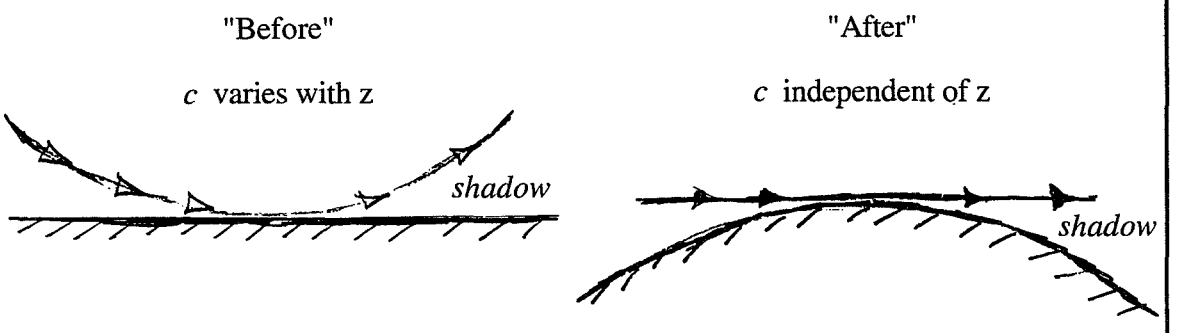

- Use a set of curvilinear coordinates where grazing ray appears straight, but ground appears curved
  - Edge of primary carpet becomes line on top of cylinder
  - Grazing ray becomes horizontal straight line
  - Crosses the top of cylinder at oblique incidence with angle χ_{graze}

DIFFRACTION BY A CYLINDER

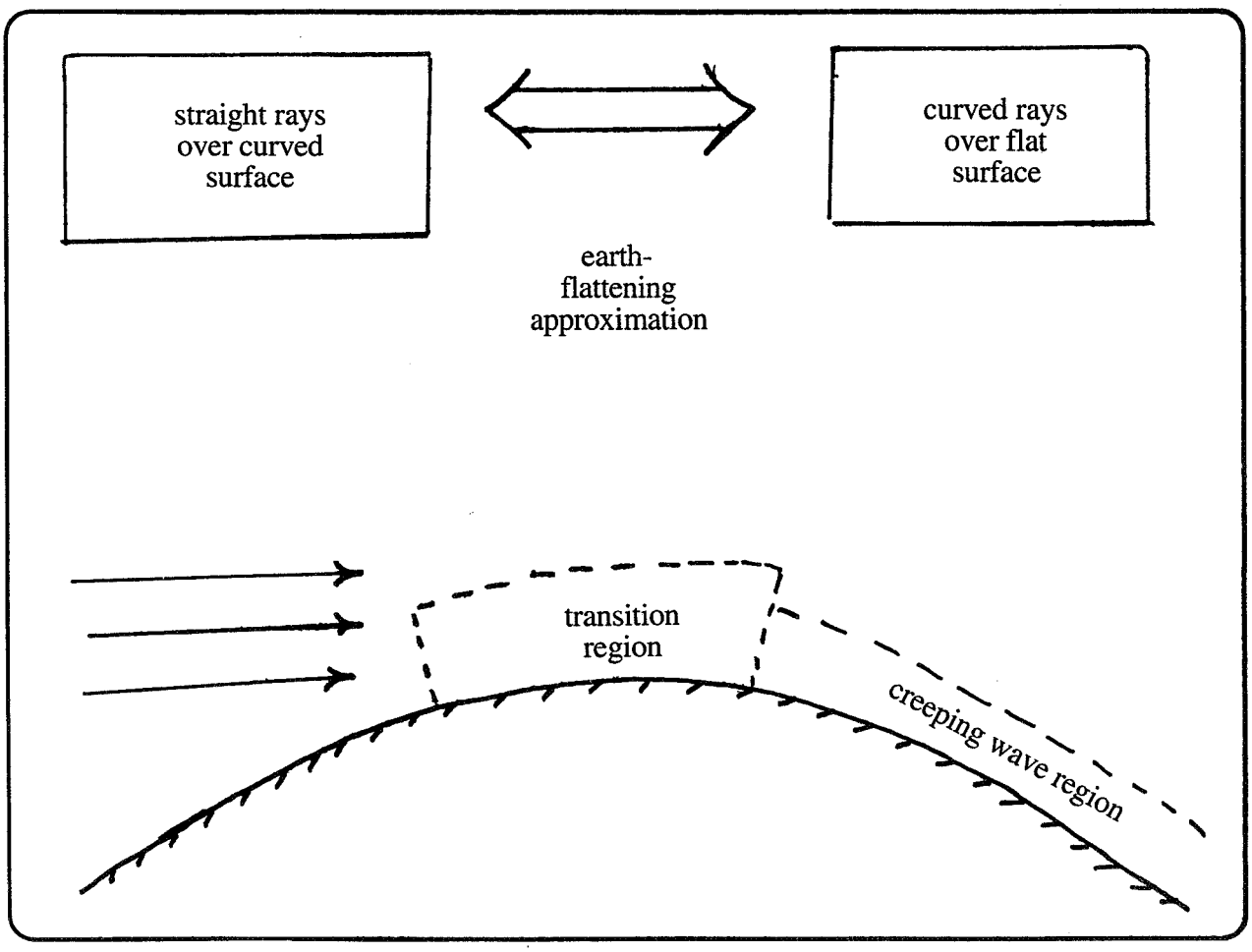

Cylinder radius of curvature:

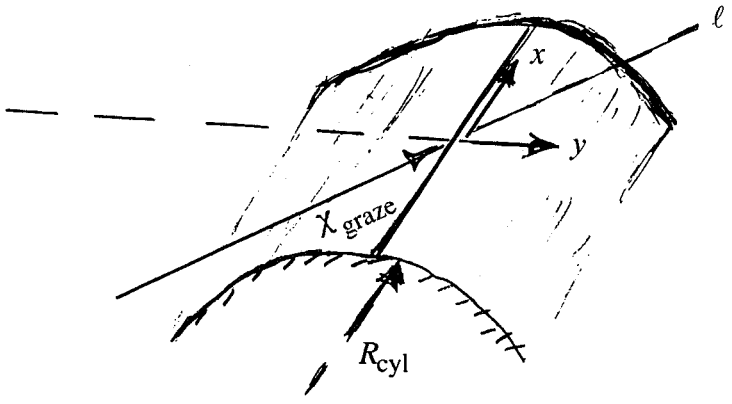

- Grazing-ray's path: $x = \ell \cos \chi_{\text{graze}}, \quad y = \ell \sin \chi_{\text{graze}}$
- Distance of ray above ground:

$$\Delta z = \frac{y^2}{2R_{\text{cyl}}} = \frac{\ell^2}{2R_{\text{graze}}}$$

- Conclude that

$$R_{\text{cyl}} = R_{\text{graze}} \sin^2 \chi_{\text{graze}}$$

Plane wave obliquely incident on a cylinder:

- Trace velocity matching principle:

$$p = p(t - [x/V_f], y, z)$$

$$\frac{\partial}{\partial x} \rightarrow \frac{1}{V_f}\frac{\partial}{\partial t}$$

- Wave equation:

$$\frac{\partial^2 p}{\partial y^2} + \frac{\partial^2 p}{\partial z^2} - \left(\frac{1}{c^2} - \frac{1}{V_f^2}\right)\frac{\partial^2 p}{\partial t^2} = 0$$

Results for normal incidence apply with transformation

$$\frac{1}{c^2} \rightarrow \quad \frac{1}{c^2} - \frac{1}{V_f^2} \quad = \quad \frac{1}{c^2}\sin^2 \chi_{\text{graze}}$$

Waveform going into transition region:

- Use N-wave of form

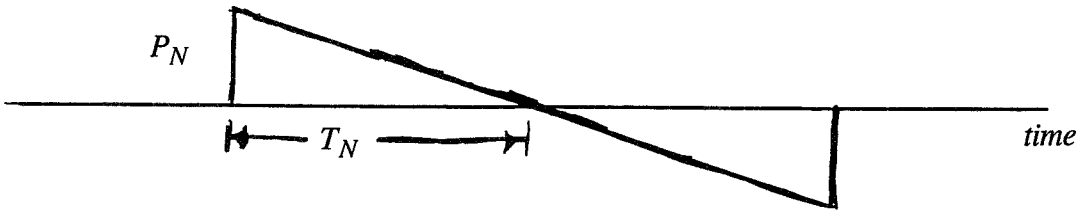

P_N = peak amplitude of N-wave
T_N = positive phase duration of N-wave

- Determine P_N and T_N by extrapolation of waveform received on the ground within the primary carpet, taking into account
  - Pressure doubling on reflection at ground
  - Geometrical spreading along ray tubes
  - Lengthening with propagation distance of T_N due to non-linear effect
  - Extra decrease of P_N with propagation distance due to non-linear effect

Fourier transform solution:

- Let incident plane wave be of the form:

$$p_{\text{inc}} = P_N f_N(\tau/T_N)$$

$$\tau = t - [y/c]\sin\chi_{\text{graze}} - [x/c]\cos\chi_{\text{graze}}$$

$$f_N(\tau/T_N) = \int_{-\infty}^{\infty} e^{-i\omega\tau}\hat{f}_N(\omega T_N)T_N d\omega$$

- Then the total solution is of the form

$$p = P_N T_N \int_{-\infty}^{\infty} e^{-i\omega(t-[x/V_f])}\hat{f}_N(\omega T_N)\text{TF}(y, z, \omega)d\omega$$

- where the transfer function TF satisfies

$$\frac{\partial^2 \text{TF}}{\partial y^2} + \frac{\partial^2 \text{TF}}{\partial z^2} + \frac{\omega^2}{c^2}\sin^2\chi_{\text{graze}}\text{TF} = 0$$

For points on the ground:

- The transfer function is given by

$$\mathrm{TF}(y, z, \omega) = e^{i[\omega/c]y \sin \chi_{\mathrm{graze}}} \quad G(\xi, 0, q)$$

$$G(\xi, 0, q) = \pi^{-1/2} \int_{-\infty}^{\infty} \frac{e^{i\alpha\xi}}{w_1'(\alpha) - q\, w_1(\alpha)} d\alpha$$

$$w_1(\alpha) = 2\pi^{1/2} e^{i\pi/6} \mathrm{Ai}(\alpha e^{i2\pi/3})$$

$$\xi = y/[2^{1/3} L_\omega]; \quad q = i(\omega c^{-1} R_{\mathrm{cyl}} \sin \chi_{\mathrm{graze}})^{1/3} \rho c / Z_S$$

$$L_\omega = \frac{R_{\mathrm{cyl}}^{2/3}}{(\omega c^{-1} \sin \chi_{\mathrm{graze}})^{1/3}} = \frac{R_{\mathrm{graze}}^{2/3} \sin \chi_{\mathrm{graze}}}{(\omega c^{-1})^{1/3}}$$

- Recall that

$$R_{\mathrm{cyl}} = R_{\mathrm{graze}} \sin^2 \chi_{\mathrm{graze}}$$

Hard ground limit:

- Transmitted pressure reduces to

$$p = P_N T_N \int_{-\infty}^{\infty} e^{-i\omega T_N \{\tau/T_N\}} \hat{f}_N(\omega T_N) G(\xi, 0, 0) d\omega$$

$$\tau = t - [y/c] \sin \chi_{\text{graze}} - [x/c] \cos \chi_{\text{graze}}$$

$$G(\xi, 0, 0) = \pi^{-1/2} \int_{-\infty}^{\infty} \frac{e^{i\alpha\xi}}{w_1'(\alpha)} d\alpha$$

$$\xi = (y/L_{\text{tran}})(\omega T_N)^{1/3}$$

- Characteristic length for N-wave deterioration through and beyond the transition region

$$L_{\text{tran}} = 2^{1/3} R_{\text{graze}}^{2/3} \sin \chi_{\text{graze}} (cT_N)^{1/3}$$

Before entering the transition region:

$$G(\xi, 0, 0) \rightarrow 2e^{-i\xi^3/3} \quad \text{as } \xi \rightarrow -\infty$$

and one recovers the N-wave

$$p \rightarrow 2P_N f_N(\tau_{\text{before}}/T_N)$$

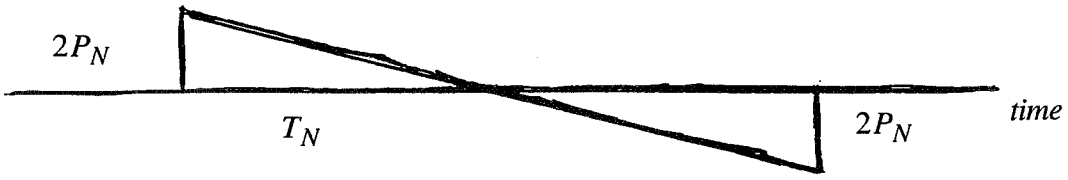

$$\tau_{\text{before}} = t - [y/c]\sin\chi_{\text{graze}} - [x/c]\cos\chi_{\text{graze}} + [y^3/(6R_{\text{graze}}^2 c)]\frac{1}{\sin^3\chi_{\text{graze}}}$$

Apparent phase velocity in lateral direction is

$$v_{ph} \approx \frac{c}{\sin\chi_{\text{graze}}}\left[1 + \frac{y^2}{2R_{\text{graze}}^2 \sin^4\chi_{\text{graze}}}\right]$$

WAVEFORM AT EDGE OF CARPET

At precisely the edge of the carpet boundary:

$y = 0$, so $\xi = 0$ for all ω

$$\left\{G(\xi, 0, 0)\right\}_{\xi=0} = 1.399$$

Thus one has an N-wave, but of reduced amplitude

$$p = 1.399 P_N f_N(\tau / T_N)$$

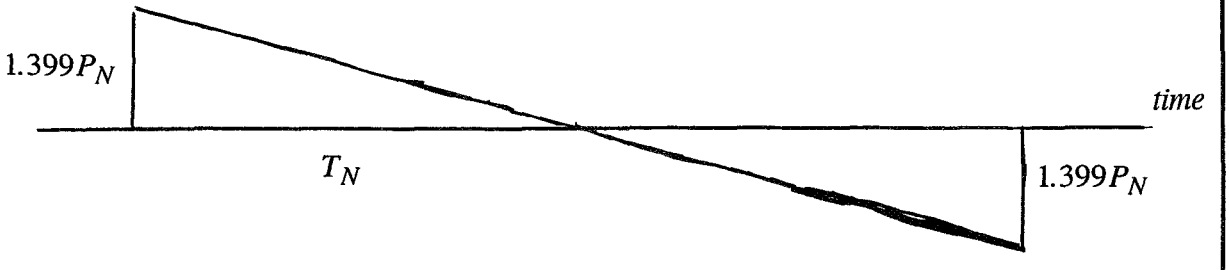

$$\tau = t - [x/c] \cos \chi_{\text{graze}}$$

Representative value for:

$$L_{\text{tran}} = 2^{1/3} R_{\text{graze}}^{2/3} \sin \chi_{\text{graze}} (cT_N)^{1/3}$$

Let $M_g = 2$, so $\sin \chi_{\text{graze}} = \sqrt{3}/2$
Let $c = 0.34\,\text{km/s}$
Let $R_{\text{graze}} = 88\,\text{km}$
Then

$$\left(\frac{cT_N}{R_{\text{graze}}}\right)^{1/3} = 0.0834$$

and one deduces

$$L_{\text{tran}} = 0.09 R_{\text{graze}} = 8\,\text{km} = 5\,\text{miles}$$

Compare with representative value of carpet half-width

$$W_{1/2} = [2 \cdot 88 \cdot 12]^{1/2} \sqrt{3}/2 = 40\,\text{km} = 25\,\text{miles}$$

To study deterioration of front of shock,
sufficient to take incident wave as a step function:

$$p = \frac{P_N}{\pi}\int_0^\infty \frac{1}{\omega}\mathrm{Im}\left[e^{-i\omega\tau}G(\xi,0,0)\right]d\omega - \frac{1}{2}G(0,0,0)P_N$$

- To examine the contribution of the higher-frequency components, it suffices to use the creeping wave approximation:

$$G \to 1.8325e^{e^{-i\pi/6}K\xi} \quad \text{as} \quad \xi \to +\infty$$

where $K = 1.0188$. Result is (for $y > 0$)

$$p = P_N\Phi_{\text{creep}}(\tau/\tau_{\text{char}}) - \frac{1}{2}G(0,0,0)P_N$$

$$\Phi_{\text{creep}}(\eta) = \frac{1.8325}{\pi}\int_0^\infty \frac{1}{\Omega}e^{-[\sqrt{3}/2]\Omega^{1/3}}\sin(\Omega\eta - [1/2]\Omega^{1/3})d\Omega$$

$$\tau_{\text{char}} = \frac{(1.088)^3y^3}{2cR_{\text{graze}}^2\sin^3\chi_{\text{graze}}}$$

HINTS FOR ANALYSIS OF FIELD DATA

For analysis of field data:

- Need at outset to identify
  - nominal location of carpet edge, origin of y
  - Mach number relative to sound speed at ground, to get χ_{graze}
  - Grazing ray radius of curvature R_{graze}, from meteorological profiles
  - N-wave amplitude P_N before reflection at ground
  - Positive phase duration T_N at the carpet edge
- Theory predicts that peak waveform versus extra lateral distance should fall on a "universal curve" if one plots p_{peak}/P_N versus y/L_{tran}
- Theory predicts that waveform shape is similar for all waveforms recorded at same value of y/L_{tran}

Rough characterization of wave evolution beyond the transition region,

- Begin with an N-wave of amplitude of $1.399P_N$ at the carpet edge ($y = 0$).
- $|G(\xi, 0, 0)|$ drops to 1/2-th of its zero-frequency value at $\xi = 1.05$.
- Frequencies which propagate with negligible attenuation to lateral distance y from carpet edge are those for which

$$\omega < \frac{2cR_{\text{graze}}^2 \sin^3 \chi_{\text{graze}}}{y^3}$$

- Propagation to lateral distance y from carpet edge is roughly equivalent to passing an N-wave of peak overpressure $1.399P_N$ through a low-pass filter with cut-off frequency

$$\omega_{\text{cut-off}} = \frac{2cR_{\text{graze}}^2 \sin^3 \chi_{\text{graze}}}{y^3}$$

ATMOSPHERIC EFFECTS ON THE RISETIME AND WAVESHAPE OF SONIC BOOMS

Richard Raspet, Henry E. Bass and Patrice Boulanger
Department of Physics and Astronomy
University of Mississippi
University, MS 38677

ABSTRACT

Accurate prediction of human response to sonic booms from proposed HSCT aircraft depends on a knowledge of the waveshape and risetime of the boom at the ground. In previous work, we have developed a numerical technique to predict the combined effects of molecular absorption and finite wave distortion on the sonic boom as it propagates from the aircraft to the top of the turbulent boundary layer. We have more recently developed a scattering center based model to calculate the effects of turbulence on the sonic boom waveform as it propagates through this boundary layer. Calculations have been performed using single scales of turbulence and compared to measurements at Edwards AFB in the late 1960s. A model of the atmosphere involving two scales each for convective and mechanical turbulence has been developed and fit to meteorological data collected during JAPE 2. Scattering calculations employing this model underpredict the number of unperturbed waveforms. In order to develop a more realistic model of the atmosphere, the JAPE 2 meteorological data has been fit to a von Karman spectrum. Results of scattering using this multi-scale model will be presented. The combination of finite wave effects with turbulent scattering predictions includes the principal effects of the atmosphere on the sonic boom from the HSCT.

INTRODUCTION

The prediction of the average environmental impact of the HSCT requires accurate modeling of the processes affecting the sonic boom waveform and risetime. We have used the enhanced Anderson algorithm to predict the risetime and waveshape of sonic booms under non-turbulent conditions. This method can also be used to predict the risetime and waveshape at the top of the turbulent planetary boundary layer.

The enhanced Anderson algorithm includes all finite wave effects and the vibrational relaxation effects of N_2, O_2, and CO_2 in combination with atmospheric H_2O. This algorithm has been compared to data from explosions[1] and sonic booms[2] and has been tested against measurements of high intensity ballistic waves from rifles and from tank guns[3]. In addition, the results of this calculation for quasi steady shocks agree with the results from the enhanced Burgers' Equation[4,5].

Figure 1 presents the results of the application of the enhanced Anderson algorithm to a predicted HSCT waveform[6]. We emphasize that the key parameter in determining the risetime of the sonic boom is the absolute humidity.

Under turbulent conditions, the risetimes of sonic booms are scattered and are occasionally as large as ten times the risetimes calculated from vibrational relaxation considerations. It is clear that turbulence is the cause of the increased risetime and peculiar waveforms observed. Analytic techniques have been used to estimate the increase in average risetimes[7, 8, 9] and to calculate perturbed waveforms due to focusing and defocusing of the waves by turbulence[10]. In such calculations, it is usually necessary to assume a single strength and turbulence scale representative of the atmospheric turbulence. The largest turbulence effects are usually identified when the largest scales are chosen as typical.

We have chosen a different approach to calculating the effects of turbulence on sonic boom risetimes and waveforms based on a simple scattering center-based theory. The scattering center-based method accurately predicted the effects of turbulence on the coherence of continuous wave signals above natural ground surfaces[11].

METHOD

The scattering center-based technique resolves atmospheric fluctuations into a sum of discrete spherically symmetric Gaussian "turbules". The total effect of the atmosphere is then calculated by summing up the scattering amplitudes. See Figure 2. The scattered amplitudes are calculated using the first Born approximation. If the complex pressure at the receiver is written as:

$$\vec{p}^{B}(\vec{r}) = \vec{p}_o(\vec{r}) + \sum_{i=1}^{N} \vec{\psi}_i^{B} \tag{1}$$

where the superscript B refers to the first Born approximation, $\vec{p}_o(\vec{r})$ is the unperturbed spherical wave, and N is the number of turbules, then

$$\vec{\psi}_i^{B} = \frac{\sqrt{\pi}}{2} q_i k^2 s^3 \frac{e^{ik(r_{st}+r_{tr})}}{r_{st}+r_{tr}} \left[\frac{1}{1 - ia}\right] e^{-Ck^2s^2/4} \tag{2}$$

where

$$C = (1 - \cos\theta_o)^2 + \sin^2\theta_o \left[\frac{1}{1 - ia}\right] \tag{3}$$

and

$$a = \frac{ks^2}{2}\left[\frac{1}{r_{st}} + \frac{1}{r_{tr}}\right] . \tag{4}$$

s defines the $1/e^2$ contour of the turbule, q_i is the index of refraction profile strength, and θ_o is the scattering angle. The geometry is indicated in Figure 3.

The initial research on continuous wave propagation modeled the atmosphere as a random sum of identical turbules. This single scale calculation was extended to impulse propagation with promising results.[12] The impulse is Fourier transformed into the frequency domain and the total scattered component at each frequency is calculated. Then the inverse Fourier transform yields the time domain waveform. The single scale calculation (s = 10m, 30m or 100m) with a fluctuating index of refraction of $\langle\mu^2\rangle = 10 \times 10^{-6}$ predicted spiked and rounded waveforms and predicted risetimes as large as 10 ms. These results encouraged us to analyze the results of the JAPE-2 tests[13,14] using the scattering center-based model.

ANALYSIS OF JAPE-2 DATA

The JAPE-2 tests consisted of simultaneous measurement of sonic boom characteristics and meteorological measurements. The wind and temperature fluctuations were measured at heights up to 30m using sonic anemometers and hot wire anemometers. The sonic boom data was analyzed by Willshire, Garber and DeVilbiss[14] and provided as computer files. The turbulence data was analyzed by Bass, Boulanger, Olsen and Chintawongvanich[15].

a.) Two Scale Model

Examination of the data showed that a single scale model of the atmosphere could not fully describe the turbulence above the ground. The time correlation of the fluctuation quantities was fit to a two scale model. See Figure 4. Table I displays the results of the analysis for a moderately turbulent day during JAPE-2.

Table I. Example of the Two Scale Model Applied to Atmospheric Data

	Wind driven 1	Wind driven 2	Temp. driven 1	Temp. driven 2
Size (meters)	117	11	74	8
Number of Eddies	1	90	1	233
$\langle \mu^2 \rangle$	$0.54\ 10^{-5}$	$0.25\ 10^{-5}$	$0.5\ 10^{-6}$	$0.4\ 10^{-6}$

The scattering calculation was performed by summing the results of four calculations - one for each scale size. The input waveform to the scattering calculation was an N-wave propagated from the flight altitude to the top of the turbulent layer using the enhanced Anderson algorithm. The results of the Anderson algorithm agree moderately with the measurements taken under low turbulence conditions. See Table II.

Table II. Comparison of Measured and Predicted Waveform Parameters for the T-38

	Measurements for the low turbulence case	Calculations using the Anderson algorithm
Peak overpressure (psf)	0.71	0.88
Risetime (ms)	0.32	0.33

Figure 5 compares the results of the measurement and prediction for T-38 overflights under moderate turbulence conditions. Although the scattering center model produces a wide distribution of risetimes, it does not predict the shift of the histogram maximum to 2 ms; rather the maximum remains at the unperturbed value of 0.3 ms. It is believed that this is due to the use of two relatively large scales to represent the atmospheric turbulence. The scattering from large turbules is predominantly in the forward direction, and large turbules are relatively sparse, so that it is easy to "miss" the receiver with

the scattered wave. The four scale model does, however, represent a significant improvement over the single scale model.

b.) von Karman Spectrum Model

The fit of the autocorrelation to two scales rather than one improved the prediction of risetimes significantly. The high occurrence of unperturbed risetimes indicated that smaller and intermediate scales were needed to fully describe the scattering of sonic booms by turbulence.

De Wolf[16] presented a technique for simulation of a turbulent atmosphere obeying the von Karman spectrum in terms of the number density of turbules.

The general form of a 3-D von Karman spectrum is given in terms of frequency by:

$$\phi(f) = \frac{a f^2}{\left(f^2 + b\right)^{\frac{11}{6}}} \tag{5}$$

where:

$$a = 4\pi\gamma C_\varepsilon^2 \left(\frac{c}{2\pi}\right)^{2/3} \tag{6}$$

and

$$b = \left(\frac{c}{2\pi L_o}\right)^2 \tag{7}$$

The coefficients a and b are determined by fitting a function $\phi(f)$ through the measured spectra. See Figure 6.

The fit parameters are then used to determine n (s), the number density of turbules of size s needed to model the fluctuating atmosphere. De Wolf's model was originally developed to predict second moments of a scattered field and therefore is designed to reproduce only second moments of the fluctuation fields. Higher moments must be accurately represented to express the temporal characteristics of an impulse. De Wolf used an index of refraction maximum for each turbule of $\pm$ 1.0 and employed a very sparse distribution. We have varied the product of q_i^2 and n (s) until the model distribution approximates the measured second and fourth moments $\langle\mu^2\rangle = 9.6 \times 10^{-6}$, $\langle\mu^4\rangle = 2.5 \times 10^{-10}$. The variation of calculated $\langle\mu^2\rangle$ with number of turbules and q_i^2 is shown in Table III.

Table III. Calculate $<\mu^2>$ and $<\mu^4>$ as a Function of Number of Turbules

Number of Turbules	Percentage of Volume	q_i^2	$\langle\mu^2\rangle$	$\langle\mu^4\rangle$
42000	8	$1.5\ 10^{-4}$	$1.2\ 10^{-5}$	$1.0\ 10^{-9}$
63000	12	$1.0\ 10^{-4}$	$1.1\ 10^{-5}$	$1.0\ 10^{-9}$
95000	18	$6.7\ 10^{-5}$	$1.0\ 10^{-5}$	$6.9\ 10^{-10}$
127000	24	$5.0\ 10^{-5}$	$1.1\ 10^{-5}$	$5.5\ 10^{-10}$
254000	48	$2.5\ 10^{-5}$	$9.9\ 10^{-6}$	$4.4\ 10^{-10}$

The turbule spatial and size distribution for each realization is determined by Monte Carlo methods. The index of refraction fluctuations along a straight line has been compared to the corresponding measured values and exhibits similar fluctuation scales and displacement.

The second improvement to the scheme was the use of the measured height of the Planetary Boundary Layer in the calculation. Figure 7 displays the temperature versus height curve for one flight during JAPE-2. One sounding is taken with the tethesonde going up and the inversion height is 400m, the other trace is the tethesonde coming down 30 minutes later and the inversion height is at 670m. The turbulent layer thickness at the time of the later sonic boom measurement was extrapolated from this as 750m.

The results of this calculation for 20 realizations are displayed in Figure 8. The maximum occurrence risetime shows a shift away from the non-turbulent risetime of 0.3 ms. The smaller and intermediate scales of turbulence have a significant effect on the risetimes of sonic booms. It is clear, however, that the shift is not large enough to match the measured data in Figure 5a.

CONCLUSION

The enhanced Anderson algorithm provides a good prediction of waveshape and risetime of the HSCT at the top of the Planetary Boundary Layer.

The scattering center-based model can be extended to predict distorted wave shapes and longer risetimes. At this stage, the scattering based model does not predict long enough average risetimes, but does show that smaller and intermediate scales are important in increasing the average risetimes.

The larger scales are the source of the dramatically distorted waveforms, but are not the source of the shift in average risetimes. The scattering center-based calculation allows the quantitative investigation and modeling of the turbulence effects discussed qualitatively by Crow, Plotkin and George, and Pierce.

REFERENCES

1. Bass, H. E.; and Raspet, Richard: Vibrational relaxation effects on the atmospheric attenuation and risetimes of explosion waves. *J. Acoust. Soc. Am.*, vol. 64, 1978, pp. 1208-1210.

2. Bass, H. E.; Ezell, J.; and Raspet, R.: Effect of vibrational relaxation on risetime of shock waves in the atmosphere. *J. Acoust. Soc. Am.*, vol. 74, 1983, pp. 1514-1517.

3. Bass, H. E.; Layton, B. A.; Bolen, L. N.; and Raspet, R.: Propagation of medium strength shock waves through the atmosphere. *J. Acoust. Soc. Am.*, vol. 82, 1987, pp. 306-310.

4. Bass, Henry E.; and Raspet, Richard: Comparison of sonic boom risetime prediction techniques. *J. Acoust. Soc. Am.*, vol. 91, 1992, pp. 1761-1768.

5. Kang, J.; and Pierce, A. D.: Contribution of molecular relaxation to rise time of sonic booms. *J. Acoust. Soc. Am.*, Supp. 1, vol. 85, 1989, p. S81.

6. Raspet, Richard; and Bass, Henry E.: Comparison of Shock Rise Time Prediction Techniques. AIAA 13th Aeroacoustics Conference, Tallahassee, FL, Oct. 22-24, 1990.

7. Crow, S. C.: Distortion of sonic bangs by atmospheric turbulence. *J. Fluid Mech.*, vol. 37, 1969, pp. 529-563.

8. Plotkin, Kenneth J.; and George, A. R.: Propagation of weak shock waves through turbulence. *J. Fluid Mech.*, vol. 54, 1972, pp. 449-467.

9. Pierce, A. D.: Statistical theory of atmospheric turbulence effects on sonic boom rise times. *J. Acoust. Soc. Am.*, vol. 49, 1971, pp. 906-924.

10. Pierce, Allan D.: Spikes on sonic boom pressure waveforms. *J. Acoust. Soc. Am.*, vol. 44, 1968, pp. 1052-1061.

11. McBride, Walton E.; Bass, Henry E.; Raspet, Richard; and Gilbert, Kenneth E.: Scattering of sound by atmospheric turbulence: A numerical simulation above a complex impedance boundary. *J. Acoust. Soc. Am.*, vol. 90, 1991, pp. 3314-3325.

12. Raspet, Richard; Bass, Henry E.; Yao, Lixin; Boulanger, Patrice; and McBride, Walton E.: Statistical and numerical study of the relationship between turbulence and sonic boom characteristics. *J. Acoust. Soc. Am.*, Revised manuscript submitted, March, 1994.

13. Kennedy, Bruce W.; Willshire, Jr., William L.; and Olsen, Robert O.: Sonic Boom Propagation Test. The Bionetics Corporation, Las Cruces, NM, Sept., 1991.

14. Willshire, Jr., William L.; Garber, Donald P.; and DeVilbiss, David W.: Flight test measurements of the effect of turbulence on sonic boom peak overpressure and rise time. *J. Acoust. Soc. Am.*, vol. 92, 1992, p. 2329.

15. Bass, Henry E.; Boulanger, Patrice; Olsen, Robert; and Chintawongvanich, Prasan: Sonic Boom Propagation Test - Low Level Turbulence Report. Physical Acoustics Research Group Report, University of Mississippi, Feb., 1993.

16. De Wolf, D. A.: A random-motion model of fluctuation in a nearly transparent medium. *Radio Science*, vol. 18 (2), 1983, pp. 138-142.

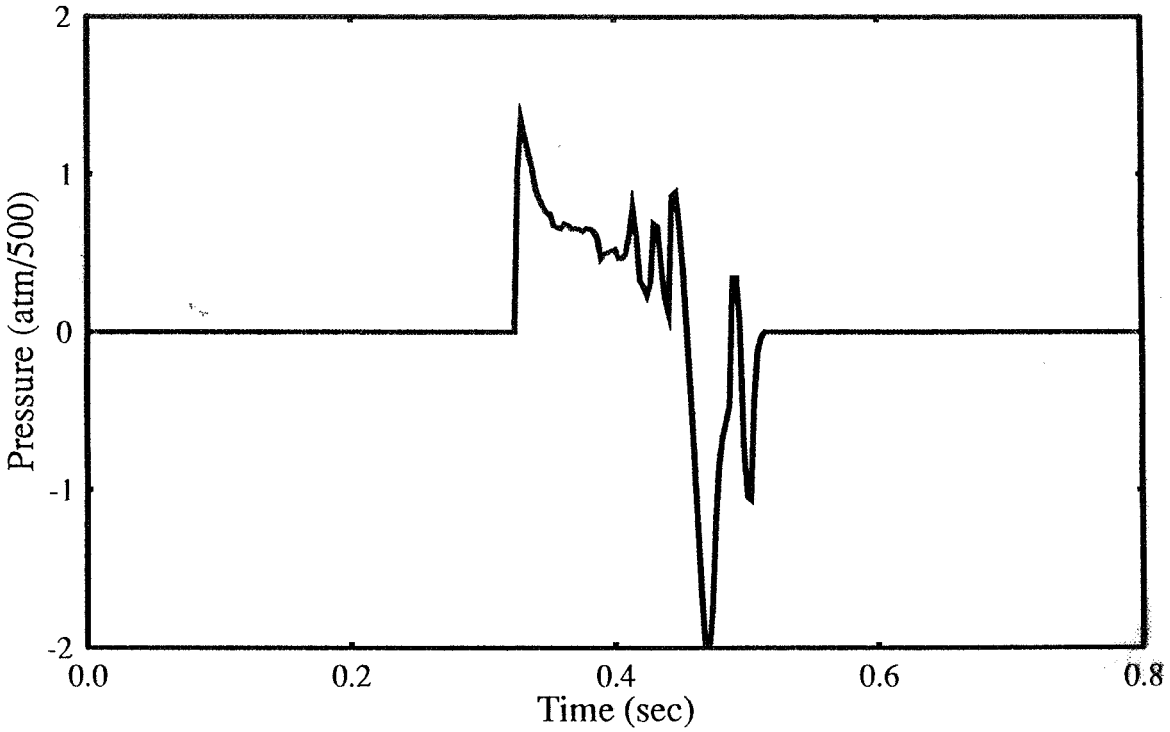

Figure 1. a.) Predicted HSCT waveform close to the aircraft.

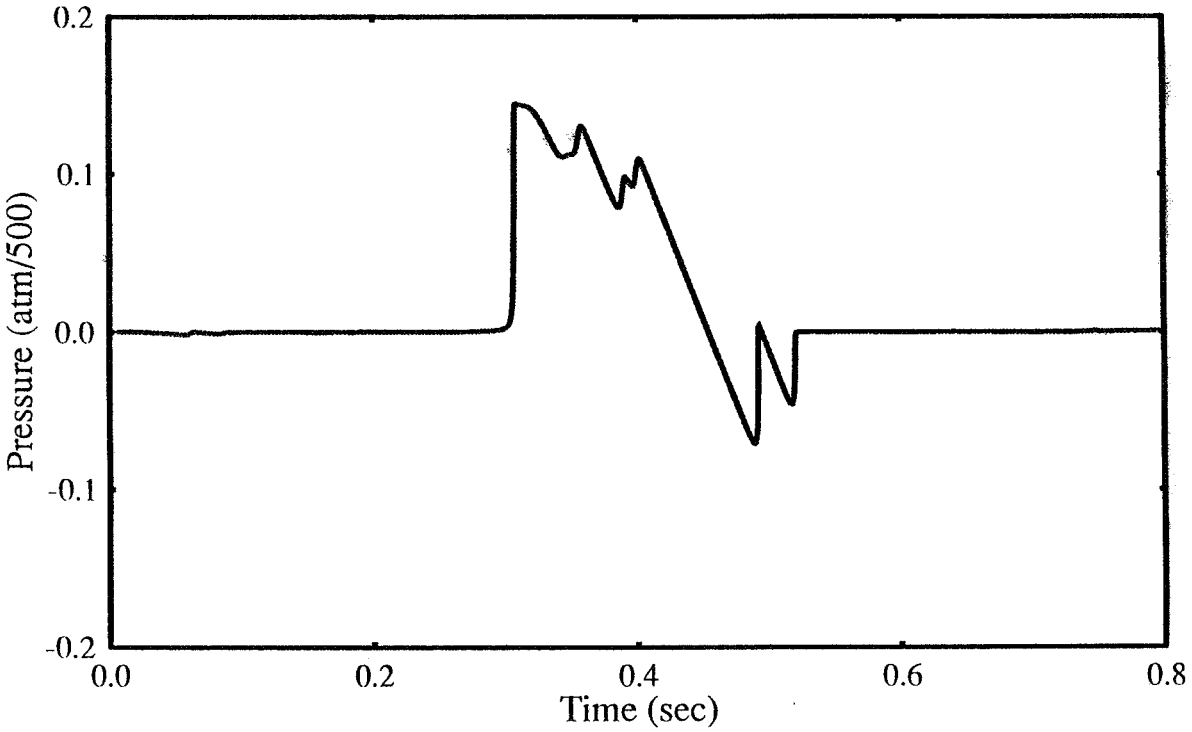

b.) HSCT waveform at the ground predicted using the enhanced Anderson algorithm.

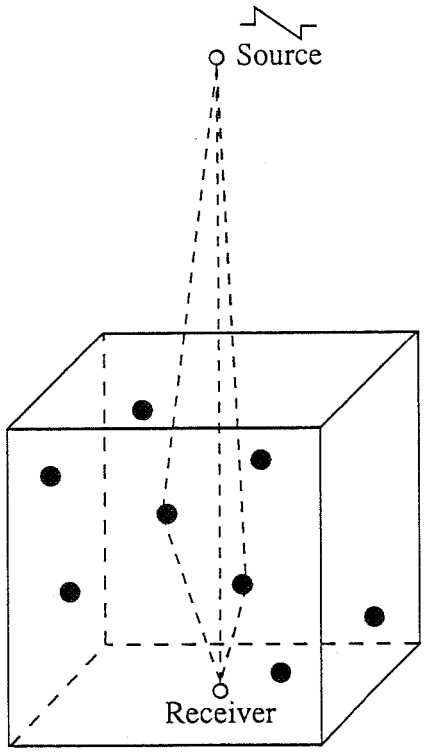

Figure 2. Scattering center calculation for sonic booms.

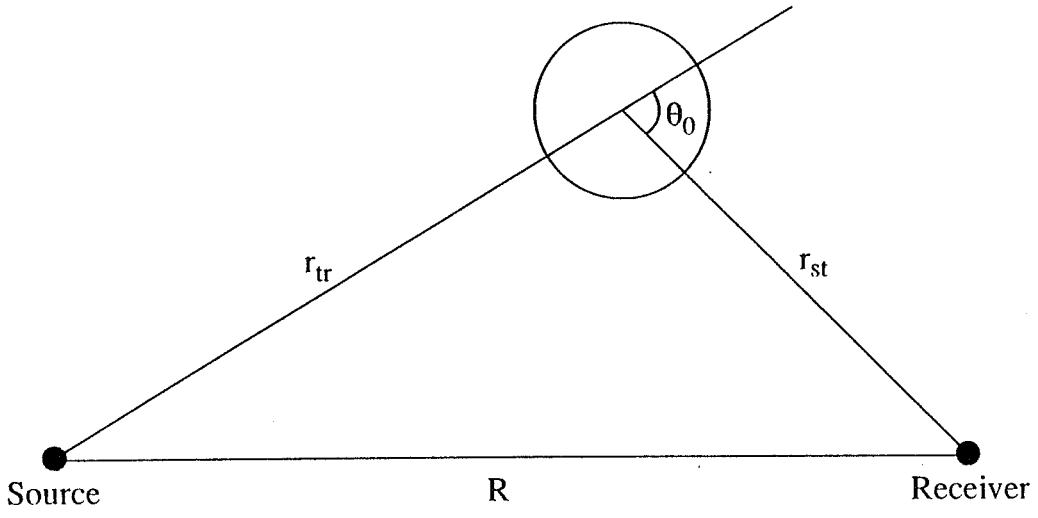

Figure 3. Geometry for the scattering calculation.

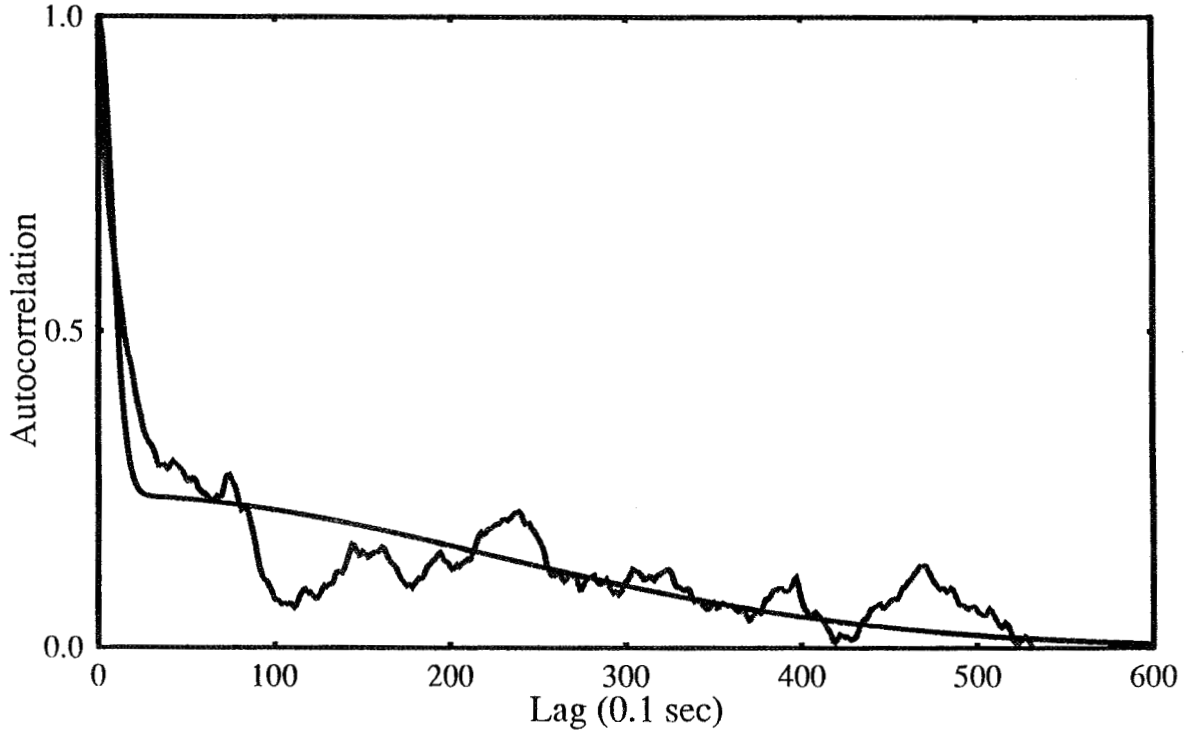

Figure 4. Two scale fit to the autocorrelation of the wind speed signal.

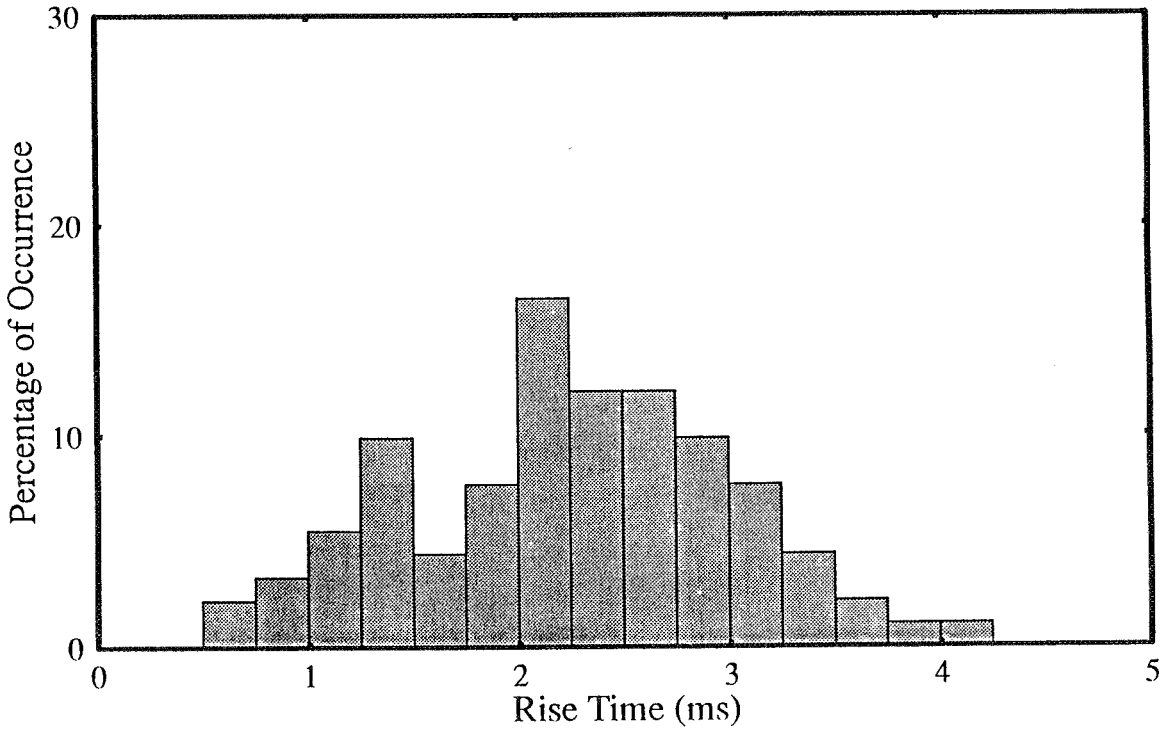

Figure 5. a.) Measured risetime distribution for the T-38 aircraft.

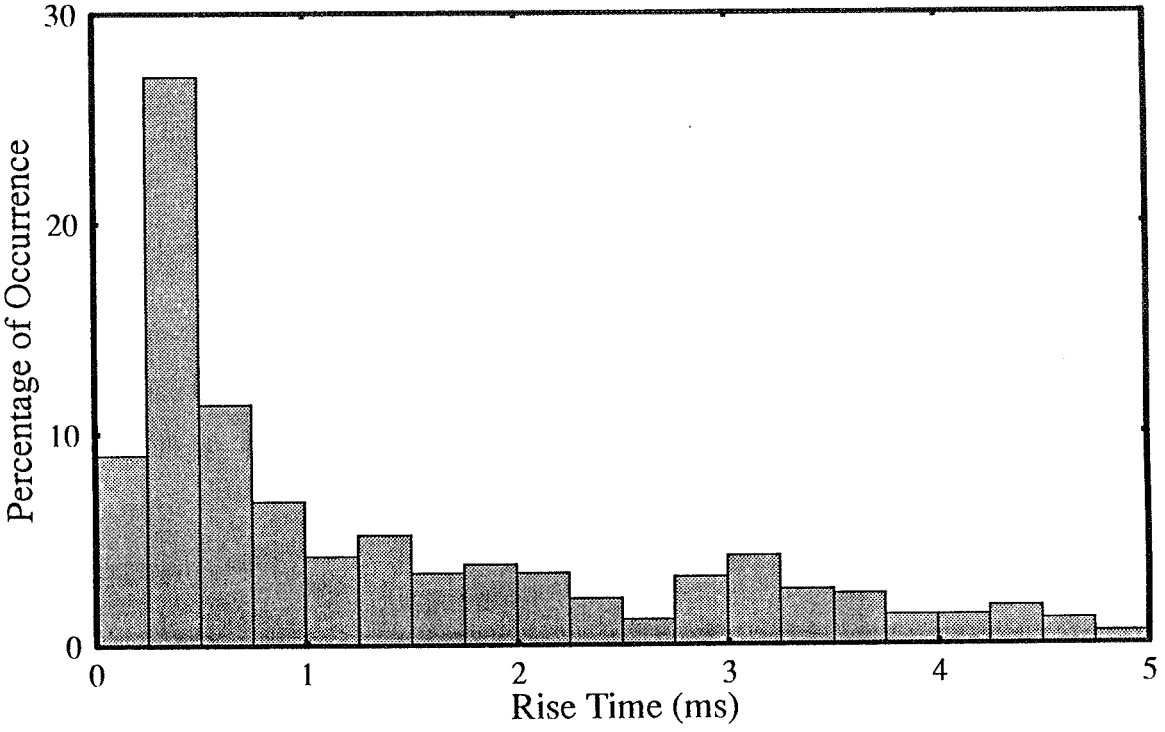

b.) Predicted distribution using the two scale model.

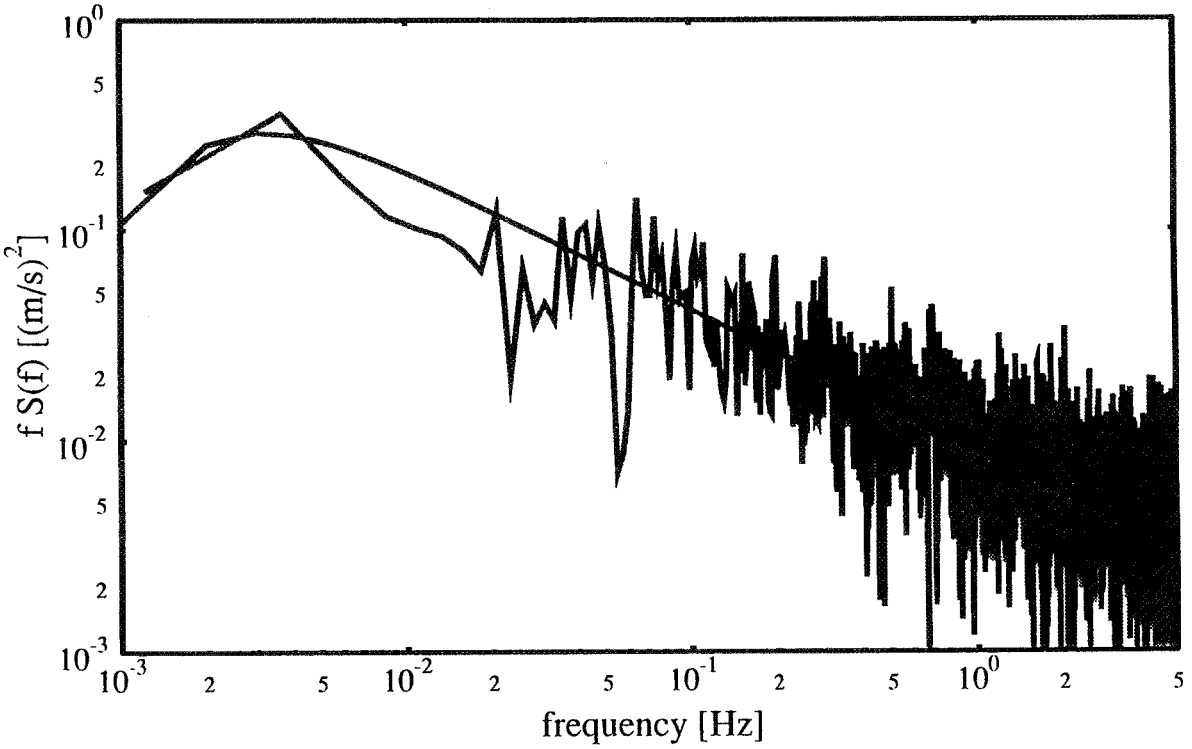

Figure 6. Fit of the von Karman spectrum to a 23 minute sample of wind data.

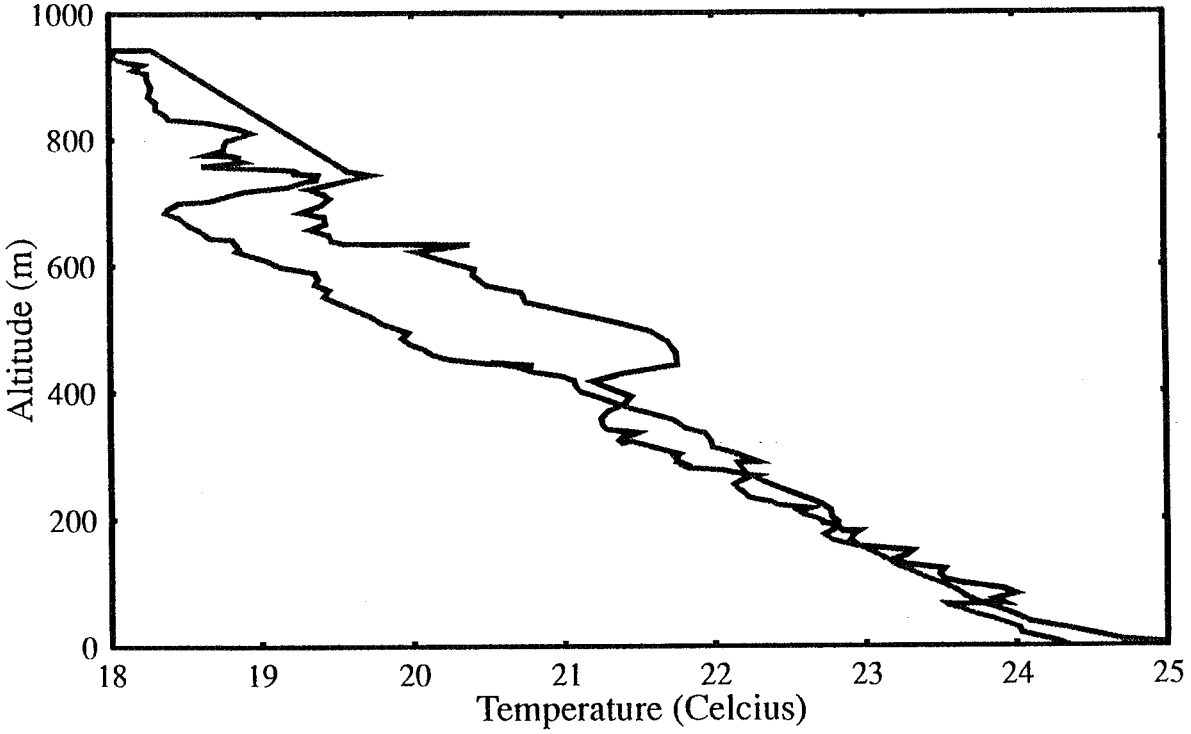

Figure 7. Temperature versus height for one flight at JAPE-2.

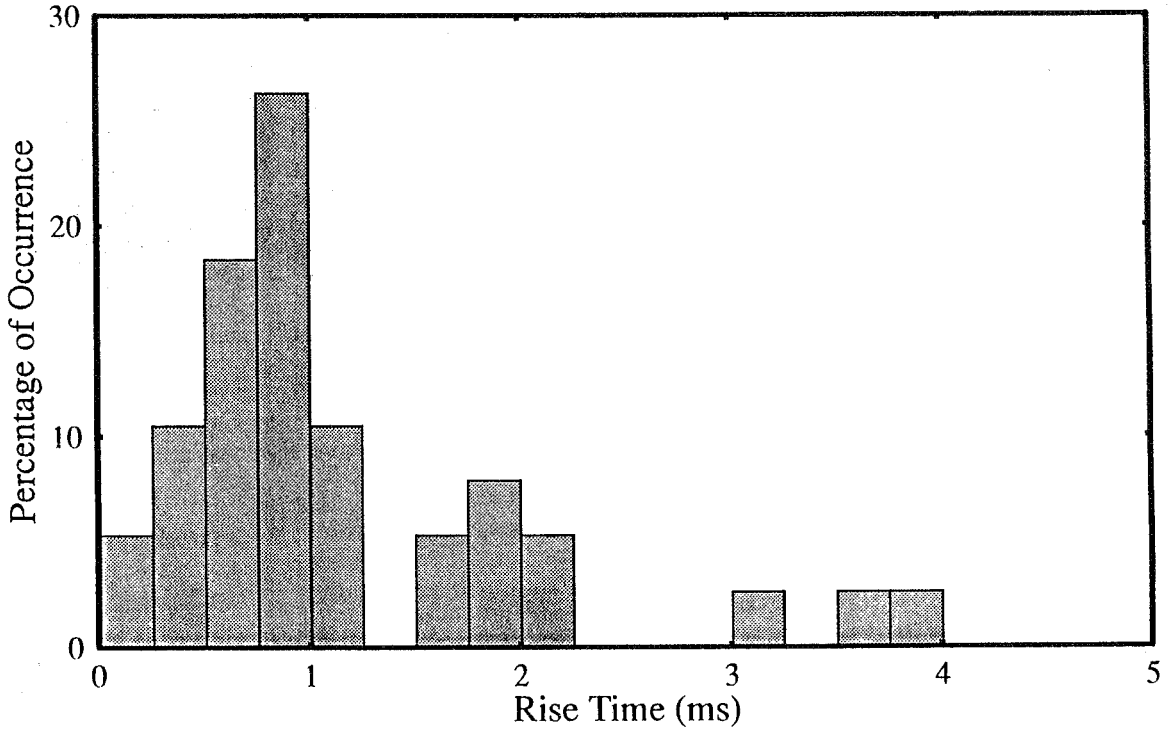

Figure 8. Prediction of risetime distribution using the von Karman spectrum. (20 realizations).

THE EFFECT OF AIRCRAFT SPEED ON THE PENETRATION OF SONIC BOOM NOISE INTO A FLAT OCEAN

Victor W. Sparrow
Penn State University
157 Hammond Building
University Park, PA 16802

ABSTRACT

As U.S. aircraft manufacturers now have focused their HSCT efforts on overwater supersonic flight, a great deal more must be known about sonic booms propagating overwater and interacting with the ocean. For example, it is thought that atmospheric turbulence effects are often much less severe over water than over land. Another important aspect of the overwater flight problem is the penetration of the sonic boom noise into the ocean, where there could be an environmental impact on sea life.

This talk will present a brief review on the penetration of sonic boom noise into a large body of water with a flat surface. It has been determined recently that faster supersonic speeds imply greater penetration of sonic boom noise into the ocean. The new theory is derived from the original Sawyers paper and from the knowledge that for level flight a boom's duration is proportional to the quantity $M/(M^2-1)^{3/8}$ where M is the Mach number. It is found that for depths of 10 m or less, the peak SPL varies less than 6 dB over a wide range of M. For greater depths, 100 m for example, increased Mach numbers may increase the SPL by 15 dB or more.

ACKNOWLEDGMENTS

The author would like to thank Dr. William Cummings for introducing the author to the present problem and Dr. Kevin Shepherd for encouraging this research. Thanks also to Drs. Domenic Maglieri and Robert W. Young for providing valuable references.

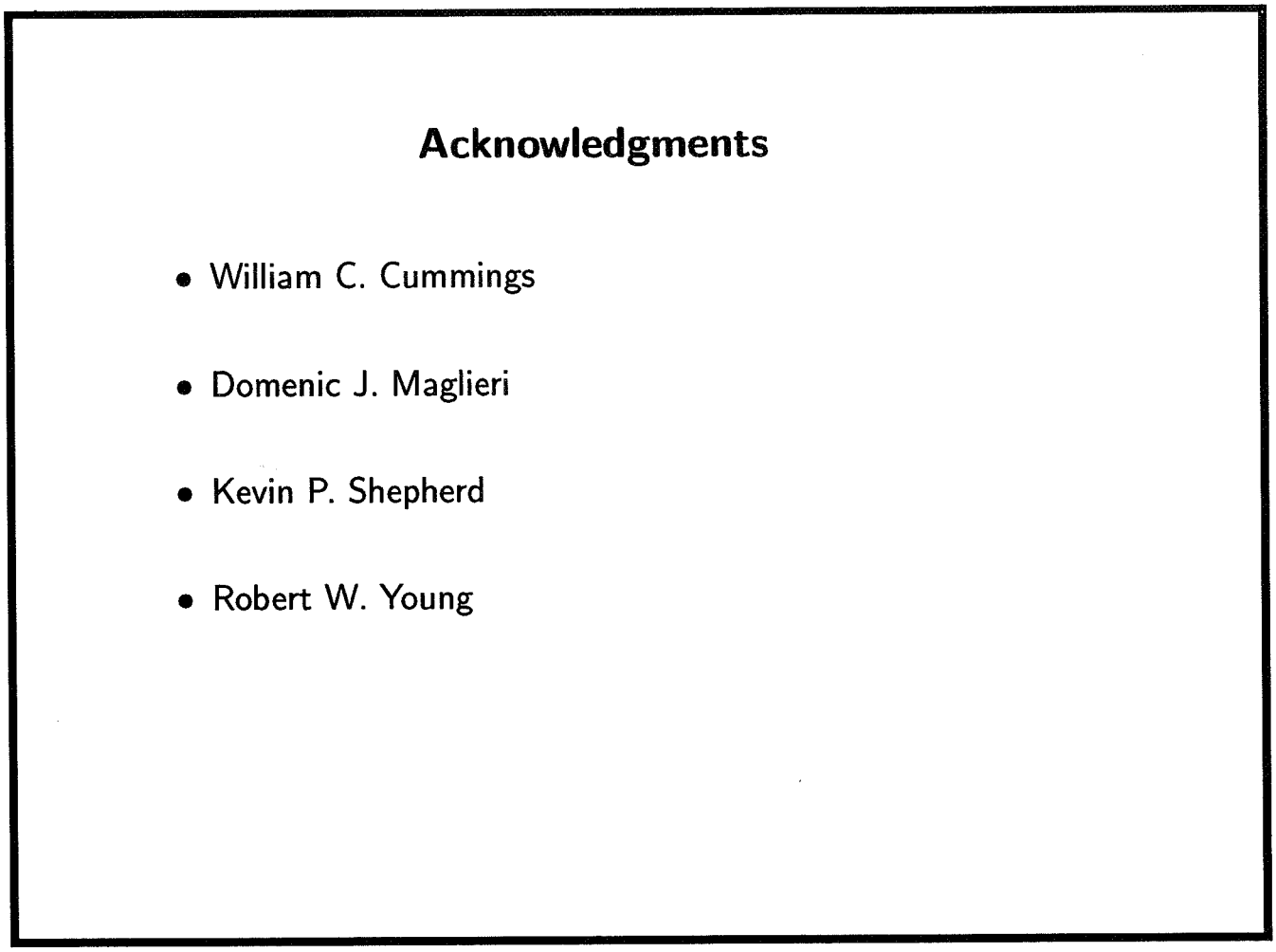

INTRODUCTION

Times are certainly changing in atmospheric propagation research for the NASA High Speed Research program. During the last few years research has focused on the effects of atmospheric turbulence on the propagation and distortion of sonic boom waves. This research has yielded many important results.

However, the U.S. aircraft manufacturers who are preparing for the construction of supersonic commercial aircraft have shifted their emphasis away from overland flight. They are now centering on flying overwater to essentially eliminate the sonic boom impact on people.

This decision has important repercussions for propagation research. It is known that atmospheric turbulence effects are much less severe over water than over land. Over land the ground heats up during the day as the sun shines, creating thermals which greatly increase atmospheric turbulence. The ocean surface, in comparison, does not heat up. The ocean acts as a great heat reservoir, and the water churning over and over keeps the surface temperature nearly constant. No thermals affecting turbulence are created.

Changing Times

- Last few years, HSR focusing on atmospheric turbulence.
- U.S. aircraft manufacturers say
  - no to overland flight
  - yes to overwater flight.
- Atmospheric turbulence much less severe over water than over land.

Since atmospheric turbulence does not seem to be as pressing an issue for the overwater program as it did for the overland program, one may ask: What are the technical challenges that will be encountered in overwater flight?

Just as in the planning of any large project, one must be concerned with environmental impact. Thus the environmental noise impact of sonic booms on wildlife should be addressed. It turns out that the local wildlife for overwater flight consists of sea life, and particularly marine mammals such as whales.

All whales breathe air, and must surface periodically. Most species spend the great majority of their time within 100 m or so of the ocean surface, many within the top 25 m.

One may then ask: How much sound gets from the air into the water? What would one hear if just under the water's surface?

Overwater brings new challenges

- Look at environmental noise impact on wildlife.

  Overwater local wildlife: marine mammals

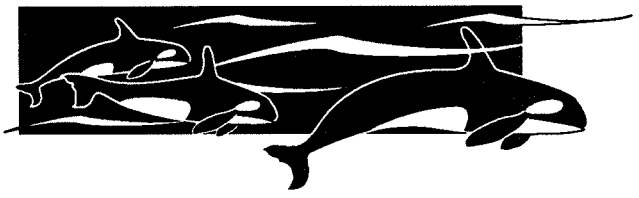

- How much sound gets from the air into the water?

It turns out that one can make predictions with reasonable certainty, as the acoustical theory has been well understood for many years. One first notices that the characteristic impedances for water and air differ greatly, approximately 415 for air and 1,500,000 for water. This means that a plane sound wave propagating in air directly toward the surface of the water at an angle of 0 degrees, called normal incidence, would have 99.8% of its energy reflected. Very little propagating sound energy gets into water.

Further it turns out that the sound from a sonic boom is not normally incident but is incident at an angle greater than the critical angle, which for the air – water interface is 13.2 degrees. This means that 100% of the incident energy is reflected. One might think that this means no sound gets into the water, but this is not the case.

When a force is applied normally to the surface of some material, the material must push back or the surface will be moved. So obviously when a sonic boom is incident on the water

Brief Review of Sound Penetration Theory

- Characteristic impedances differ greatly:

  air: $c_1\rho_1 = 415$ kg/(s m^2)

  water: $c_2\rho_2 = 1{,}500{,}000$ kg/(s m^2)

- For typical HSCT flight, sound will be incident at angles greater than the critical angle, $13.2°$.

  $\Longrightarrow$ all sound power reflected

  $\Longrightarrow$ but must still match pressure boundary condition

surface, the water must push back on the surface. What this means is that the acoustic pressure on both sides on the ocean surface must be the same. This boundary condition is important because it implies that there will be substantial sound in the water although all of the energy is reflected.

If one uses typical numbers for a projected high speed civil transport, such as Mach number of 2.1 and boom duration of 0.3 second, one can straightforwardly predict what the acoustic pressures will be under the surface of the water. Mach 2.1 implies that the incident angle will be 28.4 degrees from normal, which implies that there will be a pressure wave in the water whose amplitude decays with depth. The "fundamental" frequency of a 0.3 second boom is 3.33 Hz, and the decay of this frequency is indicated in the figure. As one can see, given a relative amplitude of 1 at the ocean surface, the amplitude decays slowly with depth. There is significant noise penetration beyond a depth of 50 m. Of course a sonic boom is composed of many component frequencies. Higher frequencies will penetrate less far beneath the surface, while lower frequencies will penetrate further.

Matching the boundary condition with typical HSCT numbers:

- Speed: Mach number, $M = 2.1$
  - $\Rightarrow$ angle of incidence $= \sin^{-1}(1/M) = 28.44°$
  - $\Rightarrow$ exponentially decaying pressure in water, $e^{-A\,2\pi f\,z}$
- Duration, $T = 0.3$ s
  - $\Rightarrow$ "fundamental" frequency, $f_0 = 3.33$ Hz:

    Much faster decay for higher f.

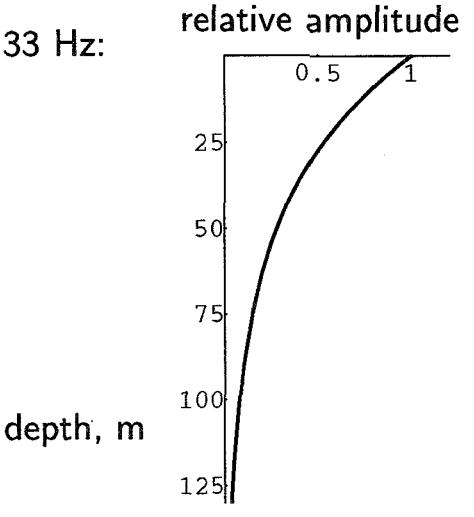

By performing a superposition of component frequencies of a real sonic boom, one can further predict what the received noise would look like at various depths under the ocean surface. For example, using the 0.3 second duration boom incident at Mach 2.1, the Fourier analysis results are shown below in the figure. It is assumed that there is a perfectly N shaped sonic boom incident on the ocean surface. One can see that at 2.5 meters depth, the tips of the N are slightly rounded, but the waveform is mostly preserved. At 25 meters depth the waveform's peak amplitude is decreased to about 45% of its amplitude at the surface, and the waveform is rounded. At a depth of 120 meters or more, the waveform is greatly smoothed but still has an amplitude of as much as 15% of its peak at the surface.

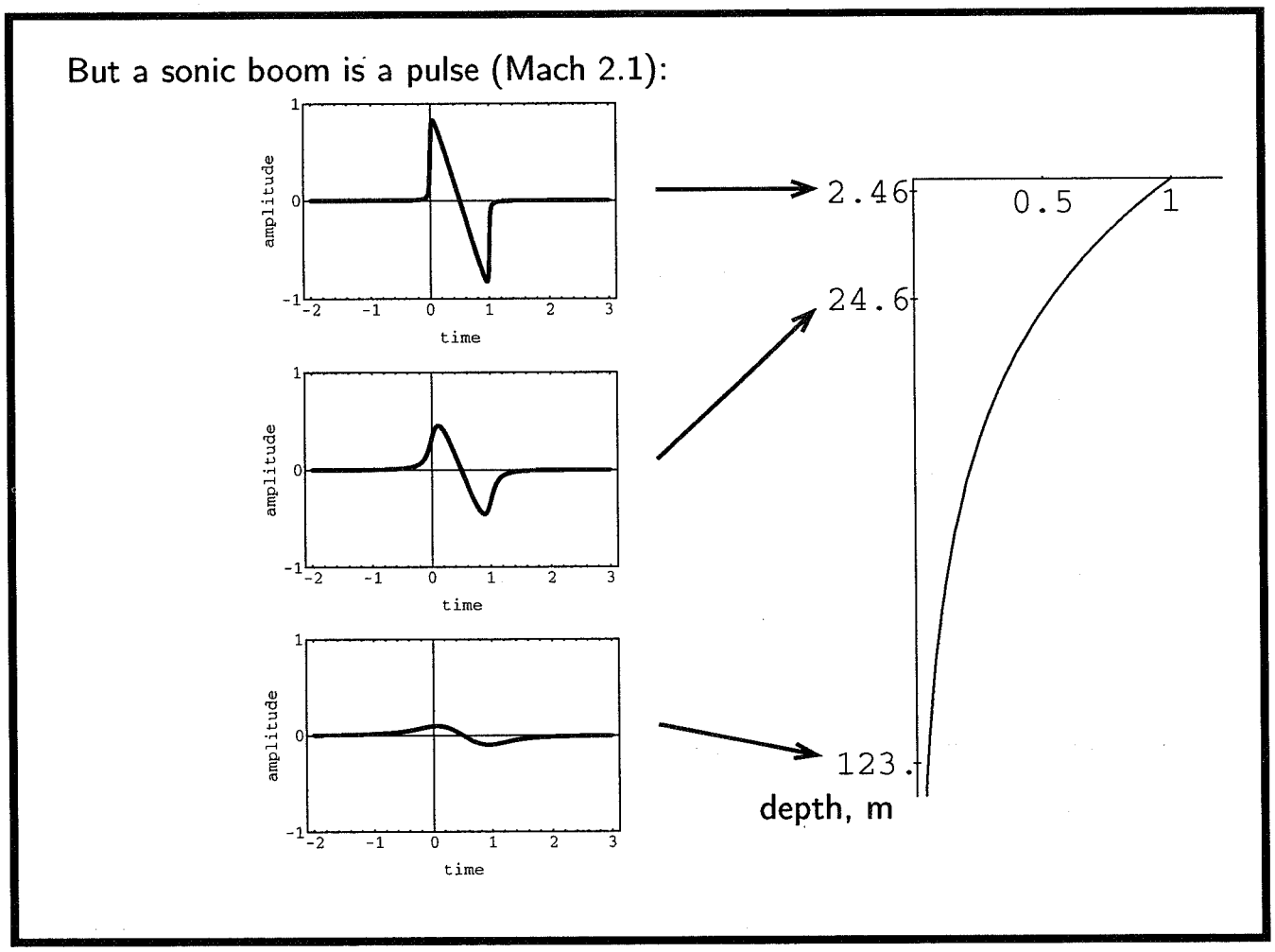

In 1968 the first theory to account for this penetration of sonic boom noise was developed by Sawyers. His theory is in terms of several nondimensionalized variables to represent time, distance, and depth. The theory assumes that the ocean is flat and is so deep that one need not account for bottom reflections. The assumption is also made that N wave shaped booms are incident on the ocean surface.

Sawyers' Theory

- Boom penetration theory due to Sawyers (1968) :

$$\pi \frac{p}{p_{\text{surface}}} = (2\tau + 2\xi - 1)\tan^{-1}\left(\frac{\tau + \xi - 1}{\zeta}\right) - (2\tau + 2\xi - 1)\tan^{-1}\left(\frac{\tau + \xi}{\zeta}\right) + \zeta \log\left[\frac{\zeta^2 + (\tau + \xi)^2}{\zeta^2 + (\tau + \xi - 1)^2}\right]$$

where τ, ξ, and ζ are nondimensionalized t, x, and z.

- Theory assumes ocean is perfectly flat, ocean is very deep, and booms are perfectly N shaped.

In 1970 Cook also closely examined the theoretical aspects of sonic boom penetration into the sea. Cook suggested several minor improvements to Sawyers' theory, but Cook noticed that the small differences between the theories were unlikely to be seen in field experiments.

In the early 1970s two separate laboratory experiments validated Sawyers' theory. Waters and Glass exploded small charges in air, modeling sonic booms, above a pond of water and measured the response of hydrophones below the water surface. Their measured waveforms closely matched those predicted by Sawyers' theory, even though their incident waves were small explosions instead of sonic booms.

Further Intrieri and Malcolm investigated the waveforms created by small supersonic projectiles. They sent such projectiles through the air over an aquarium and measured the acoustic pressure waveforms in the water. Intrieri and Malcolm's results were also in good agreement with Sawyers' theory.

- Sawyers' theory was later examined by Cook (1970), who suggested minor improvements.
- Theory validated by laboratory experiments of Waters and Glass (1970, 1972) and Intrieri and Malcolm (1973).

TODAY'S TALK: EFFECT OF AIRCRAFT SPEED

What hasn't been completely understood from Sawyers' theory alone is the effect of aircraft speed on the penetration of sonic boom noise into the ocean. As one examines Sawyers' nondimensionalized variables one can see that V, the aircraft speed, and T, the duration of the sonic boom, appear several times. Clearly to apply the Sawyers' theory correctly, one must have accurate speed and duration information.

Effect of aircraft speed?

(The major topic of this talk.)

- Examine Sawyers' nondimensionalized variables:

$$\zeta = z/(mT) \qquad \tau = t/T \qquad \xi = x/(TV)$$

where

$$m = V\left(1 - V^2/c^2_{\text{water}}\right)^{-1/2} ,$$

V - aircraft speed, and T - boom duration.

- Call $\hat{p} = p/p_{\text{surface}}$.

It turns out that the duration of the boom, T, is a function of the aircraft speed, V. This relationship is also more complicated than one might expect. Linear theory would predict that T=L/V where L is the length of the aircraft. Hence for a fixed velocity, longer aircraft (spatially) have longer sonic booms (temporally).

However, such linear theory neglects nonlinear acoustics effects. Because the sound from a sonic boom is reasonably loud, particularly near the aircraft, the sound waveform of a sonic boom lengthens as it propagates toward the ground. Thus one must account for this finite amplitude acoustical nonlinearity when determining the correct relationship between T and V.

Must be careful here: T is a function of V !

Linear theory would say:

$T = L/V$ where L is the aircraft's length.

Must include **nonlinear effects:**

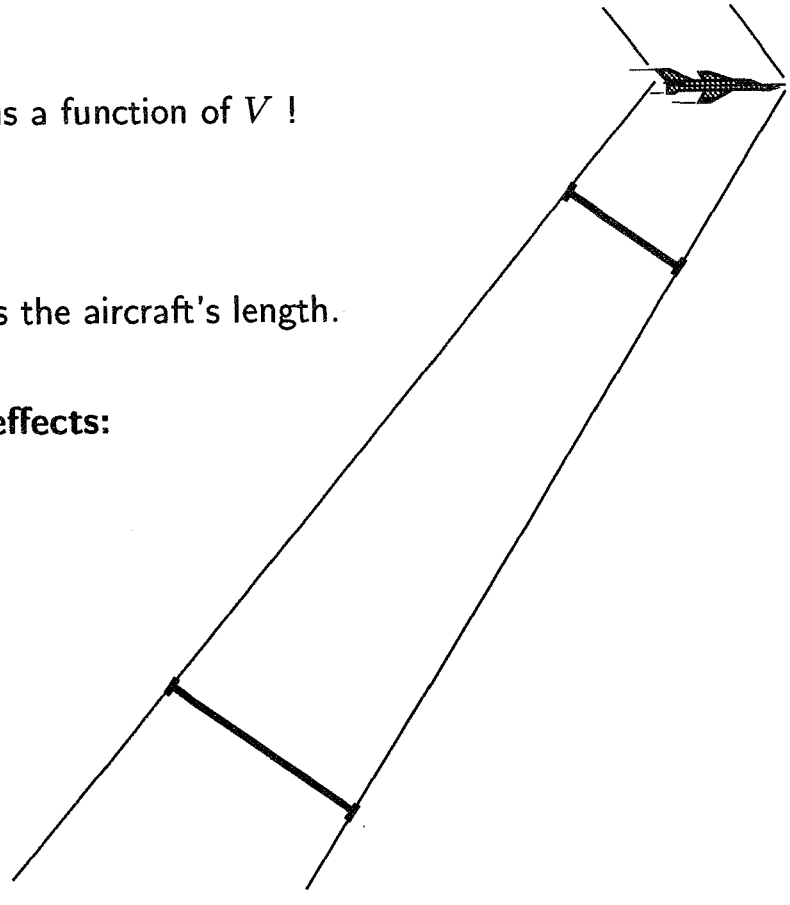

Several authors have shown that the duration of a sonic boom due to a projectile has the form shown below, as a function of Mach number, which is equal to V divided by the speed of sound. This T versus V relationship assumes that the aircraft is flying at a fixed altitude in steady flight. The theory has been compared to experimental data with good success. In spite of this, the theory assumes that there are no lift effects as one has for an airplane. More complicated theories are available.

Finite amplitude nonlinear acoustics theory predicts:

$$T = \kappa \frac{M}{(M^2 - 1)^{3/8}}$$

where κ is a constant; Pierce (1989), Maglieri and Plotkin (1991).

Assumptions:

- level flight at fixed altitude
- lift effects ignored

This theory is pretty good in describing $T = f(V)$.

Given that we now have a model relationship between T and V, and know how these factors influence the penetration of sonic boom noises into the ocean, it is time to determine what will be the maximum acoustic pressures which occur under the water's surface. One can determine the maximum pressure by taking the time derivative of the acoustic pressure from Sawyers' theory using the scaled time variable, setting this result to zero, and determining which value of scaled time satisfies the resulting equation. This procedure is necessary because the value of scaled time at which the maximum pressure occurs varies with depth.

What will be the peak pressure of the boom?

Find from:

$$\frac{\partial \hat{p}}{\partial \tau} = 0$$

to determine the value of scaled time τ at which $\hat{p}$ is a maximum.

Call this scaled time $\tau_{\mathrm{MAX}}(\zeta)$.

The maximum value of $\hat{p}$ is then

$$\hat{p}_{\mathrm{MAX}} = \hat{p}(\xi = 0,\, \zeta,\, \tau_{\mathrm{MAX}}(\zeta))$$

Shown in the figure below is the maximum pressure plotted as a function of Mach number for three different depths. The depths are 1 m, 10 m, and 100 m below the ocean surface. These curves are based on some SR-71 aircraft sonic boom experimental data in the possession of the author. The curves are based on an SR-71 traveling at a Mach number of 2.6 producing a nearly perfectly shaped N wave having a duration of 200 milliseconds.

As one can see the maximum scaled pressures generally increase with increased Mach numbers. The effect is more noticeable at deeper depths. Along the surface of the ocean the scaled maximum acoustic pressure would be 1 for all Mach numbers.

Maximum pressure as a function of Mach number, for different depths:

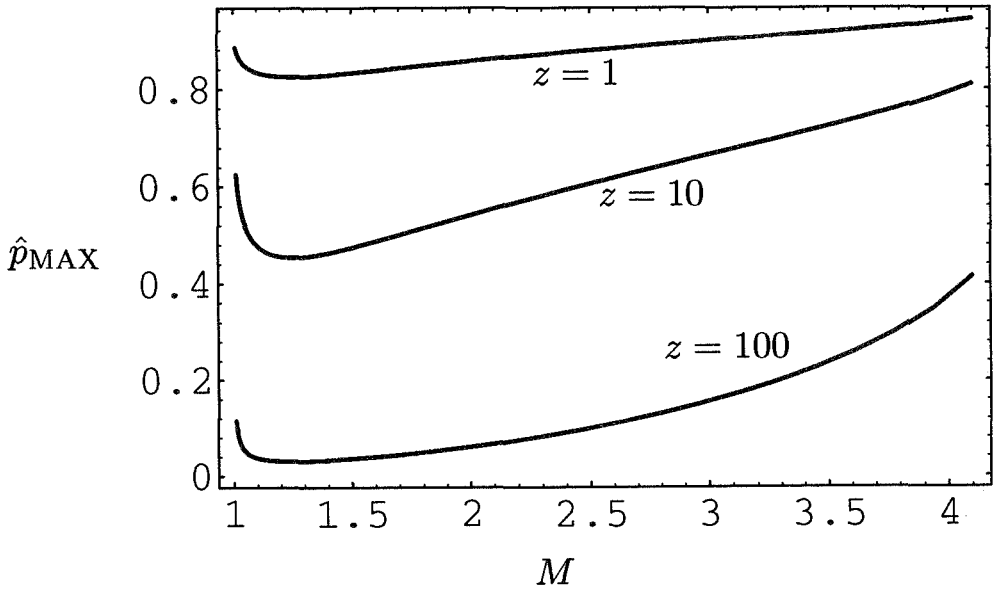

(Based on data for SR-71 aircraft: $T = 0.2$ s at $M = 2.6$.)

Shown in this figure is the same information, but on a relative decibel scale. The curve for each depth is scaled by the maximum pressure at Mach 2.6. One can see that for depths of 10 m or less, the maximum sound pressure level, SPL, will vary less than 6 dB over a wide range of Mach numbers. For greater depths, 100 m for example, increased Mach numbers may increase the SPL by 15 dB or more.

Maximum pressure, relative dB scale:

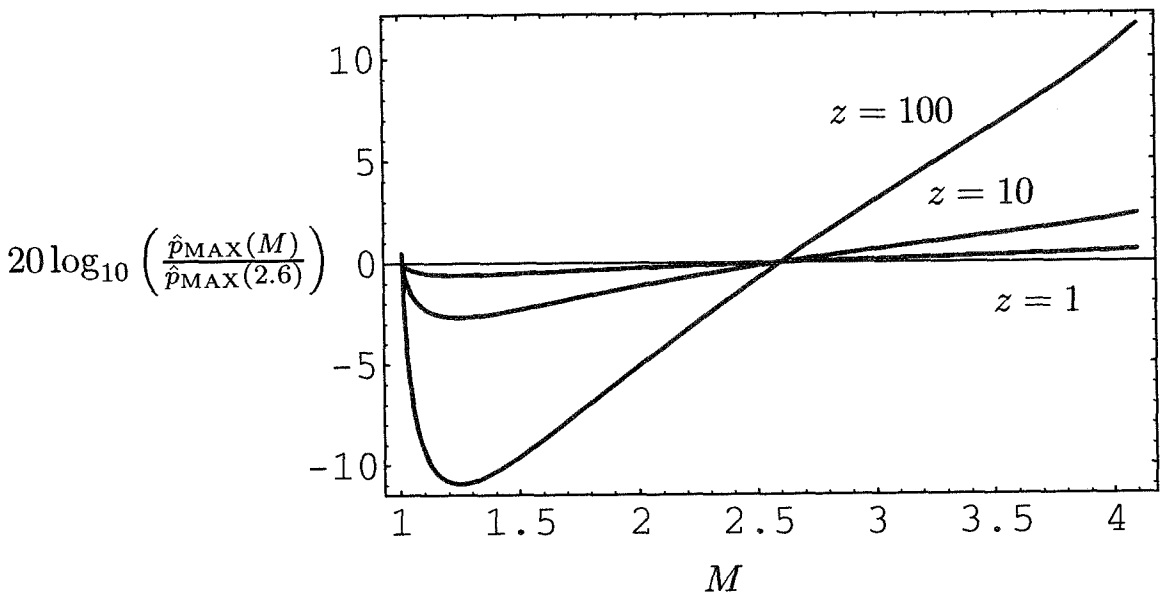

(Based on data for SR-71 aircraft: $T = 0.2$ s at $M = 2.6$.)

Instead of peak levels, one may also be interested in the time domain representations of the boom noise. Shown below are waveforms of scaled acoustic pressure versus scaled acoustic time. At the surface of the ocean the scaled pressure would have a value of unity and the duration of the boom in scaled time units would also be unity. The three columns represent an aircraft having speeds of Mach 1.4, 2.4, and 3.4. In each column the waveform is shown at depths of 1 m, 10 m, and 100 m.

One can clearly see that the waveforms at a depth of 1 m are nearly N waves. Further at 10 m the waveforms are similarly shaped and have amplitudes well in excess of 50% of the corresponding amplitude at the surface. The waveforms at 100 m are significantly smoothed out, except for high Mach numbers where a sizable waveform still exists.

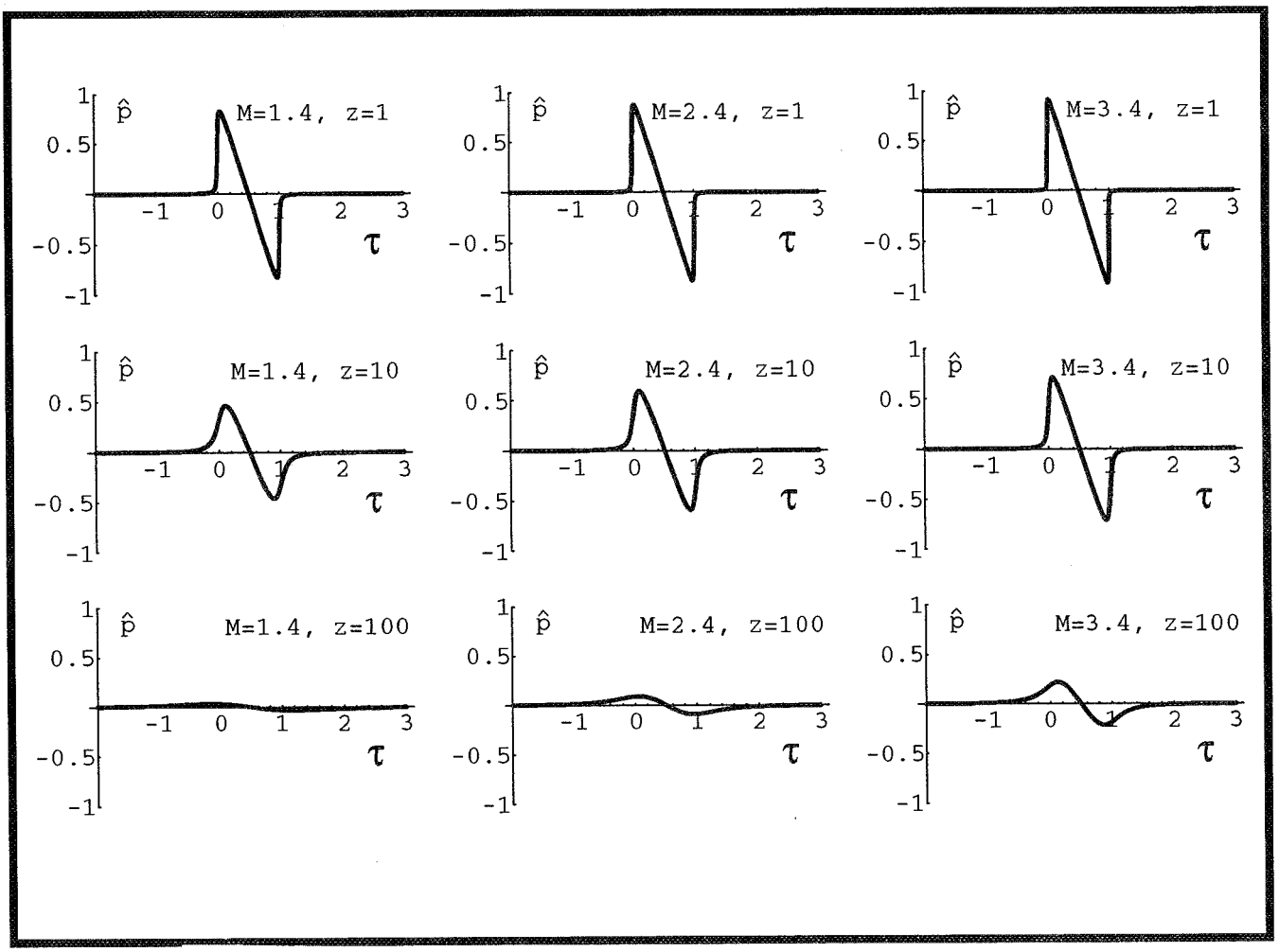

CONCLUSIONS

The major conclusion from this study is that faster flying supersonic aircraft produce sonic booms which penetrate more deeply into the ocean. The acoustic pressures experienced under the ocean's surface increase with increased Mach number.

The key to making these predictions using Sawyers' theory is an accurate functional relationship between the boom duration, T, and the aircraft velocity, V. Although the functional relationship used here has wide agreement with experimental data, it certainly could be improved upon to account for other factors such as aircraft lift and geometry.

This research is just the beginning, however. Many other factors must be taken into account to ascertain the sonic boom noise impact/non-impact on marine mammals. First of all, Sawyers' theory assumes that perfectly N shaped waves are incident. A similar theory should be developed for more realistically shaped sonic boom waveforms.

Conclusions

- Faster flying aircraft $\Longrightarrow$ increased penetration of boom noise.
- Using the correct $T = f(V)$ relationship is the key.
- More work needs to be done; this is only the beginning:

  Issues: Non N shaped waves. Include lift effects.

AN IMPORTANT UNADDRESSED ISSUE

In addition, another important issue should be addressed. The real ocean surface is rarely, if ever, flat. One should develop a boom penetration theory which takes into account the curvature of the ocean's surface.

This curvature causes the rippling surface of the ocean to act as a series of lenses, focusing and defocusing the sound under the surface. The focus spots can be considered acoustically hot, where the peak sound pressure levels could be substantially higher than in other regions below the surface. There has been no published research regarding this focusing and defocusing effect.

Another issue:

How often is the ocean perfectly flat?

Instead have **focusing** and **defocusing** for real sea surface:

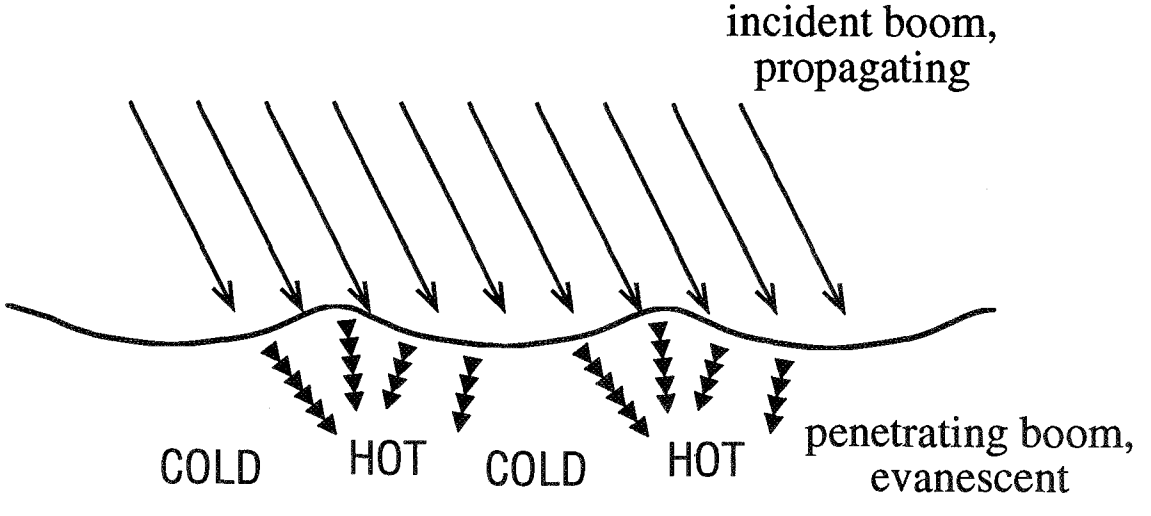

It would be standard to represent the sea surface as a superposition of Fourier modes as a first pass model. Then one could investigate the focusing effect by a number of analytical and numerical techniques.

For weak waves on the sea, called wind waves, analytical solutions would be tractable via perturbation expansion techniques available in modern symbolic algebra packages.

For wind waves of higher amplitude one could look into either analytical or analytical/numerical solutions to the Kirchhoff-Helmholtz integral equations. Such integral equations have been used to examine the propagation of constant frequency sound from air into water with a rippled surface. The extension of this methodology to sonic booms seems straightforward.

Further one can also perform finite difference calculations with conformal grids to model the penetration of sound in the air into the ocean. Such calculations would be invaluable for validating the perturbation expansion and Kirchhoff approaches. Hence, there are a number of methods available today for predicting the focusing effect.

Describe sea surface by Fourier superposition of many modes.

How to handle:

- Weak wind waves: Analytical perturbation solution via *Mathematica.*
- Higher wind waves: Kirchhoff-Helmholtz integral formulation.
  (Others have looked at this but not for sonic booms.)
- For comparison: Finite difference time domain calculations.

REFERENCES

Cook, R.: Penetration of a Sonic Boom into Water. *J. Acoust. Soc. Am.*, vol. 47, no. 5, pt. 2, 1970, pp. 1430–1436.

Intrieri, P.; and Malcolm, G.: Ballistic Range Investigation of Sonic-Boom Overpressures in Water. *AIAA J.*, vol. 11, no. 4, 1973, pp. 510–516.

Maglieri, D.; and Plotkin, K.: Sonic Boom. in *Aeroacoustics of Flight Vehicles: Theory and Practice,* Vol. 1: Noise Sources, Harvey H. Hubbard, Ed., NASA Ref. Pub. 1258, Vol. 1, WRDC Tech. Rpt. 90-3052, August 1991, p. 532.

Pierce, Allan D.: *Acoustics: An Introduction to Its Physical Principles and Applications.* Acoustical Society of America, Woodbury, NY, 1989.

Sawyers, K.: Underwater Sound Pressure from Sonic Booms. *J. Acoust. Soc. Am.*, vol. 44, no. 2, 1968, pp. 523–524.

Waters, J.: Penetration of Sonic Boom Energy into the Ocean: an Experimental Simulation. in *Noise and Vibration Control Engineering,* M. Crocker, Ed., Proc. of the Purdue Noise Control Conference, Purdue Univ., Lafayette, IN, July 14-16, 1971, pp. 554–557. Condensed from:

Waters, J.; and Glass, R.: Penetration of Sonic Boom Energy into the Ocean: An Experimental Simulation. Hydrospace Research Corp. Final Report on Contract FA70WAI–185, HRC TR 288, (June 1970), available from NTIS/DTIC as AD 711 963.

PENNSTATE

Wolfram Research Inc., *Mathematica,* Ver. 2.2 (Wolfram Research, Inc., Champaign, IL, 1993).

SIMPLE ATMOSPHERIC PERTURBATION MODELS FOR SONIC-BOOM-SIGNATURE DISTORTION STUDIES

L. J. Ehernberger
NASA Dryden Flight Research Center
Edwards, California

Morton G. Wurtele and Robert D. Sharman
University of California
Los Angeles, California

INTRODUCTION

Sonic-boom propagation from flight level to ground is influenced by wind and speed-of-sound variations resulting from temperature changes in both the mean atmospheric structure and small-scale perturbations (refs. 1–5). Meteorological behavior generally produces complex combinations of atmospheric perturbations in the form of turbulence, wind shears, up- and downdrafts, and various wave behaviors. Differences between the speed of sound at the ground and at flight level will influence the threshold flight Mach number for which the sonic boom first reaches the ground as well as the width of the resulting sonic-boom carpet (refs. 6–8). Mean atmospheric temperature and wind structure as a function of altitude vary with location and time of year. These average properties of the atmosphere are well-documented (for example, refs. 9 and 10) and have been used in many sonic-boom propagation assessments. In contrast, smaller scale atmospheric perturbations are also known to modulate the shape and amplitude of sonic-boom signatures reaching the ground, but specific perturbation models have not been established for evaluating their effects on sonic-boom propagation. The purpose of this paper is to present simple examples of atmospheric vertical temperature gradients, wind shears, and wave motions that can guide preliminary assessments of nonturbulent atmospheric perturbation effects on sonic-boom propagation to the ground. The use of simple discrete atmospheric perturbation structures can facilitate the interpretation of the resulting sonic-boom propagation anomalies as well as intercomparisons among varied flight conditions and propagation models.

Outline

- **Introduction**
  - **Example atmospheric profile**
    - **Wind shear probabilities**
      - **Temperature gradient statistics**
        - **Single mode wave model**
          - **Closing remarks**

An observed atmospheric profile is used to illustrate discrete atmospheric layers with strong wind shear and high-temperature gradient values. Statistics for vertical wind shears measured by FPS-16 radar tracking Jimsphere balloons and by the conventional upper-air rawinsonde measurements (refs. 10–14) are presented. These wind statistics and data for vertical temperature gradients in the lower stratosphere also indicate the magnitudes of nonturbulent atmospheric perturbations that may be of concern to sonic-boom propagation studies. Turbulent eddies at the Earth boundary layer distort the sonic-boom overpressure time history signature arriving at the ground. Distortions produced by turbulent layers far from the ground will tend to return to an undistorted N-wave shape signature before reaching the ground. Larger scale wind shears, temperature gradients, and oscillatory activity, such as mountain waves and other atmospheric wave motions, may act like airplane maneuvers to modulate sonic-boom signatures over distances of a few miles as a result of focusing boom overpressure into strong and weak regions.

Waves are induced by flow over topographic or cloud barriers and their effects are often visible in the resulting cloud patterns. Wave phenomena have received much qualitative attention in both observation and analysis (refs. 15–17). However, very little statistical documentation exists to quantify their intensity, and computational methods have only recently shown the capability to realistically handle wave behavior. A particular atmospheric gravity wave model, consisting of a solitary wave mode (ref. 18), is proposed here for initial evaluation of nonturbulent atmospheric perturbation effects on sonic-boom signatures at ground level. Such a model incorporates realistic combinations of vertical and horizontal wind disturbances with their attending temperature or density variations. It also approximates the real atmosphere for cases in which a succession of wave crest cloud lines are observed downwind of mountains or islands.

Influence of Atmospheric Variations on Sonic Booms

- **Mean wind and temperature profiles determine**
  - **— Threshold Mach number**
  - **— Boom carpet**
  - **— Intensity effects**
- **Small scale turbulence distorts signatures**
- **Greater "healing" distances required for quasi-stationary gradients and wave motions**
- **Assessment of effects on conventional and "shaped" signatures can be facilitated by use of discrete models and field measurements**

REAL-DAY ATMOSPHERIC PROFILE EXAMPLE

Strong weather fronts and jet-stream activity induce large temperature gradients and wind shears in the atmosphere. Horizontal temperature gradients tend to be in balance with vertical wind shears, and stable vertical temperature stratification tends to preserve wind-shear layers. Stable stratifications occur when the decrease in temperature with altitude (lapse) is less than that associated with an adiabatic process following the decrease in pressure with altitude. Thus, isothermal layers and inversion layers (where temperature actually increases with altitude) provide static stability that tends to maintain wind-shear layers. As the sonic boom propagates through the atmosphere, nonuniform changes in the speed of sound along the shock front bend the direction of propagation to produce focusing effects. Propagation speeds change directly with wind or air motion changes and with temperature. A 1-percent change in the speed of sound will be experienced for a temperature change of approximately 5 °C.

The figure below illustrates a case (April 10, 1994, Edwards CA) with both strong wind shear in a mid-tropospheric stable layer and a strong temperature inversion above the tropopause. Windspeeds increase from 23 knots at 13,000-ft altitude to more than 78 knots at 16,000 ft and reach peak speeds of 98, 110, and 114 knots at altitudes of 20,000, 25,000, and 34,000 ft, respectively. The vector wind shear, given by the wind vector change divided by the altitude interval over which the change takes place, reaches a maximum of 0.040/sec at 15,000 ft. Temperature is nearly constant or increasing with altitude between 13,300 and 16,500 ft. The vertical temperature gradient or inversion rate reaches a maximum of +8 °C/1000 ft between 15,400 and 15,800 ft.

Above the tropopause, which is marked by a minimum temperature of –66.3 °C at 42,350 ft, the temperature increases to –52.3 °C at 45,760 ft. The overall inversion rate for the 12.5 °C temperature change in this layer is 3.6 °C/1000 ft. A maximum rate of about 5 °C/1000 ft is observed between 43,000- and 44,000-ft altitude. The windspeeds begin a marked decrease with altitude above the tropopause.

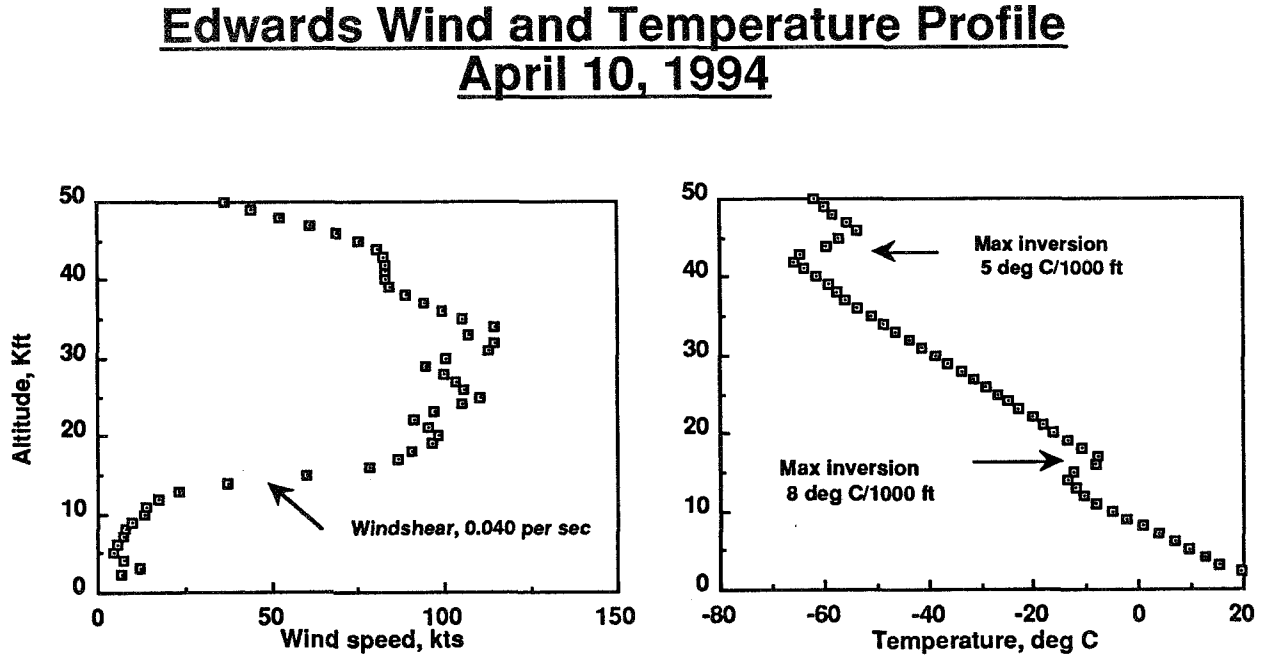

WIND SHEAR PROBABILITIES

Measured wind-shear magnitudes depend on the depth of the layer over which the shear is measured. Detailed wind-shear observations and their statistical analyses for altitudes below 60,000 ft have been abundant since the initiation of the manned Space Program. These observations have used special balloons (Jimspheres) tracked by FPS-16 radar to altitudes near 60,000 ft and conventional weather balloons to altitudes of about 100,000 ft. Jimsphere wind data studies accomplished by the NASA Marshall Space Flight Center (refs. 10-13) have provided a wealth of information on wind changes and wind shears and on the relationship between wind shear and the thickness of the altitude layer over which the shear is measured. Wind shear is measured to a reasonable accuracy over layers thicker than about 300 ft by the Jimsphere and over layers greater than about 2000-ft thick by rawinsonde balloons used for routine upper-air weather observations (ref. 12). Selected data shown below illustrate the variation of the measured wind shear as a function of the altitude thickness over which the shear is measured. To bracket a range of stronger shear values, the figure illustrates a 90-percentile curve for July, when wind shears are weaker, and a 99-percentile curve for February, when they are stronger. Wind shears exceed the values shown by these curves for 10 and 1 percent, respectively, of the observations. For convenience of application, wind shear in units of speed change per unit altitude distance can simply be expressed in units of inverse seconds (or per second).

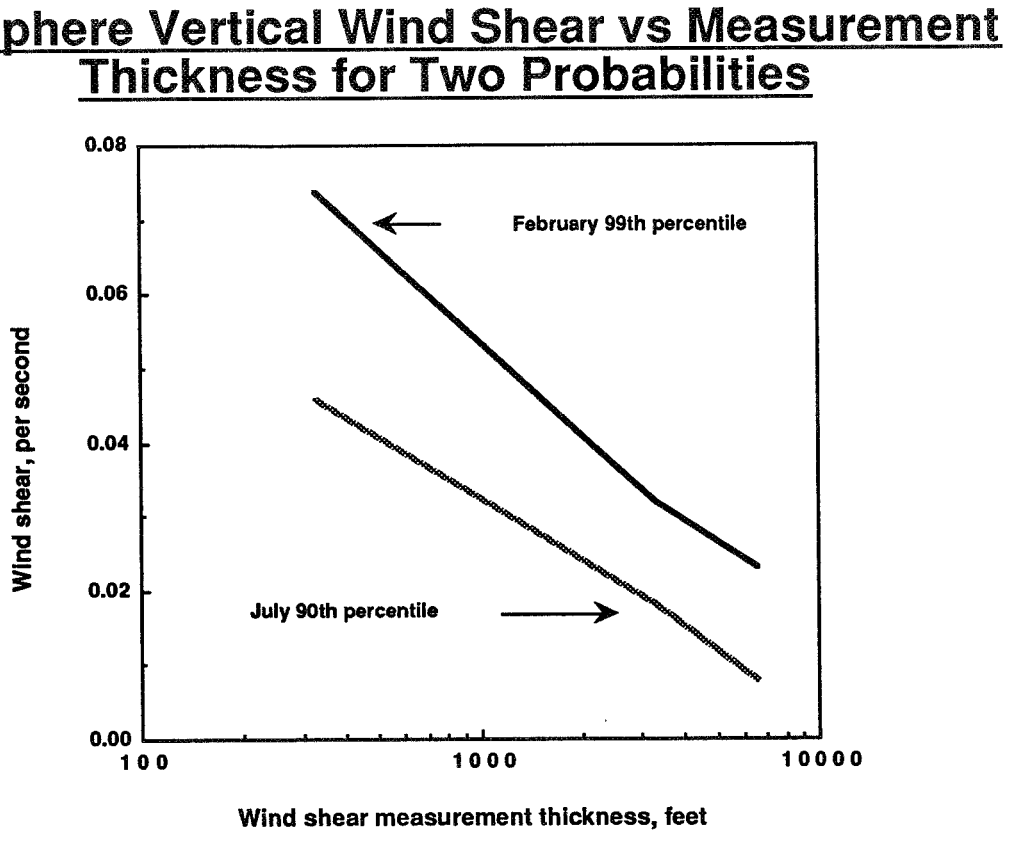

WIND SHEAR PROBABILITIES (cont'd.)

Wind shears measured over large altitude distances (or thickness scales) have a positive correlation with windspeed and therefore tend to decrease from a maximum near jet stream altitudes to minimum shear magnitudes in the middle stratosphere, just above supersonic cruise altitudes. This decrease in wind-shear magnitudes in the lower stratosphere is depicted below by curves extracted from rawinsonde data for altitudes of 45,000 and 80,000 ft (ref. 14). Based on these data the maximum shear magnitude measured in the real-day example profile (shown previously) is indicated to be beyond the 99.9-percentile value.

Example Maximum Vertical Wind Shear Probability from Rawinsonde Measurements

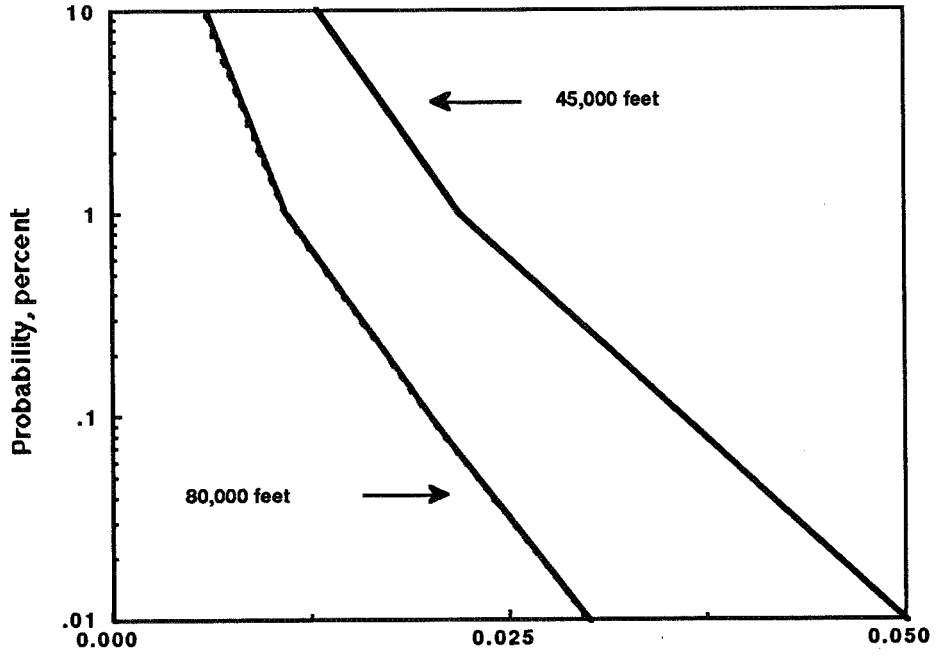

STRATOSPHERIC TEMPERATURE GRADIENT STATISTICS

Because the speed of sound in air is a direct function of ambient temperature, the sonic-boom propagation direction will bend when strong temperature gradients are traversed at an oblique angle. The strongest gradients are associated with inversion layers in the lower stratosphere. Statistical analyses of temperature gradient features have not been nearly as adequate as for windspeed and wind shear. Reference 14 reports on an examination of a limited amount of rawinsonde data for (a) strong lapse rates (temperature decrease with altitude) or (b) strong inversion rates (temperature increase with altitude) within layers surrounding the mandatory meteorological reporting levels. This study was motivated to improve the knowledge of probabilities for features associated with high-altitude turbulence experienced by supersonic cruise aircraft. Values depicting the 1.0-, 0.1-, and 0.01-percentile extremes for these data are shown below.

Note that in the lower stratosphere the magnitudes for the decreasing gradients are not as large as those for the increasing temperature gradients. At both the 0.1- and 0.01-percentile frequency of occurrence the decreasing temperature with altitude exceeds the adiabatic lapse rate (3 °C/1000 ft), presumably as a result of measurement error in some cases and strong atmospheric dynamics in others. The increasing temperature gradient at 0.01 percentile rate, 24 °C/1000 ft, is comparable to a density departure rate of approximately 10 percent/1000 ft from the standard day atmosphere, as well as to the speed of sound changing by 5 percent/1000 ft from the standard atmosphere values.

Maximum Temperature Gradients Within Layer for Selected Probabilities

Frequency exceeded	1.0 % ile	0.1% ile	0.01 % ile
Decreasing temperature gradient, °C/1000 ft	–2.9	–3.6	–4.2
Increasing temperature gradient, °C/1000 ft	10	16	24
Temperature increase, °C	8	10	12
Nominal thickness, ft for gradients above 5 °C/1000 ft	1000	2000	3000
Nominal thickness, ft for ΔT above 5.0 °C	1600	1000	500

As indicated by the data in the previous figure, temperature increases of more than 10 °C occur at a 0.1-percentile rate. Inversion rates of 5 °C/1000 ft extend over layer depths of 3000 ft at a 0.01-percentile rate of occurrence. A reciprocal situation, temperature changes of 5 °C (or greater) occurs over layer thicknesses of less than 500 ft, also at the 0.01-percentile rate of occurrence. Probability curves for the lapse (decreasing with altitude) and inversion (increasing with altitude) temperature gradients within layers of the lower stratosphere are shown in the figure below.

At times, strong inversion layers are located both above and below strong decreasing temperature (lapse) layers in the lower stratosphere. The occurrence of these strong vertical temperature gradients exhibits seasonal dependence and indicates some conditional association with high jet stream windspeeds and strong lower altitude wind-shear layers. These data indicate that lapse rates in the lower stratosphere equal or exceed the dry adiabatic and that inversion rates may exceed 10 °C/1000 ft with overall changes of more than 10 °C. In summary, strong inversions can increase the speed of sound by more than 2 percent in relatively shallow inversion layers. Depending on wind and flight headings, temperature and wind effects may combine to change the speed of sound by nearly 5 percent across layers of 1000 ft and thicker.

Probability of Maximum Temperature Gradient within Layer

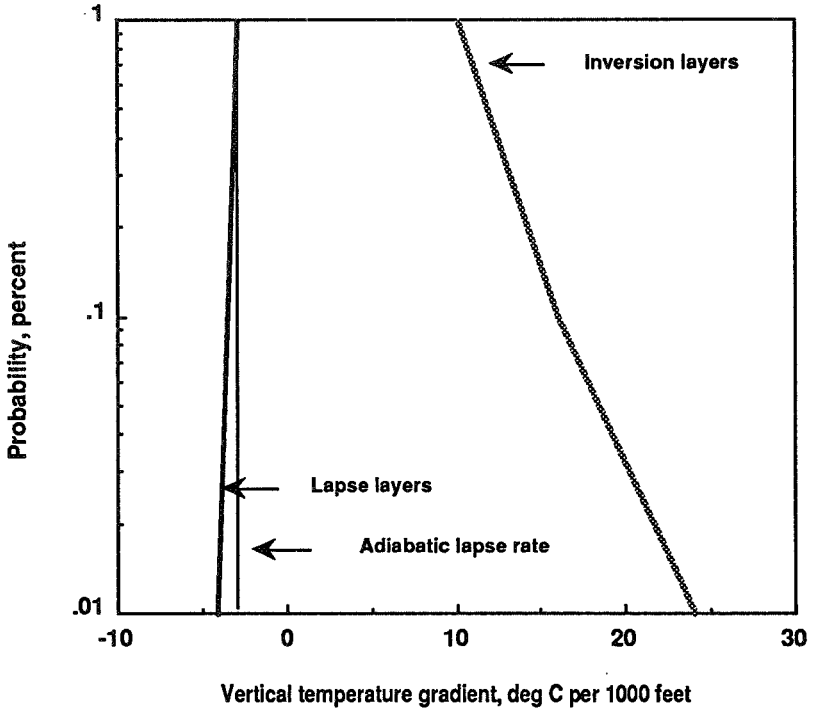

Atmospheric vertical motion perturbations are subject to wave behavior nearly all the time except when the vertical temperature profile does not provide static stability. The resulting wave behavior can exhibit multiple modes or wavelengths with both modes and amplitudes changing drastically from one altitude layer to another (see outline below). Strong gravity wave motions are experienced in both the troposphere and at proposed high-speed civil transport (HSCT) cruise altitudes in the stratosphere resulting from dynamic excitation of interactions between the force of gravity and atmospheric buoyancy. Resonant interactions are generally possible at all times when the temperature decrease with altitude is not adiabatic or superadiabatic. Under favored structures of the wind and temperature profiles, barriers to the flow, such as mountains or vigorous cumulus cloud lines, and jet stream oscillations can trigger wave motions in which the resulting vertical motions can be intense and wave amplitudes can be quite large. Such behavior, with complex upstream atmospheric structure, is often beyond solution by classical mathematical analysis.

Initial analyses of the effects of gravity wave motions on sonic-boom propagation for various flight altitudes and trajectories could be overly complicated by the presence of multiple wave modes interacting in an atmospheric structure, which changes markedly from one altitude layer to another. These complications for initial studies of wave effects on boom propagation and focusing can be alleviated by either of two restrictions.

Attributes of Atmospheric Gravity Wave Behavior

- **Motion perturbations result from interaction between**
  - **— Wind profile characteristics**
  - **— Presence of flow barriers**
  - **— Temperature profile stability or buoyance effects**
- **Wavelength distances between 5 and 50 miles are often observed**
- **Large wave amplitudes occur over the full HSCT altitude range**
- **Dominant wavelengths generally change with altitude**
- **Analytical and numerical treatment of 2-D wave behavior is**
  - **— Fairly extensive and maturing**
  - **— Lacking in field observation validation**
- **Realistic, simplified representations of wave behavior in the troposphere and lower stratosphere can be generated**

One method is to restrict attention to two-dimensional wave cases that produce high-amplitude perturbations for only one or one-and-a-half wavelengths. Another means of simplification is to restrict attention to two-dimensional wave cases that produce a single-mode (i.e., single-wavelength) trapped wave. This second simplification is believed of more general interest and is described below.

The schematic below shows a two-dimensional trapped, single-mode wave to illustrate the variation of wave induced motion perturbations in the various wave sectors. The wave is produced by a numerical simulation (ref. 18) using an analytically selected upstream profile with constant shear (depicted on the left) and stability (i.e., constant lapse rate). Flow following the streamlines experiences the greatest vertical motion perturbations at the altitude of maximum wave amplitude and at inflection points between troughs and crests. Vectors (not to scale) show downward perturbation velocities from the crest to the trough and upward velocities from the trough to the crest. Temperature perturbations also reach their greatest amplitudes at the altitude of maximum wave amplitude. Temperature increases (warming) occur in the troughs where the air has descended to higher pressures with adiabatic heating; temperature decreases (cooling) occur in the crests where the air has ascended from its upstream altitude level. Horizontal wind perturbation vectors (not to scale) show that the wave dynamics increase horizontal windspeeds in the lower section of the troughs and the upper sections of the crests. Horizontal speeds are reduced in the upper section of the troughs, where the wave amplitude decreases with altitude, and in the lower section of the crests, where rotors with reverse flow near the ground are sometimes created.

Gravity Wave Schematic with Wave-Induced Perturbation Velocity Components

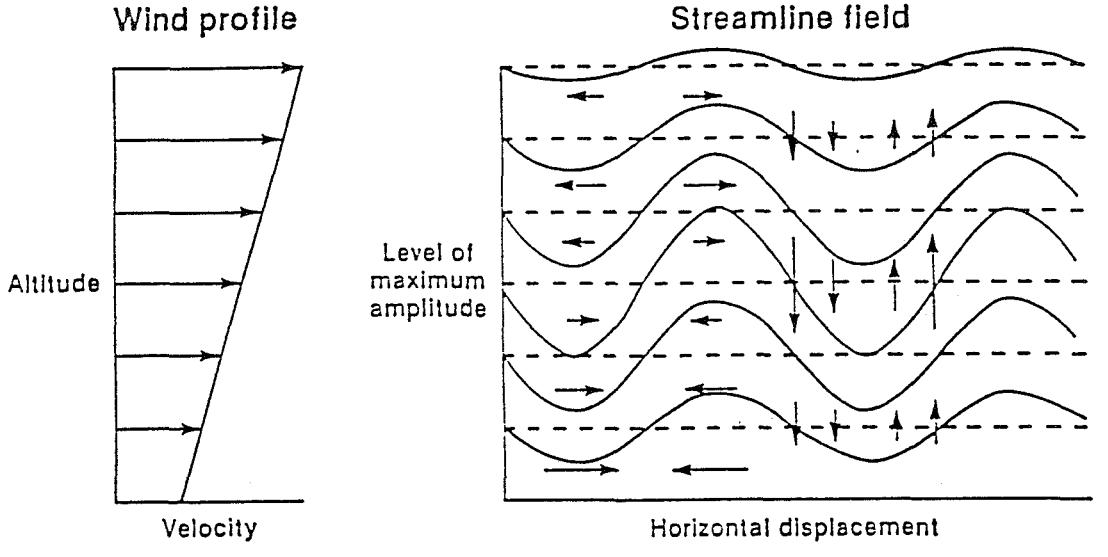

MODEL WAVE INTENSITIES

Selected barrier conditions and atmospheric structure were used to produce a single-mode wave, as described above, by both analytical solution and numerical simulation (ref. 18, Case II). This case generated a nominal intensity wave using a barrier height of approximately 1600 ft in a wind of 20 knots at the base altitude and increasing a modest 2 knots/1000-ft altitude. The temperature lapse rate was 2.25 °C/1000 ft, fairly typical of the lower troposphere and near the standard atmosphere value of about 2 °C/1000 ft. Maximum wave amplitude is attained at an altitude near 10,000 ft, where the stream function's trough-to-crest height change is approximately 4600 ft and the temperature change from trough to crest is about 3 °C. At 10,000-ft altitude the upstream windspeed is about 40 knots, and a wavelength of about 11 nmi prevails throughout the wave pattern. Horizontal windspeed varies by 16 knots from maximum to minimum at the surface and 3 to 4 knots at 15,000-ft altitude. The maximum up- and downdraft velocities are approximately 8 ft/sec. Strength of this wave would be subjectively rated as light or weak, on the basis of the induced vertical velocity and its limited extent above the barrier height. Its amplitude and wavelength are fairly representative of extended (or trapped) wave conditions in which several lines of crest clouds are observed downstream of flow barriers. A stronger wave case, in which the maximum vertical velocity is greater by a factor of at least 3, should also be used in boom propagation studies to encompass a large portion of likely wave amplitudes.

Strong temperature gradients and wind shears are generated locally within the wave structure. The boom propagation effects of similar strength shears and gradients in quasi-continuous layers should be compared with the wave cases to delineate the added focusing effects of vertical motion and wave shape. Layer slopes with respect to flightpath could be varied to cover the range experienced in the wave structures. Based on climatology and clear air turbulence experience, intensities of wind shear used for boom propagation studies should range from less than 0.010/sec (light) to more than 0.020/sec (strong). A realistic range for temperature gradients, which could combine with the wind shear, is from –3 °C/1000 ft to more than +10 °C/1000 ft.

An Approach for the Study of Boom Propagation through Atmospheric Waves

- **Lower- and mid-tropospheric wave cases**
  - **— Two representative wave intensities or amplitudes**
  - **— Flight altitudes from level of max amplitude to cruise**
  - **— Mach range at each altitude to cover most aircraft types**
- **Upper-troposphere wave cases**
  - **— Two wave intensities and flight conditions varied as above**
  - **— Limit altitude band of wave excitation**
  - **— Use both up- and down-wind headings**
- **Lower-stratosphere wave cases**
  - **— More cases to cover greater range of wind and temperature profiles**
  - **— Two wave intensities and flight conditions varied as above**

MODEL WAVE INTENSITIES (cont'd.)

Variables in the boom-propagation study will include flight altitude and Mach number as well as the wave models. Suggestions for the scope of conditions to be studied are listed below. The generation of simple, yet realistic, wave models in the upper troposphere and lower stratosphere will require added consideration of the input barrier and atmospheric structure.

CLOSING REMARKS

Atmospheric gradients and wave motions can affect sonic-boom propagation. Simple, discrete examples that can guide studies of boom propagation have been described in this paper. The specification of wave cases for boom work should initially avoid the potential complexities that could result from variation of wave amplitude and wavelength from one altitude layer to another. It is recommended that initial studies of boom propagation through wave perturbations be attended by propagation cases through similar-strength stratified layers that slope in relation to the flightpath.

- **Sonic boom propagation is subject to atmospheric turbulence, gradients and waves**
- **Complex atmospheric wave behavior can easily complicate boom propagation studies**
- **Realistic simplifications of wave behavior will facilitate the interpretation of boom propagation study resutls**
- **Comparison of wave induced boom focusing effects with those from stratified gradients of similar intensity is recommended**

REFERENCES

1. Garrick, I. E.; and Maglieri, D. J.: *A Summary of Results on Sonic-Boom Pressure-Signature Variations Associated with Atmospheric Conditions*, NASA TN D-4588, 1968.

2. Kane, E. J.; and Palmer, T. Y.: Meteorological Aspects of the Sonic Boom. SRDS Report No. RD-64-160, Federal Aviation Agency. ASTIA No. AD 610463, 1964.

3. Magilieri, Domenic J.; Hilton, David. A.; and McLeod, Norman J.: *Experiments on the Effects of Atmospheric Refraction and Airplane Accelerations on Sonic-Boom Ground-Pressure Patterns*, NASA TN D-3520, July 1966.

4. Darden, Christine M.: *Status of Sonic Boom Methodology and Understanding*, NASA CP-3027, 1988.

5. Bedard, Alfred J., Jr.: The Measurement of Sonic Boom Waveforms and Propagation Characteristics: Techniques and Challenges. AIAA-90-4004, Oct. 1990.

6. Magilieri, D. J.; Hilton, D. A.; Huckel, V.; Henderson, H. R.; and McLeod, N. J.: *Measurements of Sonic Boom Signatures from Flights at Cut-off Mach Number. Third Conference on Sonic Boon Research*, NASA SP-255, 1971, pp. 243–254.

7. Haglund, George T.; and Kane, Edward J.: *Analysis of Sonic Boom Measurements Near Shock Wave Extremities for Flight Near Mach 1.0*, NASA CR-2417, 1974.

8. Brown, Jessica G.; and Haglund, George T.: Sonic Boom Loudness Study and Airplane Configuration Development. AIAA-88-4467, Sept. 1988.

9. Smith, O. E.; and Galusha, B. W.: Range Reference Atmospheric Models. *Proceedings of 8th Conference on Probability and Statistics in Atmospheric Sciences, Hot Springs, AR, November 16–18, 1983*, pp. 94–104.

10. Johnson, D. L., ed.: *Terrestrial Environment (Climatic) Criteria Guidelines for Use in Aerospace Vehicle Development*, NASA TM-4511, [revised] Aug. 1993.

11. Scoggins, James R.: Aerodynamics of Spherical Balloon Wind Sensors in Turbulent Flows. *J. Geophysical Research*, vol. 69, no. 4, Feb. 1964.

12. Fichtl, George H.: *The Responses of Balloon and Falling Sphere Wind Sensors in Turbulent Flows*, NASA TN D-7049, Feb. 1971.

13. Vaughan, William W. : *An Investigation of the Temporal Character of Mesoscale Perturbations in the Troposphere and Stratosphere*, NASA TN D-8445, March 1977.

14. Ehernberger, L. J.; and Gutman, Nathaniel B.: *Climatological Characteristics of High Altitude Wind Shear and Lapse Rate Layers*, NASA TM-813563, Feb. 1981.

REFERENCES (cont'd.)

15. Holmboe, Jorgen; and Klieforth, Harold: Investigation of Mountain Lee Waves and the Air Flow Over the Sierra Nevada. Final Report Contract No. AF 19(604)-728, March 1957 [available as AFCRC TR 57 204, ASTIA 113 606].

16. Helvey, R.A.: Observations of Stratospheric Clear-Air Turbulence and Mountain Waves Over the Sierra Nevada Mountains—An Analysis of the U-2 Flights of 13–14 May 1964. Air Force Cambridge Research Laboratories, AFCRL-68-0001, 1967.

17. Wurtele, M. G., A. Datta, and Sharman, R. D.: *Lee Waves: Benign and Malignant,* NASA CR-186024, June 1993.

18. Wurtele, M. G. and Sharman, R. D.: *Perturbations of the Richardson Number Field by Gravity Waves*, NASA CR-176910, July 1985.

USAF SINGLE-EVENT SONIC BOOM PREDICTION MODEL: PCBoom3

Kenneth J. Plotkin
Wyle Laboratories
Micah Downing
USAF Armstrong Laboratory
Juliet A. Page
Wyle Laboratories

USAF SINGLE-EVENT SONIC BOOM PREDICTION MODEL: PCBoom3

ABSTRACT

The Air Force has developed PCBoom3, a general-purpose, single-event sonic boom prediction model. The model operates on an IBM PC or compatible, under DOS or Windows. It is accessed via an integrated environment which controls building of input cases, running boom calculations, displaying contours and signatures, and managing all associated data. The primary boom calculation is via a variation of FOBOOM, the focus-boom extension of Thomas's program. Aircraft input is either via a user-provided F-function, or simple N-wave F-functions tabulated for about 20 current aircraft. A fast boom calculation, based on Plotkin's SBORT algorithms, is included for simple N-wave F-functions in a windless atmosphere and flight altitudes up to 60,000 feet. After a run is complete, the user can access an index identifying significant events (focal zones, beginning of footprint, etc.), then plot boom amplitude contours and signatures or spectra at any point in the footprint. The primary uses of this program are expected to be operational planning and boom incident investigation. However, because of the commonality between FOBOOM and the MDBOOM program currently being used for low boom configuration design, this program is of interest to the HSCT community, especially as supersonic route planning activity increases.

The Air Force recently conducted a flight test program to evaluate the focal zone capabilities of PCBoom3. Initial results of that program validate the prediction of focal zone geometry, amplitudes, and waveforms.

[This work was sponsored by USAF AL/OEBN.]

PCBoom was developed to satisfy three basic Air Force needs. The first is a tool to predict sonic booms for use in environmental assessments of proposed actions. The second is a planning tool to minimize impact to sensitive areas. An example of this type of planning is if the operators of an offshore supersonic range would like to set daily minima for how far out the range users must go. The third application is to quantify what happened when an unintended incident does happen.

These needs lead to the requirement for a program that is relatively easy to use, runs quickly, and can be hosted on a PC. It is essential that input is as flexible as possible, and that output be available in graphical format.

AIR FORCE REQUIREMENTS

- **Single-Event Sonic Boom Impact Prediction**
- **Planning Tool**
- **Sonic Boom Incident Investigation**

The program has several methods for specifying trajectories. First, there is a file structure similar to that of FOBOOM/MDBOOM. Second, there is a general "Maneuver Driver" which allows interactive description of a maneuver. This is aimed at the planner or airspace manager who must be able to work with virtually any description of a maneuver. The interactive form of "ManD" helps the user reconcile information that may be inconsistent. Third, the program can import trajectory data from sources such as radar tracking, ACMI, or pre-computed trajectories. The program is designed to import these from a relatively benign ASCII file format. A user with unique data forms can prepare a conversion routine to this specification.

The program uses standard sonic boom ray tracing theory, and includes focus analysis via Guiraud's similitude and the Gill-Seebass numeric focus signature. Use of this program for environmental planning and claim investigation requires that it employ state-of-the-art methods.

Outputs are contours of equal overpressure (or other metrics), isopemp charts which provide a good visual interpretation of footprints and focal zones, and signatures and spectra.

GENERAL FEATURES

- **General Flight Profile Input**
- **Full Ray Tracing Scheme**
- **Non-Standard Atmosphere, With Winds**
- **Focus and Post-Focus Boom Impact Regions**
- **Outputs: Contours, Footprints (Isopemps), Signatures, Spectra**

The user works primarily with a simple pull-down menu system. The goal of this module is to set up the data stream needed by the computational modules that actually do the work. When a computational module is ready, MIM writes a batch file to execute it, then exits. The batch file ends by re-running MIM, putting the user back in the menus. This program is PC specific, but would be fairly simple to replicate on other interactive systems.

PROGRAM STRUCTURE:
MASTER INPUT MODULE (MIM)

- **Manages All Data, User Inputs, Via Simple Menu System**
- **Sets Up Runs Stream for Computational Modules**
- **Initiates Computational Modules as Separate Processes**
- **PC-Specific Interface**

The real work is done in the computational modules. These are written in Fortran 77, and for the most part are portable. Graphics are done with a PC-specific Fortran-callable plotting library with "industry standard" call styles. ManD, PCBPlot, and SIGOUT have PC-specific interactive interfaces, but these are kept isolated from the computational parts.

Boom calculations are done by either the full-theory FOBoom3 module or, for applications requiring very fast analysis, a scheme based on the rapid SBORT algorithms. Both schemes yield a file of boom signatures on the ground. This file is processed by a "footprint processor" which organizes it and indexes it for use by the output modules PCBPlot and SIGOUT.

It is worth noting that the FOBOOM3 module is derived from the same code from which MDBOOM was developed. It does not contain the proprietary configuration analysis tools, but those have been removed by blocking out subroutine calls and removing the corresponding modules. MDBOOM users may find it useful to adapt some of the new features to their work. As many routines as possible have been kept identical between the two programs, which will be of long-term benefit to maintenance of both.

COMPUTATIONAL MODULES

- **Maneuver Driver (ManD)**
- **FOBoom3 Boom Calculator**
- **SBORT Simple Boom Calculator**
- **Footprint Processor**
- **PCBPlot Footprint/Contour Output**
- **SIGOUT Signature and Spectrum Output**
- **All Written in Fortran 77**
- **"Industry Standard" Plotting Calls**

The contour plotting module will draw isopemps and contours. The isopemps – the ground intercepts of boom generated at specific times – are very useful for seeing where the boom footprint lies, and in interpreting focal zone geometry. The contours quantify the boom amplitude. Loudness is computed by the methods used by NASA–Langley, with a 125 msec auditory time constant.

PCBCont CONTOUR/FOOTPRINT MODULE

- **Isopemps (Ray/Ground Intersections)**
- **Contours of P_{max}, CSEL, ASEL, PL**
- **Interactive User Control of Plot Format**

This is an isopemp plot for a supersonic turn at constant Mach number. There is a "+" marking the beginning of the calculated maneuver, and "o"s marking the entry point. The caustic location during the turn is apparent, and the multi-valued region around the turn entry cusp can be seen.

TYPICAL FOOTPRINT ("ISOPEMP") OUTPUT

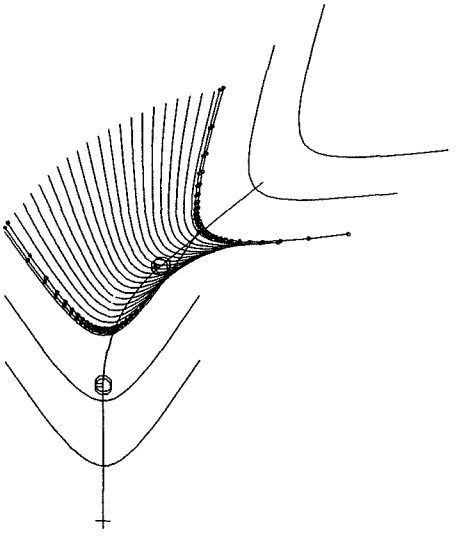

This is the corresponding overpressure contour.

TYPICAL CONTOUR OUTPUT

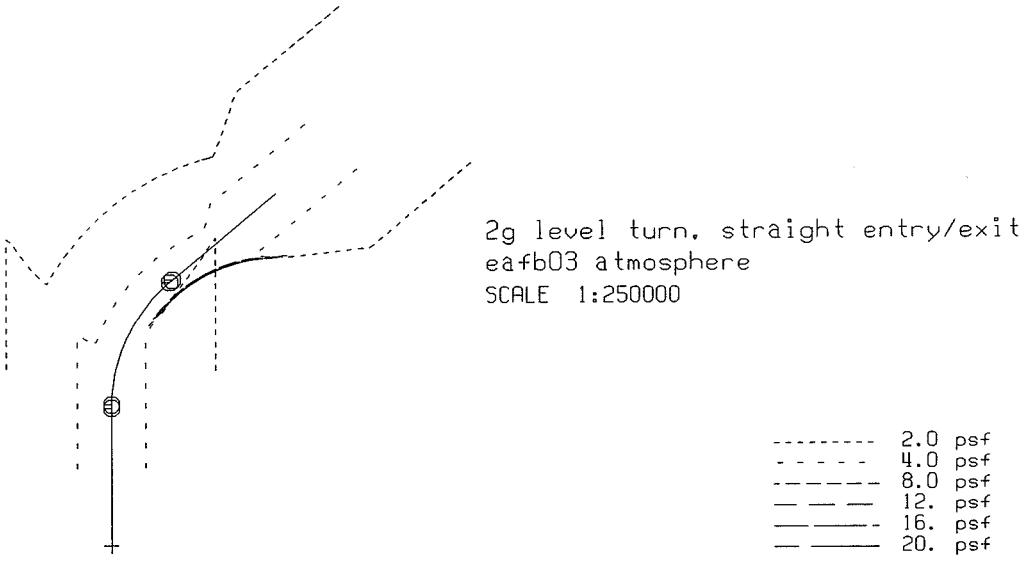

The signature output module allows plotting signatures and spectra at an arbitrary location in the footprint. It interpolates signatures between the actual computed grid points. It is aware of multiple sheets in focal regions, and the absolute phase, so it can assemble complex N–U signatures seen near focal zones. The module plots energy density spectra and residual shock spectra. Spectra can be either narrow or one-third octave band. The one-third octave band spectra are normalized by the 125 msec auditory time constant.

SIGOUT SIGNATURE/SPECTRUM MODULE

- **Plots Time History Signatures**
- **Complex "N–U" Signatures in Focal Zones**
- **Spectra and Residual Shock Spectra**

This is an example signature output. This particular one is the maximum focus condition under the flight track for an F-16 performing maximum-power level acceleration at 10,000 feet. The peak pressure is 17 psf, and the CSEL is 121.5 dB.

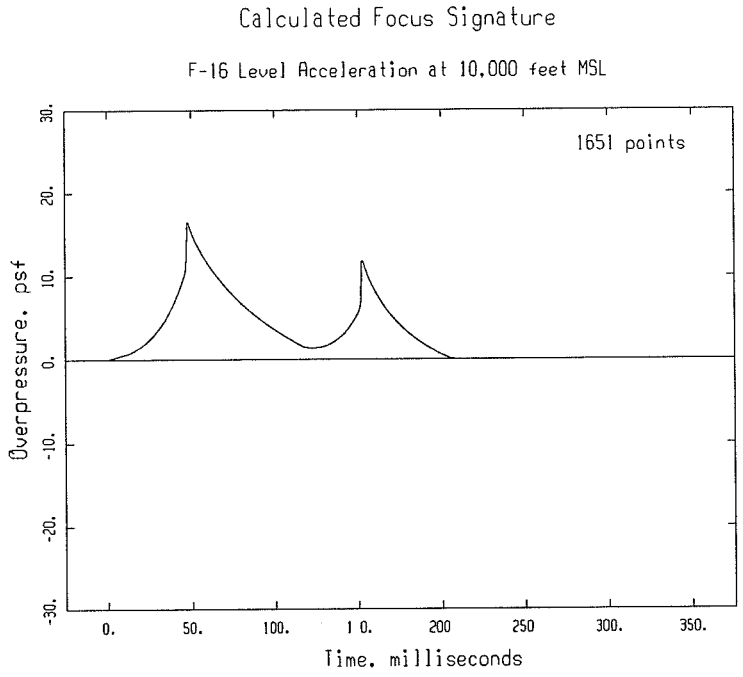

Focal zone flight tests were recently conducted. An array of BEARS with 500- to 1,000-foot spacing was placed across calculated focal zones. Observers were also located along the arrays, and the audible sensations of "distant thunder" on the shadow side, "BANG-BANG" at the focus, and "carpet boom with afterpops" filled expectations. There were 49 passes over the arrays, with a good mix of maneuver types. Except for a very few anomalous runs that missed altogether, all of the foci intercepted the expected locations. The behavior away from the focal zone itself – with N and U waves separating – agreed well with predictions. Boom amplitudes also agreed with predictions.

FLIGHT TEST VALIDATION:
Project Have BEARS

- **USAF AL/OEBN and TPS effort, April 1994, Edwards AFB**
- **F-16 Performing Level Acceleration, Diving Acceleration, Steady Turn, Pullup/Pushover Focusing Maneuvers**
- **Signatures Recorded With Arrays of USAF BEARs**
- **Excellent Results for Focal Zone Location, Geometry, Boom Amplitude**

This is a typical measured boom at the focus condition. This is for a full-throttle acceleration, corresponding to the calculated signature shown earlier. The peak pressure is 17 psf, and the CSEL is 123.8 dB. Both are in very good agreement with prediction. The shape differs somewhat, and there are spectral differences, so the scaling of the Gill-Seebass solution needs to be examined, but the result is generally quite good. Having the recorded data in digital form from the BEARs provides the first real opportunity for a detailed comparison of theory with flight test.

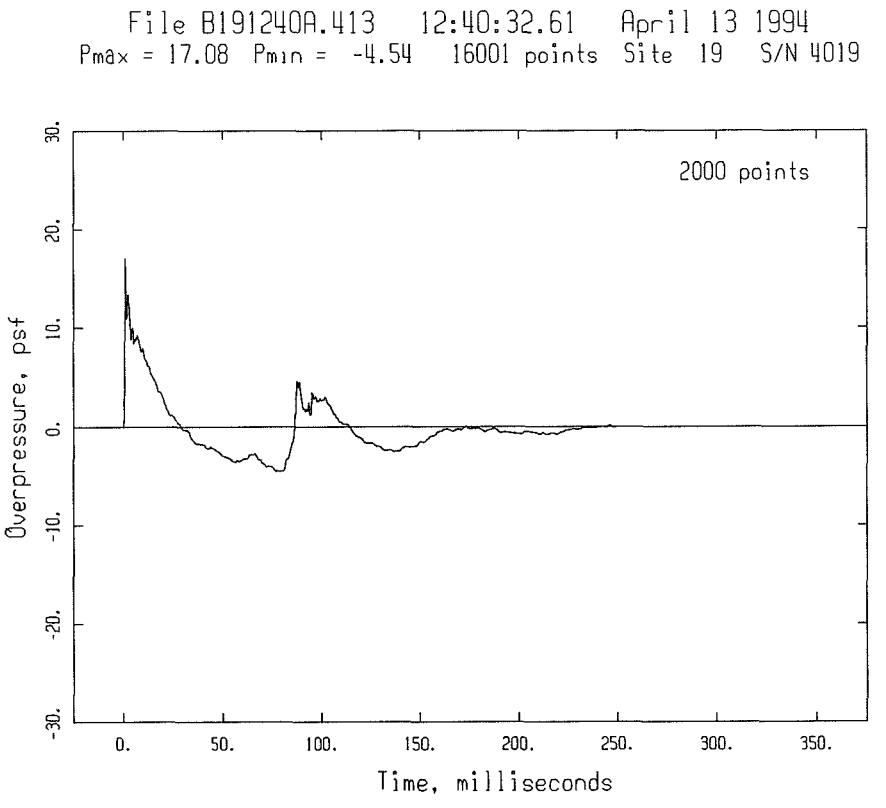

C-3.

CONCLUSIONS

- **PCBoom3 Is Nearing Completion**
- **Provides Simple Access to State-of-the-Art Sonic Boom Prediction**
- **Validation by Recent Flight Tests**
- **Commonality With MDBOOM Will Benefit the HSCT Community**
- **Expected Release in Fall 1994. Will be Available From AL/OEBN**

DERIVING A DOSAGE-RESPONSE RELATIONSHIP FOR COMMUNITY RESPONSE TO HIGH-ENERGY IMPULSIVE NOISE

Sanford Fidell and Karl S. Pearsons
BBN Systems and Technologies
A Division of Bolt Beranek and Newman Inc.
21120 Vanowen Street
Canoga Park, California 91304

INTRODUCTION

The inability to systematically predict community response to exposure to sonic booms (and other high energy impulsive sounds) is a major impediment to credible analyses of the environmental effects of supersonic flight operations. Efforts to assess community response to high energy impulsive sounds are limited in at least two important ways. First, a paucity of appropriate empirical data makes it difficult to infer a dosage-response relationship by means similar to those used in the case of general transportation noise. Second, it is unclear how well the "equal energy hypothesis" (the notion that duration, number, and level of individual events are directly interchangeable determinants of annoyance) applies to some forms of impulsive noise exposure.

Some of the issues currently under consideration by a CHABA working group addressing these problems are discussed. These include means for applying information gained in controlled exposure studies about different rates of growth of annoyance with impulsive and non-impulsive sound exposure levels, and strategies for developing a dosage-response relationship in a data-poor area.

The state of the art in prediction of community response to high energy impulsive noise exposure - essentially, sonic booms, artillery fire, and blasting - is much less advanced than prediction of community response to general transportation noise. The most obvious difference between the two cases is between an embarrassment of social survey information about the annoyance of general transportation noise and a scarcity of similar findings about the annoyance of impulsive noise.

Fields (1991) notes that more than 300 social surveys of community response to the general din of the urban environment have been conducted in the last few decades. Schultz (1978) found enough quantitative information about 161 of these data points to permit his well-known synthesis of a descriptive dosage-response relationship between Day-Night Average Sound Level and the prevalence of a consequential degree of self-reported annoyance in urban settings. Limiting themselves to the same selection criteria as Schultz (1978), Fidell, Barber and Schultz analyzed another 232 data points in 1991. Others (notably FICON, 1992) have suggested alternate fitting functions for various subsets of the same data, as summarized in Table 1 of Fidell and Pearsons (1993).

As seen in Figure 1, information about community response to general transportation noise is now so abundant - and so variable - that it is doubtful that information collected in any further social surveys can substantially affect commonly accepted fitting functions and interpretations. As a complement to purely descriptive accounts of this mass of data, efforts such as that of Green and Fidell (1991) have recently begun to develop theory-based explanations for the variability in annoyance rates in different communities with similar noise exposure.

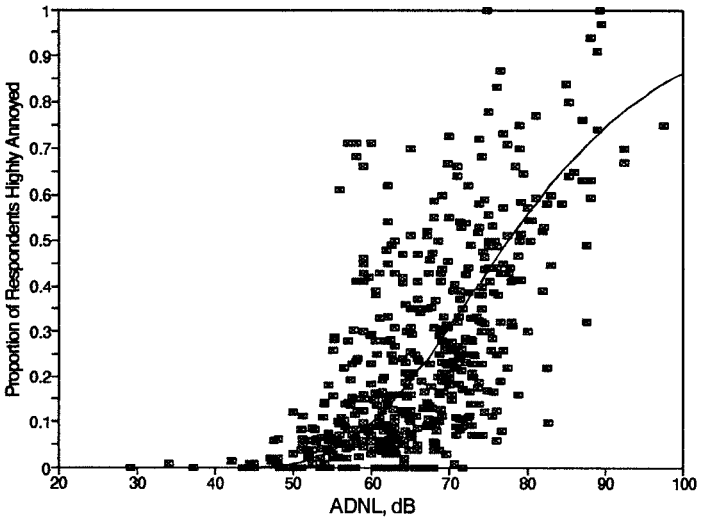

Figure 1 Social survey findings on the prevalence of annoyance associated with residential exposure to general transportation noise. (Fitting function from one parameter model of Green and Fidell, 1991.)

In contrast, only a few social surveys have been conducted on the effects of high energy impulsive noise exposure on communities, and only one well-accepted synthesis of a descriptive dosage-response relationship for these data has been completed. Figure 2 summarizes the information presently available from which a dosage-response relationship between impulsive noise exposure and the prevalence of annoyance can be directly synthesized. The data displayed in Figure 2 are derived from the well-known Oklahoma City study (Borsky, 1966); from two surveys of reactions to artillery noise (Schomer, 1985); and from a recent NASA study of reactions to sonic booms reported elsewhere in these proceedings by Fields, Moulton, Baumgartner and Imm-Thomas. All of the original noise measurements at Ft. Lewis and Ft. Bragg were modified to account for pressure doubling. The plotted values also reflect new information about the Oklahoma City noise measurements (Schomer, 1994).

The best known dosage-response relationship (that of CHABA Working Group 84) was not based on even this much information, however. Galloway (1981) was forced to develop a dosage-response relationship from only 14 data points. Another CHABA Working Group on Assessment of Community Response to High Energy Impulsive Sounds now revisiting the problem 13 years later is attempting to interpret what has been learned empirically and theoretically about community response to impulsive noise exposure in the interim.

The most obvious remedy for the paucity of information about community response to impulsive noise exposure is the conduct of several new large scale social surveys. This is not a realistic possibility for several reasons. First, opportunities to conduct surveys of adventitious exposure to high energy impulsive noise are limited. Because no civil aircraft fly supersonically over land, and because the military confines its overland supersonic operations to areas of relatively low population density, only small populations have yet experienced high levels of exposure to sonic booms on a regular, long

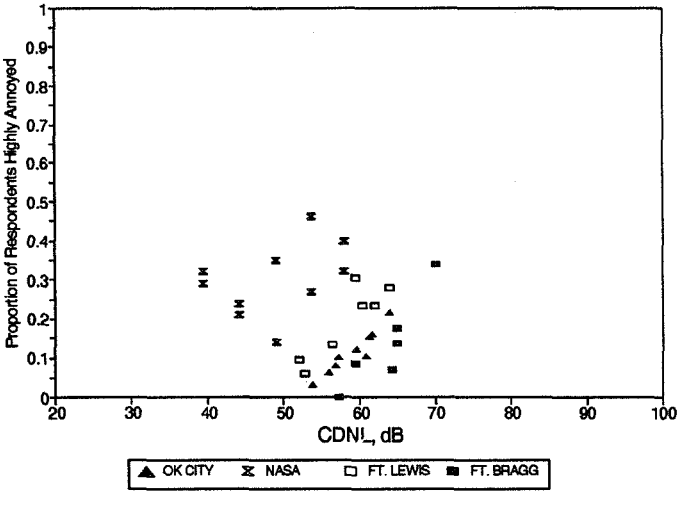

Figure 2 Social survey findings on prevalence of annoyance associated with exposure to high energy impulsive noise.

term basis. Blasting, artillery training and other sources of non-aircraft, high energy impulsive noise are also generally experienced only by localized populations.

Second, opportunities for conducting field studies involving intentional exposure of entire communities to sonic booms have been all but foreclosed in the United States since passage of the National Environmental Policy Act of 1969.

Third, it is doubtful that information about effects of sonic booms in the exposure ranges of greatest interest for purposes of developing a dosage-response relationship can ever be collected. C-weighted DNL values in systematic studies of community response to high energy impulsive noise exposure that have been conducted to date are all in the region below 70 dB. No community has yet experienced the numbers of daily supersonic flights necessary to produce greater long term impulsive noise exposure, nor is it possible for a variety of reasons to create or credibly simulate such exposure on a large scale.

Controlled studies of subjective judgments of the annoyance of individual impulsive sounds can contribute information that might be used to complement social survey findings. Kryter, Johnson and Young's (1968) field study comparing the annoyance of sonic booms to that of subsonic aircraft overflights is one source of such information that was considered by CHABA Working Group 1984. Schomer (1994) has since collected newer information about the relative annoyance of other impulsive sounds. This information was derived from direct paired comparison judgments of the annoyance of impulsive and non-impulsive noises heard in laboratory and field settings. Schomer's outdoor noise measurements of sounds presented for judgment in field testing were made at the time of signal presentations, and pressure doubled for the sake of consistency with those typically made of sonic booms.

In Schomer's data set, the annoyance created by an impulsive noise event of a given CSEL grows at twice the rate as the annoyance of a non-impulsive noise event of a numerically equivalent ASEL. This means that CDNL values cannot be directly calculated for purposes of predicting annoyance as a logarithmic sum of CSEL values of constituent noise events. Just as OSHA employs a 5 dB/doubling rule rather than a 3 dB/doubling rule for calculating noise exposure for purposes of predicting hearing damage risk, Schomer' data suggest that a 6 dB/doubling rule is required when CDNL values are used for purposes of predicting the prevalence of annoyance due to a summation of high energy impulses.

Alternatively, a greater rate of growth of annoyance for impulsive than non-impulsive noise events could be interpreted as requiring that the slope of dosage-response relationship for community response to the impulse noises be considerably steeper than the slope of the dosage-response relationship for non-impulsive noise.

One might think that a difference in the fit to the data of two dosage-response relationships with slopes differing by a factor of two would be immediately apparent from simple visual inspection. This is not the case, however, because the small number of data points and their considerable variability do not greatly constrain the shape of a fitting function. It is therefore important to explore other means for checking the reasonableness of drawing inferences for the shape of a dosage-response relationship for community response to impulsive noise exposure from the findings of controlled exposure studies.

One reasonableness check can be made by analogy with the case of predicting community response to non-impulsive noise. Green and Fidell (1991) attempted to infer the shape of a dosage-response relationship from first principles, rather than through statistical curve fitting exercises. They likened the prevalence of annoyance in a community to a response to a dose of noise exposure: like any other treatment administered to a human population, the response to the same dose can be expected to vary from individual to individual, and hence from community to community.

Green and Fidell suggested that the relationship between dose and response has two components: one associated with the effective loudness of the noise exposure, and one associated with the sum of all nonacoustic influences on self-reports of annoyance. The nonacoustic influences may be considered in the aggregate as a form of response bias. The former term establishes the slope of the dosage-response relationship, whereas the latter establishes its position along the abscissa.

Green and Fidell showed that a one-parameter model provides a good account of the relationship between exposure to general transportation noise and the prevalence of annoyance in communities. It is thus reasonable to ask whether the same model can also be applied to the case of impulsive noise exposure. The one parameter model assumes that reactions of community members to noise exposure are exponentially distributed with a mean population value, m. The value of m is assumed to be related to the Day-Night Average Sound Level by:

$$10 \log m = 0.3 L_{dn}$$

Thus, noise exposure creates a distribution of reactions within a community with a mean value that increases with the level of noise exposure. Individuals describe themselves as highly annoyed when their reactions to noise exposure exceed a criterion value for reporting annoyance. The proportion of the population describing itself as highly annoyed is predicted as

$$P = e^{-(A/m)}$$

where P is the probability of reporting high annoyance, m is defined as above, and A is the criterion value for reporting annoyance.

Figure 3 shows the fit of the Green and Fidell model to the data displayed in Figure 2. The curve is generated by the relationship shown in Equation 1. The value of the parameter that controls the slope of the curve - that is, the power to which DNL is raised to calculate the effective loudness of noise exposure - is 0.3. The horizontal position of the curve on the abscissa is determined by the average value of CDNL at which respondents describe themselves as highly annoyed in this data set.

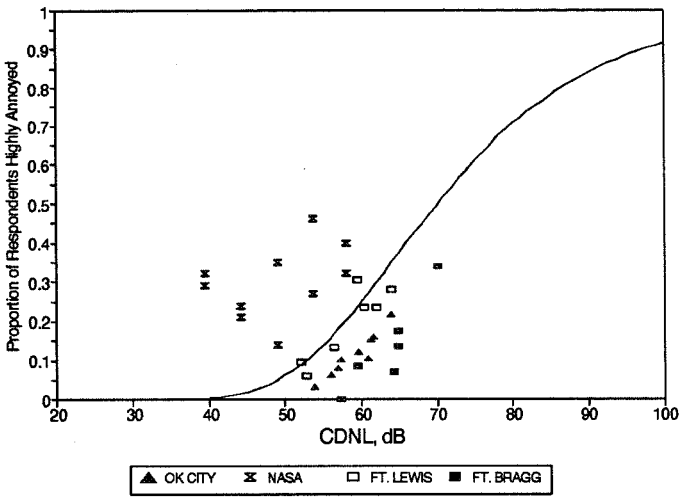

Figure 3 Fit of one parameter model (Green and Fidell, 1991) to data displayed in Figure 2, exponent = 0.3.

A predictive relationship that provides a useful account for a data set should reduce the amount of variance unaccounted for in the data set. Figure 4 shows that this is in fact the case by replotting the data of Figure 3 in a manner that removes the effects of response bias. The abscissa of Figure 4 subtracts the average response bias observed in each study (expressed in units of CDNL) from the measured CDNL values for each data point. This normalization of each data set to the average value of CDNL at which survey respondents in a study described themselves as highly annoyed effectively removes response bias, and leaves apparent the correspondence between the observed and predicted rates of growth of annoyance with exposure level. The reduction in variability in Figure 4 with respect to that of Figure 3 is readily apparent.

If annoyance with impulsive noise exposure grows with level at a rate faster than it grows for non-impulsive noise, one might expect a larger exponent for CDNL than for ADNL. Schomer (1989), for example, has suggested that a value of 0.4 might be more appropriate than 0.3. Figure 5 shows the fit of the Green and Fidell model with a value of 0.4 for its one free parameter to the same data set.

The standard deviation of the differences between the observed and predicted proportions highly annoyed for the fit shown in Figure 3 is 3.2%, while the corresponding standard deviation for the fit shown in Figure 5 is 3.8%. The differences in standard deviations are so slight that there is no compelling argument for adopting one that suggests a higher rate of growth of annoyance with exposure level in the impulsive case.

Thus, it is not yet apparent how the observations of controlled exposure studies in which the annoyance of impulsive and non-impulsive sounds are directly compared can be applied to derivation of a dosage-response relationship for the prevalence of annoyance due to high energy impulsive

sounds in communities. Further analyses of these data are expected before the current CHABA working group makes any new recommendations.

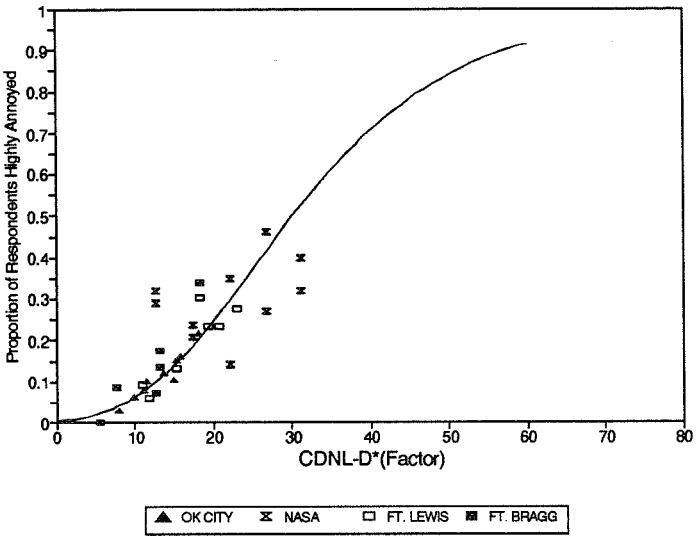

Figure 4 Reduction in variability in social survey findings displayed in Figure 3 attainable by normalization to remove effects of response bias.

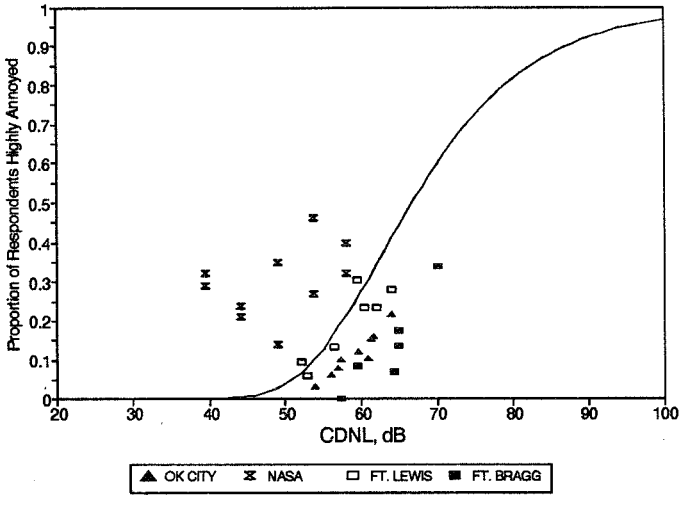

Figure 5 Fit of one parameter model (Green and Fidell, 1991) to data displayed in Figure 2, exponent = 0.4.

REFERENCES

Federal Interagency Committee on Noise (FICON). Final Report, *Airport Noise Assessment Methodologies and Metrics*, Washington, D.C., 1992.

Fidell, S.; Barber, D.; and Schultz, T. J.: Updating a Dosage-Effect Relationship for the Prevalence of Noise-Related Annoyance. *Journal of the Acoustical Society of America*, vol. 89, no. 1, 1991.

Fidell, S.; and Pearsons, K.S.: Comparison of Methods of Predicting Community Response to Impulsive and Nonimpulsive Noise. Sonic Boom Workshop, NASA Ames Research Center, Moffett Field, California, 12-14 May, 1993.

Fidell, S.; Schultz, T.J.; and Green, D.M.: A Theoretical Interpretation of the Prevalence Rate of Noise-Induced Annoyance in Residential Populations. *Journal of the Acoustical Society of America*, vol. 84, no. 6, 1988.

Fields, J.M.: An Updated Catalog of 318 Social Surveys of Residents' Reactions to Environmental Noise (1943-1989). NASA TM-187553, 1991.

Galloway, W.J.: Assèssment of Community Response to High Energy Impulsive Sounds, Report of Working Group 84, Committee on Hearing, Bioacoustics and Biomechanics, National Research Council, National Academy of Sciences, Washington, D.C., 1981.

Green, D.M.; and Fidell, S.: Variability in the Criterion for Reporting Annoyance in Community Noise Surveys. *Journal of the Acoustical Society of America*, vol. 89, no. 1, 1991.

Kryter, K.D.; Johnson, P.J.; and Young, J.P.: Psychological Experiments on Sonic Booms Conducted at Edwards Air Force Base. Final Report, Contract AF49(638)-1758. Arlington, VA: National Sonic Boom Evaluation Office, 1968.

Schomer, P.: Assessment of Community Response to Impulsive Noise. *Journal of the Acoustical Society of America*, vol. 77, no. 2, 1985.

Schomer, P.: On a Theoretical Interpretation of the Prevalence Rate of Noise-Induced Annoyance in Residential Populations - High Amplitude Impulse-Noise Environments. *Journal of the Acoustical Society of America*, vol. 86, no. 2, 1989.

Schomer, P.: Personal Communication, 1994.

Schultz, T.J.: Synthesis of Social Surveys on Noise Annoyance. *Journal of the Acoustical Society of America*, vol. 64, no. 2, 1978.

AN IN-HOME STUDY OF SUBJECTIVE RESPONSE TO SIMULATED SONIC BOOMS

David A. McCurdy[1] and Sherilyn A. Brown[2]
NASA Langley Research Center
Hampton, VA

R. David Hilliard[3]
Wyle Laboratories
Hampton, VA

INTRODUCTION

The proposed development of a second-generation supersonic commercial transport has resulted in increased research efforts to provide an environmentally acceptable aircraft. One of the enviromental issues is the impact of sonic booms on people. Aircraft designers are attempting to design the transport to produce sonic boom signatures that will have minimum impact on the public. Current supersonic commercial aircraft produce an "N-wave" sonic boom pressure signature that is considered unacceptable by the public. This has resulted in first-generation supersonic transports being banned from flying supersonically over land in the United States, a severe economic constraint. By tailoring aircraft volume and lift distributions, designers hope to produce sonic boom signatures having specific shapes other than "N-wave" that may be more acceptable to the public and could possibly permit overland supersonic flight. As part of the effort to develop a second-generation supersonic commercial transport, Langley Research Center is conducting research to study people's subjective response to sonic booms. As part of that research, a system was developed for performing studies of the subjective response of people to the occurrence of simulated sonic booms in their homes.

The In-Home Noise Generation/Response System (IHONORS) provides a degree of situational realism not available in the laboratory and a degree of control over the noise exposure not found in community surveys. The computer-controlled audio system generates the simulated sonic booms, measures the noise levels, and records the subjects' ratings and can be placed and operated in individuals' homes for extended periods of time. The system was used to conduct an in-home study of subjective response to simulated sonic booms. The primary objective of the study was to determine the effect on annoyance of the number of sonic boom occurrences in a realistic environment.

[1]Aerospace Engineer, NASA Langley Research Center, Mail Stop 463, Hampton, VA 23681-0001, Tel: (804)864-3596, Fax: (804)864-8823

[2]Aerospace Engineer, NASA Langley Research Center, Mail Stop 463, Hampton, VA 23681-0001, Tel: (804)864-3593, Fax: (804)864-8823

[3]Senior Project Engineer, Wyle Laboratories, 3200 Magruder Blvd, Hampton, VA 23666, Tel: (804)865-0000 ext.234, Fax: (804)865-8116

IN-HOME NOISE GENERATION/RESPONSE SYSTEM DIAGRAM

A diagram of the IHONORS system is shown in figure 1. The system consisted of a computer and compact disc player that played the simulated sonic booms at randomly-selected, pre-programmed times through a preamplifier and amplifier into three or four loudspeakers located in different rooms of the house. The two indoor microphones and sound level meters measured the levels of the booms as they occurred and also continuously measured the ambient noise levels in the home. The measurements were then transferred to the computer and stored on its hard disk. At the end of the day, the test subject used the trackball to answer a series of questions about his or her activities during the day and his or her subjective response to the sonic booms heard. Once a week the noise measurements and test subject responses were downloaded via a modem to a central computer. The data were then checked to ensure that the system was operating correctly.

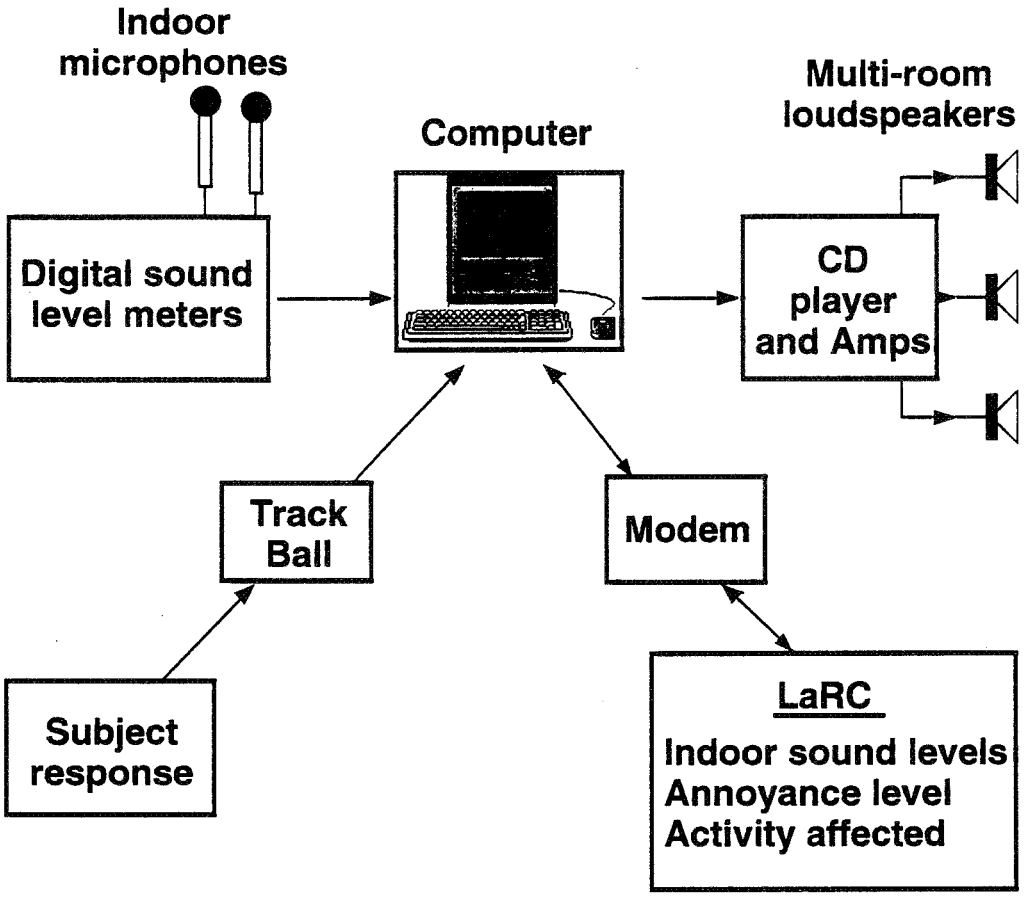

Figure 1.

Figure 2 shows the actual components as deployed in a test subject's home. Selected homes were limited to single family detached dwellings so that the simulated sonic booms would not penetrate the walls into neighbors homes as might be the case in apartments or townhouses. The range of homes selected covered the economic range from lower middle class to upper middle class. The computer, compact disc player, trackball, and monitor were placed on the shelves of a microwave oven cart. The preamplifier, amplifiers, and sound level meters were placed inside the lower cabinet of the cart. The cart was placed in a position that was convenient for the test subject and that simplified the installation of cables. Three or four loudspeakers were placed in the rooms that the test subject indicated he or she most used during the 14 hour boom period each day. The two microphones were placed in two of the rooms with loudspeakers. The system components blended in well with the existing decor in most cases and were often decorated with bric-a-brac by the test subject.

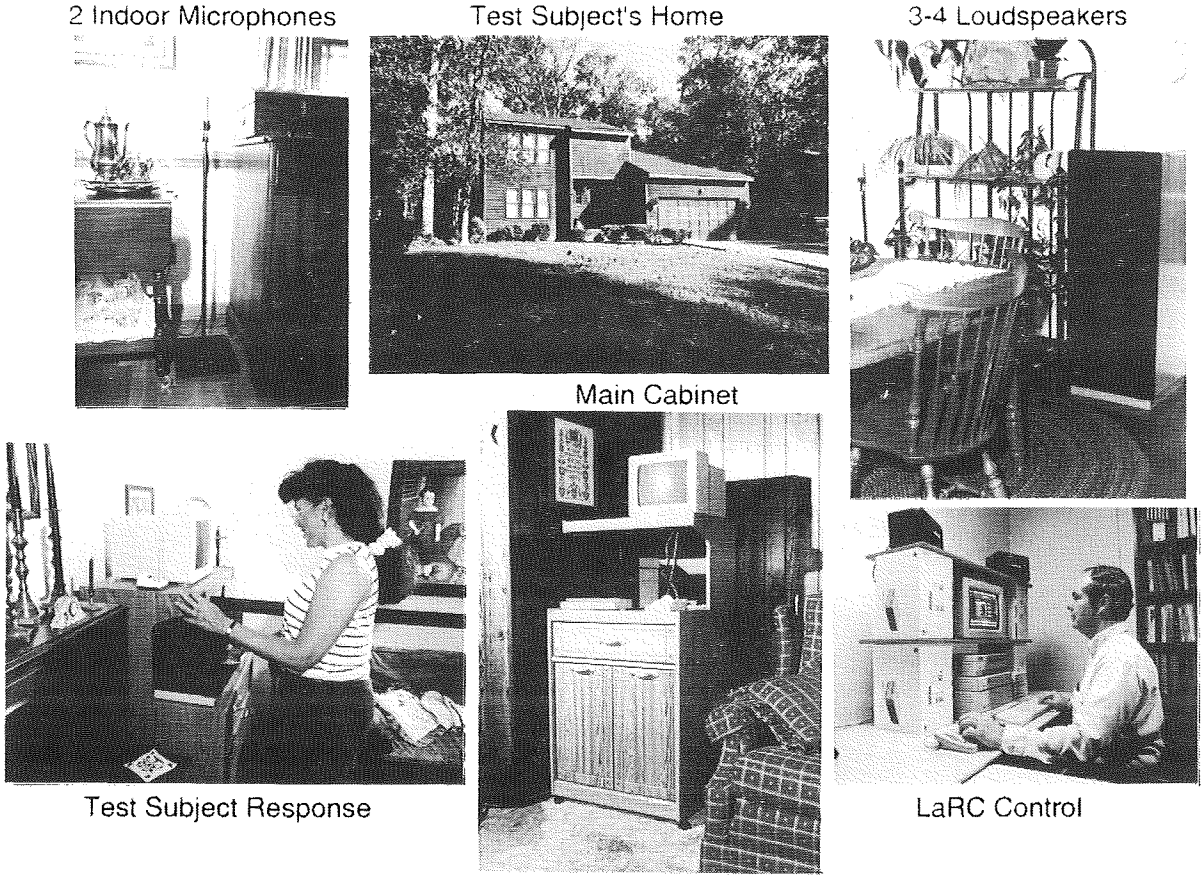

Figure 2.

TEST PLAN

The final test plan is outlined in figure 3. Eight IHONORS systems were used to conduct the in-home study of subjective response to simulated sonic booms. A system was deployed for eight weeks in each of 33 homes. Each day the system played simulated sonic booms during a 14 hour period as the test subject went about his or her normal activities. At the end of the 14 hours the test subject rated his or her annoyance to the sonic booms heard during the day. A total of 264 weeks of data including over 1800 subjective annoyance responses to daily sonic boom exposures were collected, the equivalent of five years of sonic boom exposures in realistic environments.

- February 1993 to December 1993
- 33 homes
- 8 weeks per home
- 14 hour test day (no booms during normal sleep period)
- 1848 total exposure days
- 58,443 total sonic booms

Figure 3.

EXPERIMENT DESIGN

As shown in figure 4, the sonic booms presented each day represented combinations of three sonic boom pressure signatures or waveforms, three A-weighted sound exposure levels (SEL(A)), and seven sonic boom frequencies. The SEL(A) levels used were nominally 66, 70, and 74 dB. These values covered the range of indoor sonic boom levels estimated for a variety of second-generation supersonic transport designs. The pressure waveforms represented an outdoor N-wave, an indoor N-wave, and an outdoor "shaped" wave. All the sonic booms had a rise time (τ) of four msec and a duration of 300 msec. The frequencies were 4, 10, 13, 25, 33, 44, and 63 booms per 14 hour period. Only one sonic boom waveform was presented each day. On most days the sonic boom was presented at only one SEL(A) level. On a few days the sonic boom was presented at two or three of the SEL(A) levels.

- 3 pressure signatures
  - outdoor N-wave, τ = 4 msec
  - indoor N-wave, τ = 4 msec
  - outdoor shaped, τ = 4 msec

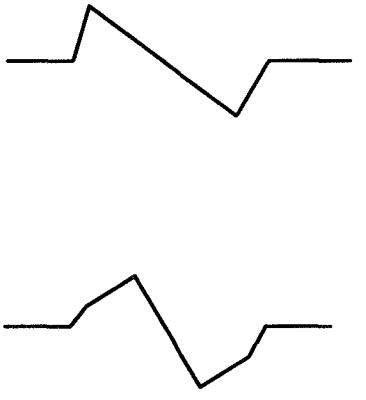

- 3 levels - 66, 70, 74 dB - SEL(A)
- 7 boom occurrence rates - 4, 10, 13, 25, 33 ,44, 63 booms per day

Figure 4.

TEST SUBJECT RESPONSES

The information obtained from the test subjects is outlined in figure 5. The computer-generated questions answered by the test subject at the end of each day are summarized as follows: (1) when were you not inside your house, (2) what activities did you do while inside your house, (3) how annoying were the sonic booms you heard today on a 0 to 10 scale, and (4) were you startled by any of the sonic booms today? In addition to the daily questions, each test subject answered pre- and post-test questionnaires similar to those used in studies surveying people exposed to aircraft-generated sonic booms.

- Pre- and post-test questionnaires
- Daily computer-generated questions
  - When were you not inside the house?
  - What activities did you do while in the house?
  - How annoying were the sonic booms you heard today? (0 to 10)
  - Were you startled by any of the sonic booms today? (Yes or no)

Figure 5.

TEST DAY SUMMARY

The eight IHONORS systems were deployed in 33 test subjects' homes for a total of 1848 exposure days. Figure 6 gives a breakdown of how the test subjects responded during those 1848 days. Over 90 percent of the time, the subjects responded with an annoyance judgment. This was better than expected. Subjects were outside of the home for the entire 14 hour period only one percent of the time. Subjects were out of town or forgot to respond to the questions less than three percent of the time. Technical problems with the system caused the loss of data on less than six percent of the days. Although the systems were designed to and did recover by themselves from power outages by rebooting, the most common technical problem was a momentary brown-out or flicker in the power supply causing the computer to lose its default memory settings but not triggering a reboot of the system.

Type of day	Number	Percentage of total
Subject responded with annoyance judgment	1676	90.7 %
Subject was outside all day	19	1.0 %
Subject did not respond	47	2.6 %
Day voided due to technical problem	106	5.7 %
Total exposure days	1848	100 %

Figure 6.

EFFECT OF NUMBER OF SONIC BOOM OCCURRENCES ON ANNOYANCE

Figures 7 and 8 illustrate the preliminary results concerning the effect of number of booms heard. Figure 7 shows subjective annoyance ratings versus the SEL(A) level of the individual sonic boom repeated during the day. The number of occurrences (n) of the boom is divided into five intervals, each having roughly the same number of data points. The linear regression lines for each interval are plotted in the figure. As illustrated in the figure, the subjective annoyance response increases as the number of occurrences of a sonic boom increases.

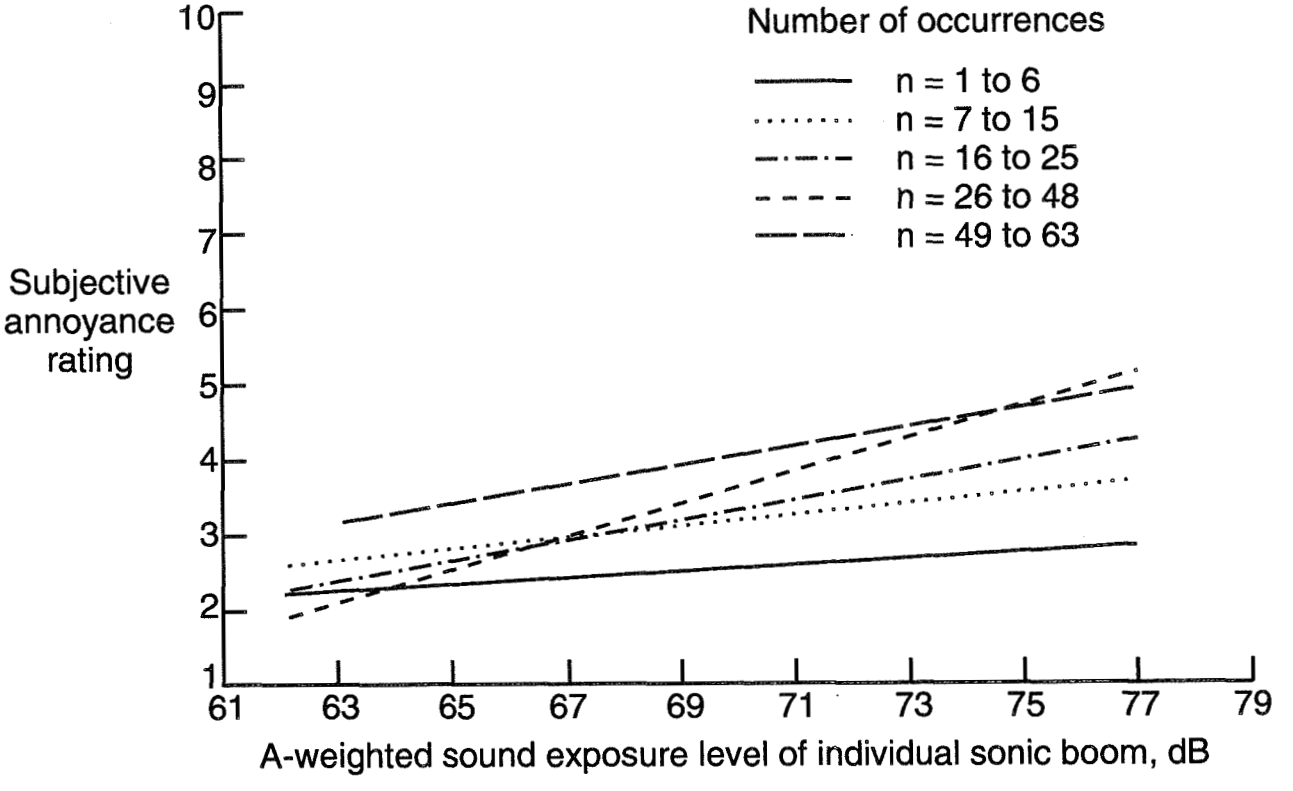

Figure 7.

This effect of number of occurrences can be modeled by the addition to the measured sonic boom level of the term *"k * log(number of occurrences)"*. Figure 8 shows the values of *"k"* and the corresponding 95% confidence intervals determined from regression analyses for each of several noise metrics. The metrics were perceived level (PL), two versions of Zwicker's loudness level (LL_Zd and LL_Zf), perceived noise level (PNL), A-weighted sound exposure level (SEL(A)), C-weighted sound exposure level (SEL(C)), and unweighted sound exposure level (SEL(U)). The metrics represent different ways of modeling the frequency response of the ear (refs. 1,2). As shown in figure 8, analyses of the data indicate that the calculated value of *"k"* ranged from 10 to 15 depending on the noise metric considered. However, for almost all the metrics, the 95% confidence interval about the calculated value includes the value of 10. Therefore, in those cases, the value of *"k"* cannot, statistically, be said to be significantly different from 10, the predicted value based on energy addition.

The two metrics whose 95% confidence intervals on *"k"* did not include the value of 10 were examined further. The value of *"k"* was calculated from the regression coefficients a_1 and a_2 for each metric. Comparison of a_2, the *"log(number of occurrences)"* coefficient, across all metrics found that the value of a_2 was constant across all metrics, indicating that the differences in *"k"* for SEL(U) and SEL(C) were due to the metric and not the effect of number of occurrences.

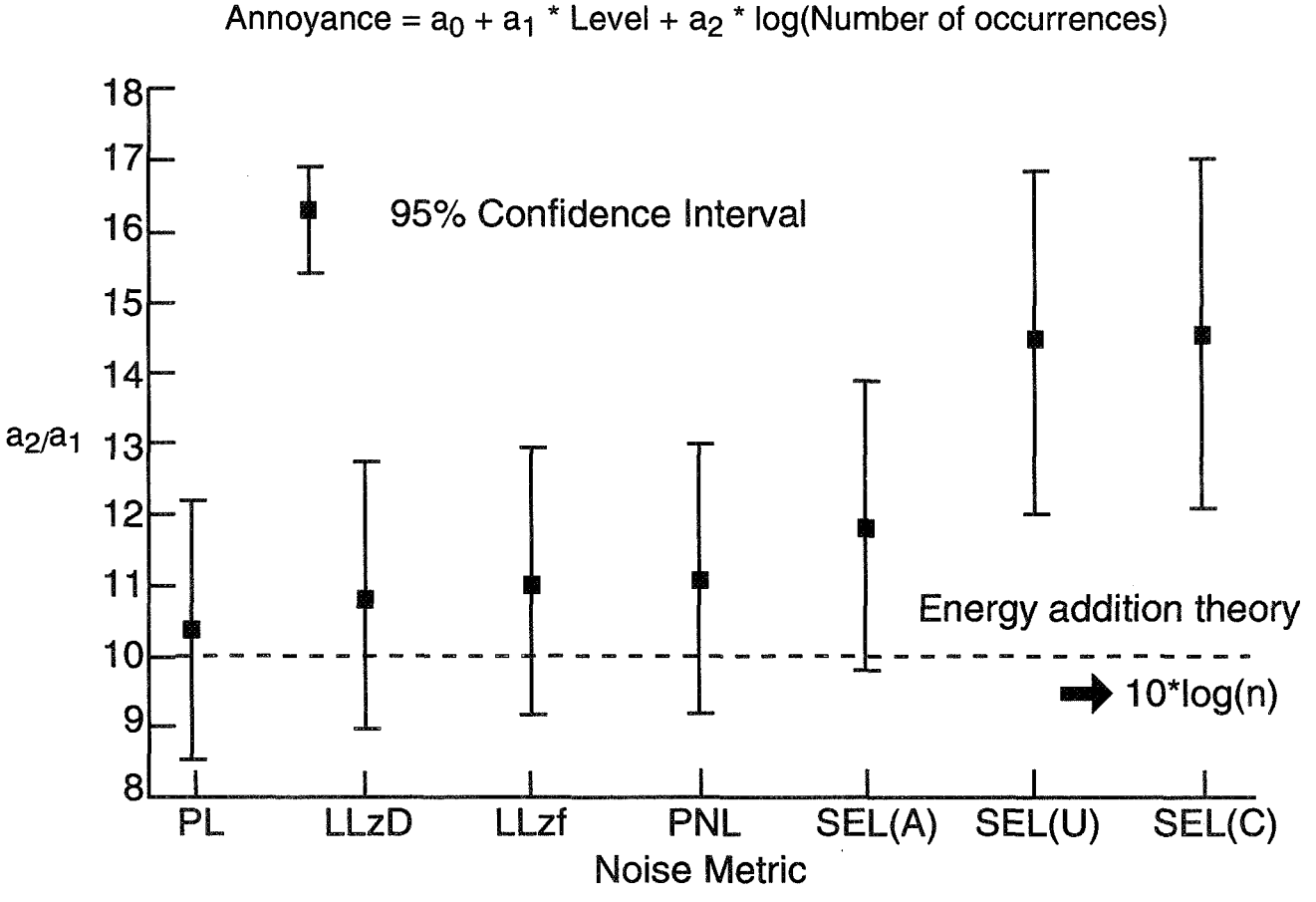

Figure 8.

COMPARISON OF NOISE METRICS

Having confirmed the model for summing the effect of multiple sonic booms, the total daily sonic boom exposure was calculated in terms of each of the noise metrics for comparison with the test subjects' daily annoyance judgments. Daily exposure is commonly expressed in terms of Day-Night Level (DNL). Day-Night Level uses "10*log(number of occurrences)" to sum multiple events and then averages the noise energy across 24 hours (ref. 2). (No late night penalties were assessed.) Although DNL is usually associated with A-weighted sound pressure level, for the purpose of this study, a DNL was calculated using each of the noise metrics.

The predictive ability of the noise metrics was then compared based on the correlation coefficients between the subjective annoyance ratings and the different DNL's. The resulting rank order of metrics is shown in figure 9. Perceived level was the best predictor of annoyance to the simulated sonic booms. Figure 9 also illustrates the subjective annoyance ratings as a function of DNL(PL) and as a function of the more commonly used DNL(A) and DNL(C). A best-fit regression line is drawn through the data in each plot.

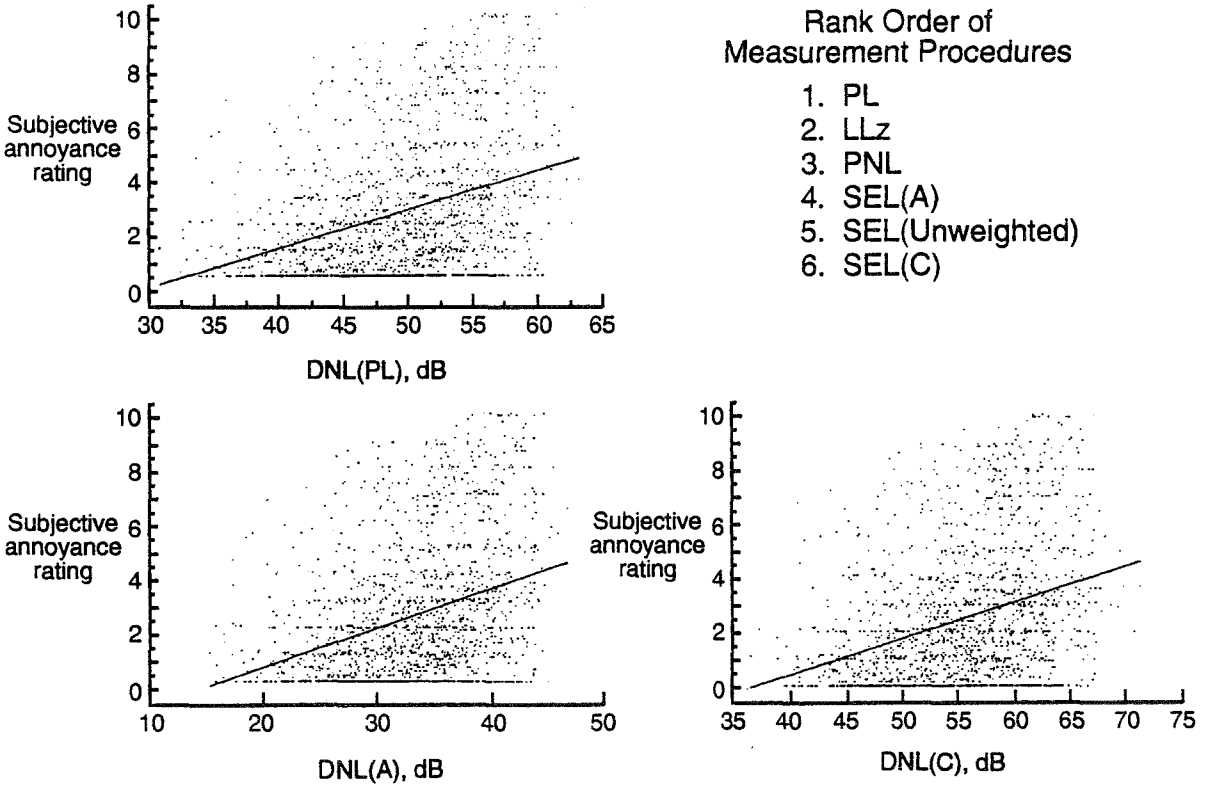

Figure 9.

EFFECT OF SONIC BOOM WAVEFORM SHAPE ON ANNOYANCE

Figure 10 shows the effect of sonic boom waveform on annoyance for noise measurements based on perceived level. The figure shows the regression line of subjective annoyance rating on day-night level based on perceived level for each of the three sonic boom waveforms used in the study. Indicator (dummy) variable analyses found no difference in either slope or intercept between the three different sonic boom waveforms. This result was the same for all the noise metrics considered.

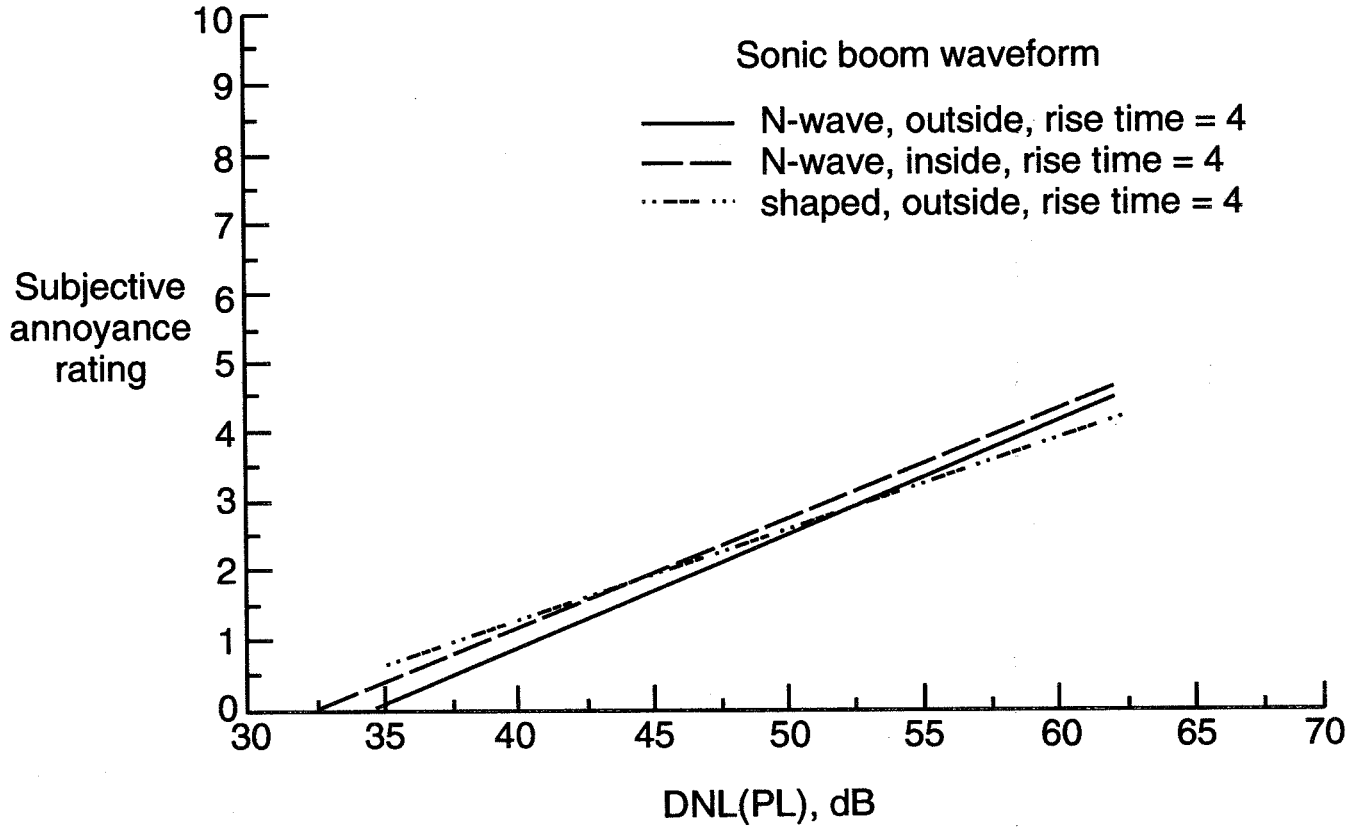

Figure 10.

EFFECT OF STARTLE ON ANNOYANCE TO SONIC BOOMS

Figure 11 shows the effect of startle on annoyance for noise measurements based on perceived level. The regression lines for both startled and not startled are shown for subjective annoyance rating plotted against day-night level based on perceived level. Indicator (dummy) variable analyses indicated a significant difference in both slope and intercept between startled and not startled by a sonic boom. Annoyance is greater when the test subject is startled and the magnitude of the increase in annoyance increases as the sonic boom exposure increases. This effect was the same for all the noise metrics considered.

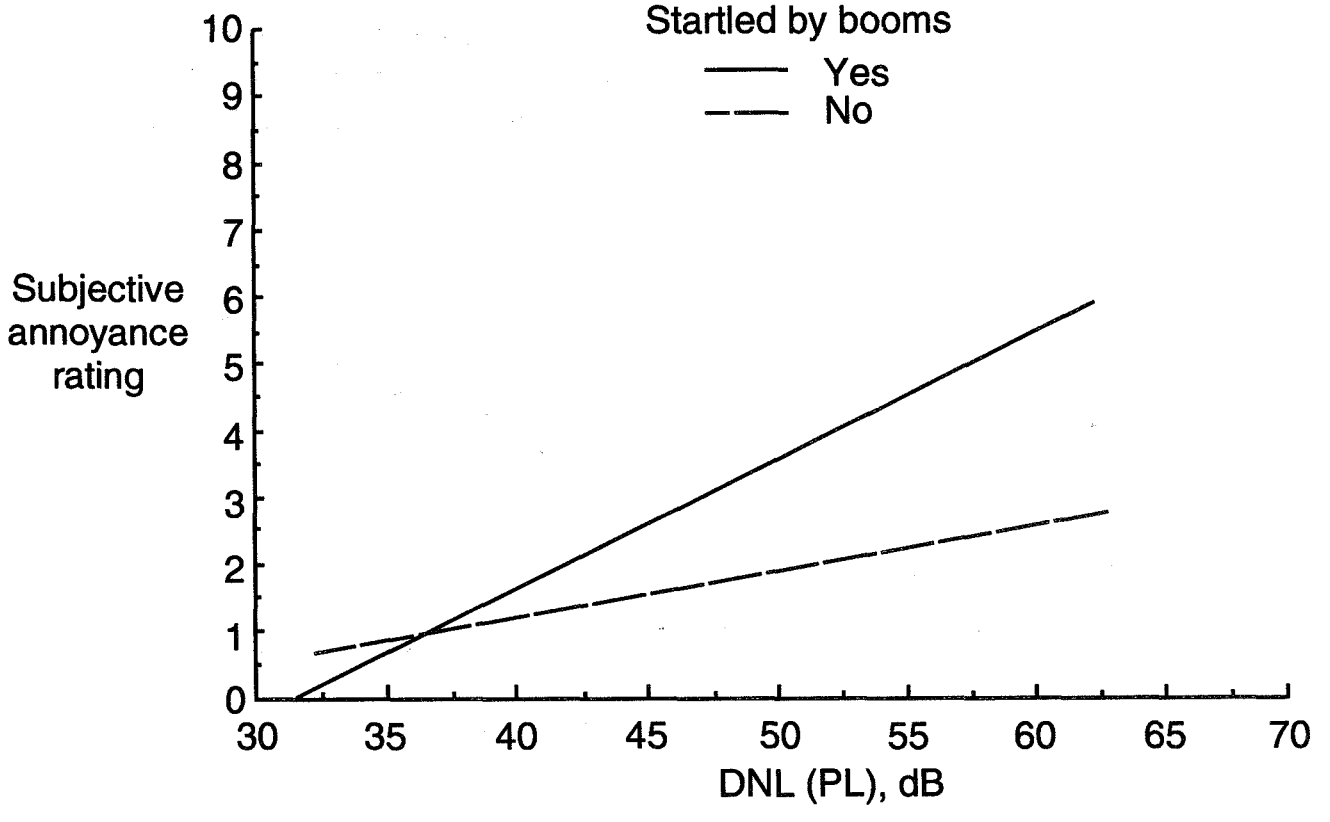

Figure 11.

PERCENTAGE OF TEST SUBJECTS HIGHLY ANNOYED AS A FUNCTION OF A-WEIGHTED DAY-NIGHT LEVEL

The impact of aircraft flyover noise has usually been examined in terms of the percent of people highly annoyed versus the outdoor A-weighted day night level. Figure 12 illustrates this dose-response relationship for the results from this study. A subjective response rating greater than seven was considered a highly annoyed response. The circles in the plot represent the results of this study using the measured indoor levels. The shaded area represents the range of data when the indoor levels are transformed to outdoor levels by the addition of a 15 to 20 dB correction for house attenuation (ref. 3). Comparison of the sonic boom data with the Federal Aviation Administration (FAA) guideline (Shultz curve, ref. 4) indicates that a greater percentage of the test subjects were highly annoyed by the simulated sonic booms than would be expected for aircraft flyover noise at a given level.

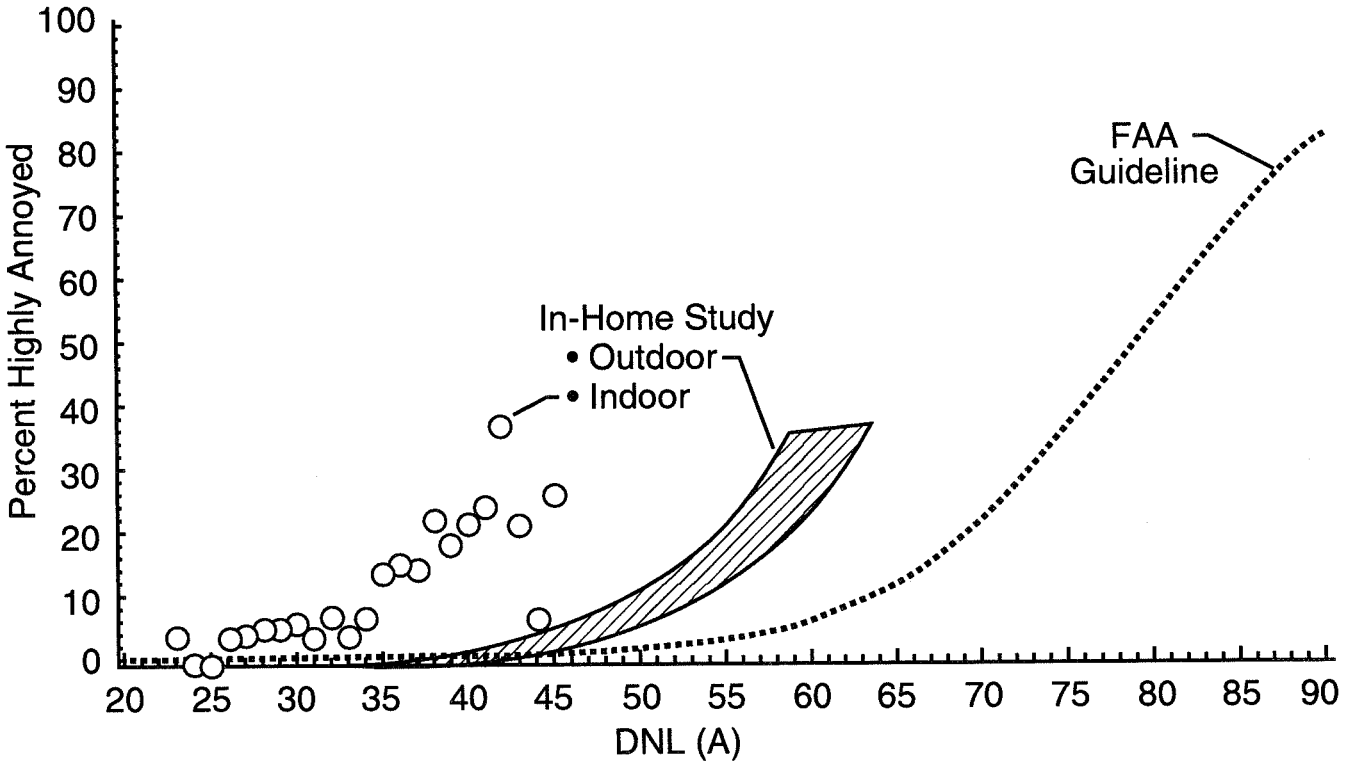

Figure 12.

PERCENTAGE OF TEST SUBJECTS HIGHLY ANNOYED AS A FUNCTION OF C-WEIGHTED DAY-NIGHT LEVEL

The impact of impulse noise has usually been examined in terms of the percent of people highly annoyed versus the outdoor C-weighted day night level. Figure 13 illustrates this dose-response relationship for the results from this study. A subjective response rating greater than seven was considered a highly annoyed response. The circles in the plot represent the results of this study using the measured indoor levels. The shaded area represents the range of data when the indoor levels are transformed to outdoor levels by the addition of a 15 to 20 dB correction for house attenuation (ref. 3). Comparison of the sonic boom data with the Committee on Hearing, Bioacoustics, and Biomechanics (CHABA) recommended curve (ref. 5) indicates that a smaller percentage of the test subjects were highly annoyed by the simulated sonic booms than would be expected by other impulse noises at a given level.

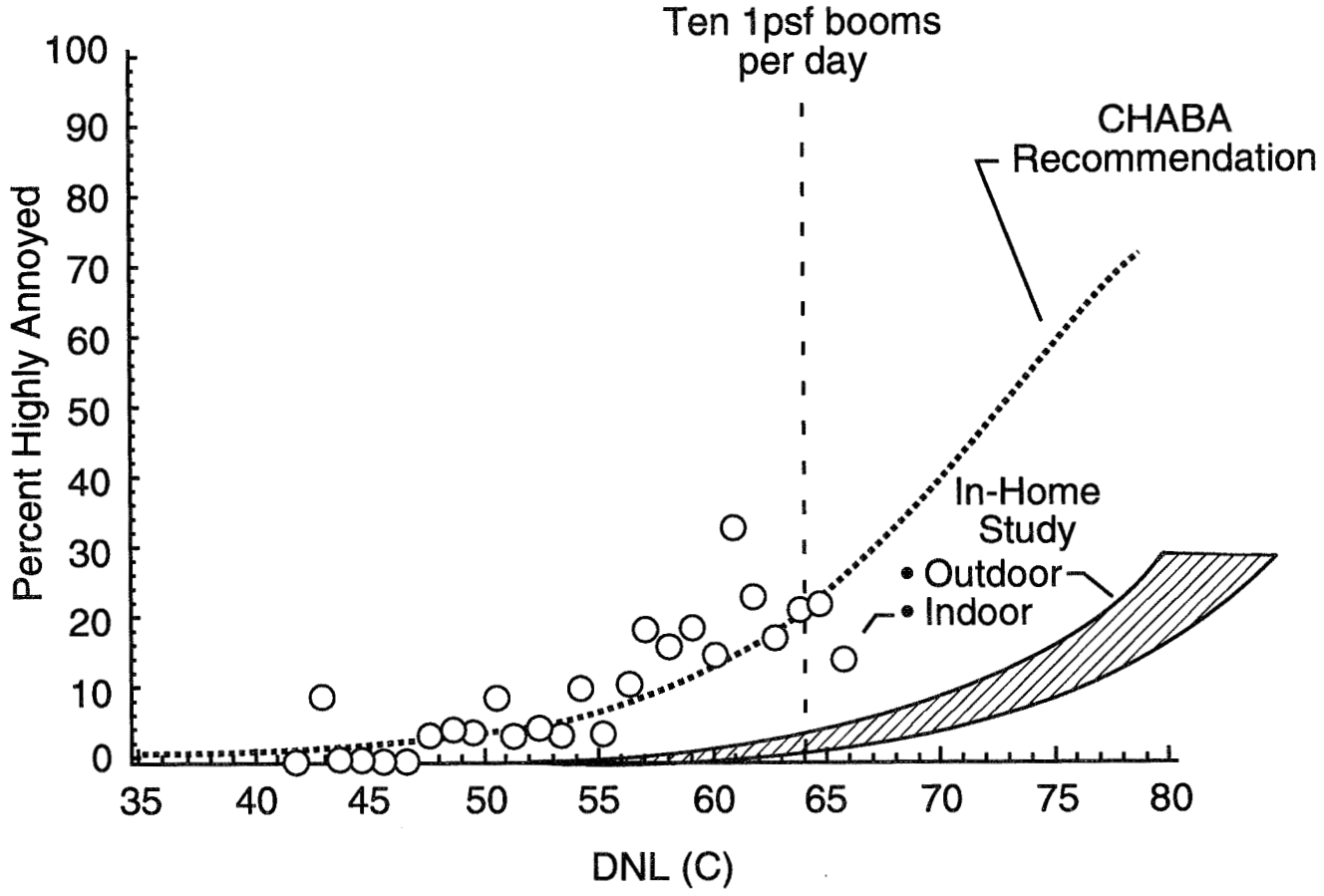

Figure 13.

CONCLUSIONS

Figure 14 summarizes the conclusions reached so far from the in-home study of subjective response to simulated sonic booms.

- Proven, reliable system for in-home testing
- In-home testing requires large resource commitment
- "Level + 10 * log(n)" confirmed for multiple occurrences
- Perceived level was best annoyance predictor
- Startle increases annoyance

Figure 14.

REFERENCES

1. Pearsons, Karl S.; and Bennett, Ricarda L.: Handbook of Noise Ratings. NASA CR-2376, 1974.

2. Bennett, Ricarda L.; and Pearsons, Karl S.: Handbook of Aircraft Noise Metrics. NASA CR-3406, 1981.

3. Leatherwood, J. D.; and Sullivan, B. M.: Loudness and Annoyance Response to Simulated Outdoor and Indoor Sonic Booms. NASA TM-107756, 1993.

4. Schultz, Theodore J.: Synthesis of Social Surveys on Noise Annoyance. Journal of the Acoustical Society of America, vol. 64, no.2, August 1978, pp 377-405. (Erratum, vol. 65, no. 3, March 1979. p. 849.)

5. National Research Council (1981) : Assessment of Community Response to High Energy Impulsive Sounds. Report of Working Group 84, Committee on Hearing, Bioacoustics, and Biomechanics, Assembly of Behavorial and Social Sciences, Washington, D.C. : National Academy of Sciences.

RESIDENTS' REACTIONS TO LONG-TERM SONIC BOOM EXPOSURE: PRELIMINARY RESULTS

James M. Fields
Independent Researcher
Silver Spring, MD

Carey Moulton
Wyle Laboratories
El Segundo, CA

Robert M. Baumgartner and Jeff Thomas
HBRS
Madison, WI

INTRODUCTION

The presentation this morning is about residents' reactions to sonic booms in a long-term sonic boom exposure environment. Although two phases of the data collection have been completed, the analysis of the data has only begun. The results are thus preliminary. The list of four authors reflects the complex multi-disciplinary character of any field study such as this one. Carey Moulton is responsible for Wyle Laboratories' acoustical data collection effort. Robert Baumgartner and Jeff Thomas of HBRS, a social science research firm, are responsible for the social survey field work and data processing. The study is supported by the NASA Langley Research Center.

The study has several objectives. The preliminary data we will consider today address two of the primary objectives. The first objective is to describe the reactions to sonic booms of people who are living where sonic booms are a routine, recurring feature of the acoustical environment. The second objective is to compare these residents' reactions to the reactions of residents who hear conventional aircraft noise around airports.

Here is an overview of the presentation. This study will first be placed in the context of previous community survey research on sonic booms. Next the noise measurement program will be briefly described and you will hear part of a social survey interview. Finally data will be presented on the residents' reactions and these reactions will be compared with reactions to conventional aircraft.

Twelve community studies of residents' reactions to sonic booms were conducted in the United States and Europe in the 1960's and early 1970's. None of the 12 studies combined three essential ingredients that are found in the present study. Residents' long-term responses are related to a measured noise environment. Sonic booms are a permanent feature of the residential environment. The respondents' do not live on a military base. The present study is important because it provides the first dose/response relationship for sonic booms that could be expected to apply to residents in civilian residential areas.

DATA COLLECTION

The present study was conducted in a Western state in five small communities near military operations areas. The communities are separated by from 18 to 104 miles and are from 50 to 150 miles from the Air Force base from which the training operations are conducted. Less than three percent of the residents have employment related to the Air Force base. Although this is a sparsely settled area, all of the respondents live in these five settlements and fewer than five percent live on a ranch or farm.

Two phases of the study have been completed. The first-phase interviews were conducted in April and May of 1993 and the second phase in December of 1993. In both phases residents were asked about sonic booms during the "last six months". Thus, before interviews could be conducted, the preceding months' booms had to be measured. Unattended noise measurements were made with Boom Event Analyzer Recorders (BEARs) (Lee, et al., 1989). The BEAR is a 16-bit microprocessor-based instrument equipped with a special pressure transducer. The BEAR continuously samples the background noise then captures and stores the wave form of loud impulsive sounds along with other identifying information. For these measurements the BEARs were set to store noise events which exceeded 107 dB, lasted at least 15 msec., had a positive pulse time of 10 msec., and a rise time of at least 6 dB/35msec. measured just before the peak. The stored events were later downloaded and examined to eliminate thunder and occasional other events that did not have acoustical profiles that are characteristic of sonic booms. The BEARs were located in weatherproof boxes on government property or in a cooperative resident's backyard at one or two locations in each community.

Depending on the site, approximately 20 to 80 percent of the days in the six months preceding the interviews were monitored with functioning BEARs. Late BEAR placement at two sites for Phase I and sporadic equipment malfunctions during both phases at all sites resulted in 20 to 80 percent monitoring rates rather than 100 percent monitoring rates. These data were used to calculate average daily exposures for each of the five sites during each of the two 6-month periods. These exposures vary from an average of one boom per day to one boom per 10 days and from a Day-night Average Noise Level (DNL) of 41 dB(A) [58 dB(C)] to 20 dB(A) [36 dB(C)].

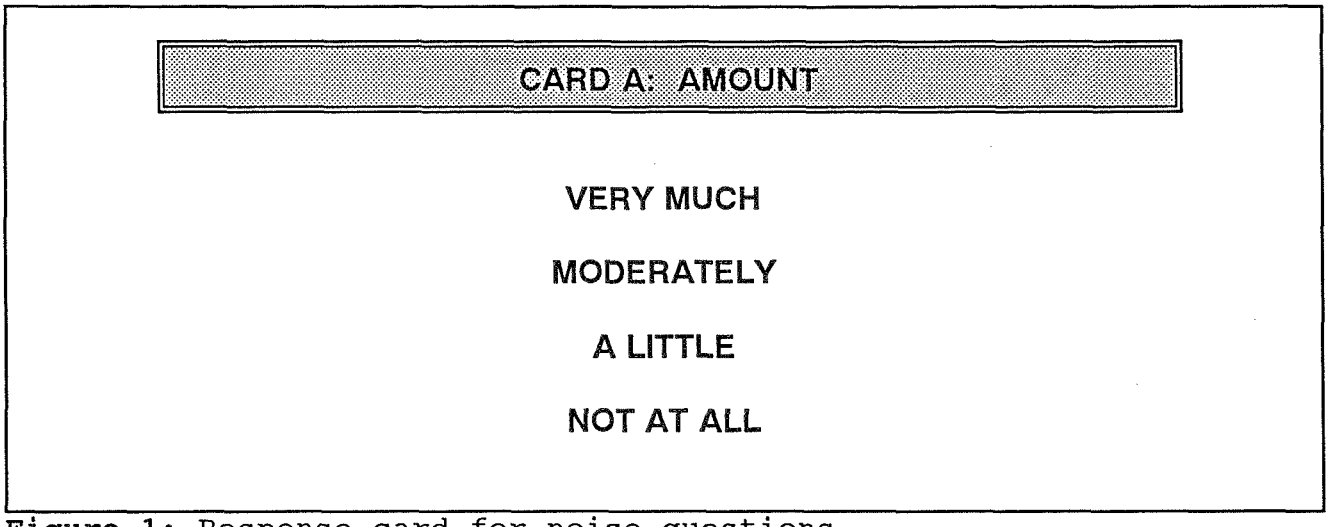

Figure 1: Response card for noise questions

Q6. We want to learn how you feel about the neighborhood right around here and about any advantages that make you feel it is a good place to live. In the six months since we last talked to you what are the one or two things you have liked most about this area?

Q7. How about any things that are disadvantages. What are the one or two disadvantages that you have disliked the most about this area in the last six months?

Figure 2: Beginning page of sonic boom questionnaire

The residents' reactions were obtained through fixed-format, interviewer-administered, face-to-face questionnaires. The questionnaire was developed during three rounds of pretests at three other locations in the United States at which booms are heard. The pretests provided the basis for improvements such as reducing unneeded material (all respondents were familiar with the term "sonic booms from jets") and maintaining rapport despite detailed questions about sonic boom effects. Interviewing procedures and the questionnaire were designed so that respondents were not initially alerted to the subject matter of the survey.

The professional interviewers on this project received an additional day of study-specific training for this study. Question-specific instructions were prepared. Control was maintained over interviewing procedures through on-site supervision, interview tape recordings and verification of 20 percent of the interviews by staff visits or follow-up telephone calls. An overall response rate of 78 percent was achieved.

Homes were randomly selected in three communities with strict procedures for identifying pre-selected respondents within homes. In the two smallest communities all eligible adults were interviewed. Due to the small study populations, about 400 of the Phase I respondents were reinterviewed during Phase II with a slightly shortened questionnaire.

Q8. Now some questions about noises you might have heard when you have been at home in the last six months.

a. What are some of the different types of noises you have heard around here? (PROBE: Anything else?) [MARK "VOL" FOR VOLUNTEERED NOISES]

b. [ASK FOR ALL NOISES NOT VOLUNTEERED] In the last six months, have you ever heard the noise from ...(cars or trucks or other road traffic going by)... when you were here at home?

[STOP!!!: COMPLETE ENTIRE LIST WITH b BEFORE STARTING c]

c. Here is an "AMOUNT" card for choosing your answer for the next question. [HAND CARD A TO RESPONDENT] [ASK FOR EACH SOUND HEARD]
During the last six months has the noise from ...(cars or trucks or other road traffic going by)...bothered or annoyed you very much, moderately, a little, or not at all?

	a,b HEARD	c. BOTHERED OR ANNOYED					
		VERY MUCH (1)	MODER-ATELY (2)	A LITTLE (3)	NOT AT ALL (4)	DK (8)	
i. Cars or trucks or other road traffic going by	1 VOL. ⇓ 2 YES ⇓	VERY 1	MODER 2	LITTLE 3	NOT 4	DK 8	
	3 NO ⇓ 4 DK ⇓						
ii. Motorcycles	1 VOL. ⇓ 2 YES ⇓	VERY 1	MODER 2	LITTLE 3	NOT 4	DK 8	
	3 NO ⇓ 4 DK ⇓						
iii. Neighbors' tools or outdoor equipment	1 VOL. ⇓ 2 YES ⇓	VERY 1	MODER 2	LITTLE 3	NOT 4	DK 8	
	3 NO ⇓ 4 DK ⇓						
iv. [REPEAT FULL QUESTION] ..Sonic booms from jets	1 VOL. ⇓ 2 YES ⇓	VERY 1	MODER 2	LITTLE 3	NOT 4 *[MARK Xs ⇒]*	DK 8	*MARK X AT Q12 & Q20*
	3 NO ⇓ 4 DK ⇓ FINISH THROUGH Q10						
v. Any other explosions or bangs or booms (besides the sonic booms) (DESCRIBE) _____	1 VOL. ⇓ 2 YES ⇓	VERY 1	MODER 2	LITTLE 3	NOT 4	DK 8	
	3 NO ⇓ 4 DK ⇓						
vi. Low-flying jet aircraft	1 VOL. ⇓ 2 YES ⇓	VERY 1	MODER 2	LITTLE 3	NOT 4	DK 8	
	3 NO ⇓ 4 DK ⇓						
vii. Any other airplanes (besides the low-flying jets) (DESCRIBE) _____	1 VOL. ⇓ 2 YES ⇓	VERY 1	MODER 2	LITTLE 3	NOT 4	DK 8	
	3 NO ⇓ 4 DK ⇓						
viii. [DESCRIBE ANY OTHER VOLUNTEERED NOISES HERE] _____	1 VOL. ⇓	VERY 1	MODER 2	LITTLE 3	NOT 4	DK 8	
	3 NO ⇓ 4 DK ⇓						

Figure 3: Second page of sonic boom questionnaire

I have a tape recording of one of the interviews for you to listen to now. The interviewer

switched on the recorder after entering the home, making the routine selection of the respondent, and obtaining permission to turn on the tape recorder. The interview begins with Question Q6. (Items Q1 to Q5 were for sample identification.) For the respondent this is almost entirely an aural event. The respondent sees only the interviewer and the occasional answer card (Figure 1). Only the interviewer sees the questionnaire, the relevant parts of which are reproduced in Figure 2 and Figure 3.

The sonic boom question (Question 8.iv in Figure 3) exactly parallels the aircraft noise question that has been previously used with over 10,000 residents near airports. The remainder of the questionnaire obtained reactions on other sonic boom annoyance scales and obtained detailed information about vibration, startle reactions, suspected damage, types of activity interference, demographic characteristics, and more general attitudes.

RESULTS

After the 1042 interviews were entered into a computer file and merged with the noise data, the reactions in each community were plotted by noise level. Figure 4 shows that at, for example, about DNL 25 to 35 dB(A), about 30 percent of the respondents said that they were "very much" annoyed by sonic booms (Question 8.iv. in Figure 3). To obtain a broader perspective on the meaning of that degree of annoyance, the respondents chose numbers to compare their feelings about sonic booms (arbitrarily set at a score of 100) with their feelings about other life-familiar events for which they could choose any number. Logarithmic averages of the ratios of their numerical ratings of sonic booms and other events indicate that the 79 percent of the respondents in the 25 to 35 dB range who expressed any annoyance with sonic booms felt that sonic booms were about as annoying as "hearing big noisy trucks if you lived near an intersection" or "having a dog next door that regularly barks in the middle of the night". As for all noise sources there is considerable variation in the respondents' reactions. In the 25 to 35 dB range, for example, about 21 percent are "not at all annoyed" by sonic booms. The remaining 79 percent who are at least a little annoyed consist of 27 percent who are "a little annoyed", 22 percent who are "moderately" annoyed, and 30 percent who choose the highest category of "very much" annoyed.

From a regulatory perspective the most important comparison is not with reactions to "barking dogs" but with reactions to other aircraft. In later analyses it is planned to relate the sonic boom results directly to 8 surveys that used the annoyance scales that are included in the sonic boom survey. The present preliminary results can be directly compared with one of those surveys; a 1985 survey of residents around five airports in the United Kingdom. Figure 4 presents this comparison for DNL (A). The figure indicates that the level of annoyance that is expressed in the sonic boom study at about 40 dB is not reached in this conventional aircraft noise study until about 60 to 70 dB.

The next figure (Figure 5) adds another line. The new line is the dose/response relationship predicted by a logistic regression analysis of 400 data points from 26 community noise survey data sets (Finegold, Harris, and von Gierke, 1994; Federal.., 1992). These 400 data points were drawn from a larger set of 453 data points that appeared in a dose/response synthesis study (Fidell, Barber, and Schultz: 1991). The new line is thus broadly consistent with the previous conclusion that sonic booms are much more annoying than other community noises.

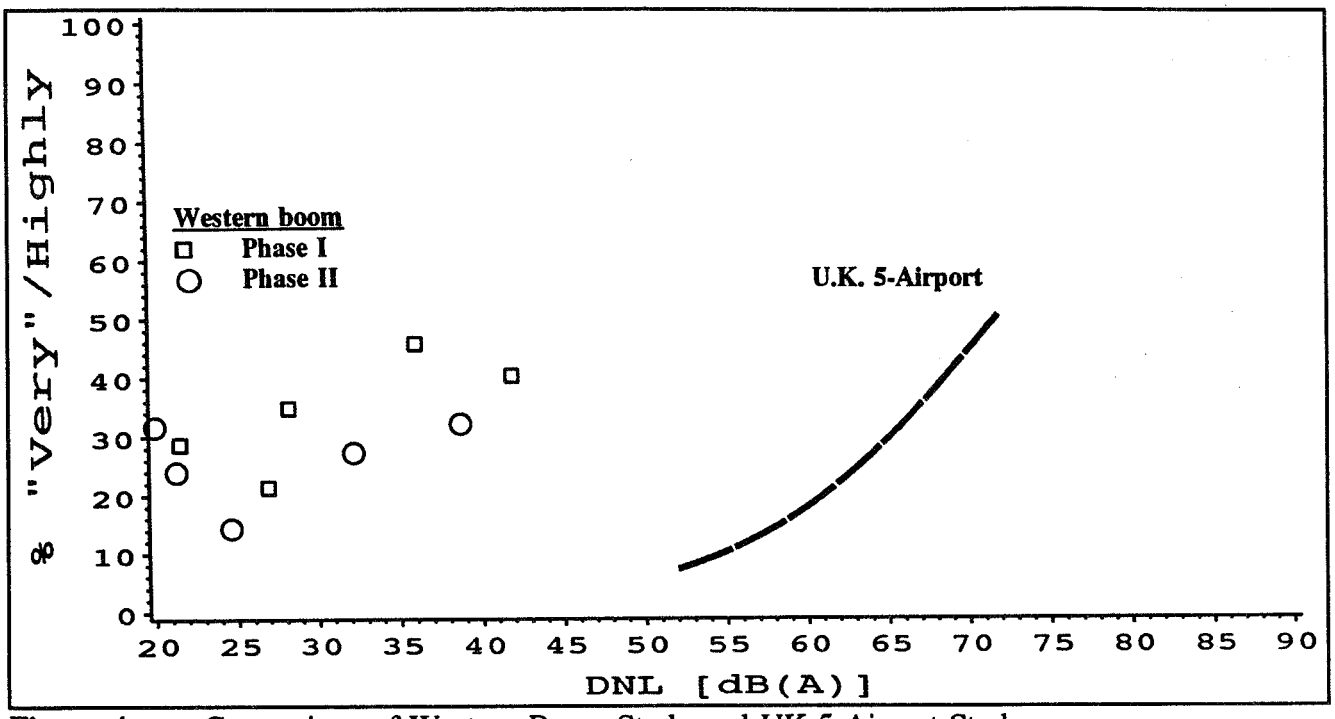

Figure 4: Comparison of Western Boom Study and UK 5-Airport Study

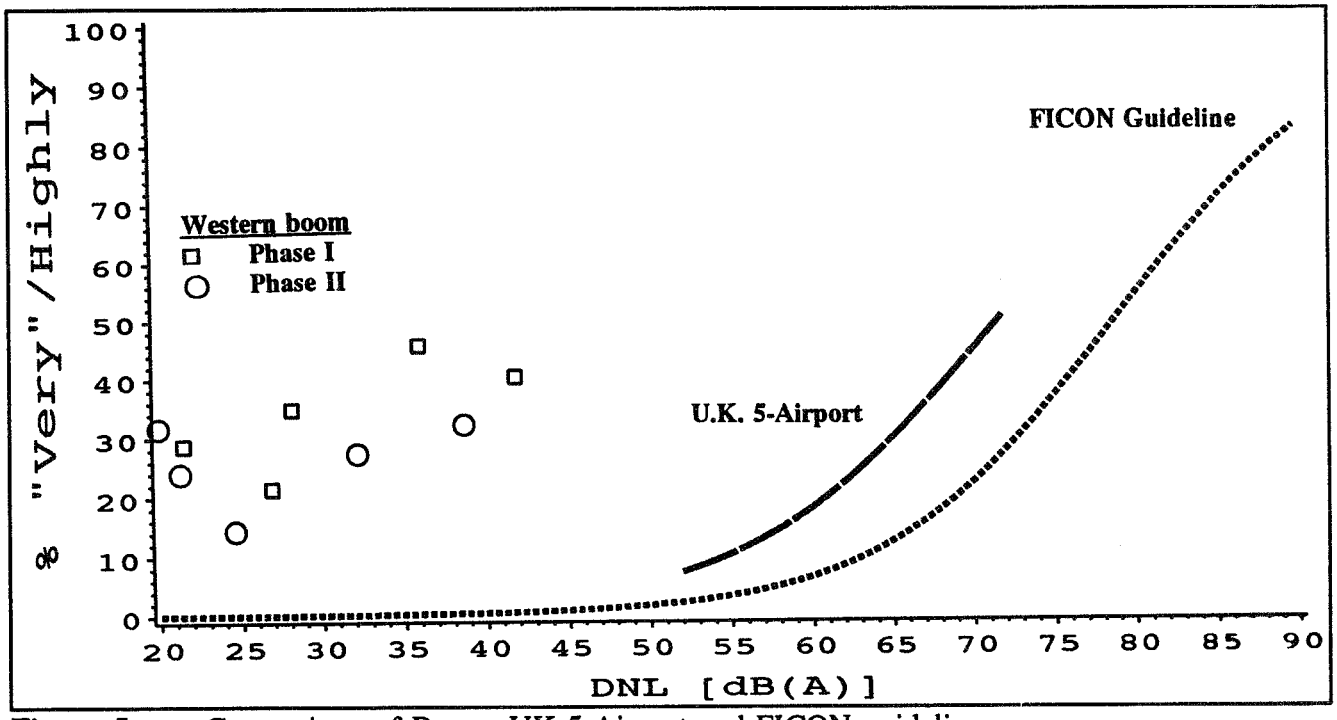

Figure 5: Comparison of Boom, UK 5-Airport and FICON guideline

In the following figure (Figure 6) the sonic boom sites are compared to all 453 data points from the complete synthesis study (Fidell, Barber, and Schultz: 1991). The general conclusion remains unchanged; sonic booms appear to be more annoying than would be predicted by other community noise data. While all of the displays of data come to this same general conclusion, several difficulties interfere with drawing more precise conclusions about the size of the difference

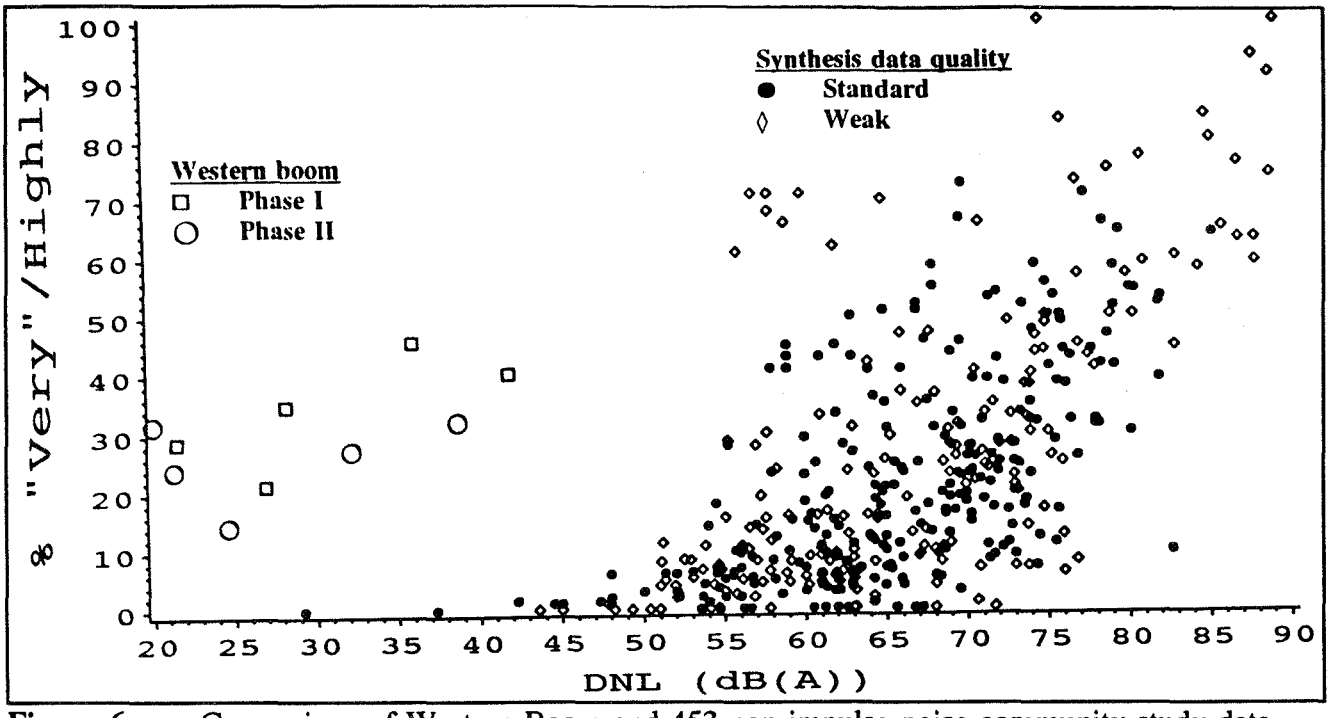

Figure 6: Comparison of Western Boom and 453 non-impulse noise community study data points

between reactions to sonic booms and to other aircraft. First, the 453 data points are based on a diverse set of annoyance questions, only one of which was the same as was used in the sonic boom survey. Second, the 453 data points represent studies of reactions to a diverse set of noise sources including aircraft, road traffic and undifferentiated community noise. Third, the 453 data points from the 29 studies differ from one another in more fundamental ways that hinder any comparison. The points marked with open symbols in Figure 6, for example, are based on data from studies with the following types of weaknesses: 1) the respondent was not asked about the measured noise environment, 2) the annoyance measure is relative to local features that vary between sites, (3) a transportation noise source is not specified in the question, or 4) the annoyance measure is a complex combination of questions that is not clearly definable as high annoyance (Fields, 1994).

Figure 6 raises one other issue; there is very little overlap between the noise levels observed for the sonic boom study and the noise levels observed for the other surveys. Although the three lowest overlapping data points in the synthesis study (between DNL 29 and 43 dB) used the same annoyance scale as was used in the boom survey, all three come from a railway noise survey in which the respondents have been shown to be less annoyed than respondents to conventional aircraft noise surveys (Fields and Walker, 1982). These very low sonic boom exposures are a result of the very low frequency of the sonic boom events. The use of energy averaging for such infrequent events has not been examined in previous studies. If it were speculated that respondents at such low levels do not react to the long-term average, but rather to the worst sonic boom days, then the sonic boom reactions should be plotted at higher noise levels. To examine the implications of such speculations, the sonic boom reactions in Figure 7 are plotted at noise levels which are DNL 14 dB(A) higher than previously. The 14 dB difference is approximately the average difference between the average noise level for all days and for the three highest days. Even after this speculative adjustment that does not make a corresponding adjustment for the three highest days around

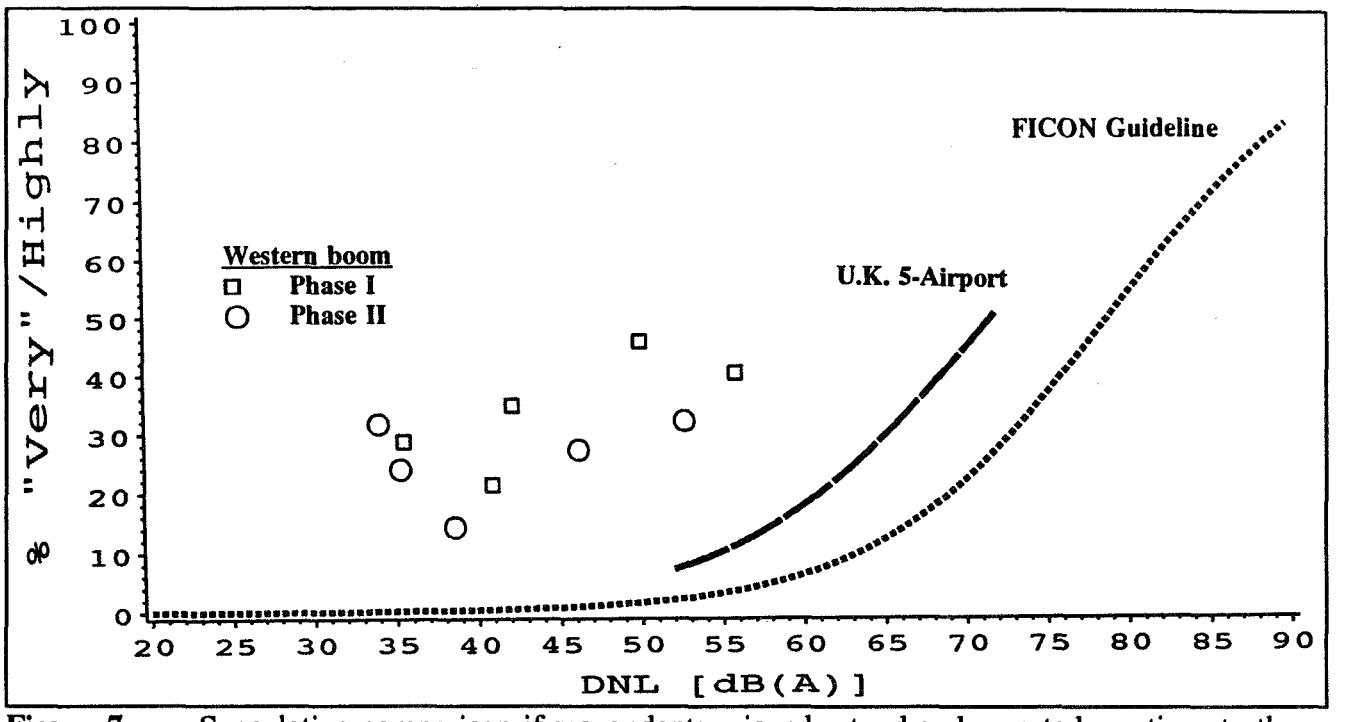

Figure 7: Speculative comparison if respondents misunderstood and reported reactions to the worst three days for only the sonic boom study

conventional airports, the sonic boom reactions are stronger than those to other noise sources.

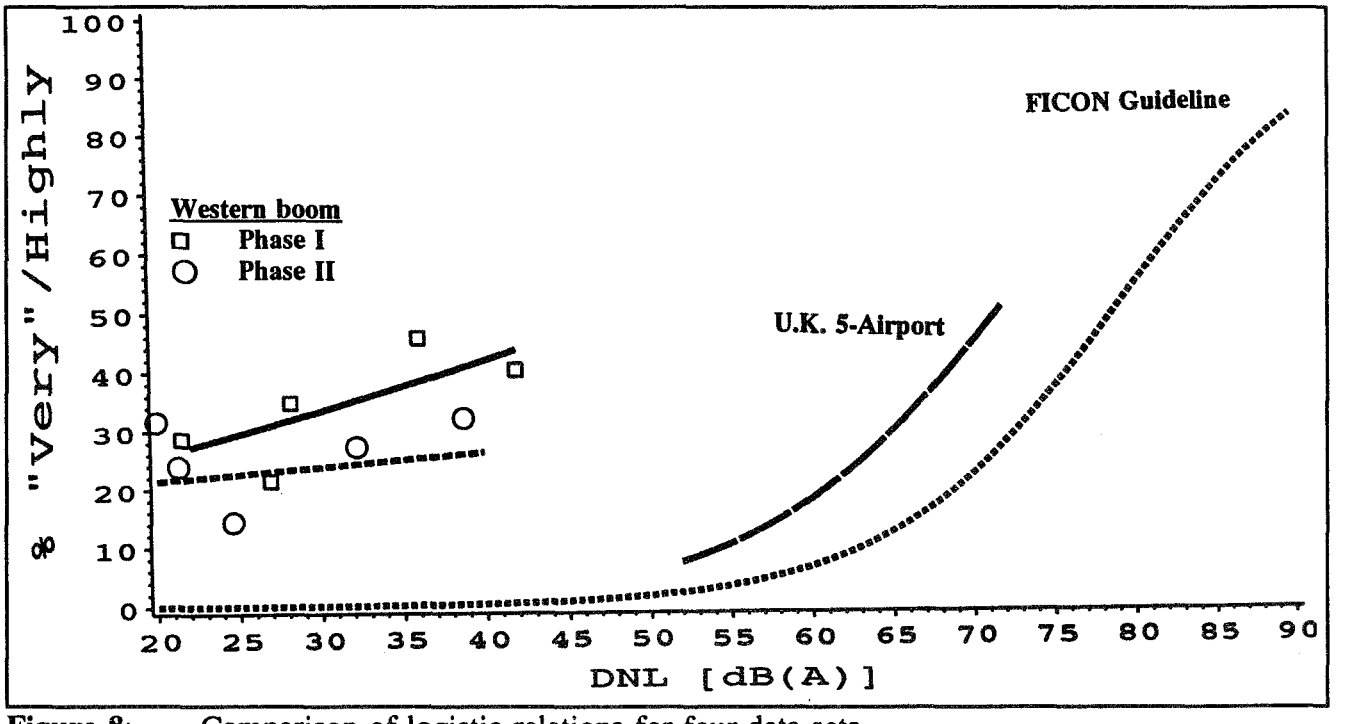

Figure 8: Comparison of logistic relations for four data sets

The final figure (Figure 8) shows four logistic regression lines; one for each of the two boom study phases, one for the five-airport UK study and one for the 400 point synthesis. This figure

raises at least one additional point: the difference between the two phases of the boom study. While we can presently theorize about the reasons for such a difference, the data have still to be examined. The precision of the noise estimates and the dose/response relationships must both be examined before these and other issues can be addressed.

It is important to conclude by emphasizing that these are preliminary results from an on-going project. An additional data collection phase is planned, some aspects of the noise data have still to be examined, and detailed analyses of the social survey data have not begun. The present data indicate that sonic booms are more annoying than would be predicted from the findings from one carefully matched aircraft noise survey and from widely-accepted summaries of dose/response relationships. More analysis is planned before the size of this difference is quantified and before explanations for the differences in reactions can be examined with these data.

REFERENCES

Federal Interagency Committee on Noise (FICON): 1992. Federal Agency Review of Selected Airport Noise Analysis Issues. FICON, Washington D.C.

Fidell, Sanford; Barber, David S. and Schultz, Theodore, J.: 1991. Updating a Dosage-effect Relationship for the Prevalence of Annoyance due to General Transportation Noise. J. Acoust. Soc. Am. Vol 89. pp. 221-233.

Fields, J.M.: 1994. A Review of an Updated Synthesis of Noise/Annoyance Relationships. NASA CR-194950. National Aeronautics and Space Administration, Washington D.C.

Fields, J.M.; and Walker, J.G.: 1982. Comparing the Relationships Between Noise Level and Annoyance in Different Surveys: A Railway Noise vs. Aircraft and Road Traffic Comparison. J. Sound Vib., vol. 81, pp. 51-80.

Finegold, Lawrence S.; Harris, Stanley C.; and von Gierke, Henning E.: 1994. Community Annoyance and Sleep Disturbance: Updated Criteria for Assessing the Impacts of General Transportation Noise on People. Noise Control Engineering J. Vol 42. pp. 25-30.

Lee, Robert A.; Crabill, Monty; Magurek, Doug; Palmer, Barbara; and Price, Dale: 1989. Air Force Boom Event Analyzer Recorder (BEAR): System Description. Report No. AAMRL-TR-89-035. Harry G. Armstrong, Aerospace Medical Research Laboratory, Wright-Patterson AFB, Ohio.

PARTICIPANTS

Dr. Richard Antcliff
Mail Stop 235A
NASA Langley Research Center
Hampton, VA 23681-0001
Ph.: 804-864-4606
FAX: 804-864-8315
E-Mail: R.R.ANTCLIFF@LARC.NASA.GOV

Mr. Daniel G. Baize
Mail Stop 412
NASA Langley Research Center
Hampton, VA 23681-0001
Ph.: 804-864-1071
FAX: 804-864-3553
E-Mail: D.G.BAIZE@LARC.NASA.GOV

Dr. Timothy J. Baker
Room D309
Dept. of Mechanical & Aeronautical Engineering
Olden Street, Engineering Quadrangle
Princeton University
Princeton, NJ 08544-5263
Ph.: 609-258-5205
FAX: 609-258-1939
E-Mail: BAKER@COUGARXP.PRINCETON.EDU

Dr. Richard Barnwell
Mail Stop 119
NASA Langley Research Center
Hampton, VA 23681-0001
Ph.: 804-864-4129
FAX: 804-864-8852
E-Mail:
RICHARD_BARNWELL@HSR.LARC.NASA.GOV

Mr. David T. Blackstock
Applied Research Laboratories
University of Texas at Austin
P.O. Box 8029
Austin, TX 78713-8029
Ph.: 512-835-3374
FAX: 512-835-3259
E-Mail: DTB@MCL.CC.UTEXAS.EDU

Mr. Percy J. Bobbitt
Eagle Aerospace, Inc.
Tower Box 77
2101 Executive Drive
Hampton, VA 23666
Ph.: 804-827-1100
FAX: 804-827-1106
E-Mail: BOBBITT@EAGLE.COM

Ms. Sherilyn A. Brown
Mail Stop 463
NASA Langley Research Center
Hampton, VA 23681-0001
Ph.: 804-864-3593
FAX: 804-864-8823
E-Mail: S.A.BROWN@LARC.NASA.GOV

Mr. David B. Bruns
Mail Stop 35-59
McDonnell Douglas Aerospace—West
3855 Lakewood Blvd.
Long Beach, CA 90846
Ph.: 310-593-8312
FAX: 310-982-7787
E-Mail:
C372746%DVSS.DECNET@LBGWY.MDC.COM

Mr. Peter P. Camacho
Mail Code 35-59
McDonnell Douglas Aerospace—West
3855 Lakewood Blvd.
Long Beach, CA 90846
Ph.: 310-593-7012
FAX: 310-982-7787
E-Mail: camacho@mdta.mdc.com (lower case)

Mr. Frank W. Cazier, Jr.
Mail Stop 462
NASA Langley Research Center
Hampton, VA 23681-0001
Ph.: 804-864-2860
FAX: 804-864-7687
E-Mail: F.W.CAZIER@LARC.NASA.GOV

Mr. Joseph R. Chambers
Mail Stop 246A
NASA Langley Research Center
Hampton, VA 23681-0001
Ph.: 804-864-6399
FAX: 804-864-6135
E-Mail: J.R.CHAMBERS@LARC.NASA.GOV

Professor Hsien K. Cheng
Dept. of Aerospace Engineering
University of Southern California
Los Angeles, CA 90089-1191
Ph.: 213-740-5365
FAX: 213-740-7774
E-Mail: CHENG@SPOCK.USC.EDU

Dr. Samson H. Cheung
MCAT Institute
Mail Stop 258-1
NASA Ames Research Center
Moffett Field, CA 94035-1000
Ph.: 415-604-4462
FAX: 415-604-4377
E-Mail: CHEUNG@NAS.NASA.GOV

Mr. Robin O. Cleveland
Applied Research Laboratories
The University of Texas at Austin
P.O. Box 8029
Austin, TX 78713-8029
Ph.: 512-835-3032
FAX: 512-835-3259
E-Mail: ROBIN@CCWF.CC.UTEXAS.EDU

Ms. Susan E. Cliff
Mail Stop 227-2
NASA Ames Research Center
Moffett Field, CA 94035-1000
Ph.: 415-604-3907
FAX: 415-604-4357
E-Mail: CLIFF@RA-IRIS.ARC.NASA.GOV

Ms. Brenda Cook
USAF HQ ACC/CEVA
Langley AFB, VA 23665-2769
Ph.: 804-764-3056/3328
FAX: 804-764-5363
E-Mail: COOKB@CEMAIL.ACC.AF.MIL

Dr. Christine M. Darden
Mail Stop 412
NASA Langley Research Center
Hampton, VA 23681-0001
Ph.: 804-864-5258
FAX: 804-864-3553
E-Mail: CMDARD@AVDOO.LARC.NASA.GOV

Ms. Latoya Deans
Mail Stop 412
NASA Langley Research Center
Hampton, VA 23681-0001
Ph.: 804-864-5258
FAX: N/A
E-Mail: N/A

Dr. J. Micah Downing
USAF AL/OEBN
2610 Seventh Street
Wright-Patterson AFB, OH 45433-7901
Ph.: 513-255-3664
FAX: 513-476-7680
E-Mail:
JMD%OSPREY@EAGLEB.AAMRL.WPAFB.AF.MIL

Mr. L. J. Ehernberger
Aerodynamics Branch
Mail Stop D-2033
P.O. Box 273
NASA Dryden Flight Research Center
Edwards, CA 93523-0273
Ph.: 805-258-3699
FAX: 805-258-2842
E-Mail: EHRE@CS1.DFRF.NASA.GOV

Dr. Sanford Fidell
BBN Systems and Technologies
21120 Vanowen Street
Canoga Park, CA 91303
Ph.: 818-226-0323
FAX: 818-716-8377
E-Mail: FIDELL@BBN.COM

Dr. James M. Fields
Consultant in Acoustics
10407 Royal Road
Silver Spring, MD 20903-1112
Ph.: 301-439-4356 / 202-512-9796
FAX: 301-439-4356
E-Mail: JFIELDS@CAP.GWU.EDU

Dr. Kamran Fouladi
Lockheed Engineering & Sciences Co.
Mail Stop 412
NASA Langley Research Center
Hampton, VA 23681-0001
Ph.: 804-864-5993
FAX: 804-864-3553
E-Mail: FOULADI@AVD00.LARC.NASA.GOV

Mr. Edward A. Haering, Jr.
Aerodynamics Branch
Mail Stop D-2033
P.O. Box 273
NASA Dryden Flight Research Center
Edwards, CA 93523-0273
Ph.: 805-258-3696
FAX: 805-258-2842
E-Mail: HAERING@CS1.DFRF.NASA.GOV

Mr. George T. Haglund
Mail Stop 6H-FK
Boeing Commercial Airplane Group
P.O. Box 3707
Seattle, WA 98124-2207
Ph.: 206-965-3773
FAX: 206-234-4543
E-Mail: N/A

Mr. Jerry N. Hefner
Mail Stop 462
NASA Langley Research Center
Hampton, VA 23681-0001
Ph.: 804-864-3640
FAX: 804-864-7687
E-Mail: J.N.HEFNER@LARC.NASA.GOV

Mr. R. David Hilliard
Wyle Laboratories
Mail Stop 239
NASA Langley Research Center
Hampton, VA 23681-0001
Ph.: 804-865-0000, X234
FAX: 804-865-8116
E-Mail: N/A

Mr. Harvey H. Hubbard
Mail Stop 463
NASA Langley Research Center
Hampton, VA 23681-0001
Ph.: 804-864-3610
FAX: 804-864-8823
E-Mail: N/A

Mr. Joseph Laiosa
1111 Stewart Avenue
Mail Stop C50-05
Grumman Aircraft Corporation
Bethpage, NY 11793-3582
Ph.: 516-575-0900
FAX: 516-575-1968
E-Mail: LAIOSA@GRUMMAN.COM

Dr. Jack D. Leatherwood
Mail Stop 463
NASA Langley Research Center
Hampton, VA 23681-0001
Ph.: 804-864-3591
FAX: 804-864-8823
E-Mail: J.D.LEATHERWOOD@LARC.NASA.GOV

Mr. Bart Lipkens
MacroSonix
1054 Technology Park Dr.
Glen Allen, VA 23060
Ph.: 804-262-3700
FAX: 804-266-4627
E-Mail: N/A

Mr. David P. Lux
Aerospace Projects/SR-71 Project
Mail Stop D-2071
P.O. Box 273
NASA Dryden Flight Research Center
Edwards, CA 93523-0273
Ph.: 805-258-3026
FAX: 805-258-2134
E-Mail: DAVE_LUX@QMGATE.DFRF.NASA.GOV

Mr. Robert J. Mack
Mail Stop 412
NASA Langley Research Center
Hampton, VA 23681-0001
Ph.: 804-864-5988
FAX: 804-864-3553
E-Mail: R.J.MACK@LARC.NASA.GOV

Dr. Lucio Maestrello
Mail Stop 463
NASA Langley Research Center
Hampton, VA 23681-0001
Ph.: 804-864-1067
FAX: 804-864-8823
E-Mail: N/A

Mr. Domenic J. Maglieri
Eagle Engineering, Inc.
Tower Box 77
2101 Executive Drive
Hampton, VA 23666
Ph.: 804-827-1100
FAX: 804-827-1106
E-Mail: VSOTH@EAGLE.COM

Mr. Gerry L. McAninch
Mail Stop 460
NASA Langley Research Center
Hampton, VA 23681-0001
Ph.: 804-864-5269
FAX: 804-864-8290
E-Mail: G.L.MCANINCH@LARC.NASA.GOV

Mr. David A. McCurdy
Mail Stop 463
NASA Langley Research Center
Hampton, VA 23681-0001
Ph.: 804-864-3596
FAX: 804-864-8823
E-Mail: D.A.MCCURDY@LARC.NASA.GOV

Mr. John M. Morgenstern
Mail Code 35-59
McDonnell Douglas Aerospace—West
3855 Lakewood Blvd.
Long Beach, CA 90846
Ph.: 310-593-7012
FAX: 310-982-7787
E-Mail: DBRUNS@MDTA.MDC.COM

Mr. Alan K. Mortlock
Mail Code 35-29
McDonnell Douglas Aerospace—West
3855 Lakewood Blvd.
Long Beach, CA 90846
Ph.: 310-593-3937
FAX: 310-982-7787
E-Mail: N/A

Ms. Kathy E. Needleman
Lockheed Engineering & Sciences Co.
Mail Stop 412
NASA Langley Research Center
Hampton, VA 23681-0001
Ph.: 804-864-5987
FAX: 804-864-3553
E-Mail: K.E.NEEDLEMAN@LARC.NASA.GOV

Professor Allan D. Pierce
Dept. of Aerospace & Mechanical Engineering
Boston University
110 Cummington Street
Boston, MA 02215
Ph.: 617-353-4841
FAX: 617-353-5760/5866
E-Mail: ADP@BUENGA.BU.EDU

Dr. Kenneth J. Plotkin
Suite 701
Wyle Laboratories
2001 Jefferson Davis Highway
Arlington, VA 22202
Ph.: 703-415-4550
FAX: 703-415-4556
E-Mail: KPLOTKIN@ACCESS.DIGEX.NET

Mr. Joe W. Posey
Mail Stop 460
NASA Langley Research Center
Hampton, VA 23681-0001
Ph.: 804-864-7686
FAX: 804-864-8290
E-Mail: J.W.POSEY@LARC.NASA.GOV

Dr. Clemans A. Powell
Mail Stop 462
NASA Langley Research Center
Hampton, VA 23681-0001
Ph.: 804-864-3640
FAX: 804-864-7687
E-Mail: C.A.POWELL@LARC.NASA.GOV

Mr. Robert G. Rackl
Mail Stop 6H-FR
Boeing Commercial Airplane Group
P.O. Box 3707
Seattle, WA 98124-2207
Ph.: 206-965-1207
FAX: 206-237-3808
E-Mail: RGR4320@MU.CA.BOEING.COM

Dr. Richard Raspet
Dept. of Physics and Astronomy
National Center for Physical Acoustics
University of Mississippi
University, MS 38677
Ph.: 601-232-5888
FAX: 601-232-7494
E-Mail: RASPET@NSXT1.NCPA.OLEMISS.EDU

Dr. Leick D. Robinson
Science Applications International Corporation
Suite 100
13091 Pond Springs Road
Austin, TX 78729
Ph.: 512-219-5511
FAX: 512-219-5519
E-Mail: LEICK@BGA.COM

Dr. Zvi Rusak
Dept. of Mechanical Engineering, Aeronautical Engineering & Mechanics
JEC 4009
Rensselaer Polytechnic Institute
Troy, NY 12180-3590
Ph.: 518-276-3036
FAX: 518-276-2623
E-Mail: USERGLMB@MTS.RPI.EDU

Dr. Kevin P. Shepherd
Mail Stop 463
NASA Langley Research Center
Hampton, VA 23681-0001
Ph.: 804-864-3575
FAX: 804-864-8823
E-Mail: K.P.SHEPHERD@LARC.NASA.GOV

Mr. Michael J. Siclari
Mail Stop A08-35
Grumman Corporation
1111 Stewart Avenue
Bethpage, NY 11746
Ph.: 516-575-8067
FAX: 516-575-7716
E-Mail: N/A

Mr. Norbert F. Smith
Suite 120
McDonnell Douglas Aerospace
22 Enterprise Parkway
Hampton, VA 23666-5844
Ph.: 804-825-3350/838-2551
FAX: 804-838-8176
E-Mail: TBD

Dr. Victor W. Sparrow
Graduate Program in Acoustics
157 Hammond Building
The Pennsylvania State University
University Park, PA 16802
Ph.: 814-865-3162
FAX: 814-863-7222
E-Mail: SPARROW@HELMHOLTZ.PSU.EDU

Mr. David G. Stephens
Mail Stop 462
NASA Langley Research Center
Hampton, VA 23681-0001
Ph.: 804-864-3640
FAX: 804-864-7687
E-Mail: D.G.STEPHENS@LARC.NASA.GOV

Ms. Brenda M. Sullivan
Lockheed Engineering & Sciences Co.
Mail Stop 463
NASA Langley Research Center
Hampton, VA 23681-0001
Ph.: 804-864-3585
FAX: 804-864-8823
E-Mail: B.M.SULLIVAN@LARC.NASA.GOV

Mr. Louis C. Sutherland
Consultant in Acoustics
27803 Longhill Drive
Rancho Palos Verdes, CA 90274
Ph.: 310-541-1655
FAX: 310-322-9799
E-Mail: TBD

Dr. Leonard M. Weinstein
Mail Stop 170
NASA Langley Research Center
Hampton, VA 23681-0001
Ph.: 804-864-5543
FAX: 804-864-8348
E-Mail: L.M.WEINSTEIN@LARC.NASA.GOV

Mr. Alan R. Wenzel
Virginia Polytechnic Inst. & State Univ.
Mail Stop 460
NASA Langley Research Center
Hampton, VA 23681-0001
Ph.: 804-864-5267
FAX: 804-864-8290
E-Mail: N/A

Dr. Alan W. Wilhite
Mail Stop 119
NASA Langley Research Center
Hampton, VA 23681-0001
Ph.: 804-864-2982
FAX: 804-864-8852
E-Mail: A.W.WILHITE@LARC.NASA.GOV

REPORT DOCUMENTATION PAGE

Form Approved
OMB No. 0704-0188

1. AGENCY USE ONLY *(Leave blank)*	2. REPORT DATE	3. REPORT TYPE AND DATES COVERED
	October 1994	Conference Publication

4. TITLE AND SUBTITLE
High-Speed Research: 1994 Sonic Boom Workshop — Atmospheric Propagation and Acceptability Studies

5. FUNDING NUMBERS
537-03-21-03

6. AUTHOR(S)
David A. McCurdy, Editor

7. PERFORMING ORGANIZATION NAME(S) AND ADDRESS(ES)
NASA Langley Research Center
Hampton, VA 23681-0001

8. PERFORMING ORGANIZATION REPORT NUMBER
L-17434

9. SPONSORING/MONITORING AGENCY NAME(S) AND ADDRESS(ES)
National Aeronautics and Space Administration
Washington, DC 20546-0001

10. SPONSORING/MONITORING AGENCY REPORT NUMBER
NASA CP-3279

11. SUPPLEMENTARY NOTES
Point of Contact: David A. McCurdy, NASA Langley Research Center, MS 463, Hampton, VA 23681-0001
804-864-3596

12a. DISTRIBUTION/AVAILABILITY STATEMENT
Unclassified–Unlimited
Subject Category 02

12b. DISTRIBUTION CODE

13. ABSTRACT *(Maximum 200 words)*

The third High-Speed Research Sonic Boom Workshop was held at NASA Langley Research Center on June 1–3, 1994. The purpose of this workshop was to provide a forum for Government, industry, and university participants to present and discuss progress in their research. The workshop was organized into sessions dealing with atmospheric propagation; acceptability studies; and configuration design, analysis, and testing. Attendance at the workshop was by invitation only.

The workshop proceedings include papers on atmospheric propagation and acceptability studies. Papers discussing atmospheric effects on the sonic boom waveform addressed several issues. It has long been assumed that the effects of molecular relaxation are adequately accounted for by assuming that a steady state balance between absorption and nonlinear wave steepening exists. It was shown that the unsteadiness induced by the nonuniform atmosphere precludes attaining this steady state. Further, it was shown that the random atmosphere acts as a filter, effectively filtering out high frequency components of the distorted waveform. Several different propagation models were compared, and an analysis of the sonic boom at the edge of the primary carpet established that the levels there are bounded. Finally, a discussion of the levels of the sonic boom below the sea surface was presented. Papers on acceptability examined the reaction of people to long-term sonic boom exposure.

14. SUBJECT TERMS
Sonic boom extrapolation; Sonic boom acceptability; Sonic boom minimization; Atmospheric effects on sonic boom

15. NUMBER OF PAGES
230

16. PRICE CODE
A11

17. SECURITY CLASSIFICATION OF REPORT	18. SECURITY CLASSIFICATION OF THIS PAGE	19. SECURITY CLASSIFICATION OF ABSTRACT	20. LIMITATION OF ABSTRACT
Unclassified	Unclassified	Unclassified	Unclassified

National Aeronautics and
Space Administration
Langley Research Center
Mail Code 180
Hampton, VA 23681-00001

SPECIAL FOURTH-CLASS RATE
POSTAGE & FEES PAID
NASA
Permit No. G-27